On the physical interaction between ocean waves and coastal cliffs

Simon John Varley

A thesis submitted in partial fulfilment of the requirements for the University of Durham for the degree of Doctor of Philosophy

June 2018

Abstract

Wave impacts have long been posited as the primary forcing mechanism of coastal cliff recession. Recent developments in the study of hydrodynamics at coastal structures such as seawalls and breakwaters have shown that wave pressures are stochastic in nature and have a broad range of first- and second-order controls. This understanding has yet to be translated to coastal cliffs, where it is still largely assumed that wave impact characteristics can be predicted by simple deterministic formulae. Hydraulic components in coastal models are limited by the lack of in-situ measurements of waves at the cliff toe due to the difficulties in deploying instrumentation in such energetic and inaccessible environments.

To address this, I have approached the problem threefold. Monthly high-resolution terrestrial laser scanning (TLS) was undertaken over a year at multiple sites at Staithes, North Yorkshire, to evaluate the recession rate and detachment characteristics of the lower cliff section. Concurrently, wave gauges were deployed at the cliff toe of each site to monitor wave conditions. A novel method of measuring wave impacts was undertaken at one of the sites for nine low-to-low tidal cycles. New and established methods for processing this data were used.

Analysis of the erosion dataset revealed distinct temporal patterns of erosion, with accelerated erosion rates during winter. Vertical variations in detachment volumes below 0.1 m^3 related to the tidal elevation were also observed, suggesting a key marine influence. Detachment frequency and volume were found to be influenced by lithology type and joint density. Wave conditions over the study period were found to be depth-limited, yet some waves at the toe were found to be larger than those offshore due to shoaling. Wave breaking conditions were strongly influenced by platform morphology and tidal stage. Up to 9% of all waves were breaking on impact. Measurements of wave impacts revealed approximately 14% of wave exhibited high-magnitude impulsive pressures generated by breaking and broken waves. These were analysed probabilistically and found to be controlled primarily by the ratio between wave height and water depth.

These data were used to develop a conceptual model of forcing at the cliff toe, including an evaluation of the ability of waves to remove material via enhanced pressure inside discontinuities and fragmentation of weathered material. These results have broad implications concerning the process geomorphology of rock coasts and the evaluation of wave forcing in coastal models.

Contents

List of figures

List of tables

Nomenclature

A	Sunamura (1992) constant (unitless)
a	Rise time equation power law constant (unitless)
b	Rise time equation power law exponent (unitless)
c	Wave height depth limit intercept (unitless)
d	Water depth (m)
d_b	Wave breaking depth (m)
d_{cliff}	Still water depth at the cliff toe (m)
d_i	Model: water depth at index i (m)
d_{inst}	Instantaneous water depth (m)
d_{max}	Maximum water depth (m)
d_{trough}	Wave trough depth (m)
d_{wave}	Wave crest depth (m)
D_5	Dataset where sample rate = 5 Hz
D_{100}	Dataset where sample rate = 100 Hz
D_{5000}	Dataset where sample rate = 5000 Hz
D_q	Erosion detachment frequency ($^{y-1}$)
D_v	Erosion detachment volume (m^3)
E	Elevation (m ODN)
E_s	Sensor elevation (m ODN)
E_{max}	Elevation of P_{max} (m ODN)
E_{toe}	Elevation of cliff toe (m ODN)
f_r	Sunamura (1977) resisting force of rocks (unitless)
f_w	Sunamura (1977) assailing force of waves (unitless)
F	Forcing magnitude (unitless)
F_E	Cumulative forcing magnitude at elevation E (unitless)
F_{Tot}	Cumulative integrated forcing magnitude (unitless)
g	Acceleration due to gravity (ms^{-2})
H	Wave height (m)
$\overline{H}$	Mean wave height (m)
H_0	Deep water wave height (m)

$H_{1/10}$	1/10th wave height (m)
H_b	Breaking wave height (m)
H_{cliff}	Cliff toe wave height (m)
H_i	Wave height at index *i* (m)
H_m	Maximum wave height (m)
H_{RMS}	Root mean square wave height (m)
H_s	Significant wave height (m)
H_{s_i}	Significant wave height at index *i* (m)
i	Model: wave index (unitless)
i_{count}	Model: number of waves in given tide (unitless)
I	Iribarren number
J	Shoreward force per m run (kN per m run)
J_{dyn}	Dynamic shoreward force per m run (kN per m run)
J_{max}	Maximum shoreward force per m run (kN per m run)
k	Trenhaile (2000) platform attenuation constant (unitless)
K	Sunamura (1977) calibration constant (unitless)
L	Wavelength (m)
n_w	Wave index number (unitless)
p_{atmos}	Atmospheric pressure (kPa)
p_{sensor}	Absolute pressure measured at wave gauge (kPa)
P	Pressure (kPa)
P_{dyn}	Dynamic wave impact pressure component (kPa)
P_{hyd}	Hydrostatic wave impact pressure component (kPa)
P_{max}	Maximum wave impact pressure (kPa)
P_{max250}	Highest 1/250 P_{max} values in a dataset (exceedance level 99.6%)
R	Platform roughness (unitless)
S_p	Platform slope (°)
S_r	Platform ramp slope (°)
t	Time (s)
t_a	Wave peak arrival time (s)
t_{end}	Wave impact end time (s)
t_{max}	Time at pressure maximum (s)

t_P	Wave impact duration (s)
t_{rise}	Rise time (s)
t_{start}	Wave impact start time (s)
T	Mean wave period (s)
T_0	Deep water wave period (s)
T_s	Significant wave period (s)
u	Fluid particle velocity (ms^{-1})
v_c	Wave celerity (ms^{-1})
v_s	Fluid acoustic velocity (ms^{-1})
w	Platform width (m)
W_d	Inundation duration
W_q	Water level frequency
x	Wave transformation power law constant coefficient (unitless)
α	Erosion volume magnitude frequency power law constant (unitless)
β	Erosion volume magnitude frequency power law exponent (unitless)
γ	Wave height depth-limited constant of proportionality (unitless)
θ	Cliff aspect (°)
κ	Wave transformation power law exponent (unitless)
λ	Exponential distribution rate parameter (unitless)
ξ	Wave energy density (Jm^{-2})
ξ_{cliff}	Cliff toe wave energy density (Jm^{-2})
$\xi_{difference}$	Percentage difference between offshore and cliff toe wave energy density (Jm^{-2})
$\xi_{offshore}$	Offshore wave energy density (Jm^{-2})
ξ_{total}	Overall percentage of offshore wave energy density at the cliff toe (Jm^{-2})
ρ	Density of seawater (kg m^{-3})
ς	Blackmore and Hewson (1984) aeration constant (unitless)
τ	Joint spacing (m)
υ	Tidal range (m)
χ	Erosion rate (m y^{-1})
φ	Sample rate (Hz)

Declaration and statement of copyright

I confirm that no part of the material presented in this thesis has previously been submitted by me or any other person for a degree in this or any other university. In all cases, where is relevant, material from the work of others has been acknowledged.

Simon John Varley

Department of Geography

Durham University

Submitted - June 2018

Acknowledgements

This thesis would not have been possible without the ideas, support and encouragement from my two supervisors, Dr Nick Rosser and Dr Matt Brain. They have been immeasurably patient, motivating and accommodating throughout, having guided and assisted me through the distilling of early ideas into achievable aims, fieldwork planning, data analysis and writing stages (despite the destruction of a wide range of field equipment). In addition, my honorary supervisor Dr Emma Vann Jones has also been a great help in developing ideas and techniques. I would also like to acknowledge ICL Fertilizers Ltd, who provided the funding for this project, as well as Stephen Lishman and Malcolm Robertshaw from the Department of Physics, who assisted in the design and construction of my field equipment. Further thanks go to my examiners, Dr Rich Hardy and Dr Mark Dickson, for an informative and interesting viva, despite the time difference.

I wish to thank all those who assisted me in fieldwork on the often cold, wet and windy Yorkshire coast: Bertie, Clare, Callum, Beverley, Rich, Emma and Sam all provided their time, skills and company for very little reward (apart from the genuine pleasure of the world's greatest brownies at Willow Cake Shop). Merv's excellent assistance and advice in the workshop was also invaluable. A special thanks goes to my three CoBRA team mates: Zuzanna, Saskia and in particular Jess, who were all generous with their time and expertise in the field and in the office.

Thanks you to all my friends in the Department of Geography for the Manley Room chat, regular pub larks and for generally being the type of people who never want to discuss work. Particular gratitude to Callum and Ed for providing frequent and enjoyable bicycle-based escapism, and making me forget "the fear". Huge thanks to my family for the pragmatic advice and plenty of delightful holiday diversions. Finally, I am completely indebted to the patience and all-over wonderfulness of my girlfriend Beverley, who has endured my grumpiness, monotonic lectures about wave physics and occasional existential panic with a love and kindness unsurpassed.

"Remember, when discoursing about water, to induce first experience, then reason."

Leonardo Da Vinci (1452 – 1519)

1. Introduction

1.1. Context and Rationale

Marine-driven mechanical erosion at the cliff toe has long been established as a principle external driving force of coastal cliff erosion (Wilcock *et al.*, 1998; Young *et al.*, 2009; Earlie *et al.*, 2015). Recent investigations into marine conditions on shore platforms have been concerned with wave transformation and energy dissipation (Beetham and Kench, 2011; Ogawa, 2013; Young *et al.*, 2016), wave energy delivery to the cliff (Adams *et al.*, 2005; Norman *et al.*, 2013; Young *et al.*, 2013) and breaker zone dynamics (Blenkinsopp *et al.*, 2011; Brodie *et al.*, 2012; Almeida *et al.*, 2013; Martins *et al.*, 2016). Terrestrial laser scanning (TLS) (Rosser *et al.*, 2005; Dewez *et al.*, 2013; Johnstone *et al.*, 2016; Whadcoat, 2017), photogrammetry (Lim *et al.*, 2005; D ornbusch, Moses, *et al.*, 2008) and airborne LiDAR (Young *et al.*, 2009; Katz and Mushkin, 2013; Obu *et al.*, 2016; Palaseanu-Lovejoy *et al.*, 2016) have also started to become commonplace to capture long-term, high-resolution erosion data from rock coast settings (Moses *et al.*, 2014). It has become clear that the relationship between environmental drivers of erosion and cliff recession rates are highly complex and non-linear (Vann Jones *et al.*, 2015).

There is some debate as to whether marine forcing is important in all rock coast environments (Stephenson and Kirk, 2000b) and it is likely that the relative importance of marine and subaerial processes vary between settings (Sunamura, 1992; Naylor *et al.*, 2010). Where marine processes do dominate however, the processes by which wave action damages rock and removes material from the cliff toe remain elusive. A variety of rock damage mechanisms have been put forward, including wave quarrying (Trenhaile, 1987; Tsujimoto, 1987; Taylor, 2003; Collins and Sitar, 2008), abrasion (Robinson, 1977b; Naylor *et al.*, 2010; Kline *et al.*, 2014) and cavitation (Sanders, 1968a; Stephenson, 1997), yet field validation and quantification of their relative importance of these in the field has yet to be undertaken.

Ocean wave hydrodynamics have been studied in the context of impacts on to coastal structures (Green, 1989; Oumeraci *et al.*, 1999; Raby *et al.*, 2016).

Waves that break directly on to vertical surfaces have been established as a potential major driver of damage to sea walls (Blackmore and Hewson, 1984; Md Noar and Greenhow, 2015), breakwaters (Goda, 1974; Oumeraci *et al.*, 2001; Cuomo *et al.*, 2010) and dikes (Van Doorslaer *et al.*, 2017; Yang, 2017). High-magnitude, short duration “impulsive” impact pressure events have been identified as crucial damage mechanisms (N. W. H. Allsop, Vicinanza, *et al.*, 1996; Momber, 2004a) by providing a critical load condition for failure. These have been studied in considerable detail numerically (Cooker and Peregrine, 1990a; Plumerault *et al.*, 2012), experimentally (Whillock, 1987; Kirkgoz, 1995; Hofland *et al.*, 2010) and in the field (Rouville *et al.*, 1938; Crawford, 1999; Bullock *et al.*, 2005). Impulsive pressures are associated with specific hydrodynamic conditions and appear stochastic in their occurrence. Müller (1997) proposed that compression forces produced during wave impacts propagate into open fissures in engineered coastal structures, leading to substantially enhanced tensile forces (Taylor, 2003) within blockwork causing discrete blocks to be quarried (Wolters and Müller, 2004). Arming breaking waves with suspended or entrained sediment has also been suggested to enhance abrasion (Sanders, 1968a) or wedging (Robinson, 1977b). Large dynamic pressures have to date only been inferred in natural coastal settings by observations of intertidal boulder movements (Noormets *et al.*, 2004) and by inference from artificial environments (Sunamura, 1992; Stephenson, 1997) and logical probability (Trenhaile, 1987). In-situ measurements of these phenomena would yield greater understanding of marine drivers of hard rock coastal change (Naylor *et al.*, 2010).

Models of wave forcing of cliff retreat (Trenhaile, 2000; Walkden and Hall, 2005; Ashton *et al.*, 2011; Matsumoto, Dickson and Kench, 2016) use theoretical pressure magnitude distribution profiles or those derived empirically from physical scale models. The occurrence of impulsive pressures has been shown to be related to the breaking condition on impact (Hull and Müller, 2002), which is in turn related to controls on wave breaking, namely water depth and wave height (Kirkgoz and Akoz, 2005). Sea level rise is usually assumed to promote cliff recession by focusing wave breaking further shorewards and up and on to cliffs (Shaw *et al.*, 1998), yet the nature of breaking wave forces in a rock coast

environment are poorly constrained; the effects of future sea level rise and changing wave climates (Ashton *et al.*, 2011) may more complex than previously thought due to the highly sensitive nature of impulsive impacts (Trenhaile, 2014). Furthermore, fluctuating wave heights (Aarnes *et al.*, 2017) and changes in the magnitude and frequency of storms (IPCC, 2014) may also play a role in modifying breaking wave dynamics.

In order to understand how waves at the cliff toe act to remove material from the rock mass, wave pressures must be observed directly at the cliff toe at a spatial and temporal resolution capable of detecting the impulsive conditions potentially responsible for wave quarrying.

1.2. Approach

There is therefore a clear requirement for a detailed investigation into the hydrodynamics of wave impact on coastal rock cliffs integrated with long-term monitoring of local and regional wave metrics and cliff erosion. The limitations of Froude scaling – whereby impact pressures are generally overestimated when using scaled physical models (Whillock, 1987; Cooker and Peregrine, 1990a) – and dissimilarities in wave transformation on shore platforms (Blackmore and Hewson, 1984) mean hydrodynamic conditions are unique between environments, thus require in-situ observations. Previous studies have been concerned with shore-normal impacts of waves on smooth, homogenous, short vertical walls rather than natural cliffs, and consider only instantaneous rather than iterative effects (e.g. Kirkgöz (1992)).

Naylor *et al.* (2010) favoured the development of new field techniques to quantify forcing processes and inform, calibrate and evaluate existing coastal evolution models, specifically the link between wave forces and rock backwearing. High-frequency pressure sensors have been successfully used to detect wave impact characteristics on vertical and sub-vertical coastal structures (Bird *et al.*, 1998). This approach could therefore be replicated on coastal cliffs fronted by shore platforms. Any such measurement should be correspondingly accompanied by measurements of cliff toe wave and tidal

metrics in order to expound the relationship between breaking wave occurrence, breaking condition and pressure characteristics.

In order to investigate this relationship, it is possible to observe material removed specifically from around the cliff toe intertidal zone over time using repeat TLS (Vann Jones *et al.*, 2015), and correlate this with observed wave action during the period. Whilst eroded material may not be wholly attributable to wave action, the type of erosion mechanism can be inferred using the resultant cliff face morphological characteristics (Robinson, 1977b). This provides a full suite of observations linking cliff toe hydrodynamics directly with wave pressures and possible causal mechanisms of cliff toe erosion..

1.3. Research aims and objectives

The aim of this research is to examine the magnitude and vertical distribution of wave impact pressures on rock coasts and explore their role in the mechanisms of cliff toe erosion. Rock cliffs may be thought of as analogous to coastal structures and as such, are subject to comparable forces which may drive wave erosion. Further deductions from the findings reveal potential implications for quantifying wave forcing in coastal models. To fulfil this investigation, I have conceived the following objectives:

- To characterise erosion of the marine influenced zone of the cliff using TLS;
- To monitor wave conditions at the cliff toe and investigate the relationships between offshore and cliff toe wave conditions;
- To devise a novel method of quantifying wave impact pressures at the cliff toe;
- To obtain measurements of wave impact pressures at the cliff toe and quantify their magnitude, frequency and vertical distribution;
- To develop a modified conceptual model of the mechanisms that control marine-driven cliff erosion.

1.4. Thesis outline

This thesis is comprised of nine chapters inclusive of this introduction. A summary of each chapter is outlined here:

Chapter 2 is a review of the relevant recent literature regarding the current understanding of wave impacts and the extent to which coastal models incorporate this into the quantification of wave forcing. A review of the present understanding of rock damage by wave action is also presented.

Chapter 3 describes the study site: the shore platform and rock coast cliff at Staithes, North Yorkshire, UK. The geology, climate, marine conditions and geomorphological context are described. A review of the previous work on the site is undertaken, alongside a rationale for the erosion monitoring method and selection of the sites.

Chapter 4 describes the erosion monitoring undertaken at each site over the 369-day study period. A description of the field and methods and data processing is followed by a description of the platform morphology and an evaluation of the spatial and temporal characteristics of the measured erosion. Variables and trends within the erosion and platform morphology datasets are compared, which identify a focus for further investigation of wave hydrodynamics in the following chapters.

Chapter 5 is an exploration of the wave conditions at the cliff toe between sites. The monitoring method and processing of one year of offshore and cliff toe wave data are described. The relationships between offshore and cliff toe wave heights, wave energy density and local water depths are investigated. A model describing how the cliff toe wave height is modified by platform morphology is presented, alongside an estimation of the wave height depth-limit and breaker occurrences at each site. The propensity for waves to be breaking on impact at the cliff toe provides context for the subsequent wave impact investigations.

Chapter 6 describes the methodology developed here in order to directly quantify wave impact pressures at the cliff toe. The equipment design, deployment and sample regime rationale are described. Processing stages,

including the extraction of wave impact events and wave characterisation, are outlined, followed by a short of the results.

Chapter 7 constitutes the results of the wave impact pressure measurements at the cliff toe described in Chapter 6. I categorise the measured pressures into those which occur on fully submerged sensors and in alternating air/water conditions. Impacts from the latter are shown to produce both hydrostatic pulsating and dynamic impulsive loads on the sensor. Impulsive loads are shown to occur in a probabilistic distribution based on the ratio of the wave height and water depth. The implications for the quantification of wave forcing in coastal models are discussed.

Chapter 8 is a discussion of the findings of the previous chapters. Firstly, a comparison between the lower cliff erosion data and the cliff toe wave conditions is made, focusing on the increase in the rate of erosion of small detachments about the highest astronomical tide (HAT). Lastly, a modified conceptual model of cliff erosion is presented, outlining two mechanisms identified in the previous chapters by which waves can remove material: quarrying and platelet fragmentation. There is a discussion of the interplay between wave forcing and rock resistance, including the potential role of weathering and the extent to which impulsive pressures are effective in each context.

Chapter 9 concludes the thesis, summarising the results and outlining the original contribution to knowledge. Additionally, I describe the limitations inherent in the investigation and suggest avenues for future research.

2. Literature Review

2.1. Introduction

2.1.1. Characteristics of rock coast cliffs

Rock coast cliffs are formed by a broad range of erosive processes due to their exposure at the margin of the marine and terrestrial environments. The occurrence of a wide variety of cliff morphologies and dynamics is an expression of the complex interactions between environmental forcing and the mechanical properties of the rocks themselves (Lim, 2014). Characteristic landforms and morphologies emerge despite these variations in environmental conditions, providing evidence to support the concept of equifinality on rock coasts (Cruslock *et al.*, 2010). Of the 20,500 km of coastline surrounding the British Isles, over half is formed in cohesive sediments and resistant rocks that develop into shore platforms and cliffs. Most follow a relatively standard morphological pattern: a steep to vertical cliff face at the landward edge of the platform, fronted by a gently sloping platform surface up to 300 m wide. Steps, scarps and beaches comprised of locally accumulated sediment may also be present (Moses, 2014). Worldwide, two distinct platform morphologies have been identified: type A platforms exhibit a gentle uniform seaward slope; type B platforms are defined by a semi-horizontal ledge fronted by a steep seaward cliff exposed at low tide. Both adjoin vertical to sub-vertical cliffs or bluffs on the landward edge (Sunamura, 2015). It is generally accepted that platform slope increases with tidal range, such that type A platforms are most common in macro-tidal environments such as the UK, where gradients typically vary between 1.5° to over 4° (Trenhaile, 1987).

2.1.2. Rock coast dynamics

Lee (2008) described rock coasts as dynamic systems dictated by the interplay between forcing mechanisms and the resistance of the rock mass to damage. Sunamura (1992) describes the critical condition for the development of cliff backwearing to be when the assailing force of waves exceeds the resisting force of rocks. In this model, rock resistance is a function of mechanical strength, which in turn is dictated by lithology and structure (Figure 2.1).

Subaerial and marine weathering act to reduce the rock resisting force. Other processes, such as cliff front sediment drapes (Kline *et al.*, 2014) and encrusting organisms (Naylor and Viles, 2002) may also modify the rock resistance. Wave assailing force comprises of hydraulic and mechanical action (Sunamura, 1994). These in turn are controlled by offshore wave energy and the subsequent transformation processes experienced as waves propagate from deep water to the cliff toe (Stephenson, 1997).

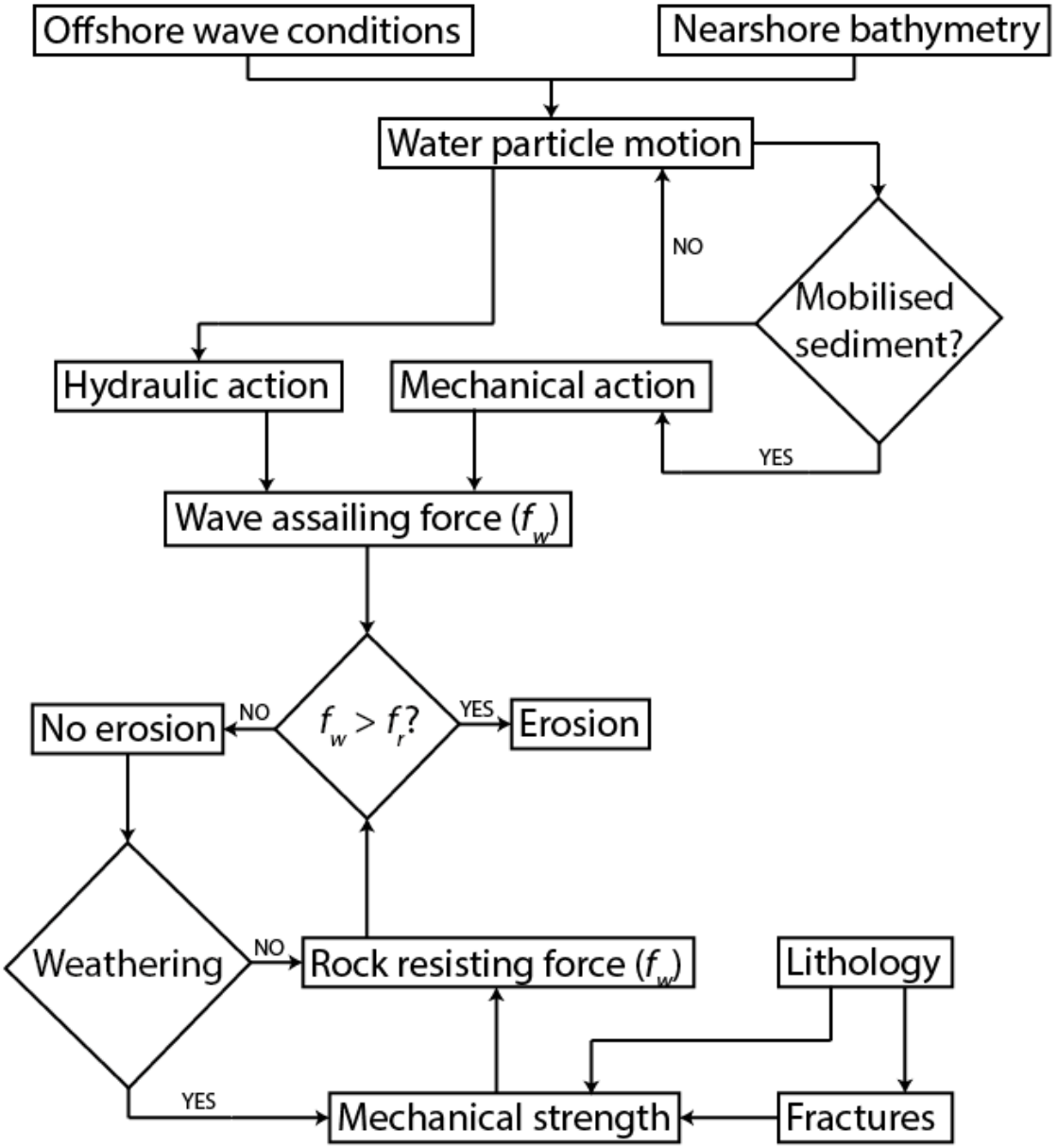

Figure 2.1: Conceptual model flow of the factors influencing rock coast erosion. Adapted from Sunamura (1994).

An understanding of the fundamental processes involved in shaping coastal cliffs is vital to coastal science and management, particularly in the context of the uncertainties surrounding climate change, increased storminess and sea level rise (French and Burningham, 2009). However, until recently rock coasts had been partly neglected in recent literature in favour of soft coast morphodynamics. This may be partly due to the less rapid response of these coasts to environmental forcing, as well as the perceived lower economic and ecological value of cliffed coasts when compared with, for example, wetlands, marshes and estuaries. Consequently, understanding of the fundamental drivers and interactions between the mechanisms controlling weathering and erosion on rock coasts is poor when compared with other geomorphological processes such as fluvial incision and glacial dynamics (Naylor *et al.*, 2010).

2.1.3. Hydraulic processes at the cliff toe

Stephenson and Kirk (2000) argued that waves do not play an active role in micro-tidal rock coast development due to the high energy dissipation rates across shore platforms. Energy delivery across shore platforms by gravity waves can be limited by wave-height attenuation, and therefore independent of incident wave conditions. This limits energy transfer to the cliff even during the largest storms (Ogawa *et al.*, 2015). Furthermore, Carter (1991) argued that rock strength relative to wave energy is too high for wave forcing to have an effect, and that cliff retreat rate is mainly controlled by weathering at joints and faults. However, recent advances in high-resolution monitoring of rock cliffs have enabled researchers to monitor wave-cliff interactions in unprecedented detail. This has allowed cliff retreat to be studied over annual or decadal timescales, permitting a more representative cliff response to forcing.

Rosser *et al.* (2005) used repeat terrestrial laser scanning (TLS) to provide evidence towards the archetypal cliff retreat model of wave notch development and vertical failure propagation. Direct measurements of the net effect of wave cliff impacts over time have shown high energy transfer rates to clifftops (Young *et al.*, 2013) and episodic failure directly related to storm activity (Earlie *et al.*, 2015). It has been demonstrated that coastal recession rates attributed to direct

wave action can be twice that caused by weathering alone (Wilcock *et al.*, 1998) and five times that resulting from rainfall seepage (Young *et al.*, 2009).

Our understanding of wave assailing forces has been advanced considerably in recent years through the analysis of high spatial and temporal resolution wave impact pressure measurements, motivated by a requirement for improved design methods for wave loading on coastal structures (e.g. Cuomo *et al.*, (2010); Stagonas *et al.* (2015)). However, little is known about wave behaviour in rock coast settings, whether such high impact forces occur and if so, their influence on rock erosion.

In this chapter, I discuss the current state of understanding of the characteristics of wave impacts on coastal structures (Section 2.2). This is then compared with the current methods of quantifying wave forcing and rock resistance (Section 2.3), alongside the present state of knowledge regarding the mechanisms by which wave action drives erosion (Section 2.4). A summary of each section is included for clarity. Finally, I summarise this review and show that although contemporary understanding of coastal evolution considers wave impact pressures and their interaction with the cliff, these are highly simplified and overlook the complexity observed in these phenomena in other environments (Section 2.5).

2.1.4. Rock coast terminology

The commonly used zones and terms used in rock coast literature and this study are summarised in Figure 2.2. The term shore platform refers to the rock platform abutting the cliff on the foreshore.

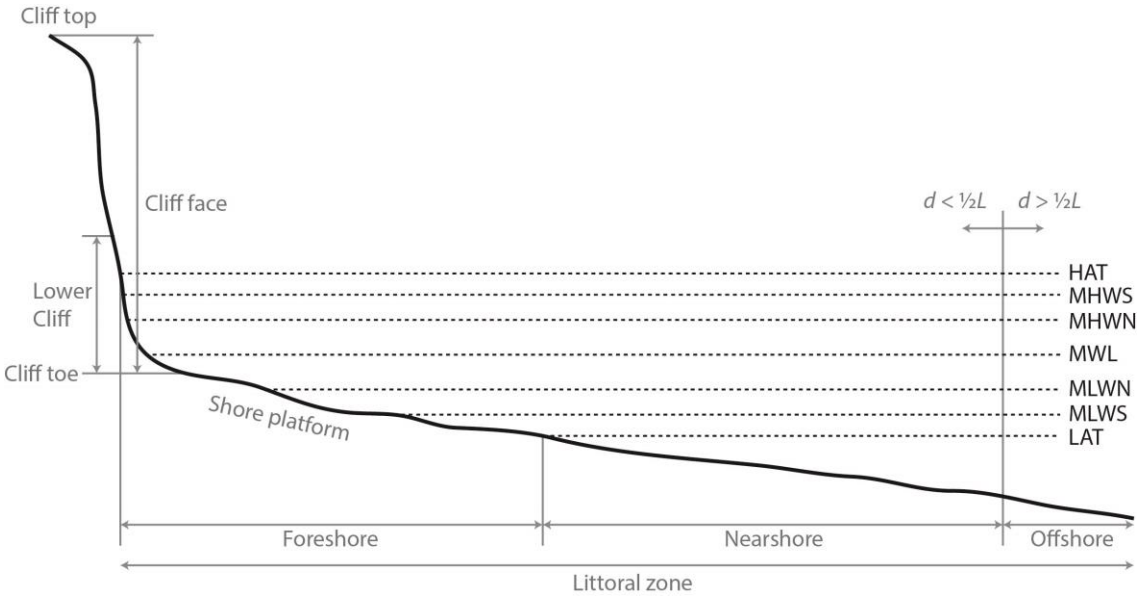

Figure 2.2: Definitions of the coastal zones and tidal stages used in this study. HAT = highest astronomical tide; MHWS = mean high water spring; MHWN = mean high water neap; MWL = mean water level; MLWN = mean low water neap; MLWS = mean low water spring; LAT = lowest astronomical tide. The offshore zone is defined as when the water depth (d) is greater than half the wavelength (L) of the surface gravity waves. The lower cliff is an approximation of the inundated zone, bounded by the platform and the elevation of the highest wave peaks (run up).

2.2. Characteristics of wave impacts

2.2.1. Introduction and wave impact terminology

In this section I discuss field, flume and numerical investigations of wave impacts on coastal structures. It is shown that the findings and techniques used in the study of wave impacts on coastal structures should be extended to wave action at rock coast cliffs.

Since, as it will be shown, that wave impact pressure characteristics are dependent on wave morphology, wave breaker type on impact must be defined when considering wave loading. Due to the difficulties in measuring such impacts, there is no agreed standard of breaker definitions. As such, I have based the breaker classifications used in this study on those of Walkden (1999) and Bullock *et al.* (2007). Unbroken waves (Figure 2.3A) may be termed sloshing, clapotis or standing waves; vertical impacts (Figure 2.3B) may be

termed flip-through or perfect breaking; overturning impacts (Figure 2.3C) may be termed air-pocket impacts; broken wave impacts (Figure 2.3D) may be termed turbulent bores. Additionally, terms for the types of impact pressure loading are also variable: quasi-hydrostatic pressures are known as pulsating impacts; dynamic pressures are known as shock, impact or impulsive pressures. I will use pulsating and impulsive in this study.

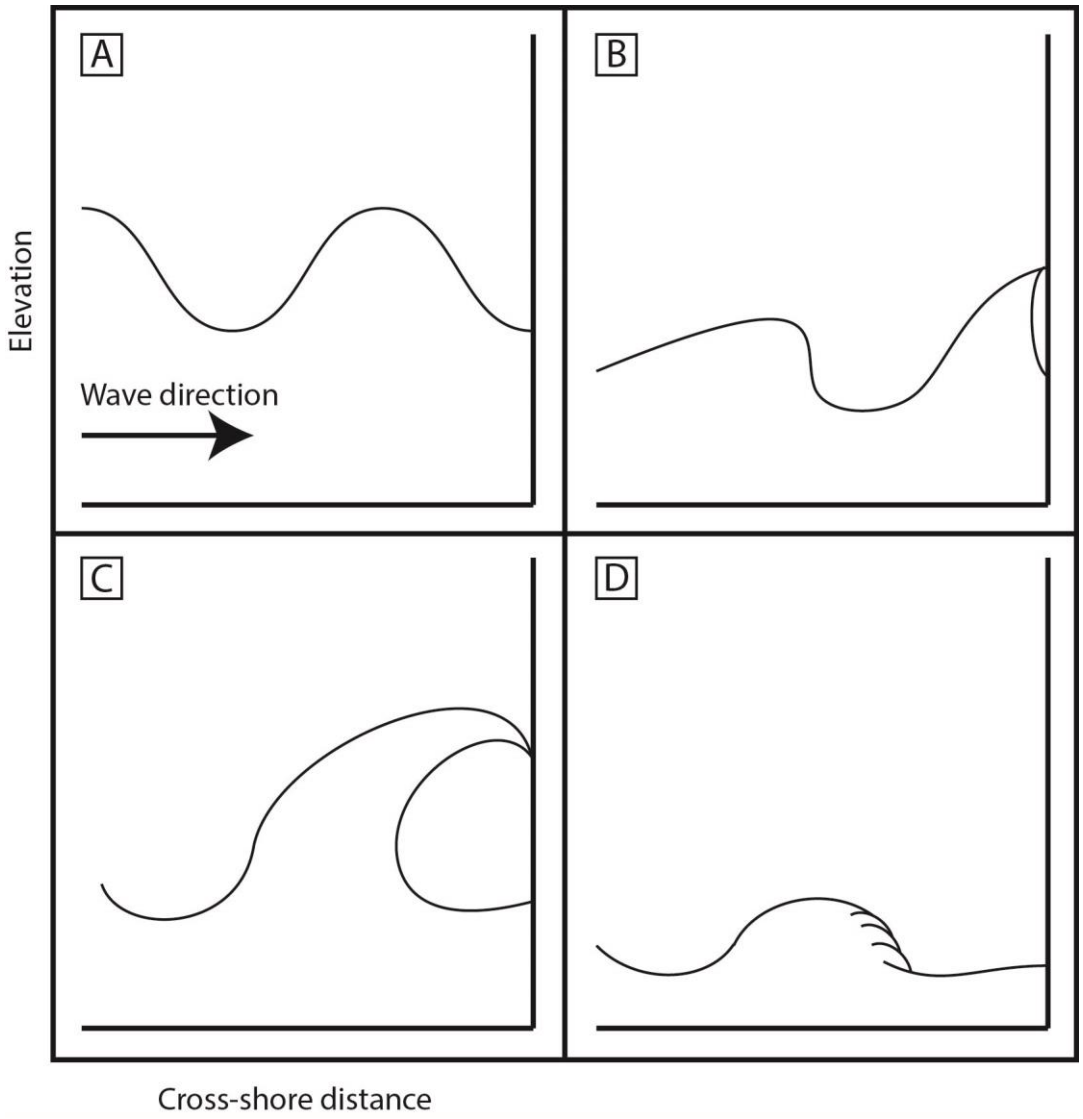

Figure 2.3: Four types of wave impacts on a vertical structure: A) unbroken, B) vertical, C) overturning, and D) broken. Note that intermediate shapes exist between these members.

Whilst wave breaker types at the cliff toe are determined largely by the wave transformation processes of shoaling, breaking and bore propagation in the surf

zone before eventual impact at the cliff toe (Peregrine, 2003), these influences are well-understood and have been extensively modelled (Norman, 2012; Ruessink *et al.*, 2012) and measured (Farrell *et al.*, 2009; Ogawa *et al.*, 2011; Poate *et al.*, 2016; Stephenson *et al.*, 2018). As such, they will be referred to only in the context of their influence on breaking wave impacts in this review. Further discussion on the influence these have can be found in Chapter 5.

2.2.2. Types of impact pressure

The simplest form of wave interaction with a coastal structure is that of an unbroken wave, generating pulsating pressures normal to the structure (Figure 2.3A). Sainflou's (1928) mathematical model is commonly used to predict pulsating pressures. It is derived from trochoidal wave theory is based on the orbital paths of the particles of water within the wave. Bagnold (1939) found that if a wave front is broken or breaking on impact (Figure 2.3B-D), the Sainflou (1928) model breaks down and high-magnitude, short duration “impulsive” pressures are produced normal to the impact surface (Figure 2.4). As such, breaking or broken waves often generate impact pressures above hydrostatic pressure (Miller *et al.*, 1974).

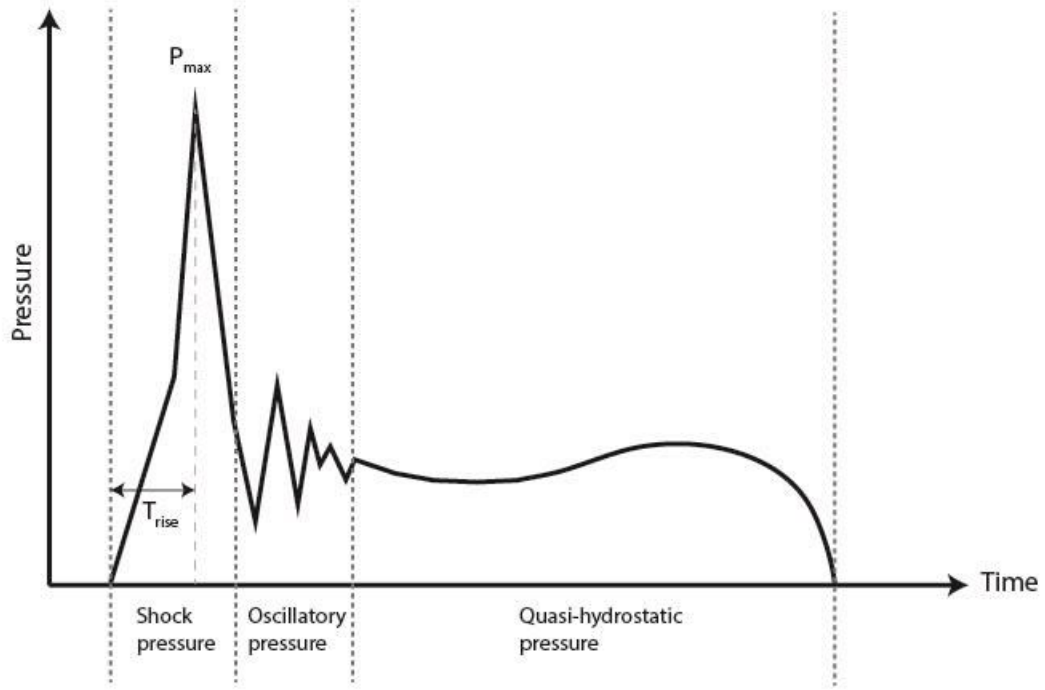

Figure 2.4: Illustrative impulsive impact pressure time history, with a short rise time (t_{rise}) and a maximum pressure (P_{max}) larger than the theoretical hydrostatic pressure according to Sainflou (1928). This characteristic signal is comprised of the initial dynamic component of the impulsive peak, followed by a low magnitude oscillating and quasi-hydrostatic pressure. Redrawn from Crawford (1999); not to scale.

The rise time (t_{rise}) of the initial pressure impact (Figure 2.4) is inversely proportional to the pressure maximum (P_{max}). This relationship is broadly accepted by most researchers (Kuribayashi *et al.*, 1959; Muraki, 1966; Cuomo *et al.*, 2010). Blackmore and Hewson (1984) suggested that that the product P_{max} in kPa and t_{rise} in seconds can be no greater than 3.1.

Bagnold (1939) suggested that impulsive pressures were due to the rapid deceleration of the water mass concomitant with the adiabatic compression of a thin air lens between the water mass and the wall (Mitsuyasu, 1966). This is known as the air piston model, in which P_{max} decreases rapidly away from the periphery of the air lens, and the characteristic pressure time history is generated by air leakage from the lens upwards with the spray during compression.

However, the air piston model has been disputed by a number of researchers, who favour the explanation that the initial pressure spike is generated by water hammer (Section 2.4.1.3). Experiments by Nagai and Otsubo (1968) and Nagai and Kurata (1974) on 1/20-scale breakwaters showed that the air piston model substantially over-predicts P_{max}, and that it is unlikely that impulsive pressures require an air lens. However, Nagai and Kurata (1974) showed that impact pressures are always an order of magnitude less (Lundgren, 1969) than those predicted by the water hammer expression. This was also cited by Blackmore and Hewson (1984) as the reason for the overestimation of pressures by CERC (1984). Mogridge and Jamieson (1980) suggested that the oscillatory pressure after the initial pressure spike (Figure 2.4) may in turn be generated by compression shocks in an air lens. This is supported by mathematical modelling by Peregrine (2003).

Weggel and Maxwell (1970) classified impulsive impacts into two groups: ordinary pressures and significant pressures. Ordinary pressures were spatially localised, high-magnitude impacts. Significant impacts were those that occurred most frequently and over a large spatial area. It is suggested that although both types were of very short duration, they contribute to the deterioration of the impacted material and that significant pressures may act to dislodge already weakened blocks.

2.2.3. Magnitude and frequency of impact pressures

2.2.3.1. Probabilistic understanding of wave impacts

The magnitude and frequency of impulsive pressures are very difficult to predict. Wide scatter was found between impulsive pressure maxima from nominally identical waves in flume experiments by Garcia (1968). Denny (1951) found that impulsive pressures exceeding 70 times the hydrostatic were found to occur in 1/100 waves in smooth water and 1/1000 in disturbed water. Denny (1951) concluded that in the field, a vertical surface under attack from 1 m high waves may experience multiple impacts of over 500 kPa, yet the magnitudes of individual waves would be seemingly random. Bullock *et al.* (2005) experimented with large-scale flumes and found that wave pressures are so sensitive to small changes in wave height, breaker shape, water depth and

foreshore bathymetry, that it is very difficult to predict the occurrence of impulsive pressures under set conditions.

Consequently, even a series of nominally identical waves can have greatly variable impact characteristics, although the total momentum flux and impulse pressures are approximately equal between each wave. As such, the stochastic nature of impulsive pressures on coastal structures explains the wide variation in P_{max} amongst the range of studies which directly measure wave impact forces in the field. This has led researchers to approach the issue probabilistically.

Oumeraci *et al.* (2001) used large, 3-dimensional wave basins and flumes to investigate the distributions of wave impact pressures. They found that the Sainflou (1928) method was adequate for estimating pulsating impacts, but that widely-used deterministic models for impulsive pressures (Bagnold, 1939; Ross, 1954; Minikin, 1963; Goda, 1974) were inadequate, citing their probabilistic nature (Kortenhaus and Oumeraci, 1998). Allsop *et al.* (1996b) suggested that wave impact pressures are highly variable, hence in any given sea state they are best described statistically than by any single value. Analyses used the average of the highest 1/250 waves (P_{max250}) based on a sample size of 500 waves or more. Pulsating loads fitted a Weibull distribution, but impulsive pressures deviated from this considerably, exceeding the pulsating loads at the equivalent probabilities. Impulsive pressures were better represented by a log-normal distribution. Pressures start to exceed the pulsating load values when the wave height (H) / depth (d) ratio exceeds 0.35, which is suggested as a lower limit for conditions allowing direct impacts on the wall (Allsop and Vicinanza, 1996). As such, the H/d ratio is a key component of impulsive pressure prediction, as it dictates the breaking condition of the wave.

2.2.3.2. Direct field measurements of wave impacts

This section is concerned with the range of measurements of maximum impact pressure (P_{max}) due to wave impact obtained in the field, which provide a broad understanding of the magnitude and frequency of large wave pressures in a natural environment. A range of investigations is summarised in

Table 2.1.

The first study to measure wave pressures in the field was undertaken by Rouville *et al.* (1938) on the harbour wall at Dieppe, using a vertical array of piezo-electric strain gauge pressure sensors. A P_{max} value at 690 kPa was obtained (for a 2.5m wave) during the intermittent three year monitoring period, still one of the highest impact pressures every recorded on a coastal structure. Only 2% impacts measured caused pressures greater than the hydrostatic, demonstrating the stochastic nature of impulsive pressures and their sensitivity to the hydrodynamic conditions. Further evidence for this comes from Cot (1954) and Kuribayashi *et al.* (1959), who used strain gauges to measure P_{max} values of 98 kPa for a 2.5m wave and 150 kPa for a 4.5m wave respectively. These are considerably lower than Rouville *et al.* (1938) and, in the case of Cot (1954), an order of magnitude lower for the same wave height. Kuribayashi *et al.* (1959) and Muraki (1966) also provided further field evidence to show that breaking waves exert much larger impulsive pressures than unbroken waves, and that the frequency of occurrence of impulsive pressures in the field is very low.

Allsop *et al.* (1996) used eight strain gauges at 500Hz at the La Collette breakwater, Jersey and observed a sequencing of impulsive pressures up to 3-5 times larger than hydrostatic once every 20 – 60s, or around once every 3-8 waves. This is a considerably higher estimate of impulsive pressure frequency than Rouville *et al.* (1938), which may reflect the higher sample rate used. Crawford (1999) deployed strain gauges vertically up the Alderney breakwater and recorded impact pressure and aeration at 500 Hz. A large dataset over two winter seasons was collected, although only a small number of waves with heights over 2m were observed. A P_{max} of 396 kPa was measured, indicating that high pressures are possible even during relatively quiescent wave conditions. A continuation of Crawford's (1999) experiments were undertaken by Bredmose *et al.* (2003) and Bullock *et al.* (2003; 2005). These studies of Alderney breakwater provide the largest maximum impact pressure every recorded on a vertical surface (P_{max} = 746 kPa), but wave heights were not recorded.

Large-scale field experiments were carried out by Blackmore (1982) at four seawalls located around SW England. Up to nine strain gauges in either vertical or cruciform arrays were installed on the vertical faces. Wave magnitudes in relation to wave heights were found to be comparable with those of Miller *et al.* (1974) on beaches. Along with Rossi (1984), these experiments showed that the pressure predictions in the widely-used CERC (1984) were overestimating by an order of magnitude. Blackmore and Hewson (1984) found that in over 350 hours of pressure data from the Ilfracombe seawall, impulsive pressures occurred in only 1 in 2500 wave impacts. An equation derived from the results to predict wave impact pressures (in kPa) in shoaling coastal waters on a vertical structure using wave celerity (or crest velocity) (v_s) was proposed:

$$P = \varsigma \cdot \rho \cdot T \cdot \mathrm{v}_s{}^2 \qquad (2\text{-}1)$$

This uses a coefficient ς, which is dependent on the degree of aeration of the water (discussed further in Section 2.2.5.4). By using v_s, it assumes that the total wave momentum is reduced to zero on impact. As such, it does not take into account reflected energy. Unlike other equations quantifying wave impact pressure (Section 2.3.1) this equation neglects wave height (H), casting doubt on the importance of this parameter in dictating impact pressure.

Table 2.1: Summary of all the known measurements taken of wave impact pressures in the field. Wave height (H) is measured at the structure.

Study	**Location**	**Location type**	***H***	**Equipment**	P_{max} **(kPa)**
Stevenson (1874)	Skerryvore Rocks (UK)	Rubble Mound	-	Dynamometer	291
	Bell Rock (UK)	Rubble Mound	-	Dynamometer	145
	Dunbar Harbour (UK)	Vertical Wall	6.1	Dynamometer	375
	Buckie (UK)	Vertical Wall	6.1	Dynamometer	322
	Penzance	Vertical Wall	-	Dynamometer	96
	Oswego Harbour (USA)	Vertical Wall	5.5	Dynamometer	45
	Milwaukee Bay (USA)	Vertical Wall	-	Dynamometer	68
	Milwaukee Bay (USA)	Vertical Wall	4.0	Dynamometer	165
Galliard (1904)	St. Augustine (USA)	Vertical Wall	1.8	Dynamometer	32
	Lake Superior, S. Pier (USA)	Vertical Wall	4.9	Dynamometer	113
	Lake Superior, S. Pier (USA)	Vertical Wall	4.0	Dynamometer	79
	Lake Superior, E. Brkwtr(USA)	Vertical Wall	-	Dynamometer	121
	Black Rock (USA)	Vertical Wall	-	Dynamometer	99
Molitor (1935)	Lake Ontario (USA)	Vertical Wall	2.8	Dynamometer	30
Hiroi (1920)	Otaru Harbour (Japan)	Vertical Wall	-	Dynamometer	345
Luiggi (1922)	Port of Valparaiso (Chile)	Vertical Wall	7.0	Stone Grading	322
Rouville (1938)	Dieppe (France)	Vertical Wall	2.5	Strain gauge	690
Cot (1954)	Le Havre (France)	Vertical Wall	2.5	Pressure cell	98
Kuribayashi (1959)	Haboro Harbour (Japan)	Vertical Wall	4.5	Strain gauge	110

Miller (1974)	Cape Cod (USA)	Beach surf zone	0.9	Strain gauge	41
Marchi *et al.* (1975)	Genoa (Italy)	Vertical Wall	2.0	Strain gauge	-
Jones and Demetropoulos (1968)	Anglesey (UK)	Rock platform	6.4	Dynamometer	113
Blackmore (1982)	Seaford (UK)	Vertical wall	0.9	Strain gauge	49
	Ilfracombe (UK)	Vertical Wall	1.3	Strain gauge	27
	Teignmouth (UK)	Vertical Wall	0.9	Strain gauge	19
Rossi (1984)	Ilfracombe (UK)	Vertical Wall	-	Strain gauge	133
Van Heteren *et al.* (1989)	East Scheldt (Netherlands)	Vertical Wall	2.0	Strain gauge	-
Blackmore and Hewson (1984)	Ilfracombe (UK)	Vertical Wall	1.3	Strain gauge	26.7
Palumbi (1984)	Tatoosh Island (USA)	Rock platform	-	Dynamometer	7.1
Fuji (1988)	Usujiri (Japan)	Rock platform	-	Dynamometer	14
Grune (1988	Eiderdamm (Netherlands)	Sloping Wall	-	Strain gauge	69
	Wangerooge (Netherlands)	Sloping Wall	-	Strain gauge	59
Griffiths (1991)	Bovisand (UK)	Vertical Wall	-	Strain gauge	50
Muller and Whittaker (1996)	Islay (UK)	Vertical Wall	2.8	Strain gauge	51
Howarth *et al.* (1996)	La Collette (UK)	Vertical Wall	0.7	Strain gauge	150
Martin *et al.* (1996)	Santander (Spain)	Rubble Mound	5.9	Strain gauge	-
Bird *et al.* (1998)	Alderney (UK)	Vertical Wall	3.1	Strain gauge	85
Crawford (1999)	Alderney (UK)	Vertical Wall	2.0	Strain gauge	396
Bredmose *et al.* (2003)	Alderney (UK)	Vertical Wall	-	Strain gauge	Yes
Bullock *et al.* (2003)	Alderney (UK)	Vertical Wall	-	Strain gauge	Yes
Helmuth and Denny (2003)	Pacific Grove (USA)	Rock platform	2.5	Dynamometer	-

Wave impacts have been measured directly on shore platforms, but using spring dynamometers. These instruments used a steel plate attached to a calibrated spring: as force is exerted onto the plate, rods transfer the movement onto a recording strip. Jones and Demetropoulos (1968) used a dynamometer deployed on a rocky shore on Anglesey and found a positive relationship between wave height and wave pressure on the platform, alongside a P_{max} of 113 kPa during estimated wave heights of 6.4m. Palumbi (1984) measured a P_{max} of only 7.1 kPa for waves at a number of sites on Tatoosh Island (USA), but the sea state during measurements was not measured. However, it was found that pressures increased where waves were observed to break over the dynamometer. This was also observed by Fuji (1988).

The most recent study to measure wave pressures on rocky shores was undertaken by Helmuth and Denny (2003) at 221 sites around Pacific Grove, California. Dynamometers deployed in the intertidal zone showed that whilst P_{max} positively correlated with measured wave height, the maximum wave force was seen to have a definable limit dependent on the local topography. A topographic index was developed as a measure of site 'exposure' to wave forces, and was seen to explain up to 35% of the overall variation in measured force. These findings have potential implications for coastal cliffs fronted by rock platforms, as it is unclear whether this same relationship may exist for maximum wave pressure on the cliff face. However, Crawford (1999) points out that, since each dynamometer only records one measurement per deployment, it is impossible to determine whether the maxima all occurred simultaneously within the same wave, hence inferences regarding spatial or temporal pressure variations and structural response cannot be made reliably using dynamometers.

2.2.4. Vertical impact pressure profiles

There is general agreement that the elevation of maximum impact pressure magnitude on a vertical structure (E_{max}) during wave impact occurs around the still water depth (d_{cliff}). This is supported by a variety of field measurements (Gaillard, 1904; Molitor, 1935; Rouville *et al.*, 1938; Kuribayashi *et al.*, 1959),

yet some place E_{max} below (Cot, 1954), marginally above (Bredmose *et al.*, 2003) and 1 m above (Allsop *et al.*, 1996) the still water depth.

Hiroi (1920) assumed that wave pressures occurred uniformly up the impact surface. However, subsequent studies have shown that two-dimensional pressure profiles for breaking waves can be highly complex (Figure 2.5). Minikin (1963) used the results from Bagnold (1939) and Rouville *et al.* (1938) to develop a model of E_{max} at d_{cliff} with a parabolic decay to zero at half the breaking wave height below and above d_{cliff}. This model was supported by experiments by Garcia (1968) and Kirkgoz (1995). In contrast, Goda (1974) described wave pressure distributed trapezoidally, peaking at d_{cliff}, reducing to zero at the wave crest and to hydrostatic pressure at the base. Blackmore (1982) and with Rossi (1984) found that peak pressures occur at d_{cliff} and form a triangular distribution vertically across the surface. Various scale corrections to these models are described in Oumeraci *et al.* (1999).

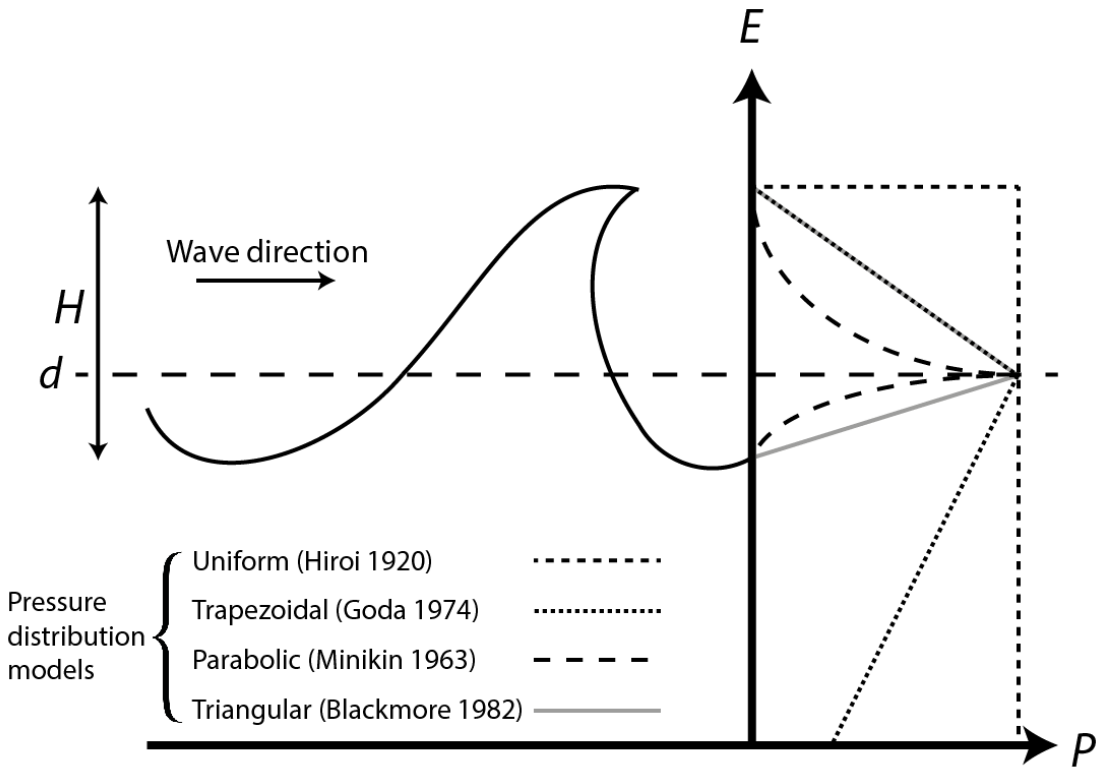

Figure 2.5: Conceptual model of various modelled wave impact distribution profiles, whereby induced pressure (*P*) on the vertical wall varies with elevation (*E*) and dictated by the wave height (*H*) and water depth (*d*). Adapted from Kraus (1996).

Allsop *et al.* (1996a) found that the trapezoidal model does not hold during direct wave impacts, and the peak was slightly above the water depth. This general disagreement highlights the need for additional field measurements of wave pressure profiles.

2.2.5. Variables controlling impact pressure

In section 2.2.3 and 2.2.4 I demonstrated that field and experimental studies have revealed considerable variation in maximum pressure (P_{max}) and the vertical distribution of pressure during wave impacts. As such, wave forcing at the cliff toe is difficult to predict using simple wave measurements such as height and period. Griffiths (1993) derived a hierarchy of influences upon impact pressures using flume experiments. The location of the wave impact was found to be the most influential factor, but is not applicable to coastal cliffs, as this refers to the turning moment induced when waves impact the top of a structure. One critical finding was that impulsive impact magnitudes do not scale positively with wave height, unlike pulsating pressures. The other first-order controls identified by Griffiths (1993) are here ranked in order from most important to least important:

2.2.5.1. Wave impact geometry

Wave impact geometry refers to the angle of the wave crest to the impact surface both horizontally and vertically. Using monochromatic waves in a flume setup, Whillock (1982) found that both impulsive pressure magnitudes and total force decrease considerably with increasing wave incidence angle. Developing this notion for real waves, Allsop and Calabrese (1998) used three-dimensional waves to observe that oblique wave impacts frequently act over only a short length of any coastal structure. As such, since real waves are spatially and temporally irregular, the instantaneous wave front width on impact is often relatively short. Results indicated that impulsive impact occurrence with wave incidence angles between 15° and 45° reduced substantially, with no impulsive impacts measured at 45°.

The geometry of the structure under wave attack has also been found to have an influence on impact pressure. Carr (1954) observed that wave pressure

halved when impacting a surface sloping 30° shoreward. Furthermore, Kirkgoz (1991) showed that impact pressures can be higher on backward-sloping walls than on vertical walls. Grüne (1988) measured impact pressures and wave heights at two sloping seadykes in Germany and concluded that due to the complexities of surface morphology and sea state conditions, impulsive pressures in field data is considerably more complex than in laboratory experiments with idealised boundary conditions. This study concluded that for any detailed investigation of impulsive pressures in the field, high-speed pressure time series under real sea conditions are required. This notion is supported by other fieldworkers (Green, 1989; Howarth *et al.*, 1996; Martin *et al.*, 1996).

2.2.5.2. Wave shape and breaker type

Wave shape is the precise morphology of the wave front on impact (Section 2.2.1). Specifically, this is dictated by the breaker types shown in Figure 2.3, which in turn are controlled mainly by the *H/d* ratio (Müller *et al.*, 2008). Goda (1974) observed that the conceptual model of the three end-member wave states, increasing in steepness – unbroken, breaking and broken – is a considerable oversimplification of the hydrodynamic regime on the nearshore. There are in fact smooth transition states between the three members which make a considerable difference to the resulting impact pressures. Peregrine (2003) noted that wave steepness does not have to be large before second-order effects above hydrostatic pressures on the wall become important.

There is considerable disagreement regarding the precise wave shape which imparts the highest impact pressures. Rouville *et al.* (1938) noted characteristic pressure time series were produced when waves were seen to break directly onto the vertical surface of the breakwater. Miller *et al.* (1974) measured both breaking and broken wave impacts in the surf zone at Cape Cod National Seashore (USA) using strain gauges. They found the highest impact pressure of 41 kPa was associated with a broken wave with a maximum pre-breaking height of 0.9m. However, this may be due to the effects of aeration on a dissipative beach (Crawford, 1999). In contrast, Whillock (1987) found that the

highest pressures on a vertical sea wall are associated with overturning breakers.

A range of research has suggested that a vertical breaker impinging on a vertical face is the most efficient for momentum transfer and hence impact pressure. Numerical work by Peregrine (2003) indicated that impulsive wave impacts are largest close to the inception of overturning: a vertical impact (Lugni *et al.*, 2006; Bredmose *et al.*, 2010). This notion was supported experimentally by Hofland *et al.* (2010), who used a flume of 200m in length and waves of over 3m in height. The largest impact pressures are found in vertical impacts, which exhibited a sharp, single peak. However, conditions for near-parallel wave front impacts were found to occur very infrequently.

Further irregularities in the water surface can also affect induced pressures. Wu *et al.* (1994) stressed that surface roughness of both the impinged surface and the breaking wave front has a negative impact on impact pressure magnitude. Denny (1951) showed that perturbations on the surface of the wave front of only 4% of the wave height lead to a 50% reduction in impulsive pressure magnitude.

2.2.5.3. Wave particle velocity

Bredmose *et al.* (2003) described how particle velocity towards the impact surface on impact induces momentum transfer and hence is positively correlated with pressure magnitude. Pressure is related to the rate of velocity change (Cooker and Peregrine, 1995) which, for a near-instantaneous reduction to zero, will be higher for larger initial velocities. Wave velocity is also incorporated into the impact pressure predictions of Blackmore and Hewson (1984) (Equation 2-1).This notion has been tested by a small number of experimental studies. Using solitary waves breaking against a vertical wall, Hayashi and Hattori (1958) found a weak correlation between impulsive pressure magnitude and water velocity on impact. This was also supported in large-scale flume experiments by Cuomo *et al.* (2010) and Antoine (2009).

2.2.5.4. Water aeration

Experiments on impacting waves have confirmed that impulsive pressures are reduced considerably with entrained air. Hattori *et al.*, (1994) revealed that the largest impact pressures occur when the smallest air bubbles are trapped between the wave front and the wall. Larger air bubbles act to buffer the impact such that the pressure magnitude is lower and the corresponding rise time is longer. Bullock *et al.* (2005) also provided further evidence for this, showing that in large-scale flumes, high impact pressures correlated with low aeration levels.

In an attempt to improve understanding of the effect of water aeration, Bird *et al.* (1998) designed and tested an instrument capable of measuring both impact pressure and aeration simultaneous at the same point. Seven of these pressure aeration units (PAUs) were tested at the Alderney Breakwater in a vertical array, recording at 5 kHz. Aeration was seen to reduce considerably at the pressure peak and remain relatively consistent throughout the impact (Figure 2.6).

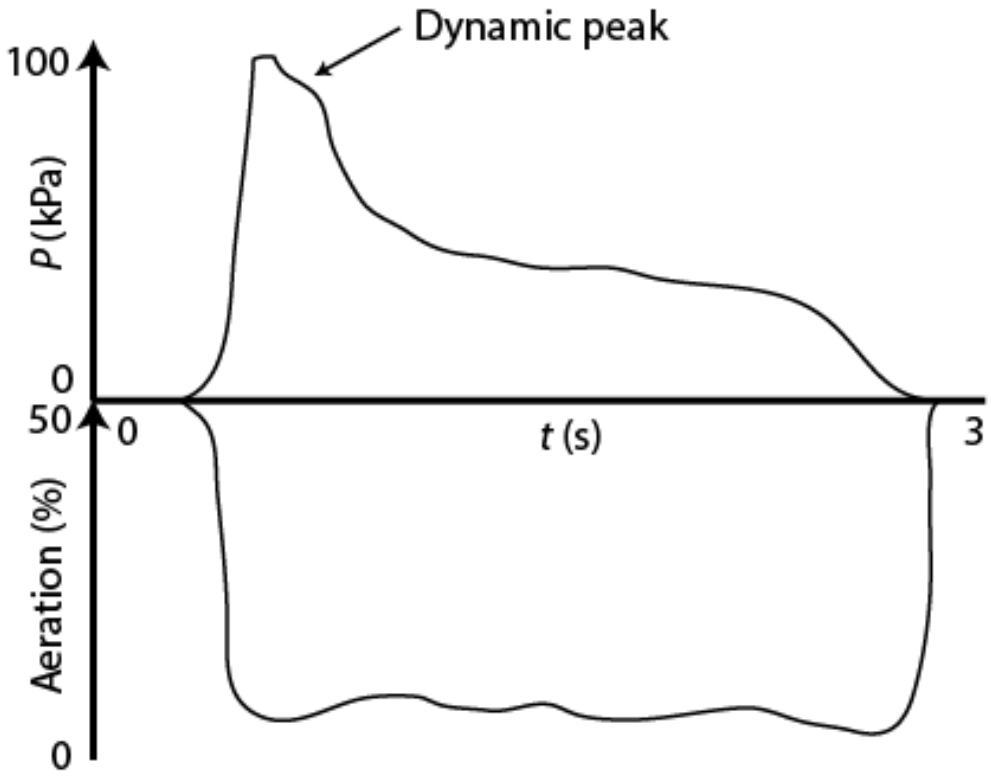

Figure 2.6: Example of the variation in pressure (*P*) and aeration during a typical impulsive wave impact measured with a PAU. Adapted from Bird *et al*. (1998)

The first field measurements of simultaneous impact pressure and aeration were undertaken by Griffiths (1993) alongside complementary model scale experiments. Initial lab tests indicated that the presence of air entrainment during wave impacts caused a reduction in the peak pressure and an increase in rise time. This trend was dependent on bubble size as well as void fraction. Impulsive pressures of over 50 kPa were recorded in the field measurements; however, only a limited number of field measurements were taken so this cannot be taken as representative. Importantly, it was posited that even in highly aerated water conditions, although water hammer effects would be significantly diminished, cavitation or air pocket/bubble collapse pressures may increase. These can create comparable magnitude pressures to water hammer and as such, may pose significant erosional potential due to the rapid fluctuations between positive and negative pressures. Allsop *et al.* (1996) also noted that it is not always true that the magnitude of the maximum impact pressure exerts the greatest stress on the structure.

Although Bullock *et al.* (2001) found a similar reduction in maximum impact pressure with entrained air, they cautioned against assuming that this precludes heavily aerated water from imparting high pressures: the highest pressure recorded in their experiments was in water with 55% aeration.

It should also be noted that the value of the aeration coefficient (ς) in Equation 2-1 (Blackmore and Hewson, 1984) is dependent on rise time, which in turn is proportional to the degree of aeration of the water. This was seen to vary with the nature of the seabed morphological features on the shoaling zone, such as beach type, gradient and water depth. The rocky shores at the Ilfracombe seawall were seen to cause multiple breaking and reforming of waves prior to impact, thus aerating the water and reducing maximum impact pressure. Hence Blackmore and Hewson (1984) suggested ς values of around 0.3 for vertical walls fronted by rocky shores, but around 0.5 for beaches, will would in turn reduce the impact pressures predicted on rocky shores by approximately 20%.

The formulation of Equation 2-1was disputed by Hedges (1985), who noted that the value of ς did not have a direct link with the degree of water aeration, shown to be proportional to maximum possible impact pressure through its reduction of

the speed of sound in water (Von Karman, 1929). This may explain the variation in measured experimental pressures due to differences in the degree of aeration across the wave.

2.2.6. Importance of field measurements

This review has highlighted the considerable advancement of knowledge regarding the magnitude and frequency of coastal wave impacts and the controls thereof. However, a large majority of the research discussed has focused on numerical and physical experiments, many of which are monochromatic waves in fresh water. Denny (1951) noted a considerable disparity between experimental and field results, and attributed this to the smoother surface of freshwater waves in a tank compared with real sea waves with superimposed capillary and ultra-gravity waves, and air entrainment in the water column. Blackmore (1982) and Rossi (1984) argued that pressures resulting from flume experiments cannot be scaled adequately to full-size impacts due to the effect of air entrainment; surface tension effects lead to water aeration always being lower in modelled waves. This was reiterated by Delmonte (1972), who showed that no contemporary theory could satisfactorily predict wave pressures from waves above 0.06 m in height, leading to the conclusion that full-scale tests should be undertaken.

Kjeldsen and Myrhaug (1979) in their experiments with deep water waves suggested that wave pressures can only reliably be evaluated in the field. Laboratory experiments are only useful in relative comparisons between situations and tend to exaggerate impact pressure that occur in nature (Whillock, 1987). Green (1989) suggested that further understanding would only be achieved through studies of random waves in the field.

2.2.7. Summary

This review has shown that:

- Unbroken waves exert lower-magnitude pulsating pressures normal to the cliff face, whilst breaking and broken waves can exert high-magnitude, short duration pressures.

- Impulsive pressures have been measured in the 10^3 kPa range, but are highly transient and difficult to predict. There is little consensus regarding the magnitude, frequency and distributions of pressures on impact.
- Direct measurements of impulsive pressures have been made successfully in the field using high-resolution (10^2 - 10^3 Hz) strain gauge pressure sensors.
- Impulsive pressures are often approached probabilistically. Control variables are impact geometry, breaker type as dictated by the breaking criterion (*H/d*), wave particle velocity and water aeration.

2.3. Marine forcing of cliff recession

The fundamental equation linking marine forcing to cliff recession was developed by Sunamura (1977) and forms the basis for many of the subsequent models of cliff erosion. Here, wave forcing (*F)* is described as being related to the assailing force of waves (f_w) and the resisting force of rocks (f_r) by the equation:

$$F = K \cdot \ln(\frac{f_w}{f_r}) \qquad (2\text{-}2)$$

where *K* is a calibration constant derived from Sunamura's (1977) wave tank experiments. The rate of horizontal erosion was said to be proportional to *F*, so that cliff erosion may only occur when $f_w > f_r$ is satisfied. Although this relationship was supported by flume experiments, it failed to give any insight into either the mechanisms at work during erosion or any quantitative values for each term as functions of wave and cliff parameters (Stephenson, 1997). The purpose of much of the research outlined in this section was to quantify the values for f_w and f_r.

Note: some models of wave assailing force use wave impact pressure and impact force interchangeably. The justification for this is from Newton’s second law and is described by Tsujimoto (1987).

2.3.1. Quantification of wave assailing force (f_w)

2.3.1.1. Sunamura model

The basic model quantifying wave assailing force as a function of the incipient marine conditions comes from Sunamura (1977; 1991; 1992), which uses a linear relationship between water density (ρ), acceleration due to gravity (g) and breaking wave height (H_b) to derive wave impact pressure (P):

$$P = A \cdot \rho \cdot g \cdot H_b \tag{2-3}$$

This holds for both breaking and broken waves. The dimensionless constant (A) accounted for the additional dynamic pressure during wave breaking, usually given as A = 5 (Sunamura, 1992).

2.3.1.2. Trenhaile models

The cross-shore profile models of Trenhaile (1983; 2000) have given valuable insight into the development and behaviour of rocky coasts under variable external conditions, including steady (Trenhaile, 2000) and increasing sea level (Trenhaile, 2001), sediment availability and accumulation (Trenhaile, 2005a) and offshore wave conditions (Trenhaile, 2011). These were the first numerical models to consider mechanical wave erosion associated with hydraulic pressure.

Wave-driven erosion in the models was described by a series of functions derived from the literature. Trenhaile (2000; 2001; 2005a) incorporated breaker height, depth and breaking distance for calculating wave assailing force, alongside thresholds for initiating lower cliff erosion and included the CERC (1984) wave force equation for broken wave impacts, given by:

$$P = 0.5 \cdot \rho \cdot g \cdot d_b \tag{2-4}$$

using breaking wave depth (d_b). Breaking wave type was determined using Battjes (1974)'s surf similarity parameter. By incorporating the following

expression for breaking wave height relative to deep water wave height H_0 and period T_0:

$$H_b = 0.39 \cdot g^{0.2} \cdot (T_0 \cdot {H_0}^2)^{0.4} \quad (2\text{-}5)$$

The force (J) at the coastline still water depth was then given by:

$$J = 0.5 \cdot \rho \frac{H_b}{0.78} \cdot e^{-k \cdot \mathrm{w}} \quad (2\text{-}6)$$

where w = platform width and k is a constant representing attenuations rates on the platform. Additional modifications to the surf stress in the model were made by Trenhaile (2011) to account for the effect of a sloping cliff toe surface (Section 2.2.5.1) on breaking wave pressures relative to a vertical surface. Effective erosional processes occurred between the wave trough and crest. No erosion took place where waves were unbroken. A tidal duration factor determined how wave energy is distributed vertically within the tidal range.

2.3.1.3. SCAPE model

The Soft Cliff and Platform Erosion (SCAPE) model developed by Walkden and Hall (2005) was designed to investigate the evolution of shore platforms using a series of alongshore-extended cross-shore profiles. Wave assailing force was represented by considering wave power in the breaking zone, rate of energy dissipation and the energy within a breaking wave. The wave force (J) under random waves with period (T) applied horizontally at the lower cliff was given by:

$$J = H_b \cdot^{\frac{13}{4}} \cdot T^{\frac{3}{2}} \quad (2\text{-}7)$$

The magnitude and vertical distribution of the wave force was controlled by a shape function based on experimental laboratory tests of erosion rate of a model glacial till shore by Skafel and Bishop (1994) and Skafel (1995). A two-state model consisting of spilling and plunging breakers was and applied below the still water depth based on their occurrence, controlled by platform gradient. This shape function therefore is based on proxy measurements of wave force rather than direct pressure or force measurements.

2.3.1.4. Castedo-Paredes model

The process-response model for unconsolidated cliff erosion developed by Castedo *et al.* (2012; 2015) was designed to incorporate the mechanical behaviour of cliff material into process models to eliminate the stochastic constituents of contemporary models. As such, the focus was on providing thorough representation of cliff failure mechanisms rather than exogenous forcing. The model represents the eroding wave forces as a combination of hydrostatic and hydrodynamic pressure, measured against resistive forces (Sunamura, 1992; Budetta *et al.*, 2000). Breaking wave force was described in the same manner as the SCAPE model (Equation 2-7), with the addition of a local slope modifier (Trenhaile, 2000). A shape function describing the vertical distribution of wave force with depth was developed using glacial till erosion rates in a similar manner to Walkden and Hall (2005). This was subsequently dependent on the breaker type (spilling or plunging), following Equation 2-5. The elevation of the force profile was controlled by a sinusoidal tidal distribution function which governed the elevation of the still water depth over time. Further modelling by Castedo *et al.* (2013) used a modified version of Trenhaile (2009), and hence incorporate the same limitations.

2.3.1.5. AEE model

Hackney *et al.* (2013) suggested that the key measure of wave forcing on an unconsolidated cliff is the total time-integrated wave energy delivery; cliff recession is subsequently dictated by defining an erosion threshold above which wave attack becomes effective. Transformation and breaker type were thus not considered.

2.3.1.6. Limber model

To explore plan-view morphology evolution of rock coasts over millennial timescales, Limber *et al.* (2014) developed a model focusing on the feedback mechanism arising from wave energy convergence and divergence at bays and headlands. Wave transformation was modelled numerically using linear wave theory using a method developed by Adams *et al.* (2002). Wave energy is transmitted from the deep ocean and modulated by the incident angle, local bathymetry and wave height. Subsequent erosion modifies the coastal

amplitude and the refraction regime, creating a feedback between morphology and wave energy. Hence wave assailing force was assumed to be equivalent to wave power density at the cliff toe.

2.3.1.7. Kline model

Kline *et al.* (2014) modelled cliff retreat as a series of feedbacks involving accumulated sediment acting as either tools for mechanical abrasion or as protection against wave attack. The wave attack module used Equation 2-3 for broken and breaking wave force. The breaking criterion was based on Komar and Gaughan (1972) and the critical breaking wave ratio was set to 1. The run-up of waves that broke before impact was calculated to assess whether the bore reached the cliff. Wave height used for the calculation of assailing force is then the difference between the maximum run-up height and the breaking wave height. An additional term for abrasional efficiency – effectively the constant A in Equation 2-3 – was developed as a function of the beach elevation relative to mean sea level. This model appears to assume that abrasion is the only erosion mechanism, which in turn is controlled by wave height at the cliff toe, as the f_w term is always modified by the abrasional efficiency.

2.3.1.8. Matsumoto model

The most recent attempt to develop an exploratory numerical model for long-term rock coast evolution was by Matsumoto *et al.* (2016). Unlike earlier models (Trenhaile, 2000), this investigation aimed to use a limited selection of processes, including detailed spatial representation of erosion mechanisms, to investigate the boundary conditions of emergent shore profiles.

As erosive mechanisms are a focus, this model comprised the most comprehensive representation of wave assailing forces, with wave transformation, breaker type and directional vector shape functions all considered. The approach followed Sunamura (1992), but divides f_w into two independently calculated perpendicular components: vertical downwearing and horizontal backwearing (Payo *et al.*, 2014). Three wave types were characterised: unbroken, breaking and broken. It was assumed that wave height is constant during wave transformation and attenuates after breaking. The attenuation coefficients were based on profile gradient, roughness and

instantaneous wave height. Thus each wave type had different wave height transformation functions applied, such that wave height (and therefore category) is determined by relative horizontal distance from breaker point.

Once breaking condition had been evaluated, the horizontal backwearing force was calculated as a function of the wave height, a scaling function determining the pressure magnitude, a shape function determining the pressure distribution and a tidal function determining the pressure elevation.

The scaling functions for each wave type were based on the order of magnitudes for wave impact types from Tsujimoto (1987). Unbroken impact magnitudes were based on Sainflou's (1928) theoretical clapotis pressure. Breaking wave impact magnitudes used empirical values derived from Ross (1954) and use the deep water wave height H_0:

$$P = 35 \cdot \rho \cdot g \cdot H_0 \tag{2-8}$$

The magnitude of broken wave impacts follow Trenhaile (2000) (Equation 2-4).

To simplify the calculations, the scaling functions were applied as an order of magnitude relative to the resistance of the cliff. Specifically, scaling values of 10^{-3}, 10^{0} and 10^{-2} were set for unbroken, breaking and broken waves respectively. Values were tuned such that broken waves could achieve erosion when rock resistance was soft.

For the pressure distribution function, the scaling function was applied at the elevation of maximum pressure, after which three shape functions were systematically applied across the parameter space: 1) a rectangular function such that pressure was uniform between the platform surface and the wave crest; 2) an exponential function with maximum pressure on or above the still water depth which attenuated exponentially up to the crest and down to the platform surface; 3) a triangular function with maximum pressure on or above the still water depth which attenuated linearly up to the crest and down to the platform surface. The rectangular and exponential functions were always applied to unbroken waves and breaking waves respectively.

The major difference between this and previous models is that although erosion in the model was controlled by a solitary boundary condition (i.e. $f_w > f_r$), wave forcing was highly spatially variable due to the differing wave types and associated pressure functions. As such, this model represents the most comprehensive deterministic application of wave assailing force to date.

2.3.1.9. Probabilistic and deterministic models

The CLIFFPLAN (Hall *et al.*, 2002; Lee *et al.*, 2002) and Hapke and Plant (2010) models address overall cliff erosion by assessing the variables probabilistically. Wave impacts are reduced to a simple function of impact hours to allow for multiple simulations under limited processing power. Whilst these have value for risk-based cliff management one a case-by-case basis, they give no insight into precise erosion mechanisms at work. A similar conclusion can be drawn regarding deterministic models (e.g. Bray and Hooke (1997)), but in this case it is the inherent uncertainty and variability in the erosion processes which is not accounted for. Simplistic representations of complex systems coupled with poor-quality historical data and uncertainty about future environmental conditions would inevitably give rise to inadequate outputs, without reflecting the processes governing the system.

2.3.1.10. Discussion: wave assailing force in coastal models

In this section I have demonstrated that a wide variety of methods exist to attempt to quantify wave assailing force. Of the models shown, the Sunamura, Trenhaile, SCAPE, Castedo-Paredes and Kline models use specific values for wave impact magnitude and distribution. Other models such as the AEE and Limber models which use wave energy as a proxy for erosivity may be useful calibrated for specific field conditions, but give no insight into the erosive mechanisms at work at the cliff face.

Whilst they acknowledge the importance of wave breaking in quantifying wave attack at the cliff toe, impact magnitude functions from these models are derived from relatively simple empirical functions that do not consider the complexities of pulsating and impulsive pressure produced at the cliff-wave junction, nor have any been validated with field data (Section 2.2.3.2). Kline *et al.* (2014) applied the formula from Sunamura (1975), which was based on flume data and

is almost certainly not scalable up to a field setting (Weggel and Maxwell, 1970; Kjeldsen and Myrhaug, 1979). The Trenhaile (2000; 2001; 2005a), Limber *et al.* (2014) and Matsumoto *et al.* (2016) models were based on the CERC (1984) formula for breaking and broken waves. This in turn was derived from a semi-empirical analysis by Minikin (1963). The Matsumoto *et al.* (2016) model also utilised Tsujimoto's (1987) formulae originating from Ross (1954). Both suffer from a lack of supporting data (Green, 1989) and unknown applicability in a rock coast environment. Matsumoto *et al.* (2016) also simplifies the wave assailing force, assuming not only that all breaking waves exhibit very high horizontal pressures, but also that they are consistently two orders of magnitude larger than broken waves at the still water depth. Whilst this simplifies the computation of assailing force, it may also greatly overestimate cumulative forcing.

Some wave force functions are inferred from proxy measurements of the erosion of known softer materials such as glacial till (Skafel, 1995), hence are of little value when applied generically to heterogeneous hard rock cliffs and assume that wave force is directly proportional to erosion. This applies to the Limber model, where the governing force functions were derived from field observations of the erosion of marsh banks (Marani *et al.*, 2011). This assumes that the parameters used, namely cliff height and material strength, are scalable by multiple orders of magnitude. Lim (2014) suggested that although the SCAPE model has been validated using historical retreat rates (Ashton *et al.*, 2011; Walkden and Hall, 2011), caution should be applied when dealing with the specific erosion mechanisms, which still require independent validation.

The elevation of maximum pressure relative to the still water depth is also inconsistent across the models. The shape function for the SCAPE model locates it below, whereas Trenhaile (2000; 2001; 2005a) and Matsumoto *et al.* (2016) apply it at or above dependent on additional factors. Noormets *et al.* (2004) demonstrated a poor consensus amongst researchers regarding this problem, and the variety of shape functions that distribute pressure in these models reflects this.

This review demonstrates that whilst standard shallow water characteristics such as wave height, period, break point and water depth are relatively easy to

model from offshore wave measurements and simple bathymetry using linear wave theory, the specific hydrodynamic conditions at the point where waves strike the lower cliff are still poorly understood.

2.3.2. Resisting force of rocks (f_r)

Sunamura (1977) describes the resisting force of rocks as a function primarily of their mechanical strength, lithology and discontinuities. Any weakening of the resisting force is generated by physical, chemical and biological weathering alongside fatigue via repetitive stresses (Sunamura, 2015).

2.3.2.1. Mechanical strength

A variety of different approaches have been used to quantify mechanical strength and it is still unclear which index is the most applicable to rock cliff erosion (Moses, 2014). Compressive strength is most commonly used to describe rock resistive force as it can be relatively simple to measure in the field using a Schmidt hammer (e.g. Stephenson and Kirk (2000); Dickson (2006); Goudie (2016)), an Equotip hardness tester (e.g. Sunamura *et al.* (2014); Swirad *et al.* (2016)), or measured in a laboratory (Sunamura, 1982; Skafel and Bishop, 1994).

Davies *et al.* (2006) found that within limestones and sandstones, compressive rock strength was a statistically significant determinant of platform width, although only a small number of sites were considered. Using this index in isolation to represent rock resistance naturally assumes that the cliff is homogenous, continuous and unweathered. However, point measurements such as those from Schmidt hammers only assess the strength of a highly localised area and as such almost certainly are not representative of the entire cliff mass. To obtain an adequate estimate of cliff (compressive) strength, the dense spatial sampling required for even a relatively small cliff area would be impractical. The relationships between rock compressive strength and platform morphology found by Swirad *et al.* (2016) were extremely weak: this was attributed to a wide variation in hardness values within lithologies and the limited applicability of compressive strength as a measure of rock resistance.

Trenhaile and Kanyaya (2007) argued that tensile strength must be the primary measure of rock erosion resistance against wave quarrying, as internal pressures within rock discontinuities produced by wave impacts act outwardly to dislodge intact rock fragments. Tensile strength was also used by others (Collins and Sitar, 2008; Hansom *et al.*, 2008; Castedo *et al.*, 2012). Under this failure mode, the compressive strength within the block becomes irrelevant as cliff material removal is controlled almost exclusively by the force balance within the discontinuities, rather than the intact rock mass (Noormets *et al.*, 2004; Herterich *et al.*, 2018). Tensile strength is often equivalent to $1/10^{th}$ of the measured compressive strength (Sunamura, 1992).

2.3.2.2. Rock structure

Rock structure may be a primary control on rock resistance to wave forces. The size of individual blocks released on the shore platform from the cliff face in hard rock platforms in South Wales are controlled by the jointing and fracture patterns within the bedding planes (Naylor and Stephenson, 2010). Benumof and Griggs (1999) found a statistically significant exponential relationship between erosion rate and joint spacing for a number of cliffs in California. Brossard and Duperret (2004) found that chalk cliff recession was positively correlated with joint density. Overall platform morphology may also be influenced by large-scale geological structure (Moses, 2014).

A number of studies have attempted to quantify rock resistance using an index which encompasses some measure of intact rock strength alongside a quantitative assessment of the intensity of internal discontinuities, as suggested by Sunamura (1992). Tsujimoto (1987) combined laboratory-derived intact rock compressive strength and internal acoustic velocity measured in the field, which is used as a proxy for the density of fracturing. Similarly, Budetta *et al.* (2000) used the rock mass index, which denotes the reduction in intact rock compressive strength due to the presence of jointing. The jointing parameter comprises of measures of joint density, the number of joint sets, wall roughness, joint size and joint alteration such as infilling.

The geological strength index devised by Hoek *et al.* (1998) and utilised on rock coasts by Earlie *et al.* (2014) uses a qualitative visual assessment of the rock to

determine its vulnerability to erosion. Observations of weathering and alteration of the surface are combined with the spacing, density and orientation of the discontinuities. Dickson *et al.* (2004) used a Schmidt hammer and observations of joint density, width and orientation to assess rock resistance in the field. An empirical classification of rock strength was then produced which combines these measurements and observations: cliffs are categorised as highly resistant when joint density is low and compressive strength is high.

2.3.2.3. Weathering processes

Coastal environments are highly susceptible to weathering processes, which are most intense in the intertidal and supratidal zones (Sunamura, 2015). Salt weathering is a well-established mechanism for rock degradation in coastal settings, driven by salt crystal growth within rock discontinuities (Tingstad, 2008). In addition, wet-dry weathering is important particularly on mudstone/shale platforms and causes rock fragmentation (slaking) (Moon and Healy, 1994; Stephenson *et al.*, 2004). Freeze-thaw weathering occurs when water penetrates inside the rock structure and expands during freezing; shales are also more susceptible than other rock types (Trenhaile and Rudakas, 1981). Exfoliation of the rock surface due to expansion via insolation (Collins and Stock, 2016).

These processes act initially at the rock surface and penetrate internally over time, weakening the rock strength and producing a weathering profile. As such, rock strength tends to increase further from the exposed surface. Weathering has been shown to be easily capable of fatiguing rock with high critical strength by Eppes and Keanini (2017), until the forcing magnitude of waves, rainfall or wind is capable of dislodging platelets from the surface (following Carter and Guy (1988) and Wilcock *et al.* (1998)). This critical threshold may be very low, such that unbroken waves, or even rain and wind, can dislodge these very weak fragments and transport them from the cliff toe. Further discussion of these processes in context is undertaken in each results chapter.

2.3.2.4. Discussion: rock resistance

Moses (2014) highlighted the lack of understanding surrounding the relative significance of mechanical strength and geological structure. The considerable variation in methods for evaluating the resisting force of rocks across the rock coast literature suggests there is still no satisfactory index by which to quantify it. It is likely however, that different rock strength indices act as resistance for different processes. For example, if abrasion is occurring at the lower cliff, it is probable that the sediment striking the cliff material is acting against its compressive strength and shear strength; the joint structure is unlikely to play a key role in the rate of gradual abrasion backwearing. One measure such as compressive strength is unlikely to fully represent the rock resistance to the full range of processes at work on the lower cliff. Consequently, it is doubtful that wave tank cliff erosion experiments such as those described by Sunamura *et al.* (2014) involving structurally homogeneous model cliff material can ever yield more than an understanding of a narrow selection of erosion processes.

Additionally, erosion via block removal may be wholly unrelated to compressive strength. Alongside tensile and shear strength, other local factors such as the coefficient of friction between the rock surface and the block may be critical here (Noormets *et al.*, 2004; Trenhaile and Kanyaya, 2007).

Studies which rely exclusively on one measure of rock resistance – compressive strength (Sunamura, 1992; Stephenson and Kirk, 2000b; Brossard and Duperret, 2004; Pappalardo *et al.*, 2017), tensile strength (Hall *et al.*, 2008) or observations of the weathering patterns and discontinuities (Earlie *et al.*, 2014) – are therefore limited in their capacity to understand the full breadth of erosive processes. Furthermore, the variation in all rock properties is often high even over centimetre scales: the degree of fracturing can be highly variable between and within stratigraphic boundaries (de Vilder *et al.*, 2017); rock strength reduction due to weathering can vary over multiple orders of magnitude on the centimetre scale (Viles, 2013) such as between joints; and overall strength variability within units can be considerable (Swirad *et al.*, 2016).

This large variability on the centimetre scale means that over a single lower cliff section, often a few metres in height and hundreds of metres in width, only one

weak point is required for a large section of cliff to undergo failure. The notion that erosion can only occur if the forcing magnitude exceeds the sampled rock strength therefore become questionable. Whilst this concept may be valid under controlled experimental conditions (Thiruvengadem, 1965), damage through cyclic loading, crack initiation, lengthening and failure on the lower cliff may occur locally at any weak point on the face, leading to failure and erosion of nominally resistant rock. The studies which attempt to capture this variation by using a combined strength measurement and weathering and fracture observations address this to an extent, but fail to quantitatively assess the magnitude required for rock damage to occur. This makes assessing the ability and rapidity of wave assailing force to actively erode the lower cliff challenging.

2.3.3. Summary

Models of marine forcing of cliff recession have been evaluated. This review has shown that:

- The quantification of wave assailing force is often highly simplified, utilising predictive formulae which generally over-predict or under-predict wave impact pressures and not necessarily applicable to coastal cliffs.
- As such, the full hydrodynamic complexities of wave impacts which were demonstrated in Section 2.2 are not captured by current models.
- The resisting force of rocks against marine forcing is poorly understood and often over-simplified. This makes directly comparing assailing and resisting forces difficult to justify.

2.4. Modes of rock damage by wave action

The interactions between water, air and rock at the cliff toe are multifaceted and highly variable both spatially and temporally. The notion that erosion occurs once the assailing force of waves exceeds some level of rock resistance (Sunamura, 1977) is a simplification of the modes by which water can damage the cliff material. Furthermore, lower cliff erosion by wave action is not a simple function of wave erosivity, but is contingent on environmental variables, rock characteristics and weathering patterns. Figure 2.7 summarises the seven key

modes by which water can interact with rock surfaces outlined by Sanders (1968), King (1972), Robinson (1977a) and Hampton and Griggs (2004).

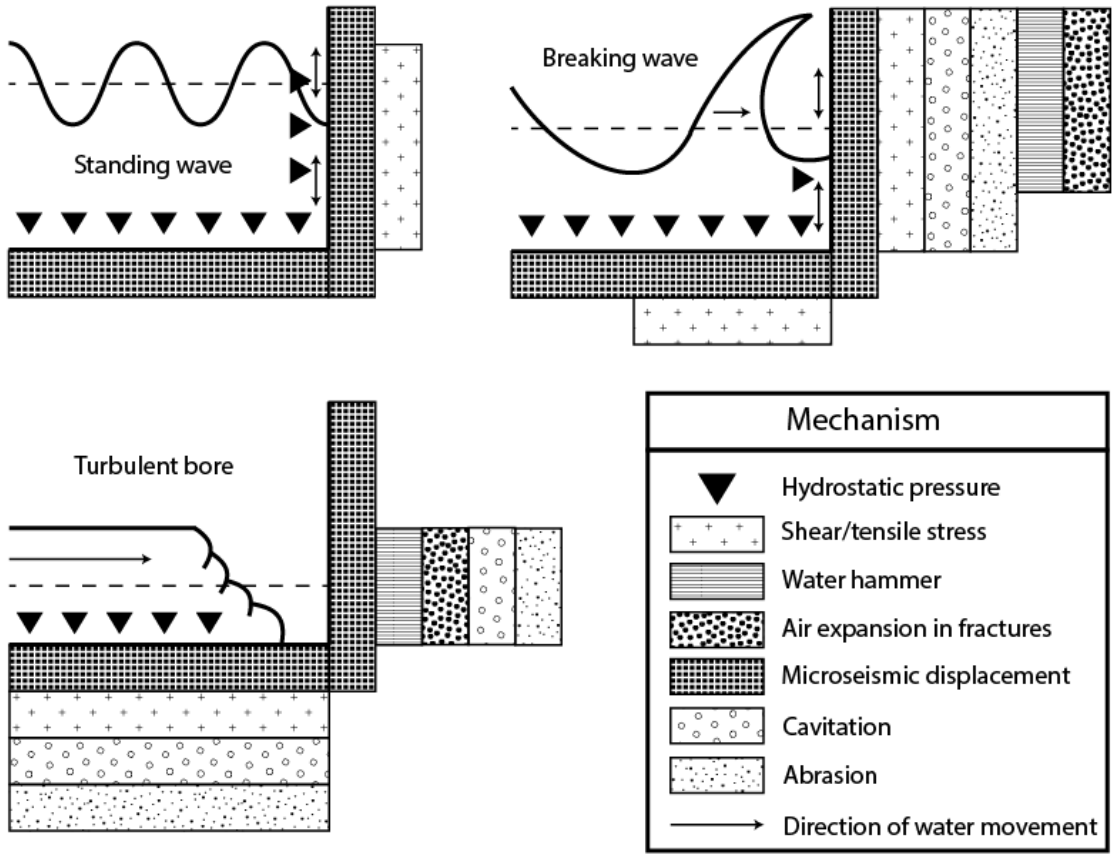

Figure 2.7: Overview of the modes of hydraulic and mechanical interactions between waves and the lower cliff. Adapted from Sanders (1968).

2.4.1. Modes

2.4.1.1. Hydrostatic pressure

Sanders (1968) and Trenhaile (1987) suggested that the application of hydrostatic pressure to the cliff may be capable of rock damage. Water levels exceeding the elevation of the cliff toe will exert pressures that are nominally hydrostatic if only standing waves are present, as the wave energy itself is predominantly reflected (Sainflou, 1928). Hydrostatic pressure is a function of water depth and hence is sensitive to both tidal stage and wave height. Allirot *et al.* (1977) and Tien *et al.*, (1990) proposed that it is the alternating compression and release during wave propagation across the rock that is the effective mechanism.

An increase in hydrostatic pressure in the water column may cause a pore pressure rise in the cliff, reducing effective stress and reducing shear strength, but this is likely to be too small to be effective. Taylor (2003) used the hydrostatic equation to calculate a maximum tidal hydrostatic pressure of 12 kPa in the water column at a depth (*d*) of 1.2 m on the Kaikoura Peninsula, New Zealand:

$$P = \rho \cdot g \cdot d \tag{2-9}$$

The maximum pressure fluctuations due to incident waves were an additional 5 kPa. These pressures were at least three orders of magnitude less than the equivalent compressive strength of the mudstone cliffs (around 22,000 kPa).

The presence of water may also reduce the value of stress failure due to decreasing internal friction, weakened intergranular cement and non-rehealing fractures. The immersion of low-porosity rocks can reduce their compressive strength by up to 10% (Burdine, 1963).

2.4.1.2. Shear and tensile stress

Sunamura (1992) proposed that the friction caused by the oscillatory movement of water at the cliff toe may be an effective mechanism for erosion (Figure 2.8). The notion of shear stresses created by waves is also conceptually supported by Trenhaile (1987) and Tsujimoto (1987). Most research focuses on the shear stresses created when waves propagate across the nearshore, but there has been little regarding the erosivity of water moving across the lower cliff. Estimates of shear stress are usually obtained from boundary layer velocity measurements (Barnes *et al.*, 2009) and are common in sedimentary environments (Cheng *et al.*, 1999), but direct measurements are rare (Park *et al.*, 2016).

There are two cases whereby water abrasion can occur at the cliff toe: standing wave oscillations and breaking wave vertical jets (Figure 2.8C). In the first case, the water at the cliff toe oscillates vertically as the wave peaks have no horizontal motion (Bagnold, 1939). This motion is most rapid between the crest

and trough of the wave at the surface (Hansom *et al.*, 2008). Similar shearing can be produced via wave run-up and down of a non-vertical cliff.

When investigating the formation of shore-normal grooves in unconsolidated sandstone, Williams *et al.* (2017) modelled the total shear stress generated by combined swash and backwash events as up to 0.012 kPa. Sunamura (1975) undertook flume experiments with standing waves at model cliffs, but was unable to measure the shearing force directly. However, he concluded that as no erosion occurred in the expected zone, the shear force was a geomorphically negligible mechanism.

When a breaking wave impacts the cliff face, some of its forward momentum is converted to vertical motion, creating a jet of water travelling up the cliff face, which can exert a shear stress (Tsujimoto, 1987) (Figure 2.8C). The receding of the water mass may subsequently exert a tensile force on the cliff face. Tsujimoto (1987) assumed that the larger the compressive force of the wave – controlled by the factors discussed in Section 2.2 – the larger the associated shear and tensile forces. Vertical jets are described numerically by Cooker and Peregrine (1990) and measured experimentally by Bullock *et al.* (2007). Neither gives an indication as to the possible magnitude of such forces.

Tensile forces may also be produced by hydraulic action at the cliff toe. Bradley and Griggs (1976) suggest quarrying of rock particles and larger blocks bounded by joints may be caused in part by tensile forces created by fluid drag, alongside changes in pressure of pore fluids. This plucking effect is caused by fluid motion parallel to the uneven rock surface (Figure 2.8B-D), pulling looser material away from the cliff face.

Falling water after a large wave impact may also cause erosion (Figure 2.8D). Vertical jets from wave impacts can thrust water up to 70 m above the impact zone at up to 77 ms^{-1} (Rouville *et al.*, 1938). Short downfall pressure peaks of over 220 kPa resulting from the subsequent impact of the falling water mass have been measured experimentally (Wolters *et al.*, 2005). These pressures were measured on the horizontal blockwork behind a breakwater and as such are not representative of a vertical or sub-vertical cliff.

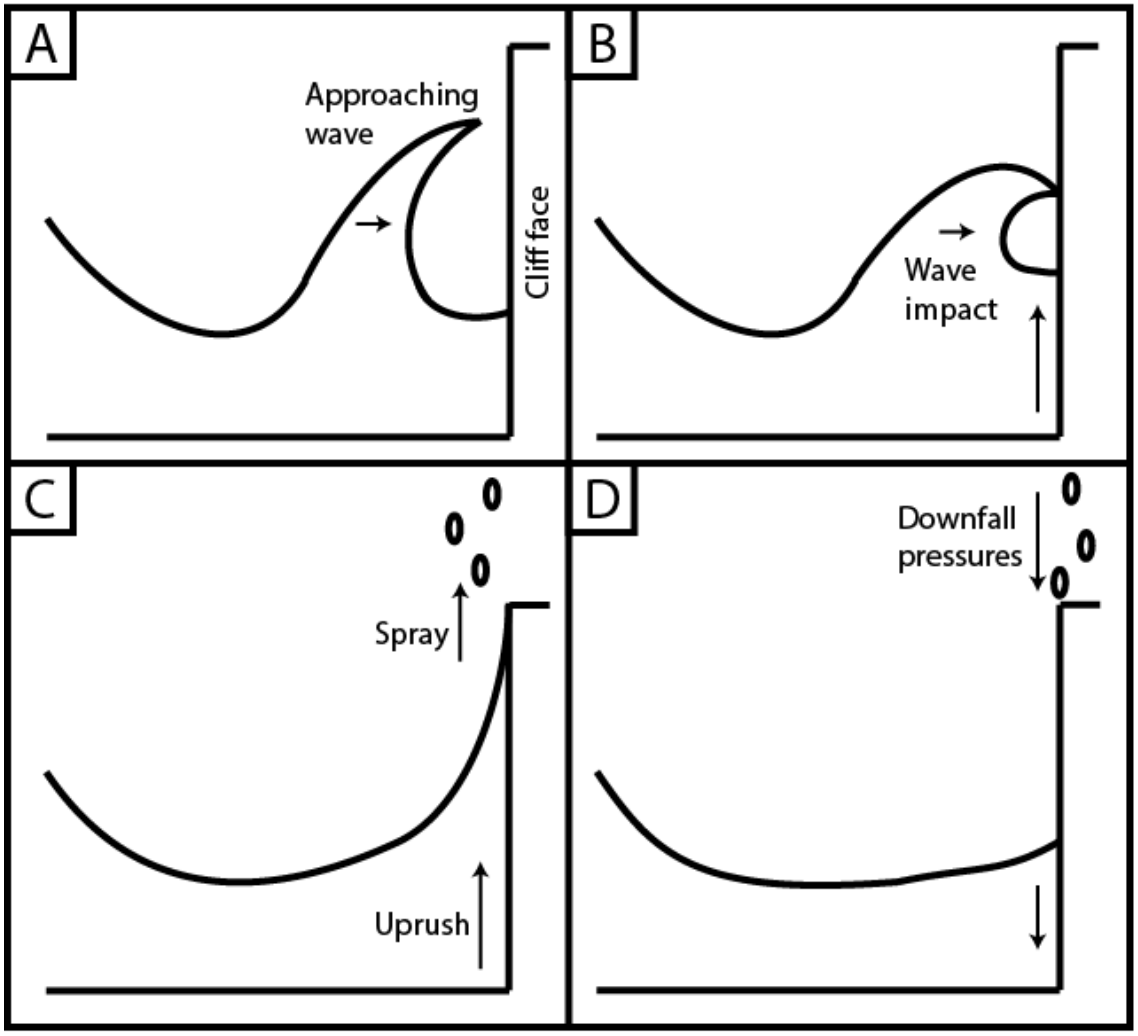

Figure 2.8: Illustration of the development of wave-induced stresses on the cliff face over the course of a breaking wave impact. A) breaking wave approaching the cliff face; B) compressive pressures on the face as momentum is transferred from water particles; C) uprush produced by vertical jets post-breaking, creating shear and tensile stresses, and spray; D) downfall pressures induced by the falling water mass.

2.4.1.3. Water hammer

Water hammer refers to the impulsive pressure generated by an impacting wave directly against a rock face (Section 2.2.2). This mechanism occurs when the surging water particles undergo a momentum change when forced to stop by the surface of the cliff. This process operates at the wave front where air and water alternate (Lundgren, 1969). Although much research on cliff erosion cite water hammer as a major mechanism for wave-induced rock damage (e.g.

Sanders (1968); Trenhaile (1987); Sunamura (1992)), no evidence has yet been put forward for its effectiveness against undamaged rock, or what the geomorphic consequence of water hammer might be on a rock coast.

Water hammer has been shown to initiate fracture in laboratory-based geomechanical studies. Forman and Secor (1974) observed spalling failures in limestone when subject to high-pressure (13 MPa) water jets. During the initial impact period, high-amplitude compression waves emanate from the impact point (Figure 2.9), which become tensile and cause fracturing. As such, assuming the fluid particle velocity (u) is reduced to zero on impact, the dynamic pressure magnitude (P_{dyn}) due to water hammer is determined by the acoustic velocity of the fluid (v_s) (Tijsseling and Anderson, 2004) and is given by:

$$P_{dyn} = \rho \cdot u \cdot v_s \tag{2-10}$$

Within fewer than 10 microseconds after impingement, the pressure reduces to stagnation pressure once the compression waves dissipate (Forman and Secor, 1974). Field (1999) maintains that water hammer pressures are responsible for most of the rock damage resulting from liquid impingement, in agreement with recent modelling by Jiang *et al.* (2017). Momber (2004a) observed fracture rings around a pristine core produced by liquid drop impingement. Material would subsequently be removed in fragments via lateral jetting. Water jets are more damaging when discontinuous – leading to repetitive application of water hammer – rather than continuous (Jiang *et al.*, 2017). Thiruvengadem (1965) showed that material deformation occurs after multiple, repeated impacts, so may occur even under pressures less than the intact rock strength.

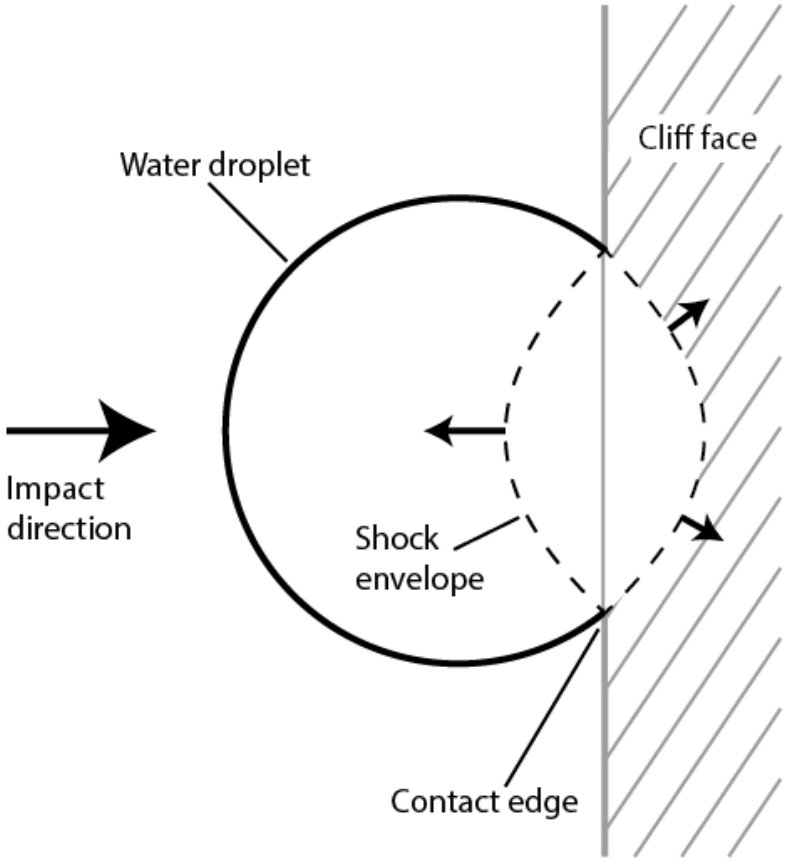

Figure 2.9: Illustration of a water droplet impacting the cliff face. Shock waves emanate from the contact edge on impact: the rock is subject to high pressure as the water behind the shock envelope is compressed. Adapted from Field (1999).

The upper limit to the magnitude of water hammer is dictated by the proportion of entrained air in the wave on impact, hence its importance in dictating impulsive pressures (Section 2.2.5.4). As such, rock coasts may exhibit a much lower propensity for water hammer due to high aeration during wave transformation (Blackmore, 1982). However, Trenhaile (1987) asserts that the high pressures generated by water hammer compensate for its relatively low frequency of occurrence.

2.4.1.4. Pressure expansion into fractures

The presence of joint sets and fissures in the rock surface are required for all rock slope failure, of which marine processes act as a catalyst (Sanders, 1968a; Robinson, 1977b; Trenhaile, 1987, 2005a; Naylor and Stephenson, 2010). There is also clear field evidence from coastal cliffs of individual blocks being

removed where pre-existing joint structures have been exploited (Caputo *et al.*, 2018), typically around mean sea level.

Hall *et al.* (2008) found that sockets in a deep-water fronted ignimbrite cliff indicated recent removal of fracture-bounded blocks. Further mathematical modelling of fractures indicated that wave forces must have exceeded the tensile strength of 1.5 MPa. This indicates that pressure waves may also propagate into these fractures and assist wave quarrying from inside the rock structure, and may be the key mechanism through which water hammer drives rock quarrying (Müller *et al.*, 2003), rather than direct impacts on to flat rock surfaces.

Muller (1997) demonstrated that compression waves from wave impacts can enter water-filled fractures and become amplified towards the back of the fracture (Figure 2.10). This pressure wave can cause high-magnitude tensile stresses inside the rock structure; tensile stress at a crack tip can be an order of magnitude higher than inside the fracture body. As wider fractures exhibit higher pressures, small cracks may be enlarged over time, leading to increased pressures and thus enhanced fracture widening, accelerating fracture propagation (Marth *et al.*, 2005). Consequently, crack tip propagation under breaking wave conditions on fractured rock could be commonplace, particularly since fracture geometries, which might be highly complex in rock cliffs, have no effect on the pressure wave (Müller *et al.*, 2003). Marth *et al.* (2005) showed that even front face pressures can vary depending on the ventilation at the crack tip (Figure 2.10), which may lead to considerable variation in wave forcing across a cliff face with a complex fracture network.

Wolters and Muller (2004) showed that partially submerged cracks, which are more common at the cliff toe, may be even more susceptible to internal tensile stresses caused by wave impacts propagation than fully submerged cracks.

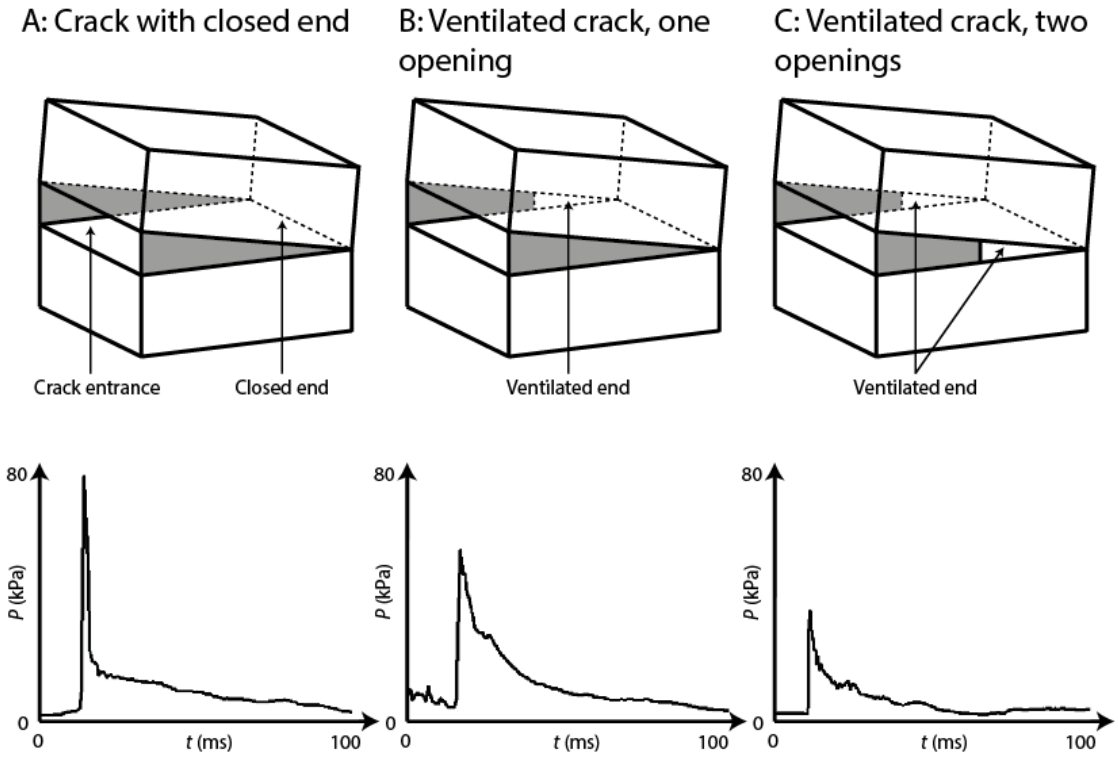

Figure 2.10: Illustration of the variation in crack front face pressure induced by wave impacts. A) Cracks with no ventilation generate the highest pressures, followed by B) one and C) two openings. Adapted from Marth *et al.* (2005).

Using Bagnold's (1939) air piston model for air compression inside joints, Taylor (2003) estimated pressures inside a 0.5 mm crack could be as high as 2,000 kPa. Still, Marth *et al.* (2005) stressed the requirement for closed cracks and joints with no lateral leakage of pressure in order to obtain these high crack tip stresses. Robinson (1977b) suggested that this manner of erosion may be more effective when entrained sand particles are wedged inside the crack, holding it open and driving repeated pressure to be cumulative, not repetitive. Once a joint-bounded block is no longer attached to the rock face, Trenhaile and Kanyaya (2007) calculated that water pressures of only 10 kPa were required to dislodge a large (~0.5 m^3) block from its position in the cliff or platform scarp.

There is some evidence to suggest this mechanism may not be dominant on all rock coasts. Davies *et al.* (2006) found that joint density was *not* correlated with platform width over a selection of rock coast sites in the UK and Japan. Intact rock compressive strength was found to have a higher correlation, but still

relatively weak. However, this may be due to the inherent rock properties in the sites studied: the most densely-jointed sequence in the study comprised of Liassic limestone, where chemical weathering may dominate (Momber, 2004b; Trenhaile, 2015).

2.4.1.5. Microseismic ground displacements

Coastal cliffs produce a measureable response to wave impacts on the lower cliff through microseismic ground shaking. Long-period swell waves and infragravity waves have been found to induce flexure in the cliff which may damage the rock via progressive fatigue from cyclic loading (Young *et al.*, 2011), through micro-crack propagation, interaction and coalescence. This process also assumes that the zone of accumulated damage is large enough to cause damage, and that damage is cumulative through time with each load cycle.

However, Brain *et al.* (2014) suggested that rocks may require a pre-damaged condition before ground shaking becomes effective, and that critical stresses only occur in zones of limited spatial extents controlled by macro-scale stress states. Damage may only accumulate during high-energy storm events, where displacements were found to be higher and loading direction shore-normal (Brain *et al.*, 2014). Furthermore, Adams *et al.* (2005) showed that the entire cliff flexes downwards in response to wave loading, but in order to generate internal strains, differential flexing within the rock mass must be produced. These spatial and temporal limitations probably render microseismic ground displacements a relatively unimportant mechanism for direct geomorphic work.

2.4.1.6. Cavitation

Cavitation is the process whereby bubbles of vapour form and collapse in a fluid stream. Cavitation has been shown experimentally to rapidly erode concrete dam spillways (Barnes, 1956), river channels (Whipple *et al.*, 2000), rocks (Momber, 2003) and metals (Cheng and Ji, 2017). Although often cited as an erosive agent of coastal rocks (Sanders, 1968a; Trenhaile, 1987; Sunamura, 1992; Brossard and Duperret, 2004; Rampino, 2005), cavitation appears to be very poorly understood in this context. The hydrodynamic conditions in a rock coast environment are evidently very different from those of channel flows.

Particle velocity and directionality is highly variable, with shear flow occurring both parallel and perpendicular to the cliff and along the platform surface, varying with wave impact type. As yet very little research has been undertaken to evaluate the action and efficacy of cavitation at the cliff toe.

2.4.1.7. Abrasion

Abrasion refers to the array of mechanical processes involved in the wearing down of rock surfaces by sediment entrained within fluid flow. This ranges from the friction generated by the dragging or saltation of small particles across the rock surface (Sklar and Dietrich, 2001) to large clasts impacting the lower cliff in high-energy events (Williams and Roberts, 1995). Mechanical abrasion therefore requires a source of sediment coupled with a flow capable of moving sediment; the main control of abrasion efficacy is the balance between wave energy and clast mass (Blanco-Chao *et al.*, 2006). Impact stresses increase with particle mass and velocity, with sediment positioning with respect to the cliff toe, size and geometry also factors (Kline *et al.*, 2014).

Erosion by abrasion results in a characteristically smooth and spatially uniform surface, creating rounded protrusions and scarps. Percussion and scratch marks are common (Cullen and Bourke, 2018). Rounded grooves can form along structurally-controlled weaknesses (Trenhaile, 2005b). These surfaces are morphologically very different from quarried surfaces, which are often blocky and sharp, reflecting fractures or pre-existing discontinuities (Robinson, 1977b) and can actually inhibit wave quarrying mechanisms. Thus abrasion is usually dominant where there is suitable sediment availability (Naylor *et al.*, 2010). Thick accumulations of sediment can also act as cover for the lower cliff, protecting the rock surface from wave attack (Stephenson, 1997; Kline *et al.*, 2014). What is clear is that abrasion can only take place where suitable sediment is available, but can be a locally dominant process when wave and sediment conditions are met (Figure 2.11).

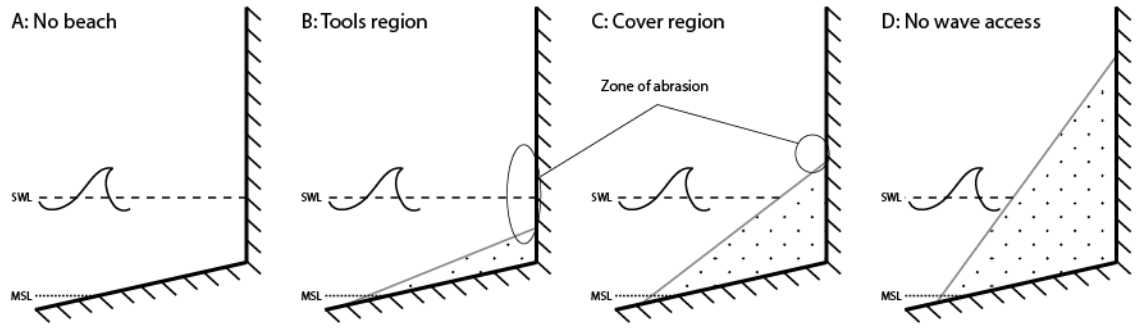

Figure 2.11: Conceptual model of tools/cover process. A) Negligible abrasion where no sediment is present; B) Sediment cover provides abrasive material for enhanced erosion; C) deeper sediment drapes provides protection of the lower cliff; D) complete sediment cover obstructs all wave energy. After Kline *et al.* (2014).

2.4.2. Summary

In this review I have demonstrated that there is considerable temporal and spatial variation in the effectiveness of the modes by which wave impacts may damage rocks and remove cliff material. In addition:

- The occurrence of any of these mechanisms remains highly speculative, with little quantitative evidence supporting them. In addition, the relative magnitude of the erosive potential of each mode is poorly understood.
- Of the modes discussed, it is likely that abrasion, water hammer, pressure expansion into fractures are truly geomorphologically effective on rock coasts, due to their relative magnitudes compared with rock resistance.
- Of these, abrasion is reasonable well-understood. However, knowledge regarding the occurrence and effects of wave impacts on rock coasts is limited, but the potential for erosion via this mechanism is high. This mechanism therefore warrants further study.

2.5. Summary and implications for coastal cliff erosion

It is evident from this review that the erosion of rock coast cliffs is driven by a combination of marine and subaerial processes underpinned by the material

properties of the cliff. Impact pressure produced by wave action is understood to be the primary mechanism behind hydraulically-driven rock damage. As such, understanding how waves interact with the lower cliff is a key component to unpicking the relative contribution of wave action.

Numerical modelling using various marine metrics such as tidal inundation, wave energy and predicted impact pressures have been used to inform the marine component of wave forcing. However, these are based on experimental and numerical data from literature primarily concerned with coastal structures and as such, may not be directly applicable to rock cliffs. High-magnitude impulsive wave impacts caused by water hammer and delivered through broken and breaking waves impinging on the lower cliff have been identified as likely primary mechanisms by which rock is damaged. Therefore, further study of their magnitude and frequency is warranted.

The key controls on the magnitude of impulsive wave impacts at coastal structures have been identified, yet it is not known to what extent these apply to natural rock coasts, nor any additional controls that might exist. Direct, in-situ measurements of impact pressures with strain-gauge pressure sensors have enabled a considerable improvement in the understanding of wave hydrodynamics on seawalls, breakwaters and in flume tanks. As such, my study will apply techniques used in these studies to a rock coast setting to evaluate the applicability of such knowledge in this environment.

Using TLS-based cliff erosion monitoring and measurements of wave conditions, the contribution of marine-driven erosion and the erosion signature of such processes can be evaluated. Providing field measurements to link cliff toe wave conditions, wave impact characteristics and subsequent erosion of the lower cliff is intended to fill the knowledge gap. In turn, this will feed into future models of cliff erosion.

This review has highlighted a number of questions regarding the present understanding of wave-driven erosion at rock coast cliffs:

- What is the relative importance of each mode of rock damage by wave action in driving cliff erosion?

- What are the dominant mechanisms by which material is removed from the cliff by wave action, and can we identify these through erosion monitoring?
- What is the interplay between the modes of rock damage and the resisting force of rocks?
- To what extent does the current understanding of wave forcing apply to rock coast cliffs?
- What are the hydrodynamic conditions at the cliff toe and do impulsive wave impacts occur?
- As such, do current predictive formulae of coastal cliff recession based on this understanding accurately represent the wave-driven contribution to overall cliff erosion?

3. Study Site

3.1. Introduction

The diverse range of material properties, structural geology and morphology of rocky coasts leads to a requirement for a field location that is not only appropriate for the study of marine hydrodynamics and erosion, but also reasonably representative of rocky coasts in general. The study area selected is the coastal foreshore immediately west of Staithes, situated along the southern North Sea in North Yorkshire, UK (Figure 3.1).

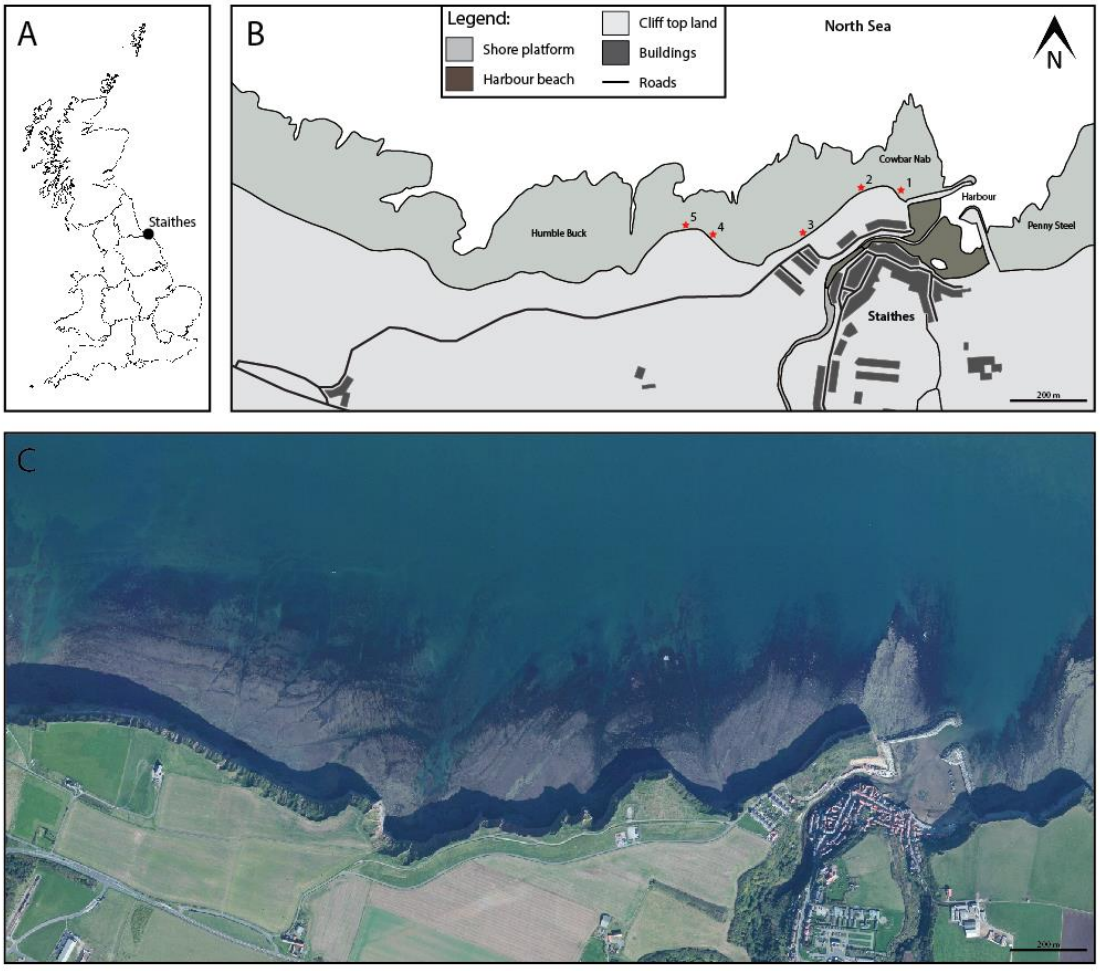

Figure 3.1: A) Location map of Staithes within the UK. B) Map of the study site, comprising of the shore platform north of Staithes, with the cliffs located between the shore platform and the cliff top land. Red stars denote site locations. C) Aerial photo of the study site (Google Maps, 2018).

The study sites are located along the cliff at the eastern harbour wall and around the base of Cowbar Nab, comprising approximately 700 m of coastline.

3.2. Site geology

The lithology of the shore platform and cliff is comprised of Lower Jurassic strata corresponding to the boundary between the Lower and Middle Lias, deposited between 199.6 – 175.6 Ma (Rawson and Wright, 2000). The cliffs at Staithes consist of the lower section of the Staithes Sandstone Formation overlaying the upper section of the Redcar Mudstone Formation. These deposits were laid down in shallow marine tropical seas in the northern Cleveland Basin. Uplift in the Cretaceous led to the inversion and consequent north-south dip seen in the cliff sections (Simms *et al.*, 2004).

The stratigraphy comprises of interbedded fossiliferous mudstones, shales, siltstones, sandstones and ironstone (Figure 3.2). The structural dip to the south of approximately 2° means the lithology of the cliff toe changes alongshore; in the study area the toe is comprised of shale and mudstone interbedded with sideritic concretions. As such, the cliff materials that are exposed to wave action vary in their erosion and weathering resistance alongshore, forming diverse cliff toe profile morphologies. The entire sequence is cut by extensional features including minor antithetic-synthetic normal fault sets and fracture swarms (Emery, 2016). Jointing can be seen within the competent strata.

The cliff tops are mantled by up to 15 m of Pleistocene silty glacial till, derived from Devensian ice to the west (Rawson and Wright, 2000). Cliffs along the study site vary between 30 – 70 m in height. The platform includes loose and cemented boulders, algal and seaweed growth and occasional quarried scarps at lithological boundaries (Figure 3.3).

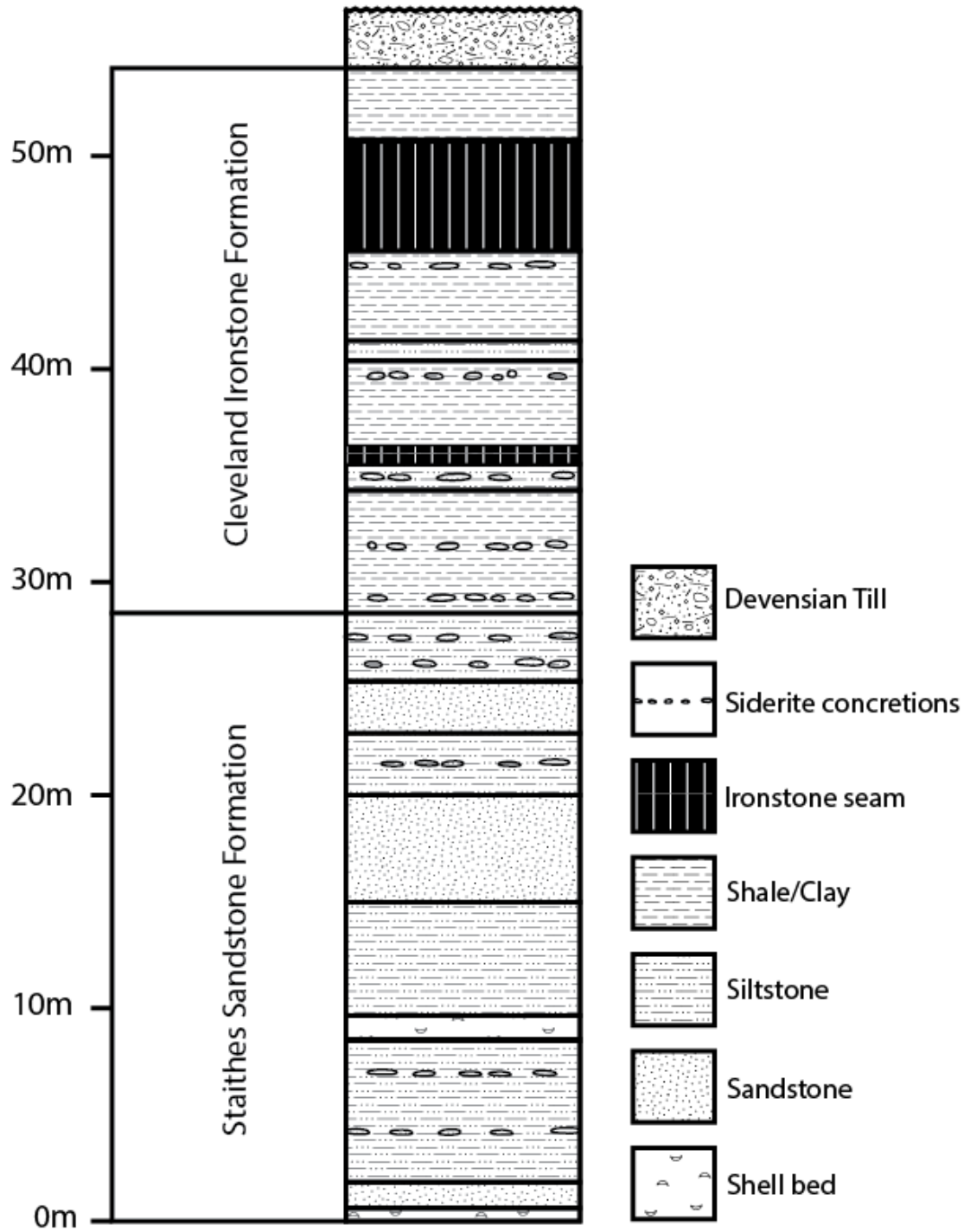

Figure 3.2: Lithological section through the cliffs at the research area. The Jurassic sedimentary rocks are capped by glacial till. After Rawson and Wright (2000).

Figure 3.3: Part of the study site at Staithes. An approximately 60 m high cliff section can be seen, fronted by a shore platform scattered with boulders and infrequent sediment pockets.

3.3. Site climate and weather

The climate of northeast England is temperate oceanic and experiences relatively cool winters and mild summers compared with the rest of the UK. Mean annual maximum temperature 1967-2016 as measured from the weather station at Loftus – 5 km to the west of the study site – is 12.4°C, with mean summer high of 18.1°C. The warmest month is July, with a mean daily maximum of 18.9°C. Mean annual minimum temperature is 6.2°C, with a mean winter low of 1.9°C. The coldest month is February, with a mean daily minimum temperature of 1.7°C (Met Office, 2017). Sea surface temperatures range from 5°C in winter to 13°C in summer. Mean annual precipitation is 588 mm, which compares with a UK average of 885 mm (Met Office, 2017). Storm precipitation rates have been measured up to 9.8 mm h^{-1}. Snow and fog are also common during winter months. During winter months, high wind speeds are produced during low pressure systems tracking northeast-wards. As such, the strongest winds are most commonly blowing from the southwest to northwest as Atlantic depressions migrate through. Local mean wind speeds of 5 ms^{-1} and maximum gusts of 41 ms^{-1} occur during winter storms (Lim *et al.*, 2010).

3.4. Site marine conditions

Tides, wind waves, swell waves and wind-driven currents are the most important hydrodynamic processes in the central North Sea (Van Der Molen and De Swart, 2001). The prominence of the Atlantic storm track to the north determines the nature of the wave climate offshore of the study site, hence the North Sea is considered to be storm wave dominated. Short-period gravity waves are produced through wind-sea surface interaction with the local wind field, which are fetch-limited due to the relatively small North Sea basin (Weisse *et al.*, 2012). These are generally superimposed on to long-period swell waves, propagating predominantly from the Norwegian and Greenland seas to the north. On average, 35% of the wave spectrum is swell waves (Boukhanovsky *et al.*, 2007). Wave climatic spectra in the western North Sea can be classified according to the combination of wind and swell waves occurring at any one time (Table 3.1). Single-peaked, wind-wave dominant seas are most common in this

area, occurring 61% of the time. The typical sea state duration is approximately 12 h (Van Der Molen and De Swart, 2001).

Table 3.1: Occurrences of climatic wave spectra in the western North Sea (Boukhanovsky *et al.*, 2007).

Class	Description	Occurrence (%)
I	Single-peaked, wind wave	61
II	Single-peaked, swell wave	6.3
III	Complex, double-peaked, fresh swell	18
IV	Complex, double-peaked, mature swell	9.8
V	Complicate seas, multi-peaked, two or more swells	4.8

Water depth variance along the northeast coast is controlled principally by a semidiurnal, macrotidal cycle. Mean low water spring of 0.8 m ODN (Ordnance Datum Newlyn) and a mean high water spring of 5.6 m ODN, give an average spring tidal amplitude of 2.4 m (Huthnance, 1991). Consequently, the still water level at the cliff toe reaches over 3 m above the platform at high spring tide, and up to 4.3 m during storm surges (Lim *et al.*, 2010). The large tidal range means that the cliff toe undergoes full submergence and emergence with each tidal cycle.

3.5. Geomorphology

3.5.1. Quaternary history

It is still unclear as to whether contemporary coastal morphology at Staithes is a direct result of material and process interactions in the Holocene, or controlled by a previously delimited landform inherited from the Pleistocene. There is considerable evidence that some hard rock coasts may have been inherited from previous interglacials, where local relative sea levels would have been comparable to today (Stone *et al.*, 1996; Blanco Chao *et al.*, 2003). Lim (2014) asserted that inheritance is not important at Staithes, but provided no

supporting evidence for this. Trenhaile (2001) argued that on tectonically stable coastlines, it is very unlikely that shore platforms could have developed wholly within the present interglacial. In contrast, the lower platforms are more stable and often support dense mats of marine organisms. This indicates that inherited shore platforms are modified at the high tide level cyclically during repeated interglacials. This phenomenon is underlined by Swirad *et al.* (2016), where LiDAR-derived shore-normal cross-sections were used to undertake a geomorphic sensitivity analysis of a 4.2 km section of the Staithes coastline. Only weak relationships were found between morphology, geology and marine forcing, highlighting a possible role of inheritance as well as material – process interaction in shaping the coastline. However, the presence of active erosional features at or near the cliff toe such as quarried scarps suggests erosion here is ongoing. As such, the site is still suitable for studying such processes despite the possible influence of inheritance on the broad-scale morphology.

3.5.2. Retreat rates and erosion monitoring

The geomorphology of the area has been studied in some detail, beginning with Agar (1960) who compared Ordnance Survey mapping between 1892 and 1960 to produce an overall retreat rate for the period. The erosion rate at Cowbar Nab at the eastern end of the study site (Figure 3.1) was calculated to be 0.05 ma^{-1}. It was found that the cliff toe at embayments were eroding 0.03 ma^{-1} faster than headlands, suggesting such deviations in planform morphology would become enhanced over time. Cliff toe erosion was also found to be comparably faster than the cliff top, indicating a continuing tendency towards ever-steeper cliff profiles. Such a trend would be implausible as a universal geomorphological regime (Lim, 2006), yet does raise interesting questions surrounding the drivers of cliff change over centurial timescales; whether marine-driven notch formation and subsequent cliff collapse drives full-scale retreat over decadal timescales, followed by some change in erosive regime after which such rates are reversed. However, sizeable error margins in calculating retreat rates using aerial mapping render such evidence highly speculative.

Since 2003, the study site has been monitored using terrestrial laser scanning (TLS), leading to substantial improvements in understanding the nature of cliff

retreat in the area. Lim *et al*. (2005) and Rosser *et al*. (2005) demonstrated the use of a combination of digital photogrammetry and TLS to overcome the inadequacies of previous techniques (such as mapping and rock inventories) in quantifying volumetric changes as cliff material is removed. Overall retreat rates in the study area were revised down to 0.024 ma^{-1} using TLS monitoring: approximately half of the previous estimates which used mapping alone. Volumetric rock yield per linear metre of coastline averaged 1 m^3 per year. Erosion rates were again found to be substantially higher at the cliff toe (0.12 ma^{-1}) than above the inundation zone (0.02 ma^{-1}) (Norman, 2012). Differential retreat rates have also been observed between lithologies, with the highest to lowest rates being in mudstone, siltstone, shale and sandstone respectively (Rosser *et al.*, 2013).

3.5.3. Marine processes at the cliff face

The coastline at Staithes is shaped by the combination of complex physical mechanisms acting at the shoreline. Robinson (1977a) surmised that sediment-free sections of coastline were subjected to a combination of sporadic block quarrying and continual spalling of the more friable shales and mudstones. Erosion rates due to quarrying were more than an order of magnitude lower than for abrasion-dominated zones where sediment was present. Abraded surfaces tended to be smooth and relatively uniform, whereas quarried sections had prominent structural planes and rough, angular faces. The tendency for beach sediment to accumulate within embayments may explain the erosion rate differences found by Agar (1960). Importantly, Robinson (1977b) discounted corrosion and abrasion as unimportant processes at Staithes due to the lithology and cliff structure respectively, lending the near sediment-free sections an ideal location to investigating hydrodynamic forcing of erosion in comparative isolation.

By coupling TLS datasets with long-term, high-resolution environmental monitoring, Rosser *et al.* (2005) associated cliff failure with extreme rainfall and storm waves. Seasonal variation in the rate of cliff toe erosion was attributed to increased wave quarrying associated with larger waves during winter. Lim *et al.* (2011) further investigated marine forcing by comparing rockfall occurrence

from the Staithes TLS data with microseismic ground movements triggered by marine and subaerial forcing. A set of critical environmental conditions, involving tide level and wind direction, was found to cause a considerable increase in both energy delivered to the cliff and material loss from the cliff. The timing of increasing levels of rockfall activity correlated with antecedent microseismic events, suggesting a possible lag time or threshold rock fatigue before final failure. Modelling of the relationship between future sea level rise and number of wave impacts concluded that the direct linear relationship assumed in most coastal cliff models is probably incorrect, implying a more complex process.

Norman *et al.* (2013) used an array of cliff-top seismometers to reveal a correlation between microseismic signals and prevailing wind, wave and tide conditions. Using this method, periods of high water level during storms were shown to provide peak energy transfer to the cliff, indicating it is under these conditions most erosion will occur, rather than during high inundation in quiescent wave conditions. In addition, Rosser *et al.* (2013) ascribed the propagation of failure upward from the cliff toe with defining the mode and rate at which marine forcing can actively erode the cliff above. Progressive upward failure occurs independently from concurrent environmental conditions after being triggered by external forcing.

Vann Jones *et al.* (2015) attempted to quantify the controls of cliff erosion using a combination of TLS, microseismic, wave climate and tide data. Results revealed a clear influence of marine processes on the volume and size of rockfalls, even those above the cliff toe. Marine-triggered failure above the cliff toe was found to occur due to either microseismic ground motions or up-cliff stress propagation of marine-driven rockfalls. Although the greatest erosion over the period was found at the cliff toe, higher regions up the cliff that corresponded to water levels during storm events did not recede quicker than the overall cliff toe. This lack of correlation is explained by variations in the shore platform bathymetry causing localised wave focusing.

Lim *et al.* (2011) outlined a requirement for the study area to deploy multiple instruments at the cliff base to provide information on specific wave effects.

Additional research into the wave conditions at the cliff toe may facilitate the isolation of marine-driven retreat. This previous work has demonstrated the considerable advantages of TLS regarding capturing high-resolution erosion data and examining erosion characteristics. As such, I utilise TLS alongside monitoring of wave conditions in my study in order to investigate the marine contribution to erosion of the lower cliff.

3.5.4. Subaerial processes at the cliff face

The regular emergence of the lower cliff between tidal cycles means the full height of the cliff is subject to subaerial weathering. Norman (2012) described the range and relative dominance of each mechanism acting at the study site. Wind erosion was found to be particularly important, with the upper cliff more exposed to stronger offshore gales. Local wind fields were shown to vary, producing multi-directional forcing on the cliff face.

The lower section of the cliff is vulnerable to cyclical wetting and drying, salt weathering (Stephenson and Kirk, 1998) and freeze/thaw (Carter and Guy, 1988; Wilcock *et al.*, 1998). Cliff seepage has also not been observed at the study site. Other extant biological agents such as algal films, boring organisms and vegetated mats (Naylor and Viles, 2002) are unstudied in the region, so it is unclear whether, if at all, they provide bio-protective or bio-erosive functions.

3.5.5. Human influences on the study site

Human activities in the past four centuries have profoundly altered the shore platform and cliffs in the region. Mine workings in the Alum Shale Member and ironstone bands have been present since the 1600s (Staniforth, 1993). Contemporary underground mine workings are also extant beneath the platform due to the Boulby Potash Mine, 700 m to the southwest, although subsidence is thought to be negligible at Staithes. It is difficult to assess the extent to which the morphology and nearshore processes have been modified by such activities. Removal of material from the shore platform could modify wave transformation across the platform (Lim, 2014); extraction from the cliff may have altered internal stress regimes and characteristic erosional surfaces.

The western harbour wall extends out from Cowbar 120 m northeastwards, starting at the eastern extent of the study site (Figure 3.1). This is constructed of rock armour comprising of large boulders of Norwegian granite, which may act to reflect or funnel incoming waves from the north. Rock armour is also present at the centre of the study site along the base of the northwest-facing cliff, designed to protect the road and cottages above.

3.6. Site selection

I selected the foreshore at Staithes as the location to investigate the hydrodynamic contribution of waves to cliff erosion due to the improvement in understanding erosive processes through long-term erosion monitoring. As such, my study builds on the understanding of marine drivers, wave transformation, wave energy delivery and lower cliff erosion already present at the site. A number of other general and site-specific factors were crucial to unpicking the role of wave impacts from other modes of cliff retreat.

3.6.1. Characteristics of the general study area

The ratio between wave height and water depth has been suggested to be a key component in dictating the breaking characteristics of a shoaling wave (Cooker and Peregrine, 1990b); as such, a wide variation in both typical wave heights and tidal elevation is crucial. The study site is macrotidal and semi-diurnal, allowing a wide range of water depths to be monitored over a relatively short period of time, and access to monitoring equipment for over four hours, twice per day. The storm-dominated wave regime and variable spectra includes locally generated wind waves and well-developed swell and a wide variation in wave heights and periods.

As discussed, platforms with little mobile sediment are required in order to isolate hydrodynamic erosion from abrasion. Aside from a shallow covering of sediment inside the embayment, the platform is relatively sediment-free, so it can be assumed that abrasion is not important here. This is supported by the quarried blocks and rough surfaces observed at the cliff toe. As the lithology is

also non-calcareous, corrosion by chemical dissolution is unlikely to be driving mechanism of erosion.

3.6.2. Characteristics of the specific sites

Each alongshore section at Staithes varies in platform width, gradient and elevation. In order to vary the transformation, refraction and shoaling properties of incident waves, I chose five study sites at which to monitor cliff erosion and wave conditions at the lower cliff (Figure 3.1). Sites were chosen specifically where boulders on the platform fronting the cliff were scarce. As such, wave transformation across the platform to the cliff toe would be less complex. Due to the dip of the bedrock, the lower cliff lithology varied between sites. This variation in incident conditions, lithology and platform morphology allowed a range of conditions to be studied. Site 1 (Figure 3.1), chosen initially for its practicality for setting up other instrumentation (Chapters 5 and 6) was deemed inappropriate for erosion measurements as the lower 3 m of the cliff was obscured by large boulders and a talus slope. These features were highly mobile and prevent a reliable sequence of DEMs from being established.

In order to ensure the cliff toe was not protected from marine forcing, sites were also chosen specifically to avoid areas of rock armour or large talus accumulations. Areas of sediment accumulation were also avoided. In addition, each site was accessible at low tide, in order to deploy and retrieve instrumentation and conduct TLS surveys.

3.7. Quantification of site morphology

Shore platform morphology is known to control wave energy flux (Stephenson and Thornton, 2005; Limber *et al.*, 2014) and breaking characteristics (Farrell *et al.*, 2009) at the cliff toe. Poate *et al.* (2016) outlined three key controls on wave transformation across shore platforms – width (w), slope (S_p) and roughness (r) – which will be quantified here. Additionally, platform elevation (E_{toe}) (which controls water depth (Trenhaile and Layzell, 1981)), ramp slope (S_r) and cliff aspect (θ) are described.

3.7.1. Site profile extraction from LiDAR data

To quantify shore platform morphology, I used data from a high-resolution LiDAR survey (~60 points per m^2) of the coastline at low- to mid-tide in mid-2015, from which a 0.5 m DEM was derived. I used shore-normal transects to calculate profile elevations (transect maps can be found in Section 5.2.1.1). The differences in profile length between sites were due to the limited seaward extent of the LiDAR dataset as well as varying platform lengths.

From the platform DEM, I calculated various measures of profile morphology (Figure 3.4). Platform width (*w*) was taken as the distance from the cliff toe to the water line at MLWN. Cliff toe elevation (E_{toe}) was calculated as the mean elevation across the site width. Platform slope (S_p) is the mean slope across *w* and ramp slope (S_r) is the mean slope of the platform from a point 10 m from the cliff toe. Roughness (*R*) was calculated for each transect as an average of the standard deviation of slope within a 3 x 3 cell window from the DEM. Lim *et al.* (2011) used standard deviation of elevation for their roughness calculations but Grohmann *et al.* (2011) recommends against this measure with coarser resolution data, hence the choice for this study. Reference water levels were taken from the British Oceanographic Data Centre, using data from the Whitby tide gauge, ~15 km to the east.

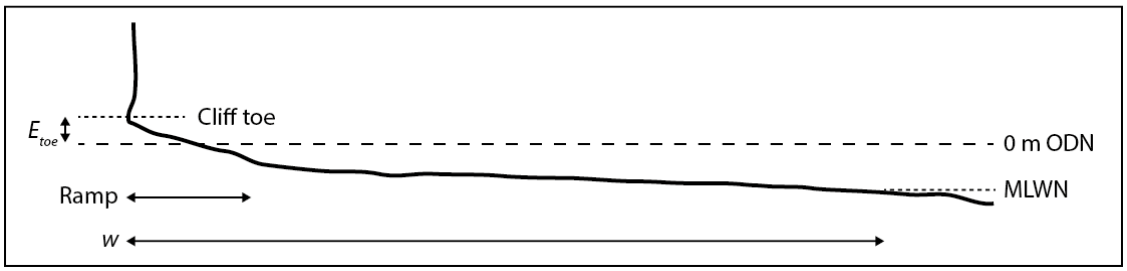

Figure 3.4: Schematic platform profile. Platform width (*w*) is shown as the distance between the cliff toe and the MLWN. Platform elevation (E_{toe}) is the elevation in relation to 0 m ODN. The platform ramp is the nearest 10 m of platform to the cliff toe.

3.7.2. Shore platform morphology

Platform profiles for Sites 2-5 and a summary of platform morphology by site can be seen in Figure 3.5 and Table 3.2 respectively. Topographic, slope (S_p) and roughness (R) maps are shown in Figure 3.6.

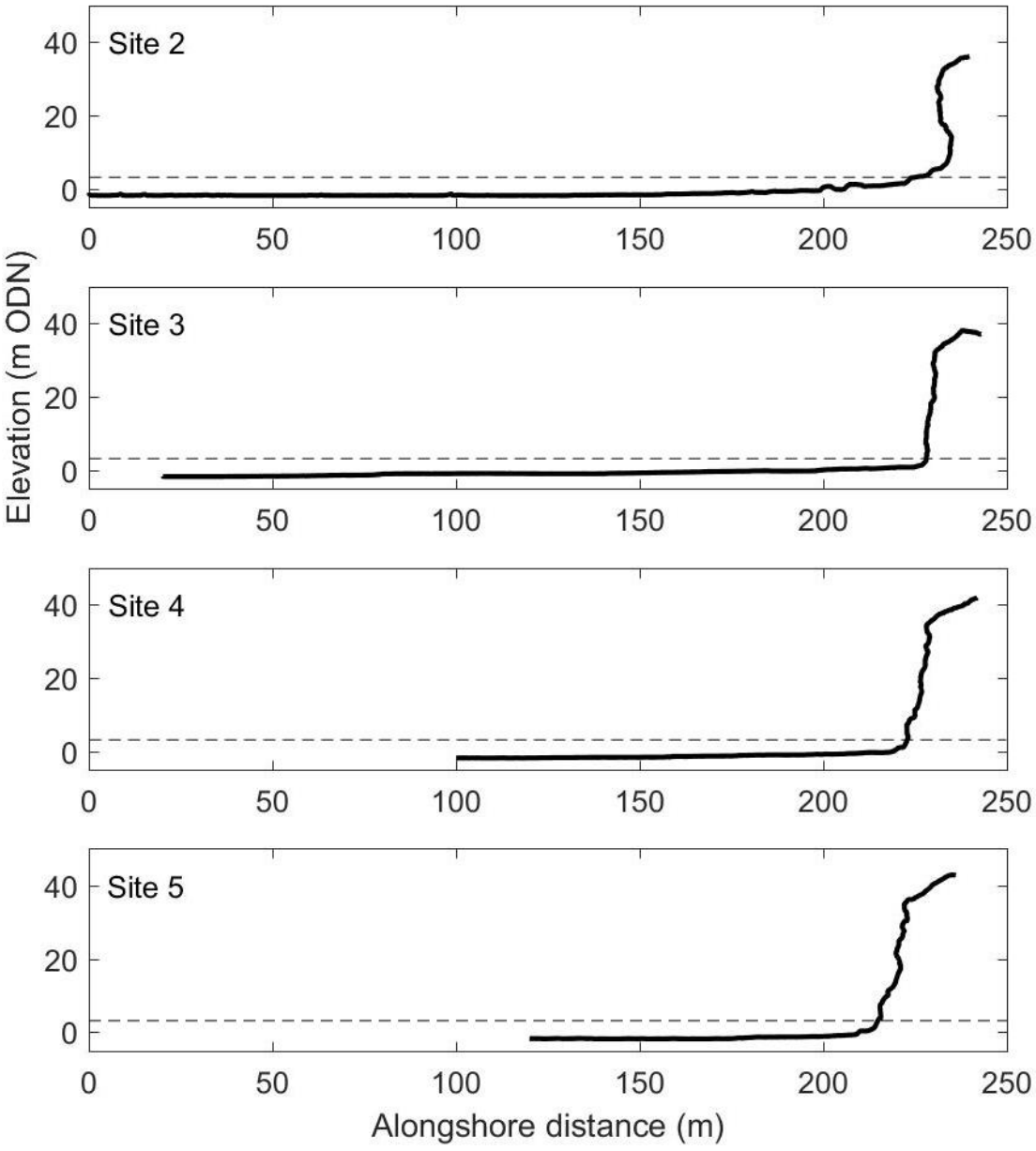

Figure 3.5: Cliff profiles for Sites 2-5 displayed relative to ODN. Dotted line represents the highest astronomical tide (HAT) level. The seaward edge of the

profile represents the limit of the aerial LiDAR DEM. Note the steeper profile at Site 3 and overhanging cliff at Site 2.

Table 3.2: Platform morphology by site derived from the DEM.

	Site 2	**Site 3**	**Site 4**	**Site 5**
Mean Slope (S_p) ± St. Dev. (°)	0.9 ± 4.7	0.8 ± 2.5	0.5 ± 2.6	0.4 ± 2.3
Ramp Slope (S_r) ± St. Dev. (°)	1.5 ± 4.8	4.6 ± 7.1	4.6 4.2	1.8 ± 2.7
Roughness (R)	0.044	0.009	0.020	0.020
Platform width (w) (m)	135	166	40	36
Cliff toe elevation (E_{toe}) (m ODN)	1.9	2.2	0.6	0.8
Aspect (θ) (°N)	0	45	320	340

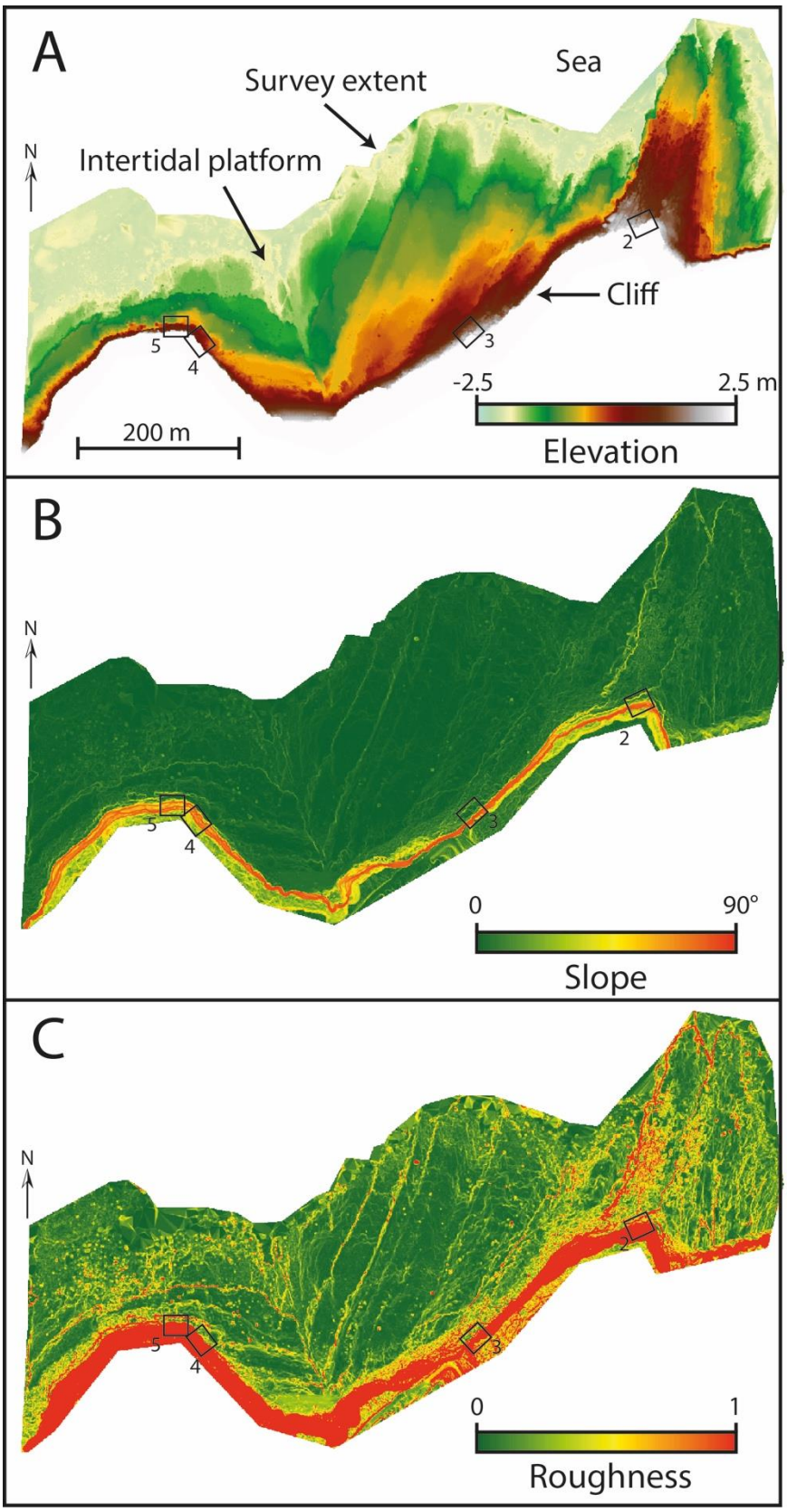

Figure 3.6: Aerial maps of survey area derived from LiDAR data. A) Platform elevation (E); B) slope (S_p) and C) normalised roughness (R) are shown. Insets show location of Sites 2-5.

Values for S_p ranged between 0.4° and 0.9° with standard deviation of up to 4.7°. Values for S_r range between 1.5° and 4.6°. These values conform to the observed slope for other similar platforms (Kennedy, 2015). Sites 3 and 4 are considerably steeper at the cliff toe than the others. Site 2 also exhibits a large scarp at the cliff toe approximately 1 m in height and 12 m in width, creating a horizontal shelf in front of the vertical portion of the cliff (Figure 3.7)

Figure 3.7: Cliff toe and face at Site 2 with fieldworker for scale. Note the cliff toe shelf extending approximately 12 m seawards from the vertical cliff face. Image was taken prior to scanning commencement and large boulders in foreground were not present during the study period.

There is considerable variation in platform width (w) between the sites, with Sites 2 and 3 over three times wider than Sites 4 and 5 (Table 3.2). Here $w \propto E_{toe}$ as it is defined relative to the MLWN: As platform slope (S_p) values are similar across the sites, where E_{toe} is lower, the distance to the water line is reduced, and hence a smaller w.

Site 2 exhibits the highest roughness (R), which can be observed on the platform in the form of boulders (< 2 m high), discontinuities and scarps (< 1 m

high). This is also exemplified by the high standard deviation for S_p at this site (4.7°). The topography across the platform is highly variable, with large sections effectively horizontal and others exhibiting steep scarps, fissures and irregularities up to 2 m vertical difference (red platform values in Figure 3.6C). The roughness values shown in Table 3.2 are not comparable to other studies due to differences in DEM resolution (Poate *et al.*, 2016) or methodology (Swirad *et al.*, 2016) and can only be used as a relative measure between sites in this study.

Cliff toe elevation (E_{toe}) varies considerably between sites, with Site 3 1.6 m above Site 5, the lowest elevation site (Figure 3.8). As the cliff toe lies below the MHWN level, Sites 4 and 5 are inundated during both spring and neap high tides. As a consequence, they undergo semidiurnal inundation. Conversely, Sites 2 and 3 are only inundated when water levels exceed neap high tide level, meaning during neap tides the cliff toe is dry. The horizontal shelf behind the cliff toe at Site 2 (Figure 3.7) only becomes inundated during highest spring tides. These values give only an indication of tidal inundation levels and do not factor in atmospheric pressure, wave setup and wind effects, which often lead to higher mean water levels (Norman, 2012). Measured cliff toe water levels are discussed in Chapter 5.

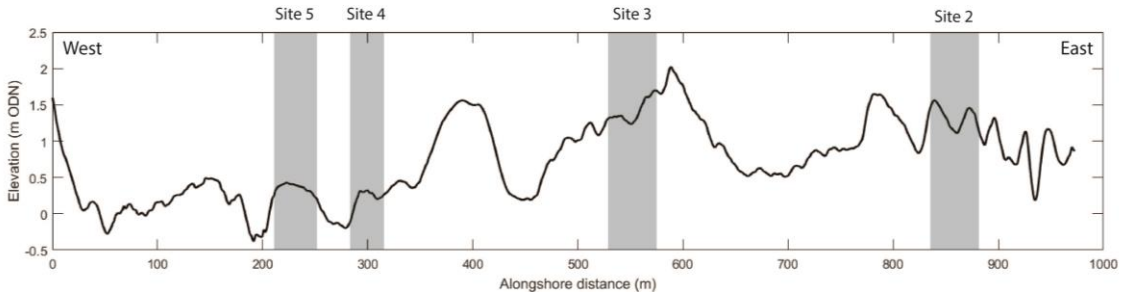

Figure 3.8: Variation in cliff toe elevation (E_{toe}) alongshore, with the locations of Sites 2-5 in grey. A reference map can be found in Figure 3.1A.

Cliff aspect (θ) also varies between sites (Table 3.2), with the largest difference between two sites approximately 85°. Cliff faces are northwest to northeast facing, varying between 320° (Site 4) and 45° (Site 3).

Sites 3-5 exhibit concave notching located above the HAT (Figure 3.5). Site 2 is also overhanging above 20 m ODN, probably related to competent sandstone layers located above this elevation. Site 2 features a prominent nose and shelf, sloping gently seawards (Figure 3.7), whereas Site 4 is sub-vertical with a short, seaward protrusion at the MHWN level.

4. Erosion characteristics of the lower cliff

4.1. Introduction

It is evident from prior investigations at rock coast cliffs that both environmental and material controls of erosion exist (Young *et al.*, 2009; Lim *et al.*, 2011). In turn, the key drivers of cliff recession may become apparent from the pattern of erosion observed in the cliff face. Rockfall behaviour across the cliff face is known to be stochastic in nature (Lee, 2008; Barkwith *et al.*, 2014). However, the marine-influenced zone at the base of the cliff is subject to continuous, repetitive marine processes, including wet-dry cycles, abrasion and wave quarrying (Robinson, 1977b). Erosion via these mechanisms occurs continuously and on a small spatial scale (Castedo *et al.*, 2017). The focus then should be on establishing whether differences in the pattern of erosion occur between areas which are influenced directly by marine action, and those which are not (Vann Jones *et al.*, 2015). It is still unclear as to what extent marine forcing influences overall cliff recession (Lim, 2014; Moses, 2014). To further understand the nature of marine-driven erosion, including both wave- and tide-driven mechanisms, high-resolution cliff face erosion data is required.

Cliff erosion has previously been measured using simple recession rates from mapping (Agar, 1960), micro-erosion meters for point measurements (Stephenson and Finlayson, 2009), and more recently photogrammetry (Lim *et al.*, 2005) and terrestrial laser scanning (TLS) (Rosser *et al.*, 2005; Abellán *et al.*, 2014; Letortu, Costa, Maquaire, *et al.*, 2015). TLS has been used extensively in the study area (Vann Jones *et al.*, 2015) and provides digital elevation models (DEMs) of cliff surfaces at a spatial resolution defined by the user. TLS can therefore capture erosion with sufficient detail to distinguish the magnitude, frequency and distribution of eroded material over an adequate temporal and spatial scale (Letortu *et al.*, 2015). Previous studies of cliff erosion have focused on the entire cliff face at a relatively low resolution ($> 10^{-2}$ m^2) in order to monitor over a large spatial scale: 10^5 m^2 of cliff area (Rosser *et al.*, 2005; Dewez *et al.*, 2013; Johnstone *et al.*, 2016).

My study focused exclusively on the erosion occurring at the lower cliff. Frequent, small-scale material loss has been observed by fieldworkers at this site but is largely outside the TLS resolution of previous studies (Norman, 2012). Therefore, an increased monitoring resolution (within the order of 10^{-6} m^3) was necessary to capture this small-scale erosion.

Over the 369-day study period between August 2016 and August 2017, I scanned the cliff with a TLS using the techniques outlined in Rosser *et al.* (2005), totalling up to ten surveys per site. Acquired point clouds were processed into a 2.5D surface and matched to successive scans to calculate volumetric change.

In this chapter I first describe the method by which TLS data were acquired and processed (Section 4.2). Next, the results are presented, focusing on the cliff geology, recession rates, detachments magnitude frequency patterns, and spatial and temporal variations in erosion characteristics. A brief analysis of the results is included, incorporating comparisons with other studies (Section 4.3). Finally, I discuss the possible implications of my findings, comparing my results with other studies and resolving the potential erosion mechanisms at work and the controls thereof (Section 4.4).

In my study, the inundation zone refers to the cliff face below the upper limit of the water level elevation. The lower cliff refers to the monitored section extending up to 10 m above the cliff toe, chosen as it encompasses the inundation and wave-influenced zone (Norman *et al.*, 2013).

4.2. Recording cliff change

4.2.1. TLS data collection

I used a Riegl VZ-1000 TLS for all the scans in this study (Table 4.1). This scanner calculates distance to a surface by measuring the time-of-flight of a reflected laser pulse. This is achieved by the use of a vertically-spinning mirror which directs the laser pulse in contiguous points up the surface, after which the scanner rotates horizontally to collect the next vertical swath.

Table 4.1: Specifications of the Reigl VZ-1000 laser scanner used in the surveys

Parameter	**Value**
Point collection speed	122,000 meas./sec at <450 m range
Beam divergence	0.3 mrad
Accuracy	8 mm
Precision	5 mm
Laser wavelength and type	Near infrared, class 1
Max. range	1400 m

Following the survey techniques of Rosser *et al.* (2013), the scanner was set up at each site on a tripod above a temporary survey point, approximately 7-10 m from the cliff toe and 1 m above the platform surface. The scanner was levelled manually and aligned facing seawards. Each high-resolution scan collected points from approximately 50 m of cliff width (Figure 4.1). In order to improve resolution to capture smaller events, the TLS was positioned closer to the cliff toe than other similar studies (e.g. Vann Jones *et al.* 2015) in an attempt to reduce beam spot sizes and ranging inaccuracies, and minimise instrumental errors (Telling *et al.*, 2017). Abellán *et al.* (2014) suggests locating the scanner less than half the distance from the scanned surface range specified by the manufacturer, a recommendation which my study followed. The aim was to capture at least a 30 x 10 m cliff section whilst minimising beam incidence angle. Vertical and horizontal point spacing were also kept to the smallest possible at this range (2×10^{-3} m).

Ground control points were not established for these surveys due to the impracticality of installing these on the vertical cliff faces, following Norman (2012). Instead, registration of successive point clouds relied upon an iterative closest-point alignment (ICP) based upon the scan geometry that relied upon minimal change between scan intervals, described in Section 4.2.2. The full scan area was approximately $3x10^3$ m^2 per site, although the area of interest in the processing stage was much smaller. The target vertical and horizontal point spacing used during collection was 2×10^{-3} m.

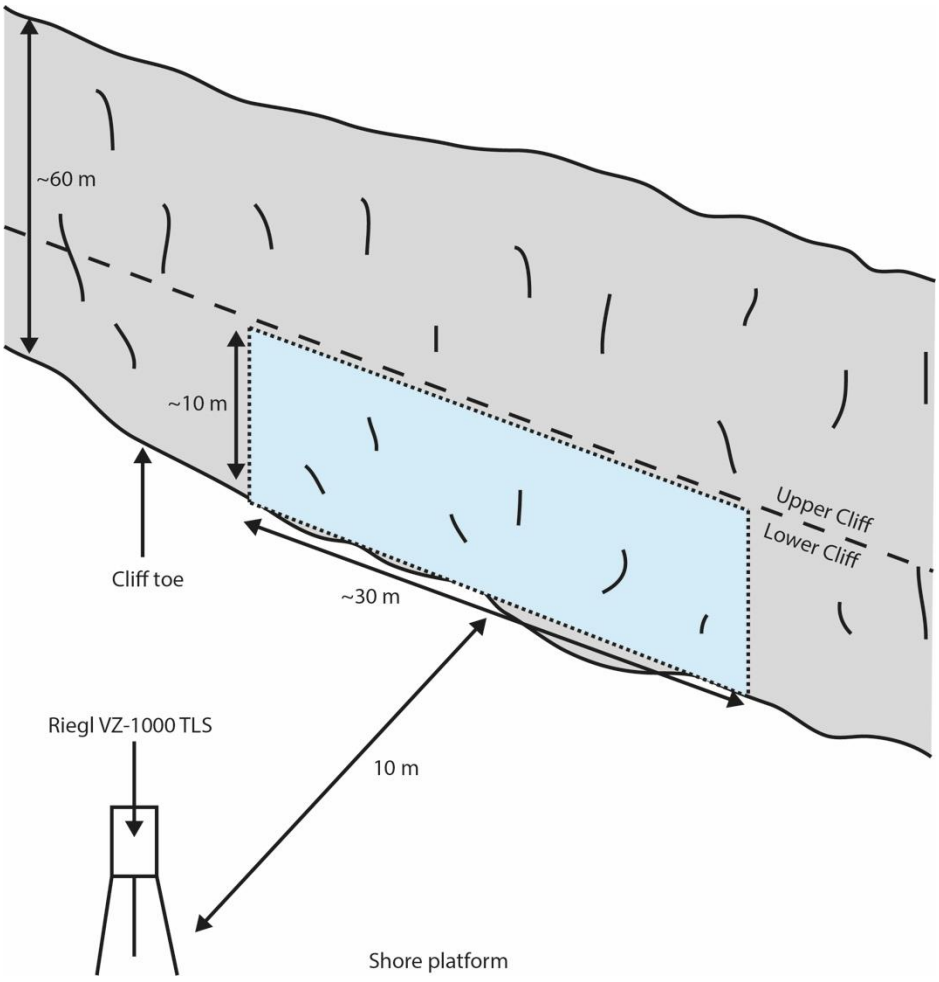

Figure 4.1: Field setup of the TLS surveys each site. The blue box delimits the area of interest for the scan. The dotted line represents the boundary below which the lower cliff is defined. The elevation of the top of the inundation zone is dependent on cliff toe elevation and hence lies up to ~4 m above the cliff toe.

Lithology and structure were identified using field observations and the TLS scan data. Joint sets were manually identified in CloudCompare and their dip

and dip direction were measured in relation to the plane normal to the cliff face. These were then plotted in Stereonet 9 *(*Cardozo and Allmendinger, 2013). I calculated mean joint spacing (*r*) along simple scanline surveys in RiScan. Here, a transect was drawn along the cliff face and the number of joints along the line was counted manually to derive a *r* value for each site and lithology.

4.2.2. Point cloud processing

Each scan consisted of a cloud containing up to 10^7 data points, with a mean point spacing of $2x10^{-3}$ m. A DEM of Difference (DoD) method was used to calculate cliff change over each scan interval, following (Rosser *et al.*, 2005). A simplified data processing workflow to produce erosion statistics from the raw data is shown in Figure 4.2. The processing steps and data quality and uncertainty are explained in detail in following sections.

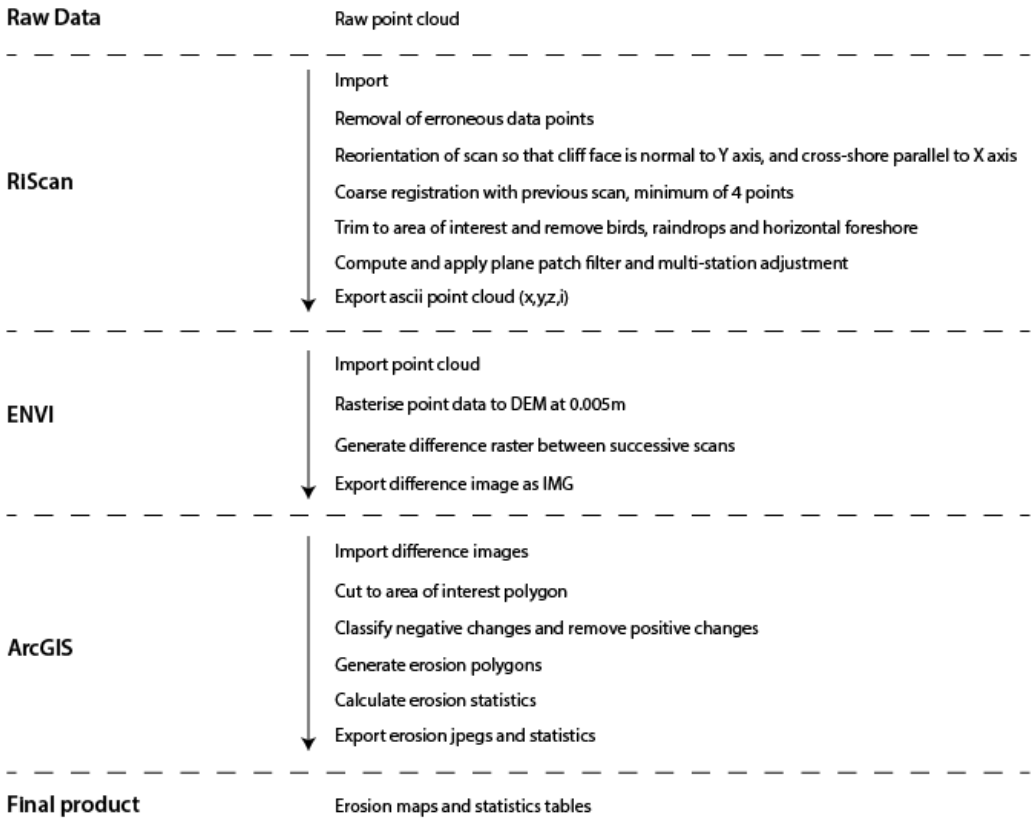

Figure 4.2: Workflow of TLS data processing steps. The left column contains the software packages used; the right column outlines the processing sequence within each software package.

4.2.2.1. Point cloud matching and quality control

The raw point cloud data were imported into RiScan. Some sections of each scan, such as the distal points and upper section of the cliff (>20 m above the cliff toe) were deleted at the outset to improve processing times in the following stages by reducing the point cloud size. The first scan at each site was reoriented in a local coordinate system whereby the cliff face was normal to the Y-axis, cross-shore parallel to the X-axis and vertically parallel to the Z-axis. This allowed the subsequent data to be projected with the cliff face itself parallel to the plane [x, y], creating a DEM where the cell values were depth normal to the cliff.

Each successive scan was then manually registered to the previous scan using a minimum of four common reference points on each scan. This minimum was used to constrain all degrees of freedom in a 3D rototranslation, enabling a fit error to be derived. The relatively small surface change between scans over the total scan area meant large areas of the cliff remained unchanged between scans, allowing reference points to be easily located. Once the scans were approximately aligned, points were removed from outside the area of interest and erroneous points, such as birds in flight, raindrops and the shore platform, were further trimmed (Figure 4.3A).

I undertook the final alignment of point clouds using RiScan's multi-station adjustment (MSA) tool. To initiate the scan matching, a plane patch filter was used to identify planar surfaces within known constraints. For comparison with previous studies, the parameters are outlined in Table 4.2. The location and normal of the resultant surfaces were matched using a multi-station adjustment (MSA) algorithm. This is a considerably more precise means of aligning scans compared to using the entire point cloud, and is less prone to error resulting from the influence of variable point-cloud density and small-scale noise in the data (Haas *et al.*, 2012).

During MSA, scans were iteratively matched to a maximum root mean square error separation (RMSE) of $< 5 \times 10^{-3}$ m (

Table 4.3). The proximity of the scanner to the cliff and the high point-cloud density from these scans meant that this a considerable improvement on the ~10^{-2} m achieved in other recent studies at this site (Rosser *et al.*, 2013), and hence is an appropriate resolution to investigate smaller-scale change. After visual confirmation of matching, each scan was exported as a set of coordinates with a precision of 1 x10^{-3} m to an ASCII file.

Table 4.2: RiScan plane patch filter parameters for comparison with other studies

Parameter	**Value**
Maximum plane error (m)	0.01
Minimum points per plane	10
Minimum search cube size (m)	0.016
Maximum search cube size (m)	2.048

Table 4.3: RiScan multi-station adjustment MSA) parameters for comparison with other studies

Parameter	**Value**
Start radius: first iteration (m)	1
Start radius: last iteration (m)	0.2
Maximum tilt angle: first iteration (°)	10
Maximum tilt angle: last iteration (°)	2
Minimum change of error 1 (m)	0.25
Minimum change of error 2 (m)	0.25
Outlier threshold	1
Final standard deviation error (m)	< 0.005

A number of sources of error were introduced during the data collection and processing of TLS point cloud data. During data collection, the return strength of the laser is affected by a number of surface factors including wetness, colour and mineral constituents of the target cliff face, alongside weather and

atmospheric conditions (Abellán *et al.*, 2014). Surface morphology is also important, particularly where uneven, rough surfaces scatter signal reflections and protruding features obstruct the cliff face behind (occlusion) (Schürch *et al.*, 2011). As such, uncertainty was approached statistically and is outlined in Section 4.2.2.3.

Changes in deposits at the cliff toe (e.g. boulders and cliff talus) between successive scans proved problematic. False erosion events were produced when mobile material was present at the cliff toe in one scan but was removed before the next. To combat this, I clipped out the lower sections of some scan areas, which produced non-rectangular cliff maps. I also clipped scan edges, as surfaces which were angled such that the laser beam has a high incidence angle also produced unreliable and inconsistent returns and hence point positions.

4.2.2.2. Raster and DoD generation

Rasters of each point cloud were generated in the geospatial imagery processing software ENVI v5.3. The imported ASCII point clouds were converted to a triangular irregular network using Delaunay triangulation, then linearly resampled onto a raster at 5 $x10^{-3}$ m resolution (Wheaton *et al.*, 2010). Here, the cliff face was re-projected on to the plane [x, y] (Figure 4.3B). This resolution was chosen such that the mean point density across the sites is higher than one point per cell. Rasters were stacked and resampled to ensure that the grid and cell extracts were coincident.

To calculate change through time, I subtracted each raster image from the previous scan, to create a DoD. In addition, the total change over the survey period from the first and final scan was calculated using the same approach. It is possible that some cumulative error may have accrued during matching with successive scans, but using the same unchanged matching features for each scan minimised this error source. Uncertainty in volumetric changes can arise from the interpolation methods used when gridding the data. J. G. Williams *et al.*, (2017) reported error as a function of detachment area and perimeter length, where higher perimeter to area ratios increase uncertainty. However, a sufficiently conservative estimate of the minimum change detection depth

(Section 4.2.2.3) provides sufficient precision to observe the volumetric changes at this scale alongside robust management of the data uncertainty. The RMSE separation between the matched scan surfaces for each time-step was below the grid resolution (5 x 10^{-3} m) and therefore fulfilled this requirement (Lim *et al.*, 2010).

Slope and hill-shade images were obtained from the DEM using a topographic modelling function (Lim *et al.*, 2011). These were used to generate cliff images over which to drape the erosion data to enhance context when viewing. These rasters were exported in ERDAS Imagine *.img format.

4.2.2.3. DoD detachment statistics

In ArcGIS, I imported the DoDs and clipped them to the final area of interest (AOI). This extended up to 10 m above the cliff toe and as wide as the data quality at the scan edges would allow, usually 25 – 35 m of cross-shore distance at the cliff toe. Changes were classified as either positive or negative, with the former representing surface apparent accretion seaward. These were removed as they were confirmed visually to be attributable to bird nests, localised cliff talus accretion and boulder movement between the scanner location and the cliff toe.

In order to address the uncertainty and determine the precision threshold above which change in cliff morphology could be detected, I identified a segment of cliff which was unaltered throughout the survey period. The DoD from each scan interval (Figure 4.4A) was then plotted as overlain kernel density functions to identify the error between each scan. The combined function (Figure 4.4B) for successive scans from all intervals forms a logistic distribution with a modal value of ~0 m. These errors were stable and persistent over time, implying systematic range uncertainty from the scanner (Figure 4.4C). Following Abellán *et al.* (2009), twice the standard deviation of error equals 0.006 m, thus quantifying scanner accuracy. Negative change was masked below 2 x10^{-2} m, so can be considered a conservative estimate of the minimum threshold. This approach was undertaken to maximise the precision of pairwise change detection between successive scans, particularly where global registration precision was less important (Schürch *et al.*, 2011). With a raster grid resolution

of 5 x10^{-3} m and a minimum event depth of 2 x10^{-2} m the smallest detectable detachment volume was 5 x 10^{-7} m^3 (0.5 cm^3).

Individual rock detachments were delimited by polygons and the volume of material removed in each was calculated (Figure 4.3C). Low point densities, zones of the raster where point density was lower than the grid resolution, occurred predominantly where occlusion produced poor matching between successive scans. These areas were masked using an 80° threshold topographic filter. Such areas constituted a small (< 1%) percentage of the AOI.

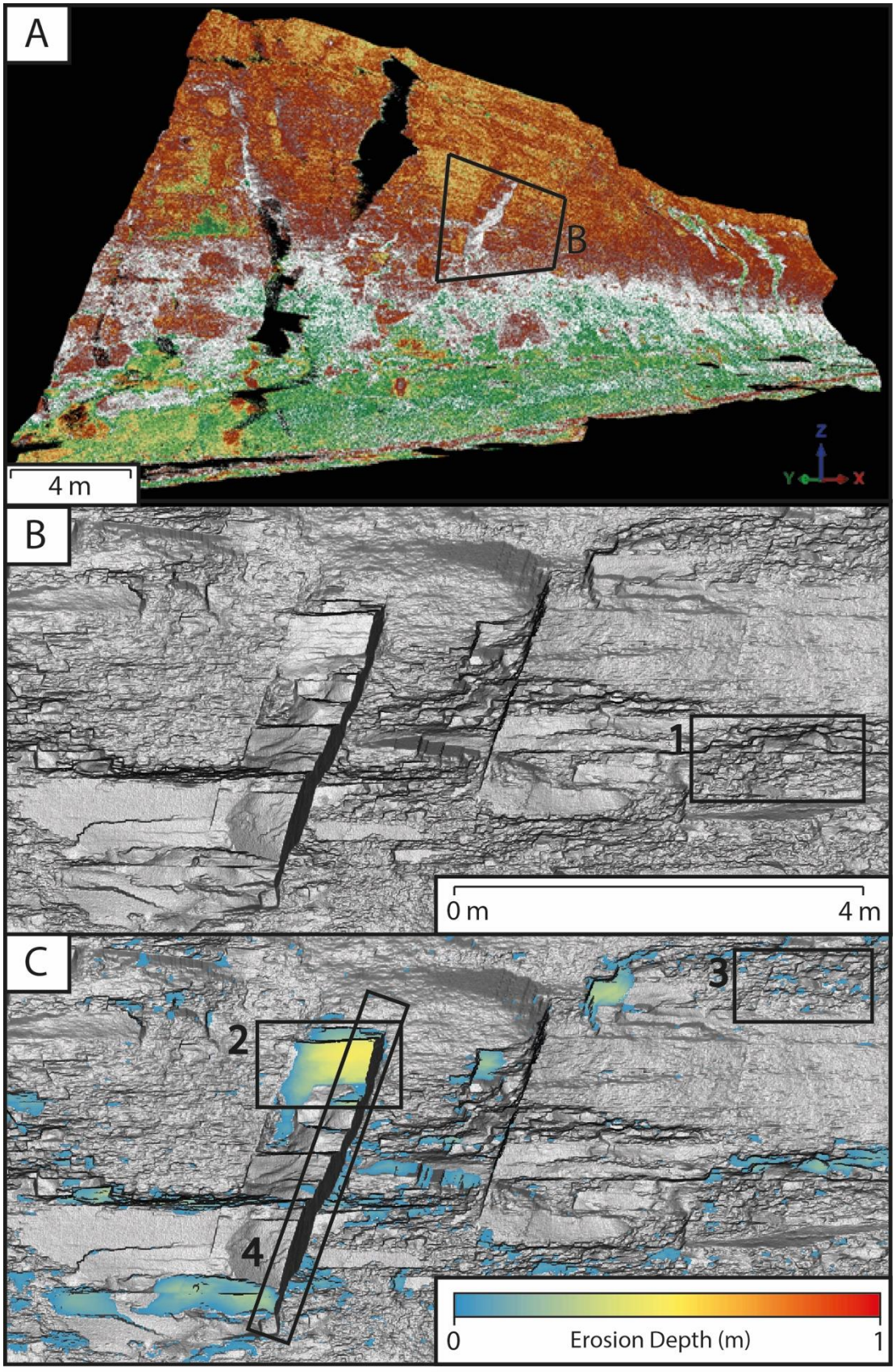
A
B
4 m
Z
Y
X
B
1
0 m
4 m
C
2
3
4
0
Erosion Depth (m)
1

Figure 4.3 (previous page): Point cloud processing stages. A) Raw point cloud of the lower cliff at Site 5 coloured by reflectivity (green = low, red = high). Black areas are occluded zones where point density is low. B) Detail of rasterised xyz coordinates from the point cloud in ENVI gridded at 0.005 m resolution, shown as topography with shaded relief. The fissile, flaky shale texture and some joint surfaces are evident (1). C) Detail of difference raster for the full annual surface change coloured by erosion depth draped over surface topography from the final scan. Two classifications of detachment can be seen: the larger central event represents a discrete block removal (2); smaller, shallower and more frequent events show shale fragmentation (3). A low point density, high-angle slope removed in the slope filter can also be seen (4).

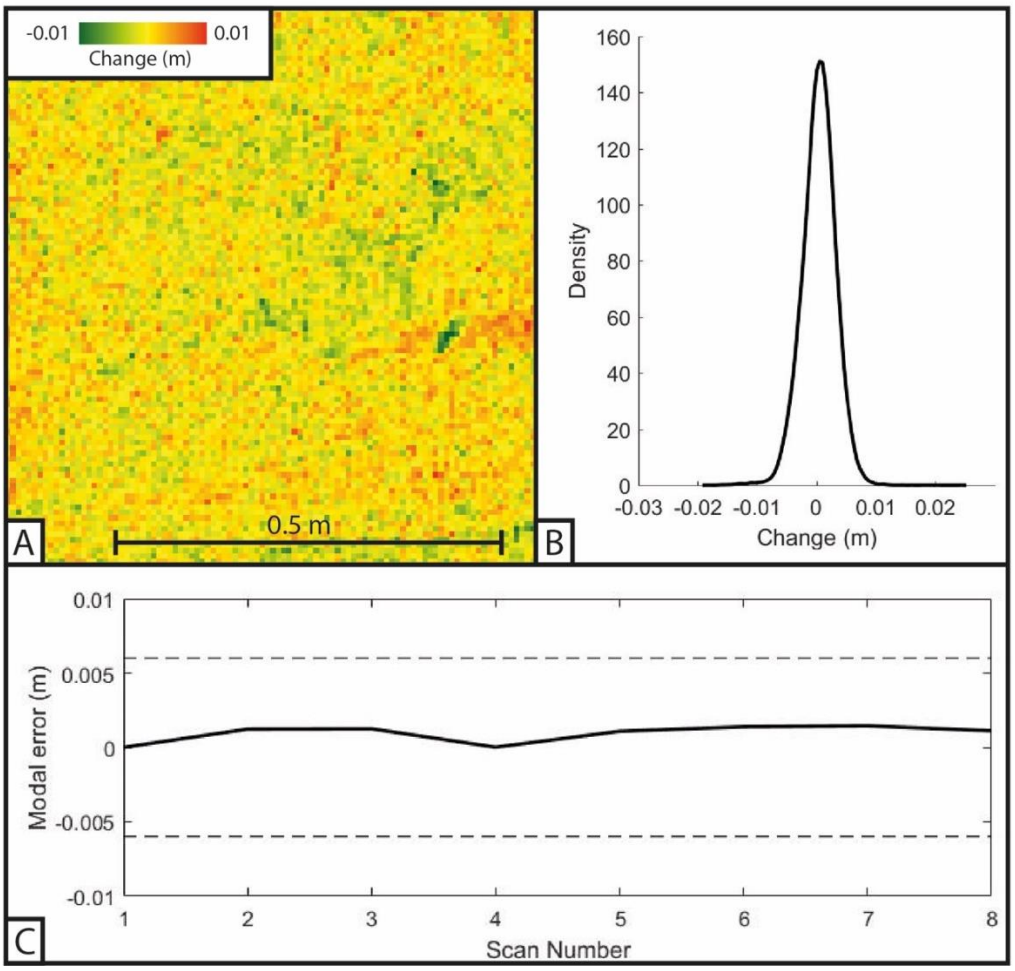

Figure 4.4: A) Sample of an unchanged cliff section of the Site 2 DoD between March 2016 and April 2016. B) Combined kernel density function of the pixel error between sequential scans in the unchanged cliff section shown in A. C) Time series of modal error across all scans at Site 2 (solid line) alongside twice the standard deviation error of 0.006 m (dotted lines).

To calculate the vertical distribution of erosion at the lower cliff, the scan area of each site was partitioned into vertical bins of 0.1 m relative to ODN. The centroid of each detachment was taken and binned according to its elevation. Rock detachment volume (D_v) and frequency (D_q) were calculated for all erosion events within each elevation bin. Since each site scan area does not have a constant width, all values were normalised for scan width for each elevation bin.

4.3. Results and analysis: Erosion of the lower cliff

4.3.1. Lower cliff lithology and structure

There were two lithologies present in the scanned sections of the lower cliff. Sites 2 and 3 were comprised of shale with a ~1 m band of siltstone running approximately 5 m above the toe. The beds are near-horizontal and dip 2° to the southeast. Due to the northerly aspect of the cliff faces, apparent dip in each scan face was to the left. Sites 4 and 5 consisted exclusively of shale. The shale was relatively friable and finely-laminated, can be broken into cm-scale platelets (Figure 4.5) and had a UCS of 16.69 MPa (Rosser *et al.*, 2013). The siltstone was more competent and homogenous, had no discernible sedimentary structure and was considerably more resistant (UCS = 30.20 MPa).

Figure 4.5: Detail from the shale at Site 5. Note the cm-scale platelets defined by horizontal laminations which break along seemingly randomly-oriented failure planes.

Joint sets within both lithologies are shown in Figure 4.6. Two major orthogonal joint sets were identified, with further non-systematic jointing common in the shale. These main joint sets were easier to observe in the siltstone than in the shale, as the latter was more prone to breaking along seemingly randomly-oriented failure planes within the bedding. Many joints in the siltstone were not confined to this layer and could be seen cross-cutting both lithologies. Joint spacing (τ) in the shale bedding was 0.7 m, 0.75 m, 1.2 m and 1.1 m for Sites 2, 3, 4, and 5 respectively. In the siltstone, τ values were 1.1 m and 2.9 m for Sites 2 and 3 respectively. As these were calculated along a simple scanline survey they should be taken as indicative values only. At Sites 2-4 the orthogonal joint sets were oriented obliquely to the cliff-normal, although some were cliff-parallel

(Figure 4.6). At Site 5 only the cliff-normal joint sets were apparent, which may reflect the friable nature of the shale lithology when joints were cliff-parallel.

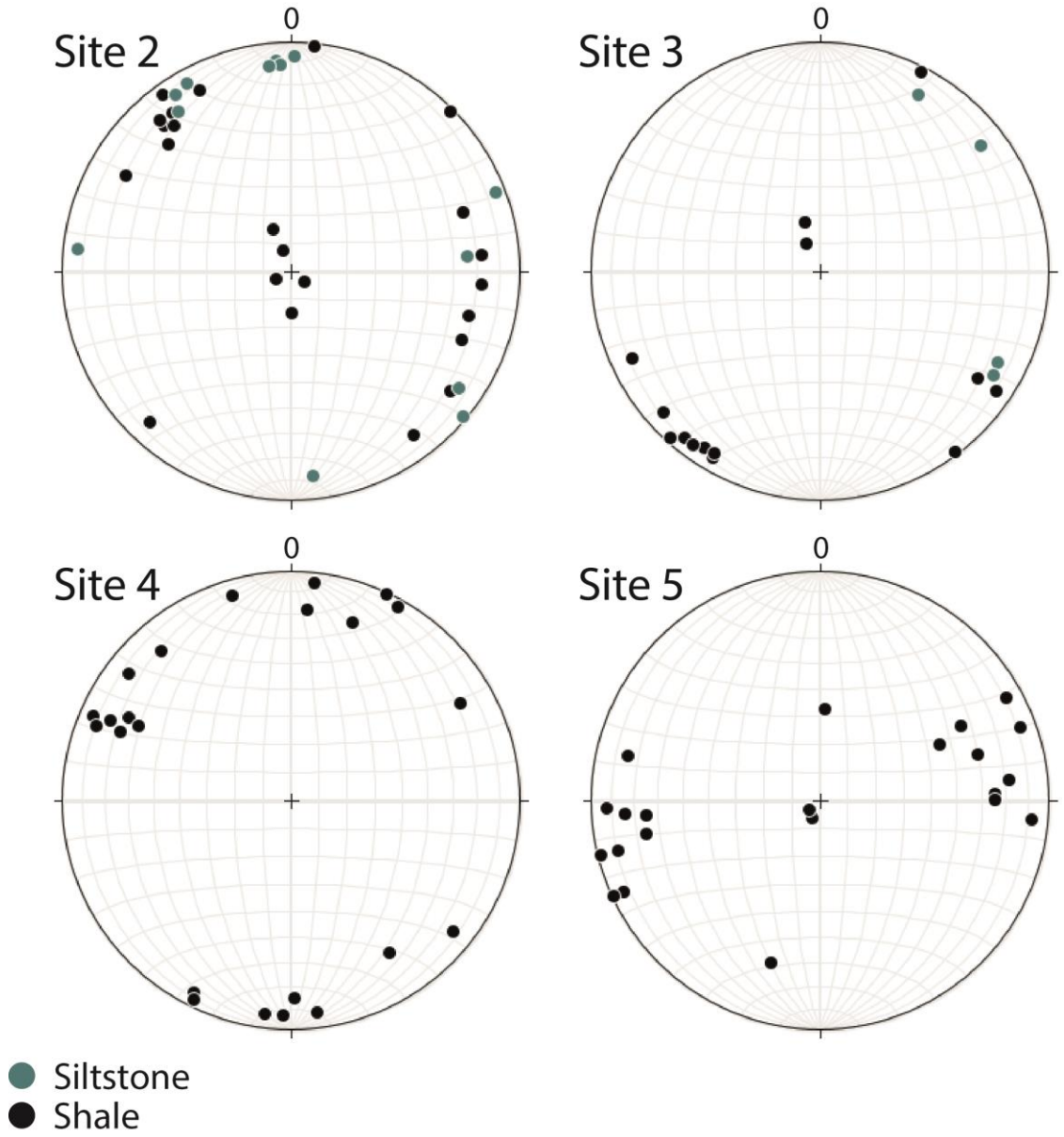

Figure 4.6: Joint orientations for Sites 2-5 relative to the cliff face plotted on lower hemisphere stereonets, where the top of the great circle (at 0) corresponds with the cliff normal. Site 2 exhibited mainly oblique jointing with some variation for both rock types, the near horizontal data are most likely bedding planes. Oblique joints and bedding planes were also seen in Site 3 in both rock types but with less variation. There was considerable spread in the orientations at Site 4 with some oblique and perpendicular jointing. Site 5 exhibited mainly perpendicular joint sets. There appeared to be 2 main orthogonal joint sets which cross-cut bedding planes, with the appearance of non-systematic joints throughout.

4.3.2. Patterns in lower cliff erosion

Table 4.4 summarises the cliff erosion seen during the study. Over the 369-day period 301,615 individual observable detachments were recorded at the lower cliff over the four sites. This equates to a total volume material loss of 134 m^3, with an average of 230 detachments per year per m^2. The mean, median and standard deviation detachment volumes (D_v) were 1.80 $x10^{-3}$ m^3, 4.56 $x10^{-6}$ m^3 and 1.27 $x10^{-1}$ m^3 respectively. Figure 4.7 displays the total erosion over the survey period for each site. The largest detachment scar across the survey area was 23 m^3 and occurred in the shale at the cliff toe at Site 3.

Table 4.4: Annual erosion statistics for Sites 2-5.

	Site 2	**Site 3**	**Site 4**	**Site 5**	
Scan area (m^2)	255.46	464.02	246.11	348.36	*Total: 1,313*
Total detachment volume (D_v) (m^3)	41.803	77.791	5.857	8.297	*Total: 133.748*
Total detachment frequency (D_q)	70,545	117,922	71,279	41,869	*Total: 301,615*
Erosion rate (χ) (m y^{-1})	0.177	0.168	0.024	0.024	*Mean: 0.095*

Erosion characteristics varied between lithologies (Table 4.5). Site 2 showed some preference for larger block detachments along the siltstone, matching approximately the joint spacing (τ) of between 1 – 3 m in this layer. Smaller, shallower events occurred in the shales both above and below the siltstone, where small platelets 10^{-6} m^3 were seen to detach from the rock mass. Very little erosion (0.13% of total volume) occurred along the siltstone at Site 3, with most concentrated in the lower 6 m of shales. Sites 4 and 5 contain no clear lithological variation with elevation, and as such have no clearly discernible lithology-related detachment pattern (Figure 4.7).

Table 4.5: Annual erosion statistics for the shale and siltstone lithologies.

	Site 2		**Site 3**	
	Shale	**Siltstone**	**Shale**	**Siltstone**
Erosion rate (χ) (m y^{-1})	0.173	0.204	0.188	0.002
Power exponent (β)	0.56	0.43	0.55	0.61
Mean detachment volume (m^3)	1.91 $x10^{-3}$	7.06 $x10^{-3}$	4.10 $x10^{-3}$	8.18 $x10^{-5}$
Median detachment volume (m^3)	4.51 $x10^{-6}$	5.56 $x10^{-6}$	4.16 $x10^{-6}$	3.16 $x10^{-6}$

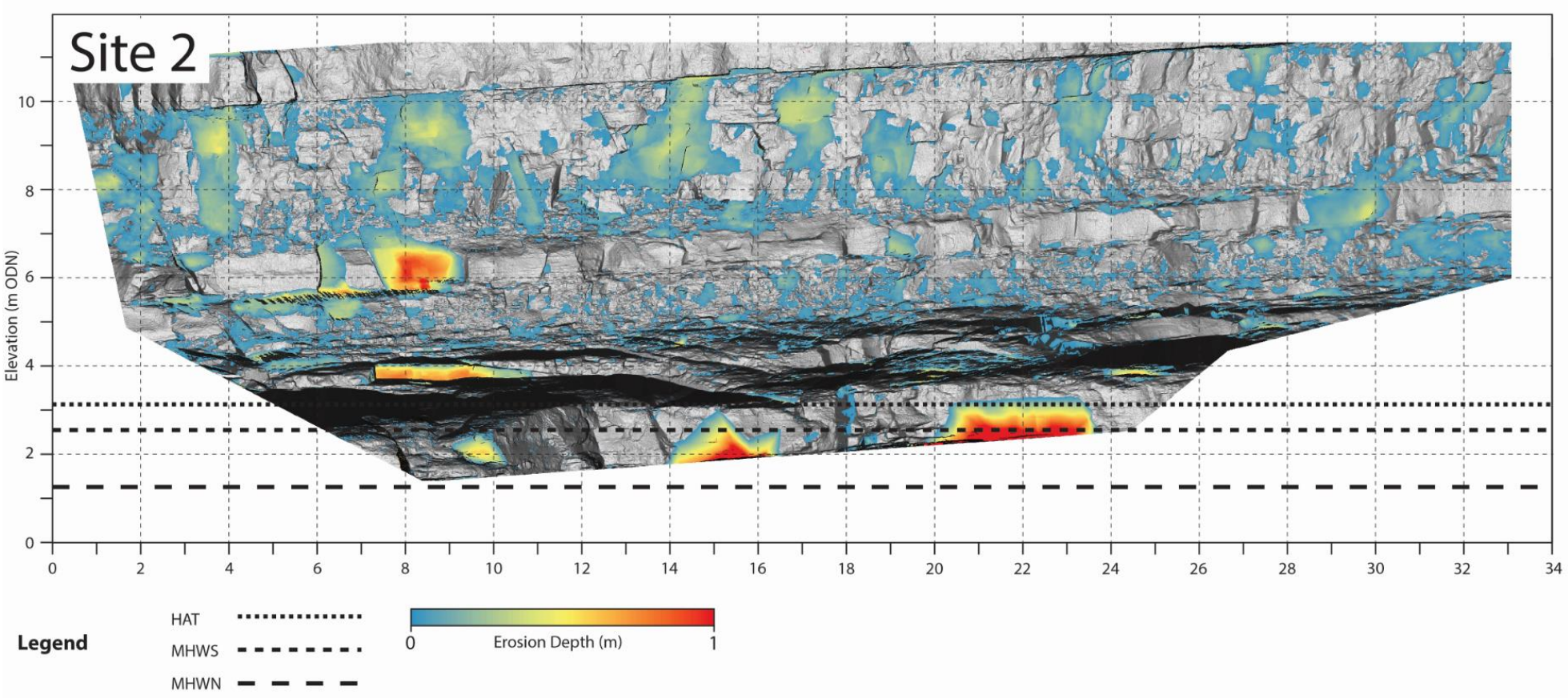
Site 2
Elevation (m ODN)
0
2
4
6
8
10
0
2
4
6
8
10
12
14
16
18
20
22
24
26
28
30
32
34
Legend
HAT
MHWS
MHWN
0
Erosion Depth (m)
1

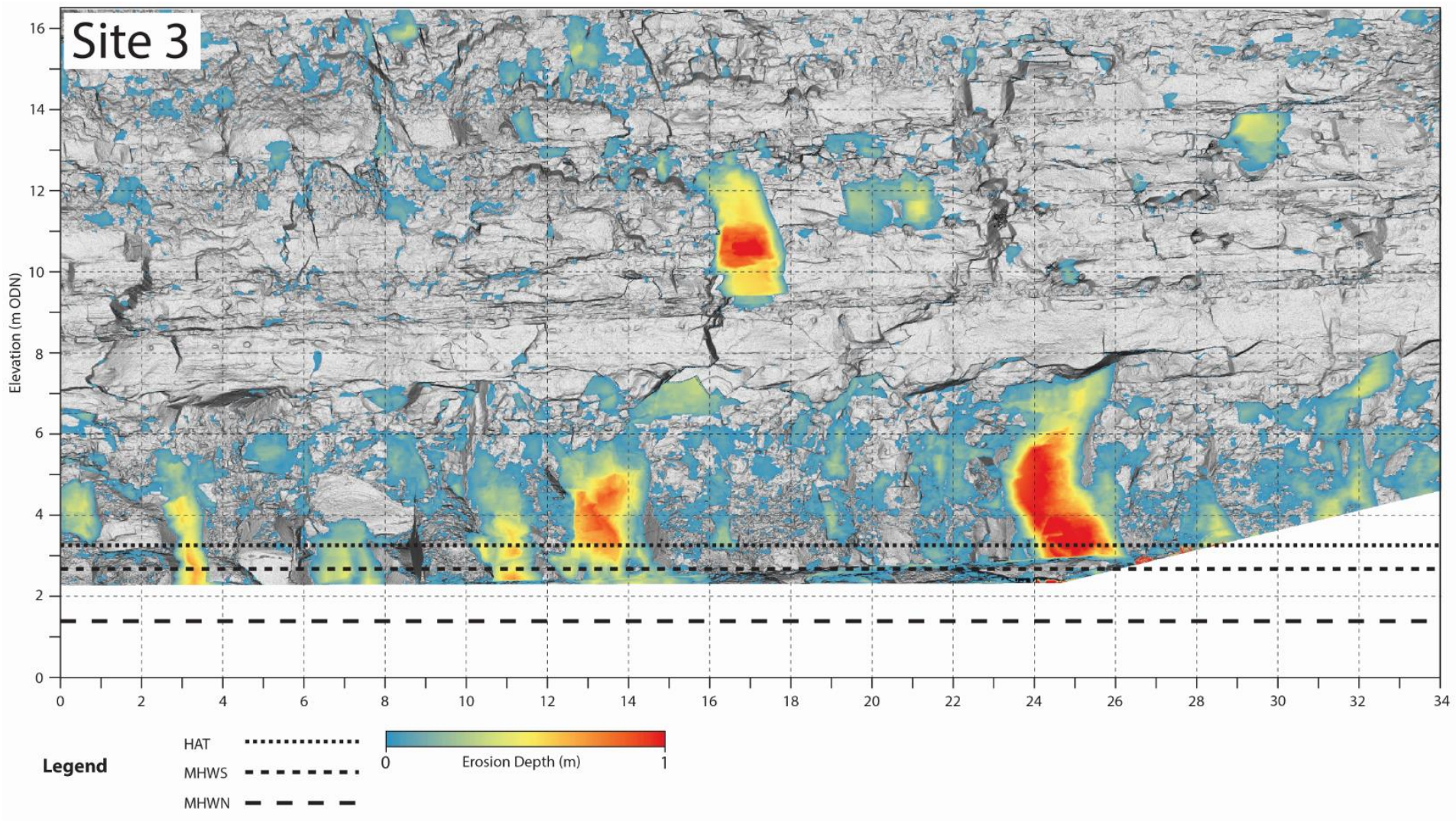
Site 3
Elevation (m ODN)
0
2
4
6
8
10
12
14
16
0
2
4
6
8
10
12
14
16
18
20
22
24
26
28
30
32
34
Legend
HAT
MHWS
MHWN
0
Erosion Depth (m)
1

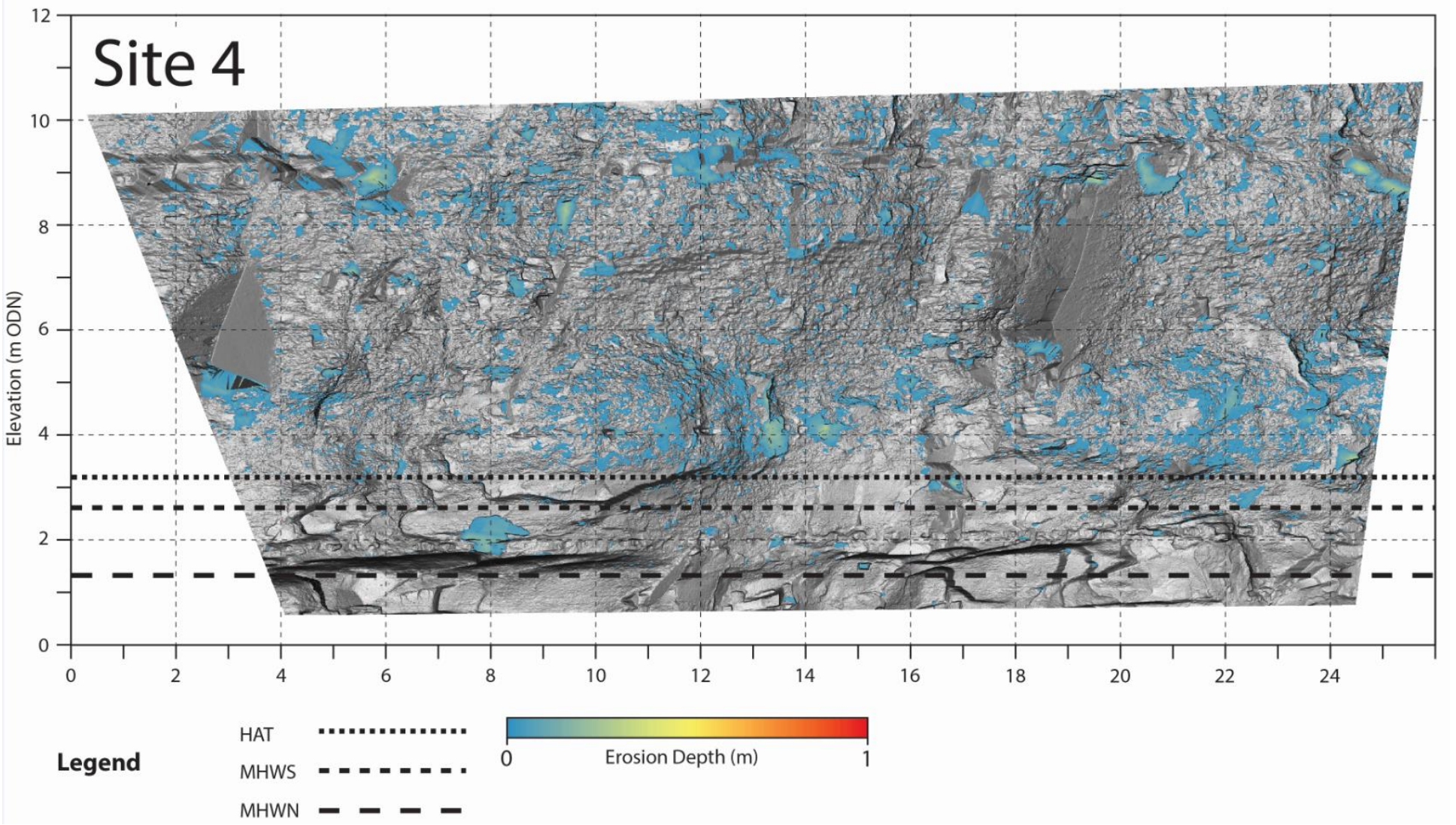
Site 4
Elevation (m ODN)
12
10
8
6
4
2
0
0
2
4
6
8
10
12
14
16
18
20
22
24
Legend
HAT
MHWS
MHWN
0
Erosion Depth (m)
1

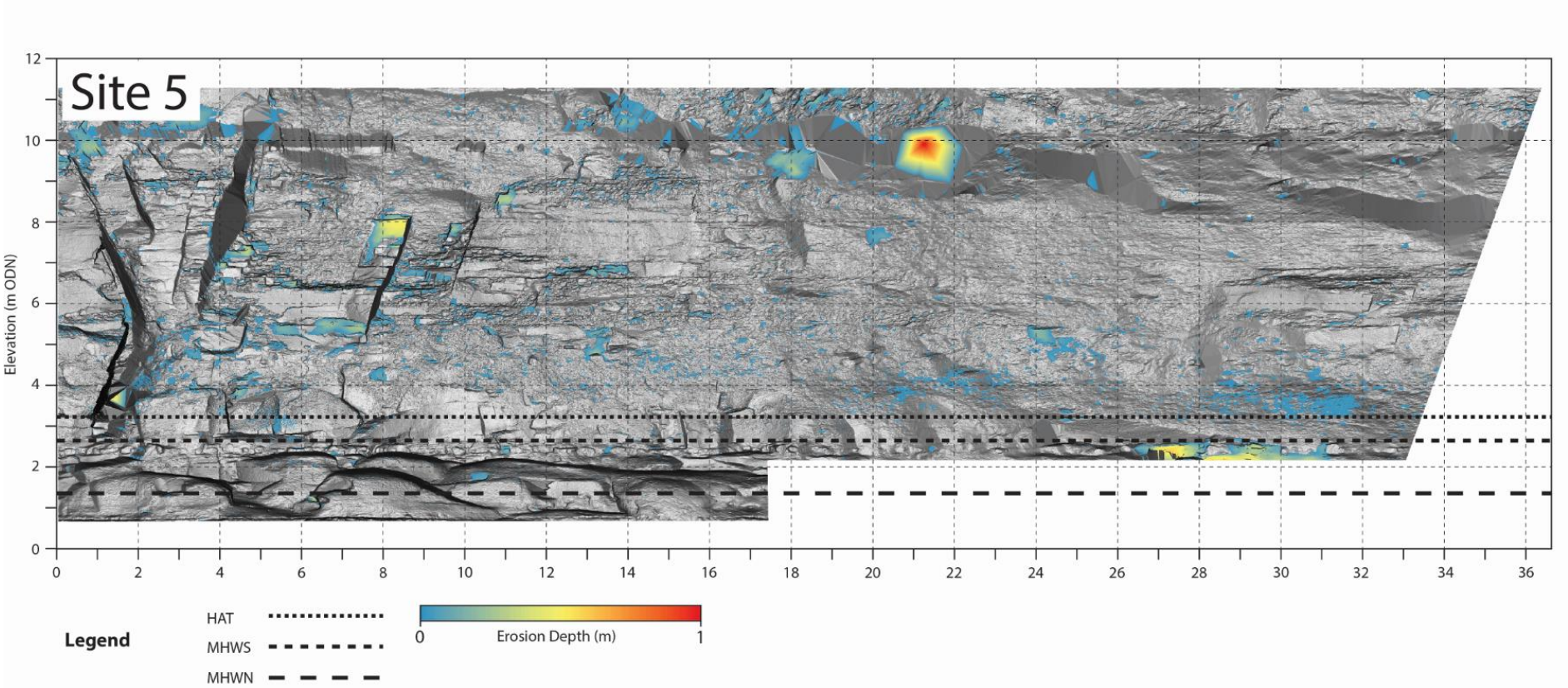

Figure 4.7: Annual cliff change between August 2016 and August 2017 for Sites 2-5, with erosion depth scale between 0 and 1 m. Horizontal black lines show the upper extent of the astronomical tides at each site.

4.3.3. Magnitude-frequency of detachment scars

To explore how the relative volume distribution of detachment scars changes with elevation, I fitted the volume magnitude-frequency distribution with a power law (Clauset *et al.*, 2009). Following Malamud *et al.* (2004), the inverse power law was of the form:

$$f(D_v) = \alpha \cdot {D_v}^{-\beta} \quad (4\text{-}1)$$

Where $f(D_v)$ is the detachment volume frequency density and α and β are constants, which were obtained from a power law fit on the non-cumulative magnitude frequency distribution function of the detachment volumes. Figure 4.8 shows the annual magnitude frequency relationship of cliff detachments across the four monitored sites. Lithological variations are shown in Table 4.5. The exponent (β) describes the relative contributions of larger and smaller detachments to overall change, where higher values indicate an increased contribution from smaller detachment volumes.

For these data, the overall power law fit across all sites was $\beta = 0.52$, significant at $p < 0.001$ with $r^2 = 0.98$. This is similar to that found by Dewez *et al.* (2013) ($\beta = 0.53$). Smaller detachment scars (< 0.1 m^3) were more frequent than larger ones (> 0.1 m^3), which constituted just 0.1% of the detachment frequency, but accumulated 88.5% of the total eroded volume (refer to cumulative density function in Figure 4.8). Due to the sampling frequency, it is unknown whether these larger scars represent a single block removal or a series of smaller, incremental detachments that occurred between surveys. Sequential scans over multiple months did show this clustering occurring in places around larger events (Section 4.3.5).

Some larger detachment scars followed structural discontinuities, joints and fractures (de Vilder *et al.*, 2017). The decrease in frequency density for the smallest events, known as 'rollover' (Malamud *et al.*, 2004), may be due to the limit of resolution at this scale, temporal clustering of erosion combining into larger scars, or a lithological control of the shale microstructure whereby fragmentation occurs most frequently at volumes larger than 10^{-6} m^3.

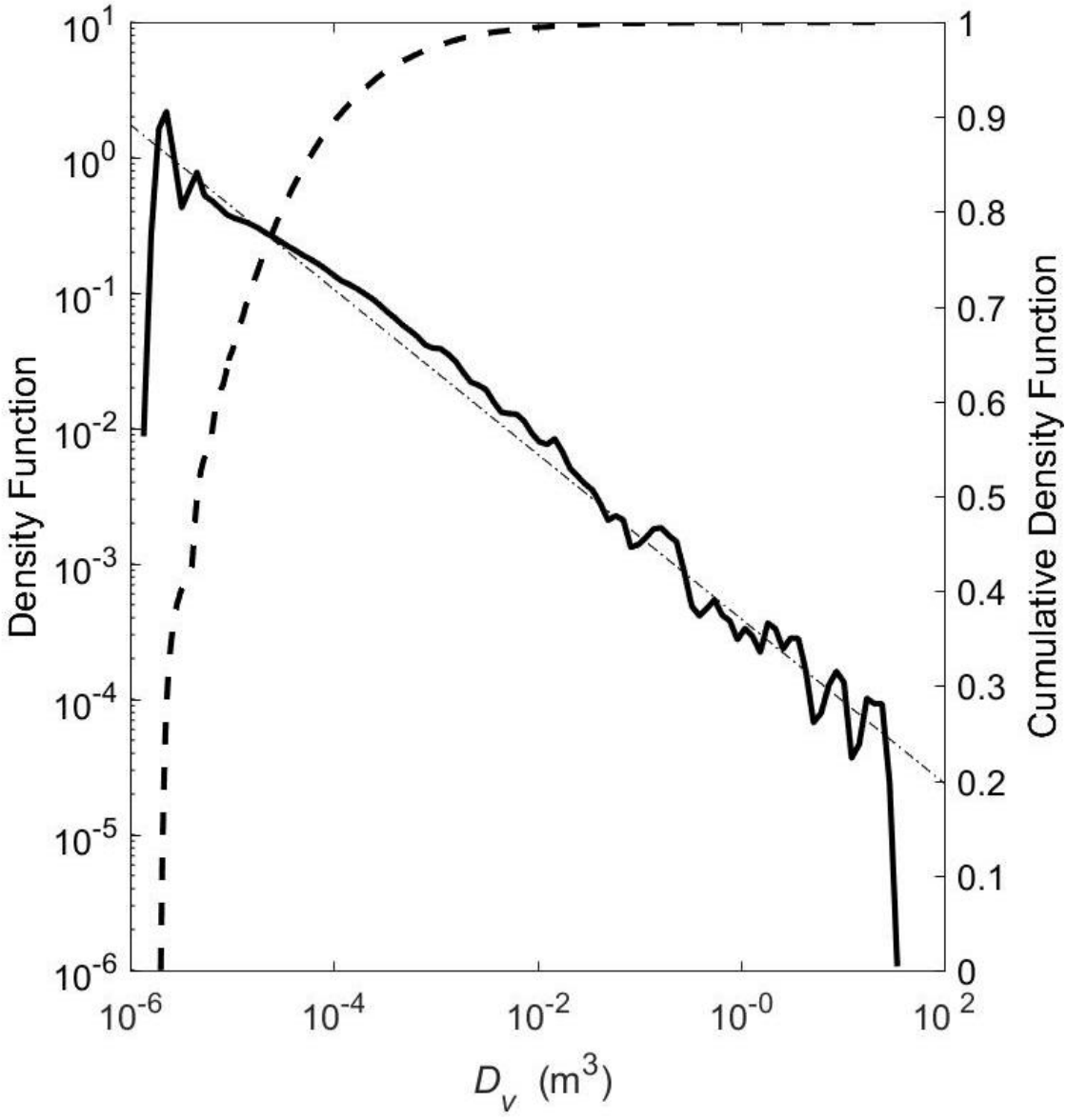

Figure 4.8: Kernel density estimate for the total annual detachment volumes across sites 2-5 (solid line). Inverse power law fit for the detachment volume frequency density where β = 0.52 (dot-dash line). Cumulative density function for the total annual detachment volumes (dashed line).

4.3.4. Vertical distribution of erosion

The vertical distribution of erosion calculated from the cliff maps in Figure 4.7, alongside cliff face profiles, is displayed in Figure 4.9.

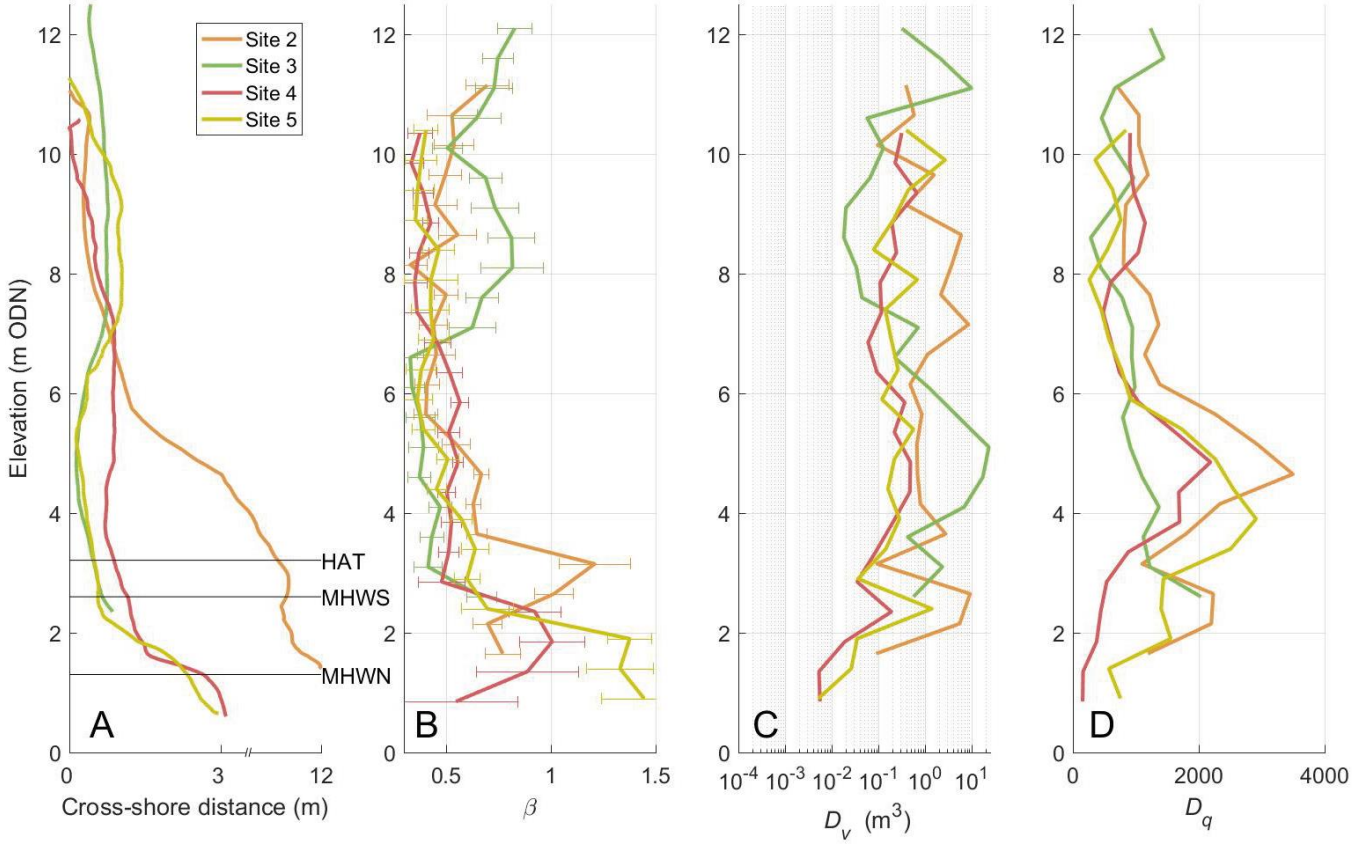

Figure 4.9: Vertical distribution of detachment statistics at the lower cliff, plotted from 0.5 m bins up the cliff face relative to ODN for Sites 2-5, normalised by bin width. A) Cliff profiles with relative astronomical tide heights, note the non-linear x-scale. B) Power law exponent (β) with 95% confidence bounds. C) Erosion volume (D_v). D) Rock detachment frequency (D_q).

Here, the mean bin value with elevation represents a combined value across each site relative to ODN. As such, the values are independent of local variations in lithology and structure. The exponent (*β)* value for each site varied with elevation above the cliff toe (Figure 4.9B). Sites 2, 4 and 5 exhibited a marked increase in *β* proximal to the intertidal zone above the 95% confidence interval; the elevation of the cliff toe at Site 3 was too high to observe this. At Site 2 this was around the HAT, whereas at Site 4 and 5 this occurred between MHWS and MHWN. This suggests that around the intertidal zone smaller detachment scars made up a higher proportion of the overall volume lost as compared to the zone above. Site 3 did not follow this pattern, and exhibited an inverse trend to the other sites, reflecting the lithological changes seen in Table 4.5. This is shown in more detail in Figure 4.10.

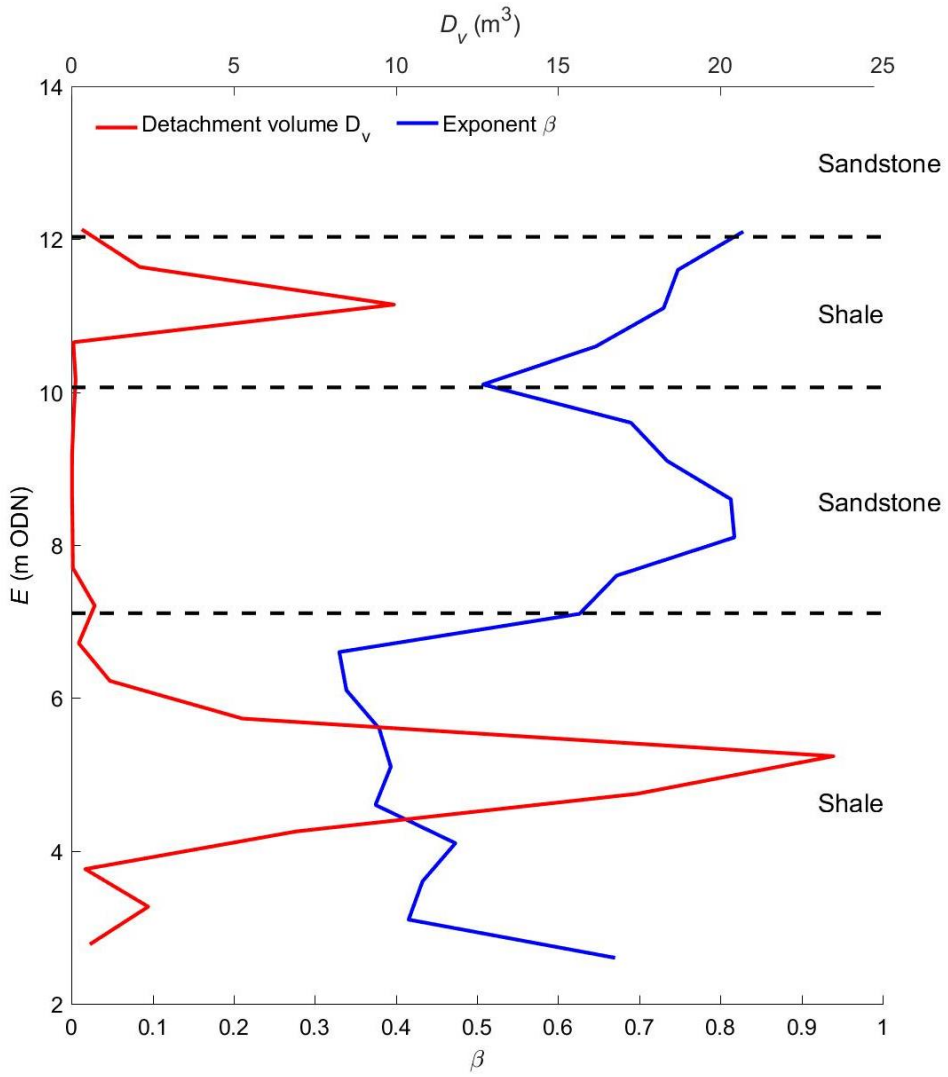

Figure 4.10: Changes in exponent (β) and detachment volume (D_v) with elevation (E) at Site 3. Lithological boundaries are shown in blacked dotted lines. Note the boundaries are larger than the actual bed, caused by bed dip.

Figure 4.9C shows the variation in detachment volume (D_v) with elevation (E). At Site 2, D_v was stable with elevation, whereas Sites 4 and 5 showed a relatively consistent up-cliff increase. Site 3 displayed a marked increase in a 2 m zone above HAT. Detachment frequency (D_q) values show a clear increase in the 2 m zone above the HAT at Sites 2, 4 and 5 (Figure 4.9D). Although D_q was considerably larger in this zone than above 8 m ODN, it was not associated with a noticeable increase in D_v, suggesting the events were not significant contributors to cliff change. Site 3 exhibits no distinct increase in the D_q in the 2 m zone above the HAT, yet the D_v increased considerably. This supports the

notion that larger detachments dominate cliff change at this site. D_V decreases considerably in the sandstone units at Site 3, corresponding with the increase in β (Figure 4.10).

Figure 4.8 shows a marked difference in the frequency of larger and smaller detachments. Figure 4.11 shows the overall erosion profile for Sites 2-5 after removing the influence of these larger events. The resulting trend shows a clear increase in D_V 1-3 m above the HAT. This is continuous across sites independent of elevation (*E*). This suggests that at this scale and over this monitoring period, smaller detachments in and above the inundation zone were temporally continuous, whereas larger events were more intermittent. Monitoring at monthly intervals may capture certain events and omit others, which contribute to the long-term volume loss. The contribution of these smaller detachments to overall volume loss may also be underestimated here, as the relatively long (monthly) scanning interval used tends to overemphasise the influence of larger detachments in the overall inventory (J. G. Williams *et al.*, 2017).

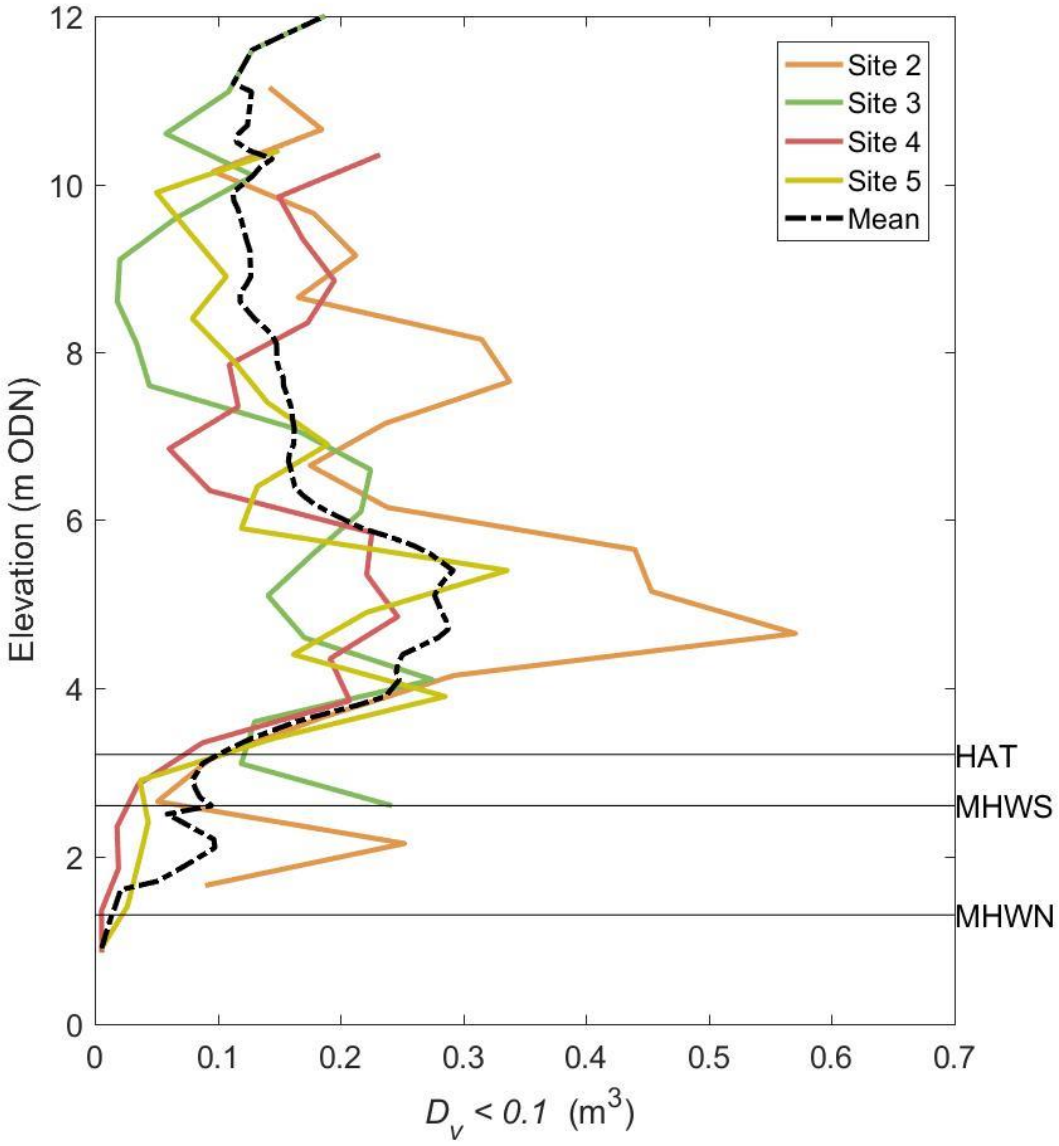

Figure 4.11: Total annual volume loss over Sites 2-5 for detachment volumes (D_v) < 0.1 m^3 in 0.1 m bins, normalised by scan area. Although Site 2 exhibits a much larger peak around 5 m ODN than the other sites, it contributes just 0.05 m^3 to the mean value at that elevation.

4.3.5. Temporal distribution of erosion

Sequential monitoring over the survey period allowed the temporal variation and distribution of erosion to be investigated at an approximately monthly interval. This is shown in Figure 4.12. Spatial event clustering through time was particularly prevalent in the lower section of Site 3. All sites exhibited some

degree of evolution in larger failure scars, where detachment scars expanded laterally over time creating contiguous areas of failure across the cliff. Clustering was more apparent in larger detachment scars.

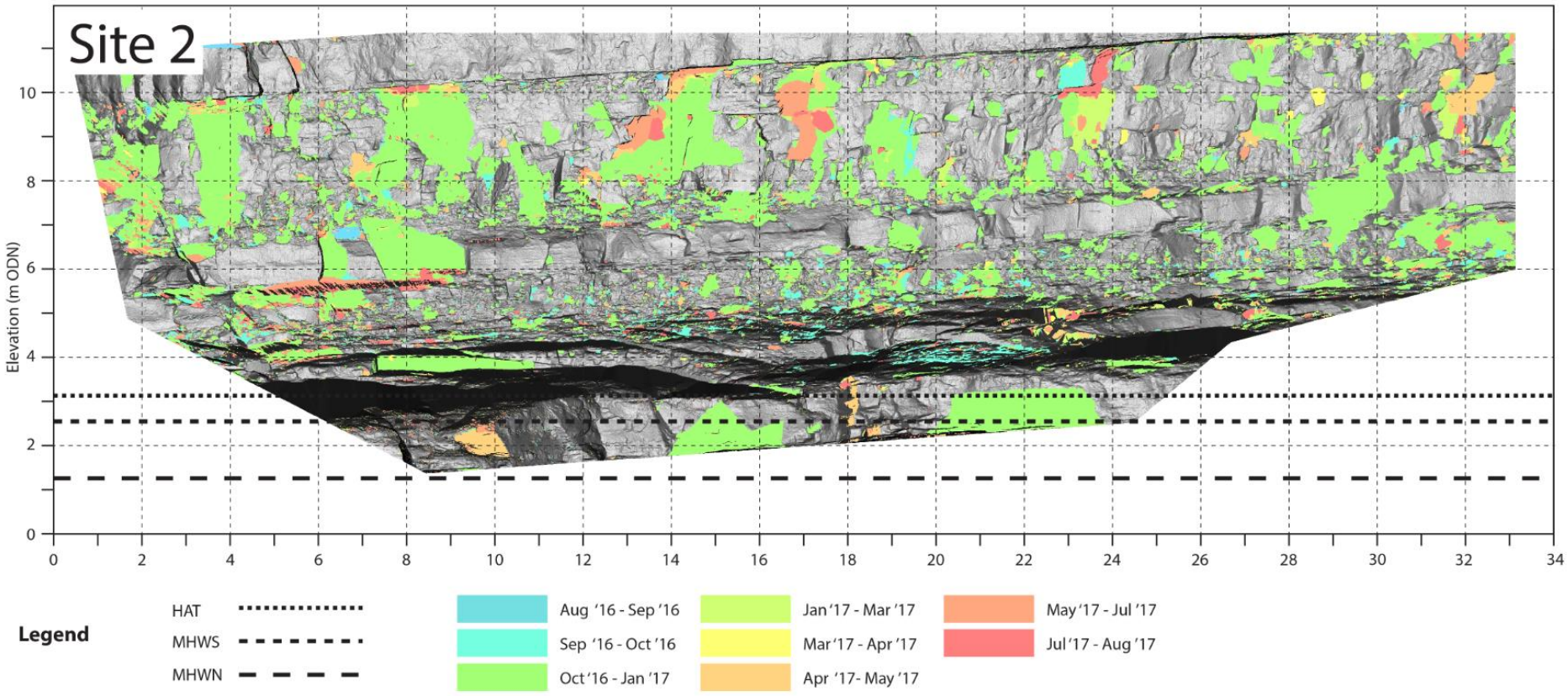
Site 2
Elevation (m ODN)
0
2
4
6
8
10
0
2
4
6
8
10
12
14
16
18
20
22
24
26
28
30
32
34
Legend
HAT
MHWS
MHWN
Aug '16 - Sep '16
Sep '16 - Oct '16
Oct '16 - Jan '17
Jan '17 - Mar '17
Mar '17 - Apr '17
Apr '17- May '17
May '17 - Jul '17
Jul '17 - Aug '17

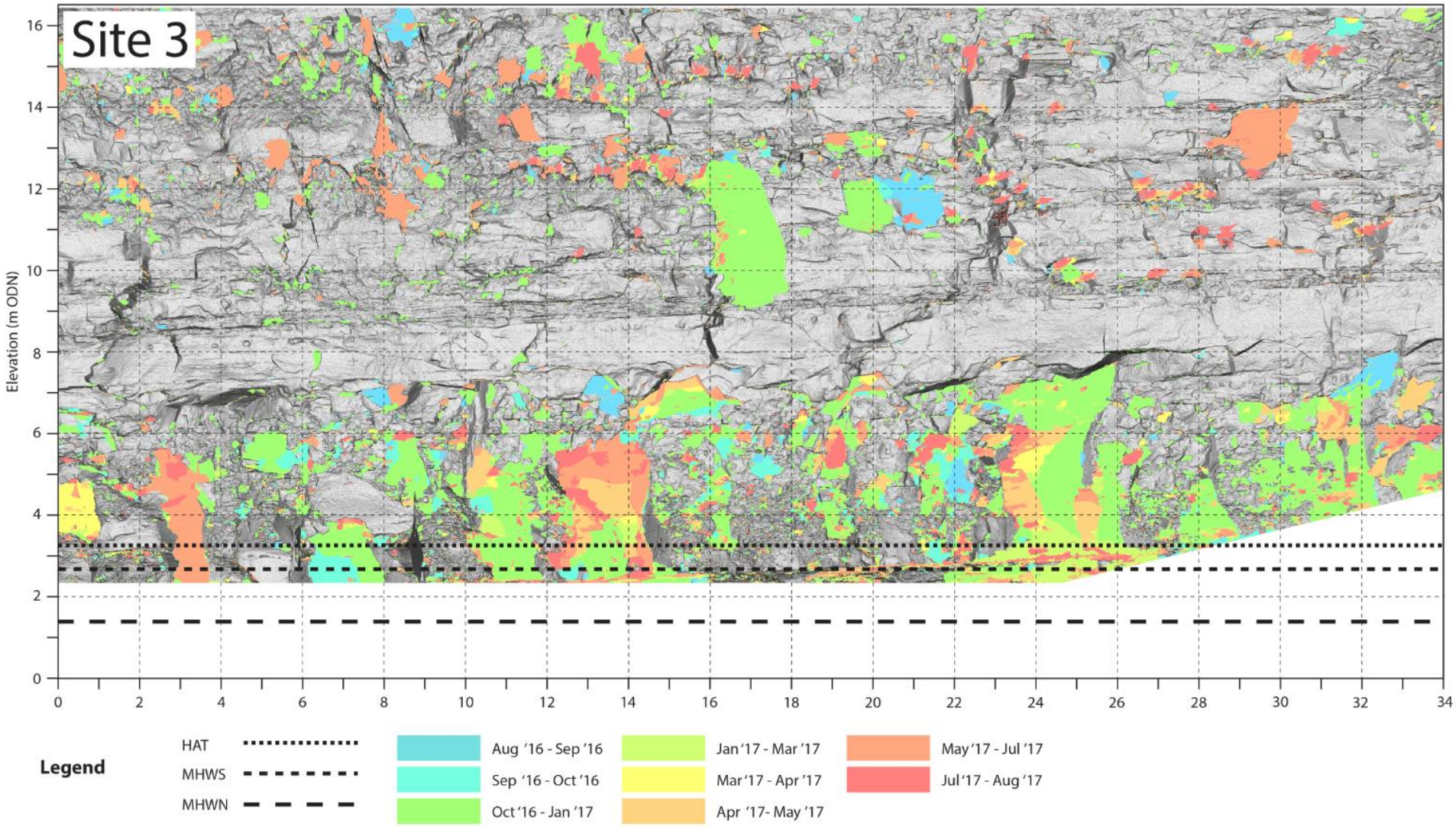
Site 3
Elevation (m ODN)
0
2
4
6
8
10
12
14
16
0
2
4
6
8
10
12
14
16
18
20
22
24
26
28
30
32
34
Legend
HAT
MHWS
MHWN
Aug '16 - Sep '16
Sep '16 - Oct '16
Oct '16 - Jan '17
Jan '17 - Mar '17
Mar '17 - Apr '17
Apr '17- May '17
May '17 - Jul '17
Jul '17 - Aug '17

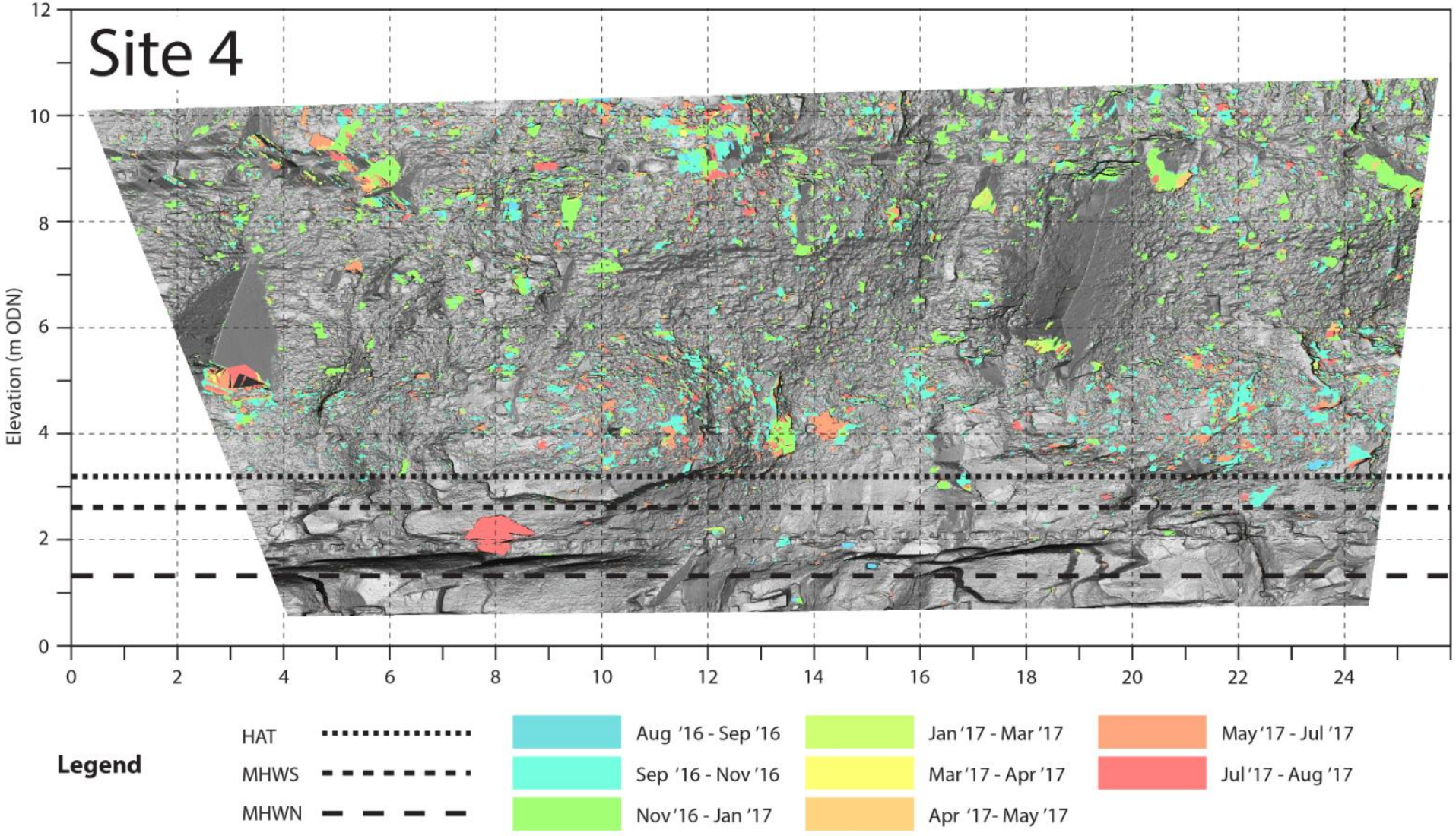
Site 4
Elevation (m ODN)
12
10
8
6
4
2
0
0
2
4
6
8
10
12
14
16
18
20
22
24
Legend
HAT
MHWS
MHWN
Aug '16 - Sep '16
Sep '16 - Nov '16
Nov '16 - Jan '17
Jan '17 - Mar '17
Mar '17 - Apr '17
Apr '17- May '17
May '17 - Jul '17
Jul '17 - Aug '17

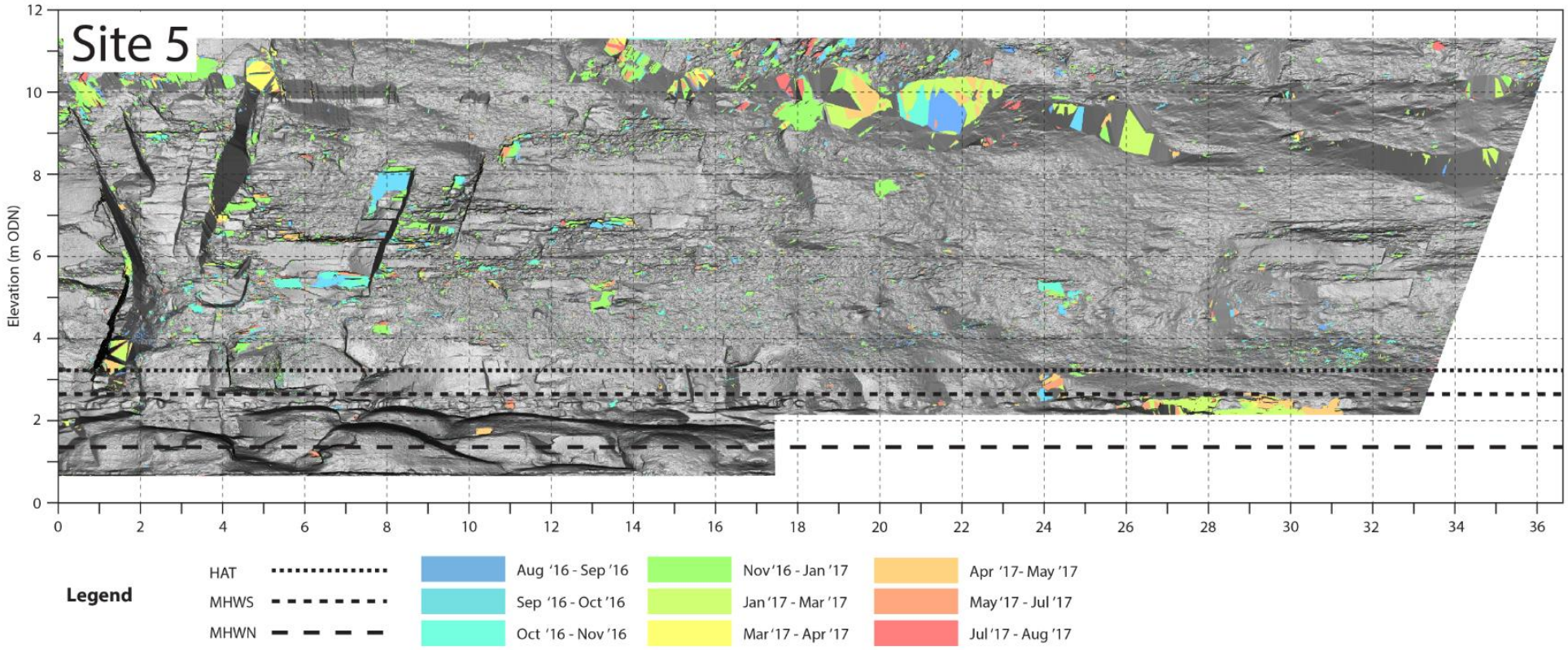

Figure 4.12: Annual cliff change between August 2016 and August 2017 for Sites 2-5, coloured by survey interval. Note occasional differences in survey interval between sites Horizontal black lines show the vertical extent of the astronomical tides at each site

Detachment statistics also showed seasonal variations. Since monitoring intervals were not regularly spaced, it was necessary to resample the data to a daily erosion rate. This was achieved by dividing the erosion volume between each scan by the number of days over which is occurred.. In addition to variations in overall volume loss between sites (Section 4.3.3), monthly detachment volumes (D_v) exhibited considerable variation over the year (Figure 4.13). For Sites 2-4, maximum daily D_v occurred during the winter months, where erosion rate during the December to March period was consistently higher than the mean daily D_v (0.06, 0.17 and 0.01 m^3 d^{-1} for Sites 2-4 respectively) over the year, peaking in January.

Although the total volume losses were of a similar order of magnitude at Sites 2 (41.8 m^3) and 3 (77.8 m^3), the difference between the highest and lowest daily D_v as a percentage of total study period loss was considerably larger for Site 2 (96.7 %) than for Site 3 (73.6 %). This suggests Site 2 experienced a much greater contribution of total erosion in the winter period than Site 3. This disparity was slightly smaller at Site 4 (90.4 %). This notion is supported by daily D_v during December to March compared with the annual D_v, which is greatest for Site 2 (63.5 %) than for Sites 3 (50.2 %) and 4 (48.9 %). Values for D_v were also consistently an order of magnitude lower for Site 4. Additionally, D_v for Site 4 had a secondary peak in August, with a magnitude of 0.0186 m^3 d^{-1} compared with 0.0309 m^3 d^{-1} for the primary January peak. This was not mirrored in the previous September, which follows the pattern of Sites 2 and 3. This partially explains the lower percentage loss for the winter months.

Site 5 did not follow the annual patterns seen in the other three sites. Here, the peak daily D_v occurred in September (0.1 m^3 d^{-1}). This contrasts considerably with the previous August (0.00482 m^3 d^{-1}), which was also the minimum value over the year. There was also a minor secondary peak in March (0.0380 m^3 d^{-1}).

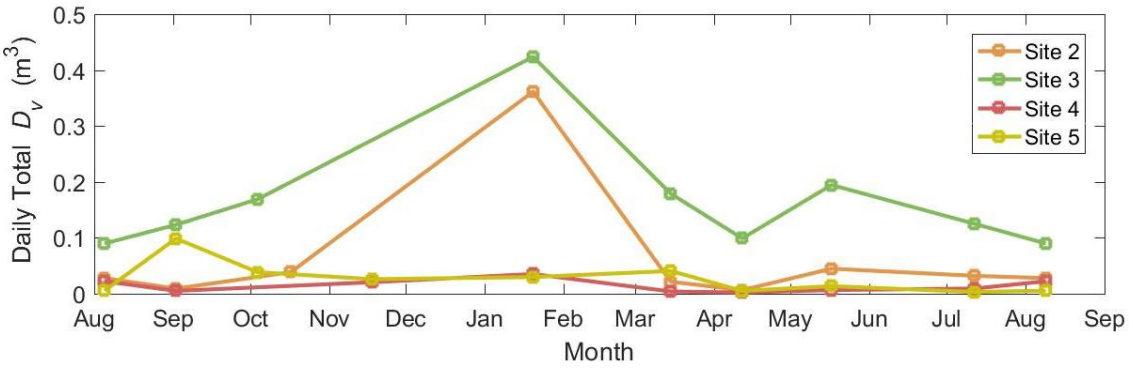

Figure 4.13: Detachment volume (D_v) per day removed from the lower cliff at Sites 2-5. Values at each data point represent the volume removed from the cliff for the previous scanning interval. Note the variable scanning interval between sites.

A less distinct pattern emerged for the difference in daily detachment frequency (D_q) occurring during each month (Figure 4.14). Sites 2 and 3 followed a similar pattern, with a marked reduction in D_q during the winter months of December to March. Peak daily D_q occurred in October for both sites (233 detachments for Site 2, 434 for Site 3), although these values were not appreciably different from those in April, May, August and September. Another decline occurred in July, which for Site 2 was larger than the winter reduction (117 detachments in March, 106 in July), but for Site 3 was considerably smaller (194 detachments in February, 286 in July). This reduction in daily D_q approximately mirrored the increase in D_v over the same period. In terms of absolute D_q, Site 3 displayed the highest detachment frequency throughout the year; approximately double that of Site 2.

Site 3 exhibited a less prominent change during winter months, although there was a slight increase in the daily D_q during winter, peaking in January (237 detachments). This is the inverse of the trend seen in Sites 2 and 3, and therefore follows the increase in D_v seen during the same period. Site 5 exhibited the same September peak as the volume loss (217 detachments), with another broader but lower peak during the late autumn and winter months. These results reflect a wider tendency in both rockfall (Dong and Guzzetti, 2005) and landslide (Dai and Lee, 2001) inventories where frequency is often unreliable and unstable: volume usually represents a more stable measure.

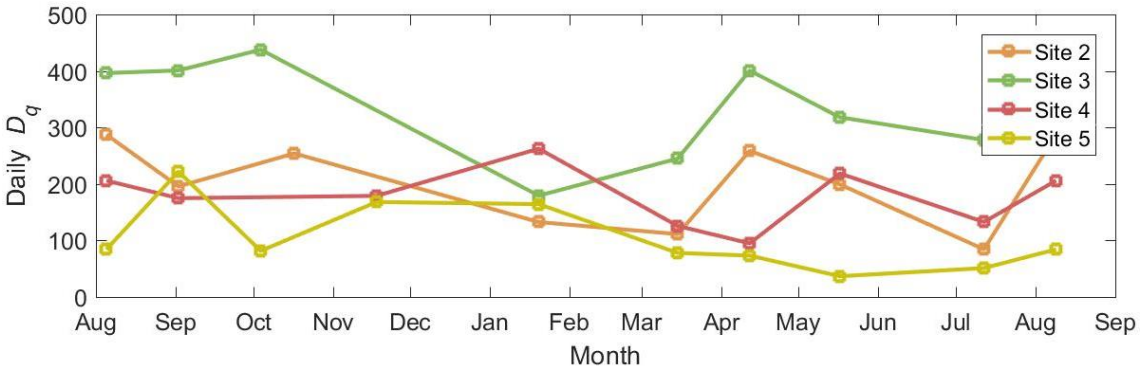

Figure 4.14: Detachment frequency (D_q) per day on the lower cliff at Sites 2-5. Values at each data point represent the values for the previous interval. Note the variable scanning interval between sites.

Monthly exponent (β) values showed a consistent pattern across all four sites (Figure 4.15). During the winter months, there was a broad trough in β values and a marked peak in spring and autumn. During summer, values returned to approximately the same as the winter values. This summer-winter, spring-autumn split occurred consistently across all sites. This can be interpreted as an increase in the contribution of smaller detachments to the overall volume loss during spring and autumn. The lower limit of the β value trough was also similar across the sites, with the lowest values ranging between 0.22 (Site 2) and 0.26 (Site 5). The magnitude of the peaks range between 0.37 (Site 5) and 0.52 (Site 4), the sites with the smallest and largest overall range of values respectively. Therefore, at Sites 2 and 4 the increase in the contribution of smaller detachments during spring and autumn was greater than at Sites 3 and 5, where the variation in β was much less.

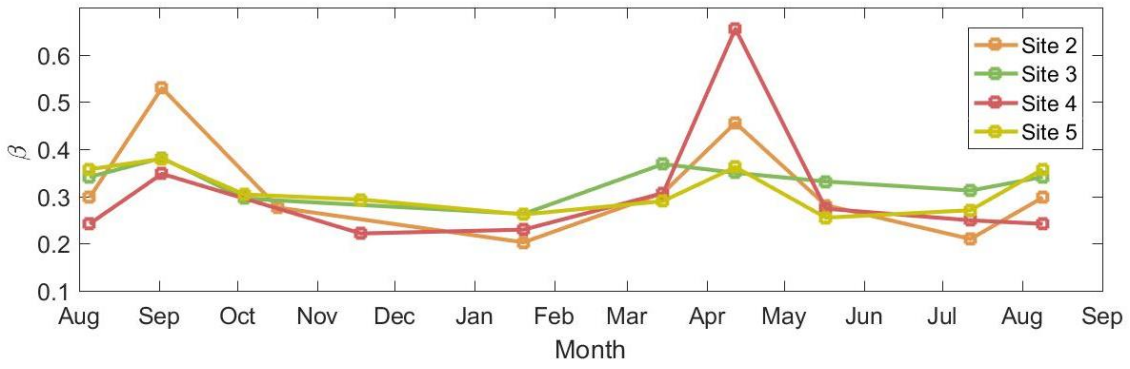

Figure 4.15: Power law exponent (β) averaged for each month on the lower cliff at Sites 2-5. Values at each data point represent the values for the previous interval. Note the variable scanning interval between sites.

4.4. Discussion: Controls on lower cliff erosion

High-resolution monthly scans of the lower cliff over multiple sites have shown considerable variation in spatial and temporal patterns of detachment behaviour. As the data here include detailed monitoring of the inundation zone, it may provide a much-improved understanding of how material is removed from the base of the cliff via marine processes. By examining trends and variables within the detachment datasets, insight into the key controls of erosion may be provided. Critically, if the marine signal is important in driving cliff erosion, it is in this dataset over the lower cliff that it should be observable. In turn, this may give further insight into how these processes drive failure propagation up the cliff face. Furthermore, whether this variation can be explained by the level of exposure to tidal fluctuations, notwithstanding wave action, may be able to offer insight into the relative importance of different marine mechanisms.

4.4.1. Lower cliff erosion rate

Overall recession rates at the study site have been acquired by previous researchers. The mean erosion rate (χ) of the total scan area in my study (9.5 $x10^{-2}$ m y^{-1}, standard deviation = 8.2 $x10^{-2}$ m y^{-1}), is 2 -3 times higher than rates across the entire vertical cliff face at Staithes calculated by Lim *et al.* (2010) (χ = 6.5 $x10^{-2}$ m y^{-1}) and Rosser *et al.* (2013) (χ = 2.9 $x10^{-2}$ m y^{-1}).

My study is generally in agreement with other authors regarding seasonal variations in erosion characteristics. Rosser *et al.* (2005) noted an increase in volume loss during the winter months and specifically a reduction in losses from the inundation zone during spring and summer. This pattern of increased erosion during winter is repeated in Robinson, (1977) and Vann Jones *et al.* (2015) for Staithes, as well as in other clastic sedimentary cliffs (Young *et al.*, 2009) and chalk cliffs (Dewez *et al.*, 2013; Letortu, Costa, Maquaire, *et al.*, 2015). The scale of this seasonality, however, is larger in my study. For example, my results show an up to 6-fold increase in winter erosion at the lower cliff, whereas Vann Jones *et al.* (2015) showed a 2-fold increase over the inundation zone. This may reflect the smaller spatial scale of my study or else variability between years.

Barlow *et al.* (2012) found that the exponent (β) exhibited higher variability ($1.12 > \beta > 2.12$) during winter but stayed relatively constrained ($1.4 > \beta > 1.8$) during the summer months. This was attributed to increased winter activity and a higher number of large failures. The values of β in my study were larger and exhibited a wider variability than the Barlow *et al.* (2012) values, which may reflect the smaller cliff area and consequently fewer large events. During the spring and autumn months, β values were within the range found for general rockfalls by Hergarten (2003), suggesting that the monitored zone behaved similarly to the full cliff face during this period. A more accurate value of β would require the cliff toe be monitored constantly throughout the year (J. G. Williams *et al.*, 2017), utilising a sampling interval which accounts for these observed seasonal fluctuations.

A range of studies have observed considerably higher erosion rates over their monitoring period at the lower cliff at Staithes than for the remainder of the cliff face above (Agar, 1960; Lim *et al.*, 2005; Rosser *et al.*, 2013). Vann Jones *et al.* (2015) found considerable differences in erosion rate (χ) of the inundated (χ = 0.11 m y^{-1}) and non-inundated (χ = 0.02 m y^{-1}) zones. Sites 4 and 5 had similar χ values to those of the inundated zone from Vann Jones *et al.* (2015), but less agreement was found in Sites 2 and 3, which were an order of magnitude higher. Some of this discrepancy may be explained by the difference in the smallest detectable detachment between the two studies, which in my study

was four orders of magnitude smaller than in Vann Jones *et al.* (2015). This can be seen when considering the detachment frequency: I found three times more detachments per m^2. Rosser *et al*. (2013) also observed faster erosion rates in the inundation zone.

If the trend of faster erosion at the lower cliff were to hold indefinitely, the cliff profile would tend to notch, steepen and eventually overhang (Lim, 2006). This pattern is not common in coastal rock cliffs due to structural and rock strength controls and limitations, leading to eventual gravity-driven collapse (Dewez *et al.*, 2013). Some studies have based their analysis on this persistent trend being the case (e.g. Furlan, 2008). If the assumption is made that the broad morphology of the cliff profile is in dynamic equilibrium (Trenhaile, 2001), then it must also be assumed that the average recession rate must be equal up the profile over a long timescale (Walkden and Hall, 2005). It is then logical to infer that studies which detect vertical disparities in erosion must be monitoring for an insufficient duration to observe the full process of cliff retreat.

At Staithes, Rosser *et al.* (2013) noted that failure propagation across the entire cliff face occurs every 10-100 years and these cliffs resurface – defined as the point at which the probability of the entire cliff face having experienced detachment ≈ 1 – on average every 28 years. This is considerably longer than the monitoring period of most studies. The data at these sites suggest that erosion of the lower cliff is continuous, the influence of which has the potential to propagate up-cliff. This is highly dependent on cliff lithology, as was seen in the intermittent siltstone erosion (Section 4.3.4)

Timescale therefore poses a problem when attributing hard rock coastal cliff erosion to marine-driven forcing alone. It is not a simple case of comparing erosion rate at the marine-influenced zone with that of the subaerial zone above (Vann Jones *et al.*, 2015), if time-averaged erosion rates are equivalent. Instead, it may be the characteristics of the erosion in the marine-influenced zone that give an indication of the nature of marine-driven erosion and its key constituents. Retreat of the cliff line above therefore should not be used to approximate the erosion rate of the lower cliff, or the drivers or triggers of erosion, without a full and detailed consideration of the mechanisms involved.

The conventional model of wave recession involves direct undercutting at the cliff toe, leading to the destabilisation of the cliff face above, creating vertical cliff profiles. This has been observed elsewhere (Marques, 2008; Kogure and Matsukura, 2010; Olsen *et al.*, 2016), with (Duperret *et al.*, 2004) or without (Moses and Robinson, 2011) preparatory notching. Wolters and Muller (2008) suggested that the critical parameter in overall cliff destabilisation is cliff steepening driven by erosion of the lower cliff. This may occur with or without notching. Concavity formation is not achievable in all geological conditions, and some rock mass structures will never facilitate notching. Where notches do not occur, instability can be generated by a steep cliff toe reinforcing high re-entrant corner stresses via incipient fracturing (Rosser *et al.*, 2013). The occurrence of notches at Staithes is variable, with Sites 3, 4 and 5 exhibiting some degree of concavity immediately above the cliff toe. Shallow ramps such as those at Sites 2 and 4 are more commonly observed in the area. This variability suggests that instead of observing a long-term trend, studies of the entire cliff face may be capturing the initial stage of a periodic cycle of the vertical progression of instability driven in part by erosion of the lower cliff.

A number of studies have attributed short-term volume loss to environmental factors (e.g. Allan *et al.*, 2006, Letortu *et al.*, 2015b, Young, 2017). Seasonal differences observed in my study show a clear prevalence of volume loss during the winter months, indicating sensitivity to prevailing conditions at this scale. Whilst other studies have attempted to directly link wholescale cliff recession with external drivers (Young *et al.*, 2009; Letortu *et al.*, 2015; Vann Jones *et al.*, 2015), unpicking the direct response of the cliff is highly problematic when it has been shown that detachments on the subaerial section of the cliff may at least in part driven by progressive upwards failure propagation (Rosser *et al.*, 2005; Hall *et al.*, 2008) alongside subaerial weathering (Johnstone *et al.*, 2016). It is unknown whether cliff flexing and microseismic ground motions play a preparatory role in weakening cliffs prior to failure (Adams *et al.*, 2005; Brain *et al.*, 2014).

By using periodic scanning, detachments were captured which may have occurred as multiple smaller events over the period as one detachment scar, as was seen for a longer timescale in the clustered detachments in the monthly

data (Figure 4.12). This makes it difficult to attribute cliff change with external forcing. Furthermore, if erosion is driven by a single extreme event, such as a storm, it would be difficult to ascribe the cliff change to this or the more frequent quiescent conditions during the survey interval (Lim *et al.*, 2010; Vann Jones *et al.*, 2015).

The importance of storms in failing and removing cliff material has been suggested by Earlie *et al.* (2015), where erosion rates of 2 orders of magnitude greater than the 50-year long-term average were observed at Porthleven, UK, over a two-week period. However, other sites do not exhibit this behaviour. Observations of erosion along a 30 km aeolinite cliff line in Israel by Katz and Mushkin (2013) showed that post-storm erosion was comparable with the long-term average, indicating storms may not be significant geomorphic agents at that site. Here, gravity-driven failure, driven in part by basal wave scouring, was responsible for the majority of erosion, with only locally significant (< 4% of cliff length) storm-related erosion.

As such, the difficulty in attributing cliff change within change detection over a month with highly variable environmental conditions to specific events, conditions or mechanisms is challenging. The erosive role of more frequent, lower magnitude marine and environmental conditions is even less well-understood than storm impacts because of this. However, the more continuous, less episodic erosion observed at the lower cliff in this study may be more representative of the direct erosive action in this zone than equivalent observations of the cliff face above.

4.4.2. Geological control on erosion

Some studies have suggested that lithology and rock structure are the dominant control on cliff erosion rate (Cruslock *et al.*, 2010; Bezerra *et al.*, 2011; Carpenter *et al.*, 2014). Geological variation exists between the rock types found at the sites in my study. The shales at Staithes had a relatively low UCS and the rock fabric means the structure fragments readily into centimetre-scale platelets (Figure 4.5); it was also seen to erode along joint boundaries.

Joint spacing (Benumof and Griggs, 1999) and joint orientation (Caputo *et al.*, 2018) have been identified as primary controls of erosion. In my study however, it is likely that rock fabric of the shale as the dominant lower cliff lithology, rather than joint structure of the full cliff, is more important in providing erosion susceptibility. Joint spacing may be more relevant where strong, competent rock dominates (Hall *et al.*, 2008). In contrast, the siltstone had a higher UCS and only appeared to erode along joint boundaries, although small detachments seen in this lithology may have been in part due to abrasive action or localised weakening by weathering.

Structural variability also existed between sites: Figure 4.6 shows that fracture planes were preferentially cliff-normal at Site 5, and tended to be oblique at the other sites. These differences explain the variation in erosion characteristics seen in each lithology, with blocky detachments following joint orientations occurring in both lithologies, but small fragmentation ($< 5 \times 10^5$ m^3) much more common in the shale.

Duperret *et al.* (2004) found that the nature and extent of the rock detachment was controlled by rock structure. The cliff-parallel joints seen in the siltstone in Site 2 but not Site 3 may explain the more frequent block erosion seen here. Frequent cliff-parallel fracture planes promote protrusion collapse, and cliff-normal jointing may amplify shoreward wave forcing (Müller *et al.*, 2003). This may explain the increased erosion at the base of Site 3 when compared with Site 2. The strength of both lithologies greatly exceed the likely instantaneous loading conditions in this environment (Noormets *et al.*, 2004). Therefore, the role of rock degradation through mechanical action and weathering is likely to be incremental and additive, meaning rock structure and propensity to weathering is probably more fundamental in controlling erosivity than rock strength alone.

Sites 2, 4 and 5 exhibited a clear increase in D_q above the HAT elevation (Figure 4.9). Site 3 did not show this, which may be due to the siltstone layer 2-5 m above the HAT (Figure 4.10). The inverse trend for Site 3 seen in the exponent (β) values when compared with the other sites may also be explained in the same manner, as the volume loss becomes dominated by larger scars.

The 2° easterly dip of the stratigraphy means that the clear reduction in the detachment frequency in that unit seen in the cliff face maps (Figure 4.7) is obscured in the profiles (Figure 4.9) as it covers different bins when averaged over the cliff width. Differential erosion rates between these lithologies was observed by Rosser *et al.* (2013), with shales and mudstones having the highest rates, but these become less important when considering long-term retreat. Therefore, this supports the notion that erosion occurs more episodically in siltstones with larger events, and more continuously in shales with smaller events (Table 4.5).

Dornbusch *et al.* (2008) highlighted that it is still unknown whether the geology of the lower cliff is more important than the geology of the entire cliff face when determining overall cliff retreat. Modelling of chalk cliffs has shown that weaker layers specifically at the lower cliff do lead to a considerable increase in cliff recession, driven by profile steepening (Carpenter *et al.*, 2014). The evidence from my study suggests that cliff toe lithology and structure must be a key factor, but only if erosion is driven solely by undercutting at the lower cliff. Observations of the cliff face profile at the site have shown the siltstone layers protruding and overhanging the mudstone and shale below.

Although not occurring in the scanned areas, some platform scarps existed where the more competent siderite layers (Simms *et al.*, 2004; Emery, 2016) were exposed within the weaker shales. An example of this can be seen in Figure 4.16. This suggests some lithological control over platform topography in the site overall. It is possible that some of the large events seen in the sandstone, particularly at Site 2, may be driven in part by undercutting in the shale, rather than direct exogenous mechanisms alone. This suggests that the characteristics of the least resistant lithology at the lower cliff determine the erosion rate of the entire face, as more resistant layers will eventually become unstable as erosion leads to profile steepening and undercutting. As such, the order of magnitude differences in erosion rate between sites cannot be explained by lithology alone, as dominant lithology and structure across all sites are very similar.

The mean value of β across all four sites was 0.52 ± 0.16. This is at the low end of the range suggested for cliff erosion by Hergarten, (2003). Dewez *et al.* (2013) found a similar value (0.53) across the entire cliff face from TLS scanning of the Mesnil Val chalk cliff, Normandy, France. Previous studies of the Staithes cliffs showed consistently smaller values outside of Hergarten's (2003) range: values of 1.73 (Rosser *et al.*, 2007), 0.8 (Lim *et al.*, 2010) and 1.4-2.12 (Barlow *et al.*, 2012) were found across the entire cliff face. Katz and Mushkin, (2013) noted a β value of 1.02 in poorly cemented aeolianite sequences. None of these studies calculated the β values specifically regarding the zone above the cliff toe or at such high resolution; these studies focused specifically on rockfalls, and not in areas such as the inundation zone where different processes such as wave quarrying may be operating.

Values of β were shown by Rosser *et al.* (2007) to vary between lithologies. As each scan incorporated fewer lithologies by virtue of their smaller spatial extent, this may partially explain the discrepancy. Alternatively, this implies that the lower cliff behaves very differently to the rest of the cliff. The size of the largest detachment seen in my data (23 m^3) was considerably smaller than in other studies in this area (e.g. 2200 m^3 in Lim *et al.* (2011)), further indicating that erosion of the lower cliff is incremental, driving instabilities leading to larger events above.

Cliff aspect (θ) also varied by 90° between sites (Section 3.6). Whilst this difference is somewhat considerable, observations of the wave directions indicate that refraction around the shallow topography of the foreshore mean that wave incidence angles vary little between sites. Sites 2, 4 and 5 are located on headlands and Site 3 is between them within a wide bay. Whilst lithology and structure can play a key role in dictating planform morphology (Wilson, 1952; Duperret *et al.*, 2004), it is unknown whether geology plays any direct role in modifying marine forcing along the coastline (Moses, 2014), beyond its influence on planform morphology.

Figure 4.16: Exposure of siderite layer (red rock) within the shales in the study area. Note the minor scarp formed around the edge of the exposure.

Lithology may also be an important control on the nature of detachment evolution. Shales displayed clustered detachment scars more frequently than the more massive siltstone. This is in agreement with Rosser *et al.* (2013) and Vann Jones *et al.* (2015), where subsequent rockfall clustering around earlier failures was more evident in shales and mudstones. Many of these compound failures appear as individual detachments within change detection over a year. As such, it is logical to assume that some of the observed monthly detachments may themselves have been composed of spatially clustered events over the survey interval.

To address the effect this has on magnitude frequency relationships, J. G. Williams *et al.* (2017) compared two rockfall inventories taken over the same area at differing scan intervals, < 1 h and 30 d. They observed an increase in β from 1.78 to 2.27 with increasing scan interval, reflecting a decrease in the proportion of larger rockfalls, although this is accompanied by an increase in volumetric uncertainty. As such, it is likely that the proportion of smaller

detachments in my dataset was higher than the results suggest, underlining the importance of these in overall erosion.

4.4.3. Platform morphology and erosion

Platform morphology at the study site is comparable with studies in similar environments. The range of values for platform slope (S_p) (0.4°-0.9°) are considerably less than the range of 1.5° to >4° identified by Kennedy (2015) for macro-tidal platforms. This is somewhat unexpected as S_p generally increases with tidal range (Trenhaile and Layzell, 1981), and a range of 6 m is large relative to the shore platforms studied (Moses, 2014; Sunamura *et al.*, 2014). These values are more similar to those studied by Stephenson and Kirk (2000) (0.5°), where the tidal range was 2.57 m at its maximum, or the type-B horizontal platforms of Ogawa *et al.* (2011), where S_p = 0.3° and the tidal range was 1.7 m.

A platform with a comparable tidal range was investigated by Poate *et al.* (2016) at Hartland Quay, North Devon. This platform has a tidal range of 7.3 m and S_p = 1.4°. This non-conformity to the general relationship could be caused in part by the lack of topographic data towards the seaward portion of the platform. Other factors could include weathering, structural or lithological controls on downwearing rates specific to this site. Lithology and rock structure can also play an important role, with bed dip and bedding depth critical to platform morphology (Moses, 2014). Furthermore, platform slope can be seen to increase considerably towards the landward edge (Figure 3.5) creating a concave upwards profile, also observed at other sites by Hills (1972) and Moses (2015).

The range of platform widths (*w*) I observed (36 – 166 m) are at the lower end of the range given by Moses (2015), similar to the meso-tidal platforms studied by Trenhaile (1999) in the UK, Canada and Japan. When considering how the platform acts as a control on wave transformation, it would be more useful to define *w* hydrodynamically, namely the distance offshore at which the wave base starts to be affected by bottom friction. However, measuring this was not feasible within my study (Section 3.7.2). Davies *et al.* (2006) suggested the fundamental control of *w* is rock uniaxial compressive strength (UCS). Swirad

et al. (2016) found a significant ($p < 0.05$) relationship between uniaxial rock strength and w at Staithes. Harder rocks were found to coincide with wider platforms, but the variability in the relationship was too large ($r^2 = 0.04$) to confirm this.

The three key morphological variables between sites were platform width (w), platform ramp slope (S_r) and cliff toe elevation (E_{toe}), which have all been identified as important variables in dictating the characteristics of the marine conditions at the cliff toe. In general, larger values for w increase wave energy dissipation before impact at the cliff (Poate *et al.*, 2016), S_r affects breaker types (Trenhaile and Layzell, 1981) and E_{toe} controls the inundation duration (W_d) (Trenhaile, 2000) and water depths (d), and hence wave breaking conditions (Noormets *et al.*, 2004; Collins and Sitar, 2008; Stephenson *et al.*, 2018).

Platform width has been shown to control the extent of the wave dissipation zone and has been used as a proxy for wave intensity, as wider platforms would dissipate more wave energy prior to reaching the cliff toe (Swirad *et al.*, 2016). Values for w at Sites 4 and 5 were considerably shorter than those of Sites 2 and 3. Stephenson *et al.*, (2017) demonstrated that wave height, and potentially therefore erosivity, can actually increase closer to the cliff toe through shoaling. Furthermore, inundation duration (W_d) at Sites 4 and 5 is greater (61% and 70% of the time respectively) than Sites 2 and 3 (32% and 36%) due to lower platform elevations. The erosion rates given by Norman (2012) for the inundated zone (0.11 m yr^{-1}) more closely match those sites which are inundated the least (0.177 and 0.168 m yr^{-1} for Sites 2 and 3 respectively), meaning W_d alone cannot explain this variation.

4.4.4. Marine forcing of erosion

It is apparent that the lower cliff behaves differently to the rest of the cliff, and that this may influence recession of the cliff face above. From Figure 4.11 it is possible to delineate a distinct boundary at approximately 6 mODN, or 3 m above the HAT, where a shift in the frequency of failure volumes occurs for detachment volumes (D_v) < 10^{-1} m^3. Whilst there was relatively little discernible relationship between erosion and elevation in the overall erosion response (Figure 4.9C), there was a marked increase of smaller detachments within this

zone. The lower cliff experiences daily inundation and therefore continuous wetting and drying cycles, yet the smallest fragment removal occurred in the section above the inundation zone, suggesting maximum erosion rates require a combination of rock degradation through weathering alongside wave forcing, occurring above the still water depth (Swenson *et al.*, 2006; Lim *et al.*, 2011). Wave quarrying may play a substantial role in cliff erosion (Moses and Robinson, 2011; Limber *et al.*, 2014), yet the present evidence suggests that the erosivity of this mechanism must be controlled by additional factors that cannot be described simply by inundation duration and the attenuation of wave energy approximated by platform width (Swirad *et al.*, 2016).

The cliff toe ramp has been identified as a common feature in some shore platform environments (Hills, 1972). Trenhaile and Layzell (1981) used ramp slope (S_r) alongside water level frequency (W_q) to determine the effectiveness of wave quarrying at the toe. In that study, W_q determined wave energy distribution up the face profile, but the tidal level must also determine the height and breaking condition of wave impacts (Kirkgöz, 1992). Water depth at the cliff toe, alongside wave height, is key to determining the forcing magnitude of wave impacts through controlling breaking conditions (Cuomo *et al.*, 2010). Crucially, it has been shown through flume experiments that when $S_r \approx 5°$, the largest wave impact pressures are produced on a vertical structure (Kirkgoz, 1982). Both Sites 3 and 4 exhibited cliff toe ramp slopes very close to this value. This implies that under specific hydrodynamic conditions these sites undergo considerably higher quarrying magnitudes than Sites 2 and 5.

Following Trenhaile and Layzell (1981), the W_q distribution up the profile was compared with the erosion distribution found in the smaller detachments (Figure 4.17). Values for W_q were extracted from the measured 15-minute water levels at the Whitby tide gauge and therefore may not accurately represent the absolute water levels above the cliff toe at the study site. To further investigate the relationship between W_q and the erosion profile of $D_v < 10^{-1}$ m^3, a cross-correlation was carried out. This is a measure of similarity between the two series, and gives a value of the displacement between them. The results revealed an elevation correlation offset of 3.6 m above the cliff toe, considerably higher than would be expected from astronomical and wave setup water level

alone. Further investigation into the influence of wave setup and height is shown in Chapter 8.

Therefore, wave impact pressures, which occur around the still water level (Kirkgoz, 1982), alongside precursory weathering, may be responsible for the majority of volume loss seen at this elevation, rather than inundation alone. Cross correlation with overall D_v, β and D_q yielded no significant result. However, erosion of small fragments from the shale occurred irrespective of this. In turn, this may drive the upward propagation of instability that ultimately controls the rate of stochastic erosion above.

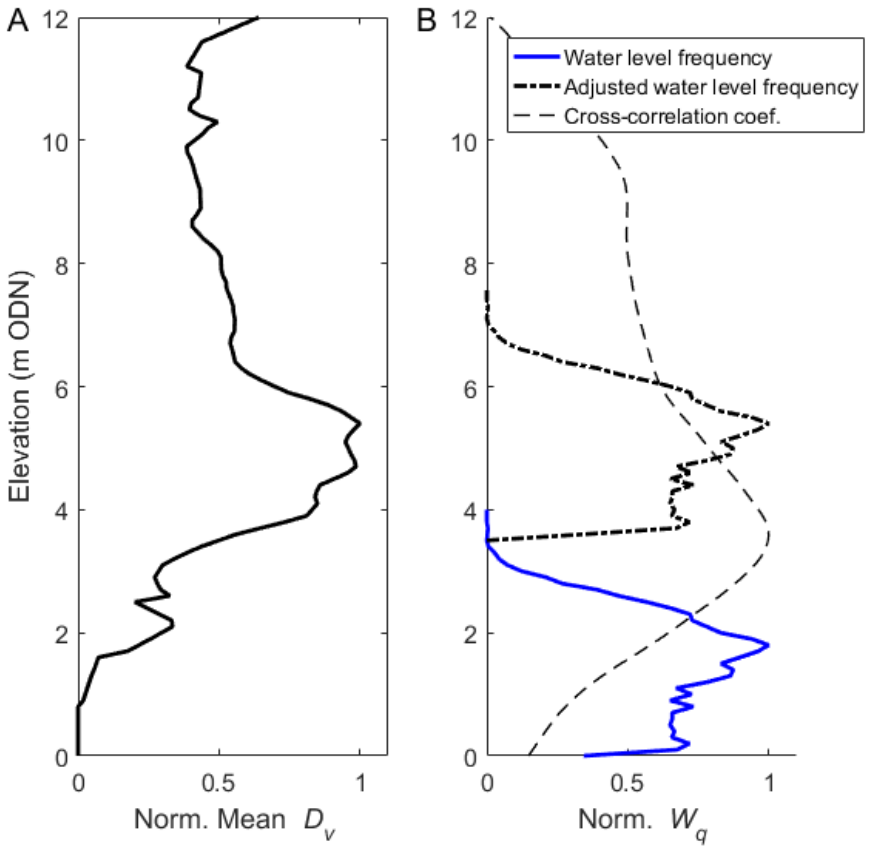

Figure 4.17: A) Normalised mean erosion volume (D_v) across Sites 2-5 of detachments $<10^{-1}$ m^3. B) Normalised water level frequency (W_q) function from measured Whitby tide gauge data over the survey period (blue), cross-correlation coefficient (dashed) of the water level function with the erosion volume, and the resultant water level function (dot-dashed) at the peak correlation level. The peak correlation of the water level function occurs at an offset of 3.6 m above the actual water levels.

4.4.5. Cliff toe hydrodynamics

Alongside geological control, it is likely that a combination of morphological and hydrodynamic conditions combine to produce the variable forcing regimes between these sites in order to create the differing erosional patterns seen in these data. The interaction between each variable is complex and each one individually cannot determine marine forcing conditions alone. For example, lower toe elevations mean that waves are attacking the cliff toe for a greater proportion of the tidal cycle. However, this does not necessarily imply greater overall forcing of the lower cliff, as toe elevations are a primary control on breaking conditions, which in turn dictate the shoreward forcing magnitude and variability (Figure 4.18). As such, maximum wave forcing is likely to arise when the most common wave heights occur at the toe elevation which allows them to break directly against the cliff.

This may explain the higher erosion rate at Site 3 for example, as the smaller, more frequent waves are more likely to break at the toe here than at Sites 4 and 5, which have lower toe elevations. This interplay is compounded by the continual water level adjustment over the tidal cycle and the likely considerable spatial variability in rock resistance thresholds to erosion, notwithstanding changes in offshore wave conditions. This is also important when considering seasonal variation. Large winter waves may not necessarily be the most damaging individually, as they are the ones most likely to dissipate more rapidly and break before the cliff toe, particularly where toe elevations are high and platform widths are large.

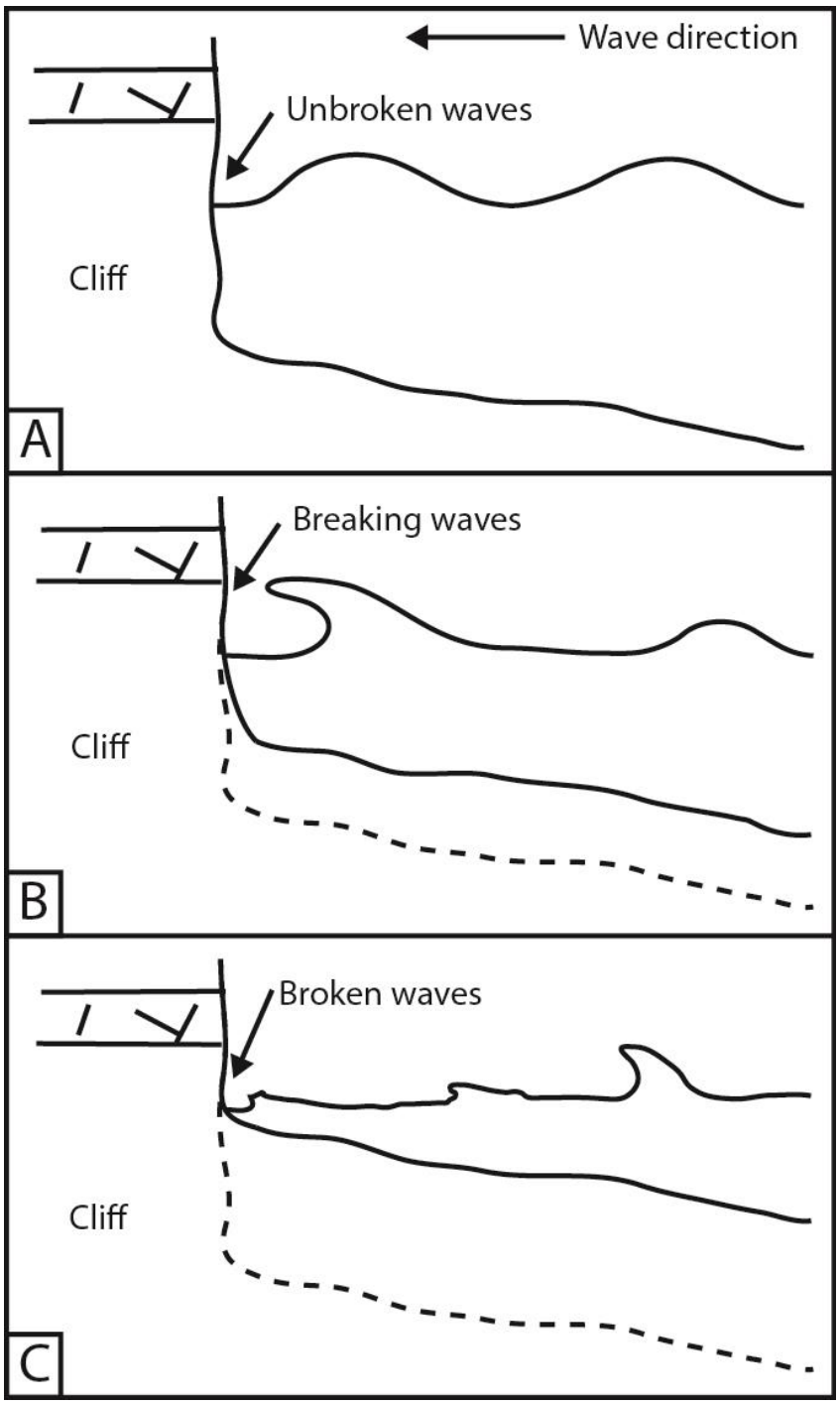

Figure 4.18: Simplified schematic demonstrating the depth limitation of breaking waves at the cliff toe at varying toe elevations. Assuming high spring tide water level and that water reaches the toe, for any given wave height, waves are more likely to be A) unbroken where the cliff toe elevation is low, B) breaking at some intermediate toe elevation, and C) broken at high toe elevations. As wave breaking conditions control wave forcing magnitude and distribution, toe elevation may regulate forcing at the toe.

Hydrodynamic variability may explain some of the variation seen in these data. There was a larger volume loss difference between the winter and summer months for Site 2 than for Site 3. The overall erosion rates for both sites were roughly equal, but Site 2 may be more influenced by marine action due to the different ramp slopes and toe elevations. Site 3 exhibited an inverse power law exponent (β) to the other sites, decreasing with elevation (Figure 4.9B). This site also has the highest toe elevation, hence will get very different wave conditions than the other sites, alongside a shorter inundation duration. As seen in Figure 4.17, tidal inundation duration alone cannot explain the erosion pattern observed, so as wave action occurs above the still water depth, this may be a key mechanism.

4.5. Conclusion: Characteristics of erosion at the lower cliff

High-resolution TLS data focused on the cliff toe was used to investigate the relationships between the spatial and temporal distributions of eroded material and the morphological characteristics of the cliff and shore platform. My analysis has shown that:

- The erosion rate of the lower cliff varied by an order of magnitude across a 500 m section of the coastline. Erosion characteristics are dominated by local scale variability.
- The lithological and structural composition of the rock mass dictated the dominant detachment characteristics, with frequent cm-scale erosion in the shale and intermittent, joint controlled detachments in the siltstone.
- The variation in erosion volumes of smaller ($< 10^{-1}$ m) fragments showed a marked increase in a 3 m zone above the HAT. Tidal inundation and weathering alone could explain the erosion seen at this elevation.
- Wave forcing may be able to explain the patterns seen in the erosion of smaller fragments in the lower cliff. This may explain both the distribution of erosion up the cliff, and the seasonal variation in erosion volume over the study period.

- These findings differ with those of horizontal, dissipative platforms in micro-tidal environments, where waves are considered too weak to influence erosion of the lower cliff. Detailed investigation of macrotidal wave conditions at the cliff toe are required to unpick the contribution of marine forcing to overall cliff recession and fully understand the drivers of cliff erosion in this environment.

5. Wave conditions at the cliff toe

5.1. Introduction

Wave processes on macrotidal shore platforms are a key driver of coastal cliff and shore platform development (Trenhaile, 2000; Matsumoto *et al.*, 2016). Wave height (H) and wave energy density (ξ) at the cliff toe (which is proportional to H^2) are often used as a measure of wave erosivity (Damgaard and Dong, 2004; Bezerra *et al.*, 2011; Marshall and Stephenson, 2011). In addition, erosivity is also a function of whether the waves are unbroken, breaking or broken on impact (Miller *et al.*, 1974; Sunamura, 1992; Oumeraci *et al.*, 1999), known as the wave breaking condition. Cliff erosion models commonly use these three variables as a key parameters in forcing erosion (Trenhaile, 2000; Walkden and Hall, 2005; Hackney *et al.*, 2013; Limber *et al.*, 2014).

Shore platforms modify H and ξ at the cliff toe, but may serve to dissipate (Ogawa *et al*, 2015) or amplify (Beetham and Kench, 2011; Stephenson *et al.*, 2018) offshore wave heights depending on the precise combination of wave conditions and bathymetry (Marshall and Stephenson, 2011; Poate *et al.*, 2016). The wave energy transfer between offshore ($\xi_{offshore}$) and the cliff toe (ξ_{cliff}) can be described as a percentage of $\xi_{offshore}$ reaching the cliff toe:

$$\xi_{difference} = 100 \cdot \frac{\xi_{cliff}}{\xi_{offshore}} \quad (5\text{-}1)$$

As such, in this study I use $\xi_{difference}$ as a measure of wave energy transfer to the cliff toe and whether the platform conditions act to dissipate ($\xi_{difference} < 100$) or amplify ($\xi_{difference} > 100$) values of $\xi_{offshore}$ at the cliff toe. The most important factors in controlling cliff toe wave conditions are tidal range, tidal inundation duration (Trenhaile and Layzell, 1981) and wave energy dissipation across a shore platform (Dickson *et al.*, 2013), which is determined in part by cliff toe elevation relative to the mean tidal elevation, roughness and slope (Poate *et al.*, 2016, 2018).

Furthermore, wave breaking condition is broadly controlled by H – most commonly stated as root-mean-squared wave height (H_{RMS}) (Farrell *et al.*, 2009) – and water depth (d_{cliff}), where:

$$H_{RMS} = \gamma d_{cliff} \quad (5\text{-}2)$$

The depth-limiting constant of proportionality (γ) ranges between 0 and 1 and determines the maximum wave height that can propagate across the platform before breaking (Farrell *et al.*, 2009), and is therefore critical in understanding the wave conditions at the cliff toe for a given water depth.

Despite this understanding, few studies have measured wave dynamics at the cliff toe itself, where energy transfer from waves to the cliff occurs. Previous research has focused on short-term (~2-14 days) measurements of wave conditions along cross-shore transects (Stephenson and Kirk, 2000b; Trenhaile and Kanyaya, 2007; Farrell *et al.*, 2009; Ogawa, 2013; Poate *et al.*, 2016; Stephenson *et al.*, 2018). This has left a considerable knowledge gap regarding wave dynamics across a wide range of incident wave conditions, particularly storm waves, and the longshore variations in cliff toe wave conditions produced by platform morphology. Without this, the link between wave conditions and erosion remains unclear.

To further understand wave conditions at the cliff toe, this section of the thesis describes my attempts to quantify the relationships between offshore waves, tides, platform morphology and cliff toe wave conditions over a longer timescale (~one year). In turn, this will provide a clearer understanding of the magnitude-frequency distribution of cliff toe wave conditions, which feeds in to the resultant wave impacts pressures (Chapter 7) and the resultant erosion (Chapter 4). In this chapter I first describe the wave data collection and processing (Section 5.2). Next, the results are presented, focusing on the offshore and cliff toe wave conditions over the study period (Section 5.3). I then analyse the relationships between the offshore and cliff toe conditions and the role of platform morphology in modifying these. Wave energy dissipation and amplification are discussed, followed by an extrapolation of the data with a discussion of the wave height depth-limiting conditions and breaking conditions at the toe

(Section 5.4). Finally, the implications of my findings with regard to wave forcing are presented (Section 5.5).

5.2. Monitoring cliff toe wave conditions

To investigate wave transformation across the platform I examined the relationship between the offshore wave conditions and those found at the cliff toe. My study is primarily concerned with relative changes in wave height and energy density between different sites around the cliff toe, hence does not consider the intermediate conditions on the platform.

5.2.1. Field data collection method

5.2.1.1. Wave gauge deployment and sampling regime

Following the methods used to measure shore platform waves by Marshall and Stephenson (2011), Dickson and Pentney (2012) and Ogawa *et al.* (2012), RBR solo D-wave pressure sensors, henceforth referred to as a wave gauge, were installed at each of the five field sites (Figure 5.1). Each wave gauge was housed inside a vented steel cage, bolted to the platform using 8 mm expansion bolts (Figure 5.2A and B), and located approximately 5 m from the cliff toe (Figure 5.2C) – the closest distance deemed safe to access(following Young *et al.* (2011)).

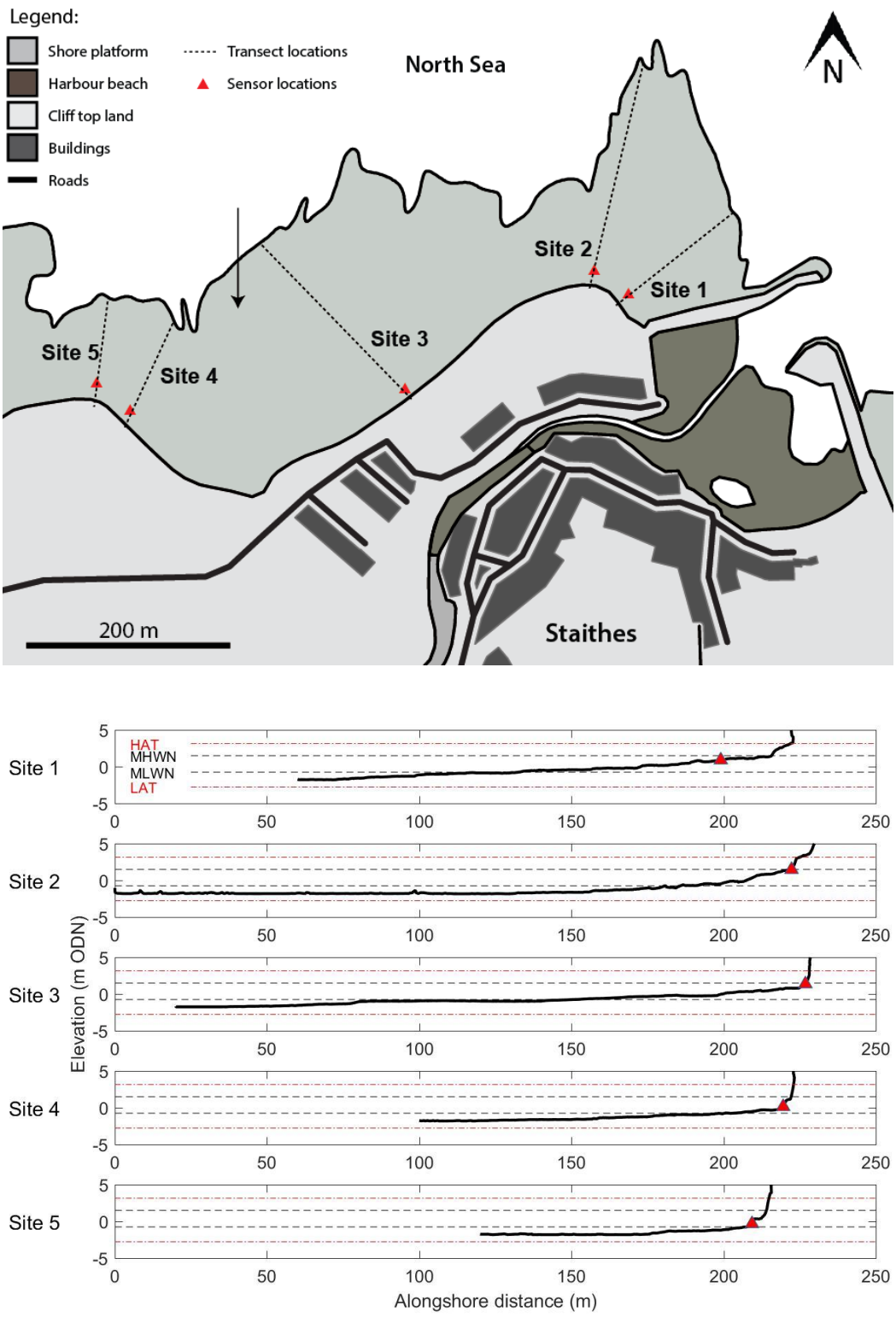

Figure 5.1: Site map, showing the locations of the five RBR Solo wave gauges on the shore platform to the north of Staithes, along with Sites 1-5 profiles showing the location of each sensor (red triangle) relative to the platform (black line) with HAT, MHWN, MLWN and LAT shown in horizontal lines.

Figure 5.2: A) RBR solo wave gauges used in the cliff toe wave monitoring; B) steel cage housing the wave gauge and bolted to the platform; C) location of the wave gauge at Site 4 (arrow).

Between 21/07/2016 and 09/08/2017, each wave gauge logged at 8 Hz for 17.1 minutes every 30 minutes, providing 8,192 (2^{13}) data points per monitoring 'burst'. These intervals were timed on the hour and 30 minutes past the hour, synchronised with the Whitby wave buoy data (Section 5.2.1.2). This sampling regime was selected in order to provide a comprehensive sample of wave conditions and allowed the wave gauges to be deployed continuously for up to three months. Data gaps occurred when the loggers were collected and returned for data download, when batteries were depleted, and due to difficulties in accessing the platform due to adverse tidal conditions (Figure 5.3).

The absolute pressure given by the RBR wave gauges have a published accuracy equivalent to 5 mm of water depth. These data are also corrected by an internal temperature sensor. However, to account for post-calibration sensor drift (0.1% y^{-1}) and provide continuity with the buoy data, I have stated *H* and *d*

measurements to the nearest 0.1 m. Internal wave gauge clock accuracy is < 15 s per deployment interval and so is appropriate for comparisons between sensors over a 30-minute measurement burst.

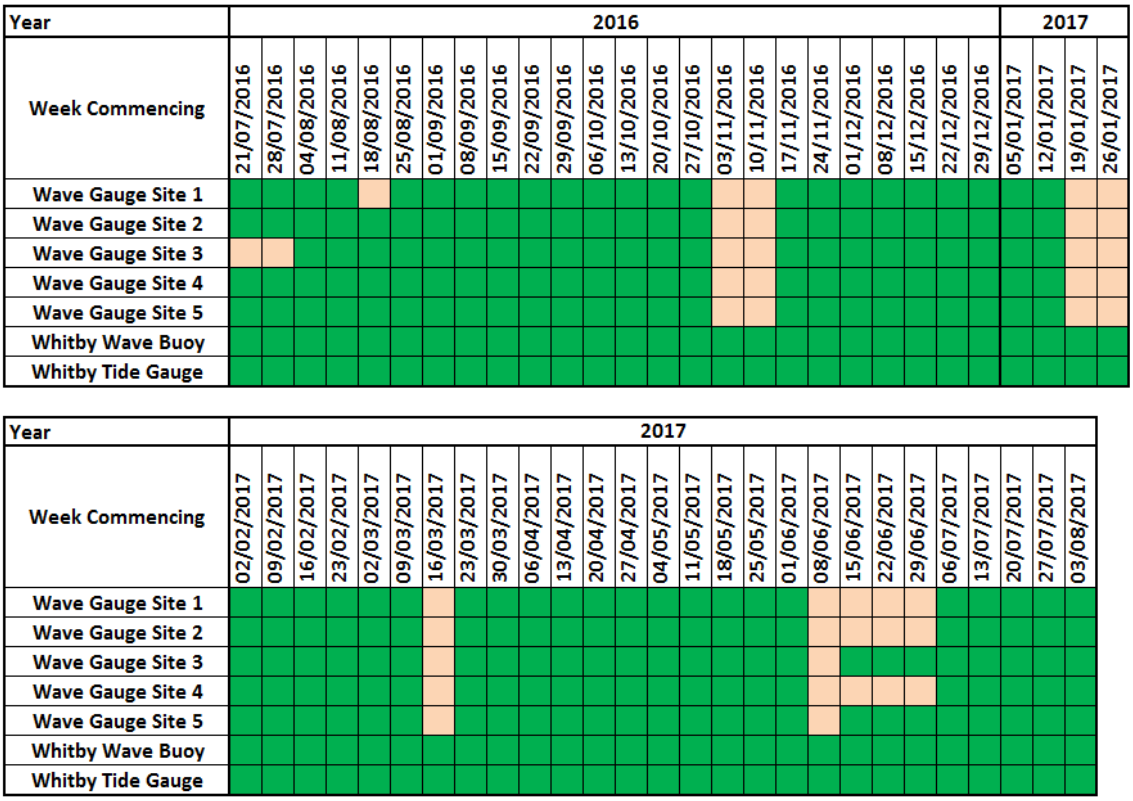

Figure 5.3: Gantt chart of wave and tide data collection. Green blocks indicate a full week of continuous data collection and beige blocks indicate data gaps.

5.2.1.2. Offshore wave and barometric pressure data

I obtained offshore wave data from the nearest available wave buoy at Whitby, 15 km to the southeast of Staithes (Channel Coastal Observatory, 2017). Here, sea surface elevation data are measured using a Datawell Directional WaveRider Mk III buoy at approximately 17 m water depth. Heave, north and west displacements are measured continuously at 1 Hz, from which I calculated wave statistics in 30-minute intervals, starting on the hour and 30 minutes past the hour. I obtained these data from the Channel Coast Observatory database; available uninterrupted throughout the study period (Figure 5.3). Barometric pressure used in the depth correction (Section 5.2.2.2) for the pressure sensor was obtained from the Met Office weather station at Loftus, located 5 km to the

west of the study site. This was provided hourly and linearly interpolated to provide estimates of values at 30-minute intervals to match those of the pressure sensor bursts, following Young *et al.* (2011).

Measurements obtained from the buoy have a sensor accuracy of < 1% of the measured value (Gibbons *et al.*, 2005). As such, the maximum instrumental error for the *H* observations extracted for the study period was ±0.07 m. I have stated values to the nearest 0.1 m as a conservative level of uncertainty based upon this sensor accuracy.

5.2.1.3. Tide gauge water level data

I took regional water elevations from the National Tide Gauge Network site at Whitby Harbour as measured by a Valeport Tidemaster pressure transducer logging at 8 Hz. Here, tidal elevations are derived as an average reading over a 15-minute measurement period and published by the British Oceanographic Data Centre (BODC, 2017). I resampled these to 30-minute values in order to match them with the wave gauge and buoy data.

5.2.2. Field data processing

The following section describes the data processing used to obtain wave statistics for each 30-minute time interval over the study period.

5.2.2.1. Offshore waves statistics

Significant wave height (H_s) (height (m) of the highest third of waves in each 30-minute monitoring burst), maximum wave height (H_m) – height of the highest wave in the burst – and mean wave period (*T*) – the mean of all wave periods (s) in the burst – were obtained automatically from the wave buoy (Channel Coastal Observatory, 2017).

The mean depth of water at the wave buoy is approximately 17 m, meaning that moderate to large waves for the study area (>1.6 m) may already have been affected by bottom friction prior to being recorded at the buoy, depending on *L* (Holthuijsen, 2009). However, the precise nature of wave transformation between deep and shallow water is beyond the scope of this study; only relative changes between low and high energy conditions between sites on the platform

were of concern. Furthermore, as noted by Vann Jones *et al.* (2015), a large majority of the wavelengths observed in this study were below the threshold at which waves become influenced by bottom friction. As such, I have used the deep water wave theory for the equations in this section.

I calculated wave energy density per unit area of sea surface (ξ) (Jm^{-2}) from H_{RMS} and seawater density (ρ) (1027 kg m^{-3}) using linear wave theory (Holthuijsen, 2009):

$$\xi = \frac{\rho\, g\, {H_{RMS}}^2}{8} \tag{5-3}$$

Here, H_{RMS} (m) was obtained from H_s using the ratio between wave statistics in a typical Rayleigh-distributed sea state (Holthuijsen, 2009):

$$H_{RMS} = \frac{\sqrt{2}\, H_s}{2} \tag{5-4}$$

Following Sunamura *et al.* (2014), I calculated deep water wavelength (L) using acceleration due to gravity (g = 9.81 ms^{-2}) according to Battjes (1974):

$$L = \frac{g}{2\pi}\, T^2 \tag{5-5}$$

Breaker heights (H_b): the maximum shoaled height (m) of incident waves prior to breaking, were estimated from offshore H_s and T using linear wave theory (Komar and Gaughan, 1972):

$$H_b = 0.39 g^{0.2} (T {H_s}^2)^{0.4} \tag{5-6}$$

.

5.2.2.2. Cliff toe wave statistics

The following calculations were made automatically in RBR Ruskin, and will be briefly summarised here. Each sensor is designed to measure the instantaneous absolute pressure of the water above. To calculate the depth of water above the sensor (d), the “Simplified” method of the form:

$$d = \frac{p_{sensor} - p_{atmos}}{0.980665\rho} \tag{5-7}$$

was used, where d = water depth, p_{sensor} = absolute pressure measured by the sensor and p_{atmos} = atmospheric pressure (Gibbons *et al.*, 2005). Depths were thus measured at a sampling frequency of 8 Hz, which gave a minimum detectable T set by the Nyquist criterion as 0.25 s, and a maximum T, defined by the ratio of sample rate to the number of samples, as 1,024 s. Following Stephenson *et al.* (2018), I used the values for H_s and T for each burst calculated from the water level time series automatically by Ruskin. H_{RMS} for the cliff toe and ξ_{cliff} were calculated automatically in Ruskin using Equations 5-3 and 5-4 (after Brayne, 2015).

5.2.2.3. Cliff toe water depth

I obtained changes in water depth due to tidal fluctuations and wave setup, also known as the still water depth (d_{cliff}), from RBR Ruskin by taking the mean value of the water level variations measured across each burst to remove wave noise (Gibbons *et al.*, 2005). These depths constitute the time-averaged sum of the combined tidal surge and set-up water levels above each sensor.

5.3. Results: Wave conditions over the study period

This section summarises the wave conditions measured over the duration of the study. Over the 369-day study period, I obtained 17,640 30-minute offshore and cliff toe wave and tide measurements, constituting 8,820 hours over 710 semidiurnal tidal cycles and 25 spring-to-spring tide cycles.

5.3.1. Offshore wave conditions

Time series of H_s, T and tidal elevation during the study period are displayed in Figure 5.4 and summary statistics are shown in Table 5.1. Values for H_s were lognormally distributed, showing a positive skew and low mean value (1.0 m) compared with the range (7.3 m) (Figure 5.5). The largest waves occurred during October-February, where mean H_s = 1.2 m, with the notable exception of December, where mean H_s was lower than average (0.7 m) (Figure 5.4A). Storm conditions are defined by NECO (2017) as having a return period of 0.25 years, or a threshold of 3.25 m. This was exceeded ten times over the study

period (Figure 5.4A), demonstrating that the number of storm events experienced during the study period was 2.5 times higher than average.

Although storm threshold exceedance was more common during winter, two such events occurred during April and May. Note that due to gaps in the cliff toe wave gauge datasets, some of the buoy data presented does not feature in the following analysis. The largest storm (13/01/2017 – 14/01/2017, buoy H_s = 7.3 m) was not captured by the wave gauges. As such, the largest storm in the dataset used in analysis here occurred on 22/11/2016, where at the buoy H_s = 5.0 m. Six of the ten storms were captured using the wave gauges.

Table 5.1: Summary significant wave height (H_s) statistics for offshore and cliff toe measurements over the study period. Note that that maximum H_s event was not captured by the wave gauges.

	Offshore	**Cliff toe**
Mean H_s	1.0 m	0.6 m
Median H_s	0.7 m	0.5 m
Maximum H_s	7.3 m	2.5 m
Standard deviation H_s	0.7 m	0.4 m

Values for T were also more likely to be longer during the winter months and during storms: T = 15.1 s during the largest storm, in contrast to a mean value of 4.8 s (Figure 5.4B). The highest astronomical tide (HAT) for Whitby (3.15 m ODN) occurred three times during the study period (Figure 5.4C). Storms were associated with large tidal residuals: the difference between predicted (astronomical) and measured tides (Figure 5.4D). The maximum recorded tidal residual was 1.49 m on 26/12/2016. The maximum recorded surge level – the sum of the predicted tide and tidal residual – at Whitby was 3.72 m ODN, representing a tidal residual of 0.57 m. Wave directions were highly variable over the study period (Figure 5.6), with the highest frequency occurring in southwest, northwest and easterly.

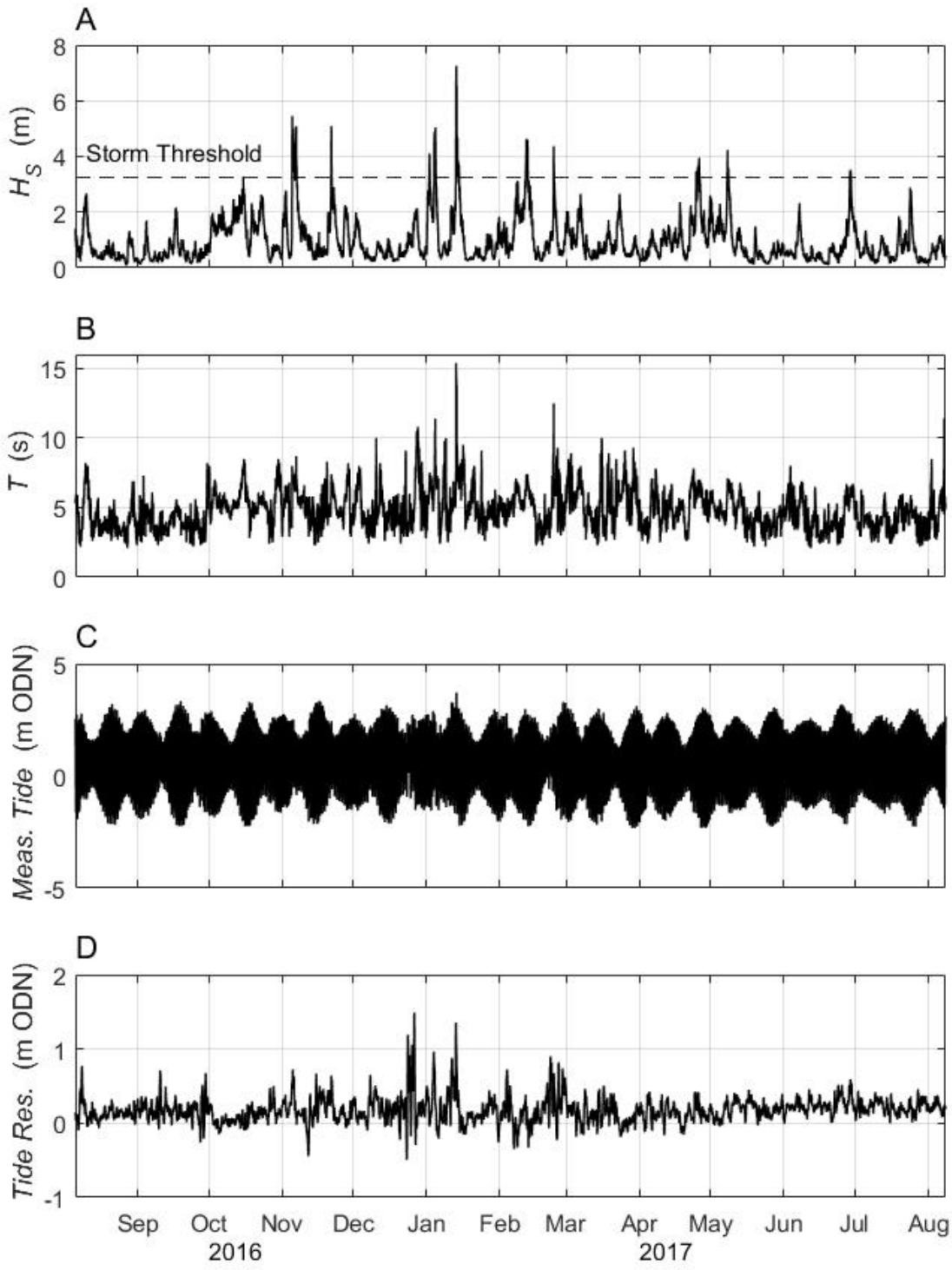

Figure 5.4: A) Offshore significant wave height (H_s) with storm threshold (3.25 m); B) mean period (T); C) measured tide heights; D) tidal residual over the study period 21/07/2016 - 09/08/2017.

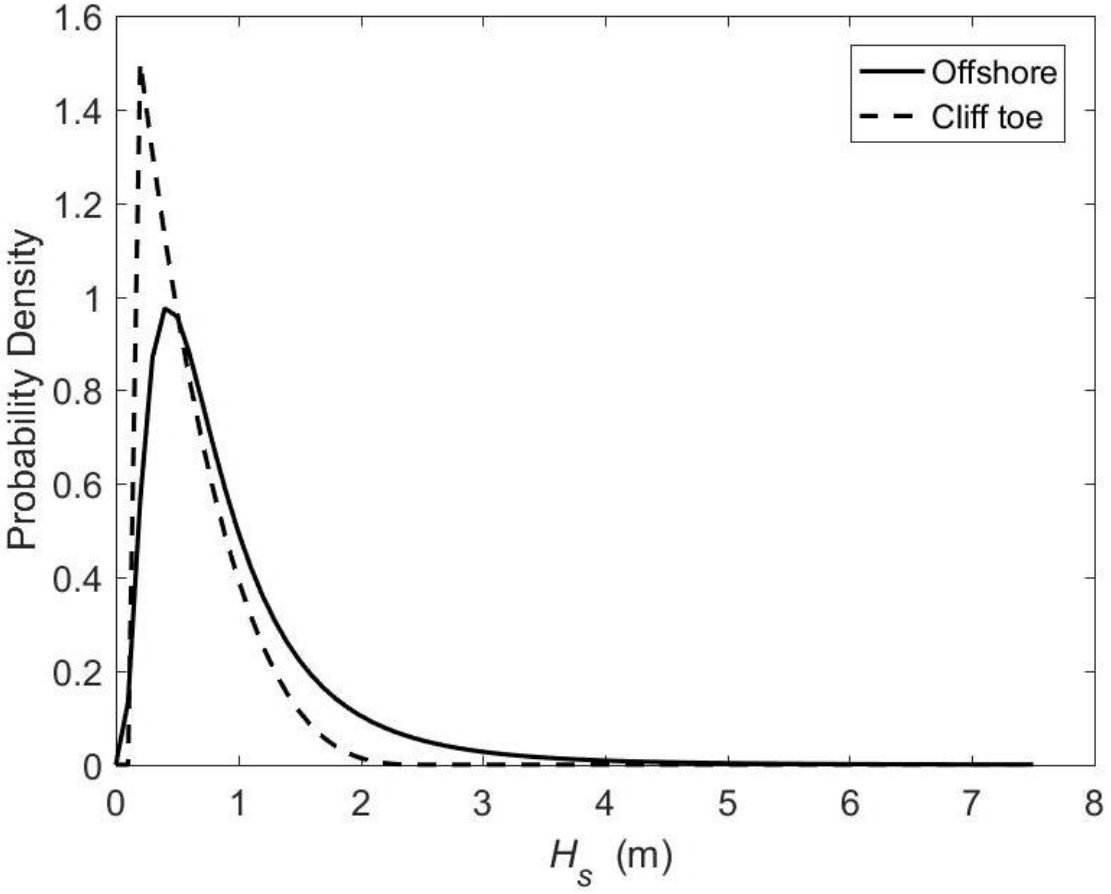

Figure 5.5: Probability density functions for the significant wave heights (H_s) recorded offshore by the wave buoy (solid line) and at the cliff toe (dashed line) over the study period. Offshore H_s values were lognormally distributed (*mean* = 0.73, *standard deviation* = -0.32) and cliff toe H_s values followed a generalised Pareto distribution (*shape* = -0.24, *scale* = 0.58, *threshold* = 0.10).

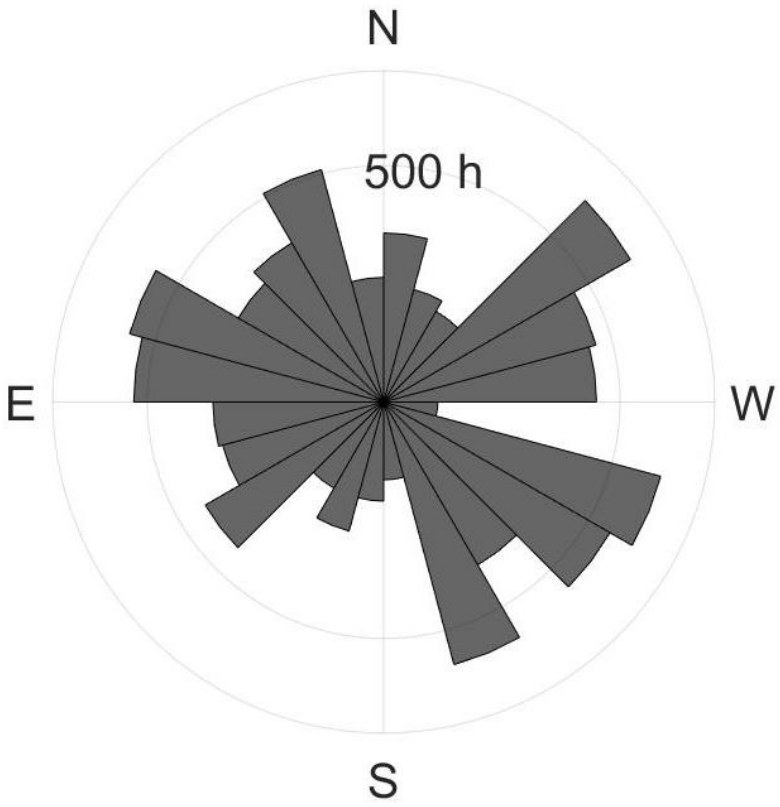

Figure 5.6: Rose plot of the frequency of wave direction by number of hours in the study period 21/07/2016 - 09/08/2017.

5.3.2. Cliff toe wave conditions

A time series of cliff toe wave conditions for each of the five sites and the wave buoy data is displayed in Figure 5.7. As all cliff toe monitoring sites were located above low tide elevations, gaps occur in the cliff toe datasets during low tide. Cliff toe H_s values exhibited a different distribution to those offshore, fitting a generalised Pareto distribution. This distribution type is characterised by a shorter tail and a more dominant positive skew than the lognormally distributed offshore H_s data (Figure 5.5). This demonstrates a smaller, narrower range of H_s values for the cliff toe compare with offshore (Table 5.1).

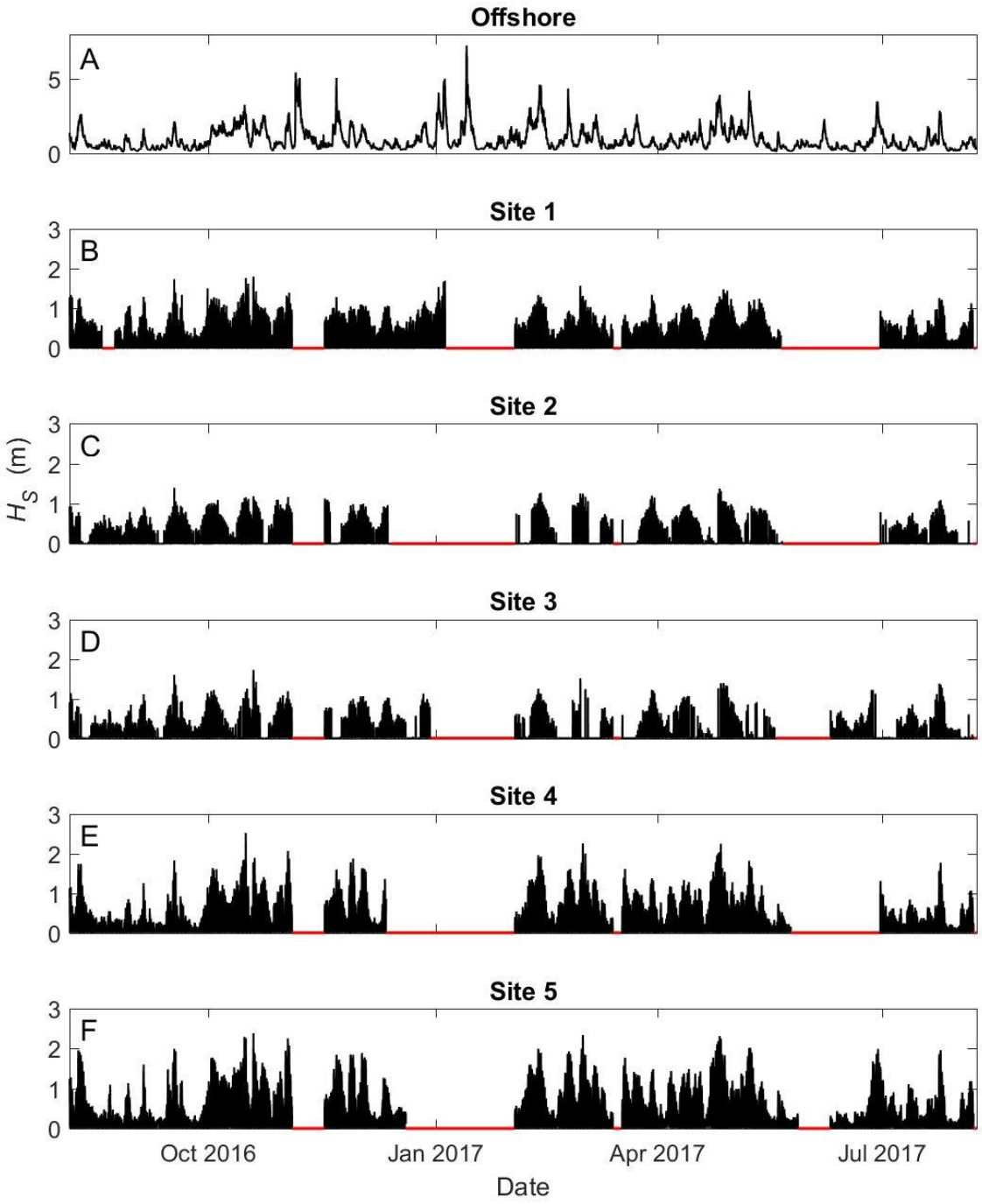

Figure 5.7: A) Offshore and cliff toe significant wave heights (H_s) for the wave buoy and B-F) all sites. Red lines indicate that no data were recorded. Values of 0 indicate that water were levels too low to reach the instrument. Note the period in January 2017 where no data were collected.

5.4. Analysis and discussion: Cliff toe wave characteristics

5.4.1. Relationship between offshore and cliff toe wave heights

To investigate the range of wave conditions at the cliff toe, I assessed the relationship between offshore and cliff toe wave conditions. In this section I describe the relationship between offshore and cliff toe wave height, and discuss how this varies between sites due to platform morphology.

5.4.1.1. Offshore and cliff toe wave height

Offshore waves are modified via wave transformation prior to arriving at the cliff toe. The extent to which offshore H_s determines cliff toe H_s is displayed in Figure 5.8. There is a positive correlation between offshore wave conditions and those at the cliff toe at all sites. The majority of the data points lie where $H_s > 1$ m, with point density decreasing over higher H_s as a result of the lower frequency of larger waves within the lognormal distribution. The data conform to a power law model of the form:

$$\text{Cliff } H_s = x(\text{Offshore } H_s)^{\kappa} \quad (5\text{-}8)$$

where x and κ are the constant and power exponent, respectively. This power law is significant ($p < 0.001$) for each individual site (Figure 5.8A-E) and the combined data (Figure 5.8F). Values for x and κ for each site and for the combined sites are provided in Table 5.2.

The power model provides a superior coefficient of determination when compared with a linear model (power fit $r^2 = 0.47$, linear fit $r^2 = 0.44$ for the combined data) and reduced root mean square error (power fit RMSE = 0.22, linear fit RMSE = 0.28 for the combined data). Other non-linear fits (polynomial, exponential and logarithmic) were also found to be statistically inferior to the power fit. In addition, a power model for wave transformation makes physical sense; with a linear fit, the model intercepts the y-axis above the origin, implying that when offshore $H_s = 0$, cliff toe $H_s > 0$, which is highly unlikely as the majority of measured waves are generated offshore (Holthuijsen, 2009). The power

model intercepts the graphical origin, such that when offshore H_s = 0, cliff toe H_s = 0.

A power law model suggests that increasing offshore H_s values produce progressively smaller increases in cliff toe H_s. Extrapolating this trend to very large (H_s = 6 m) offshore waves indicates very small (0.2 m) cliff toe increase as a result of a large (1.0 m) offshore increase. This suggests that wave heights at the cliff toe are depth-limited and conform to a measurable *H/d* limit.

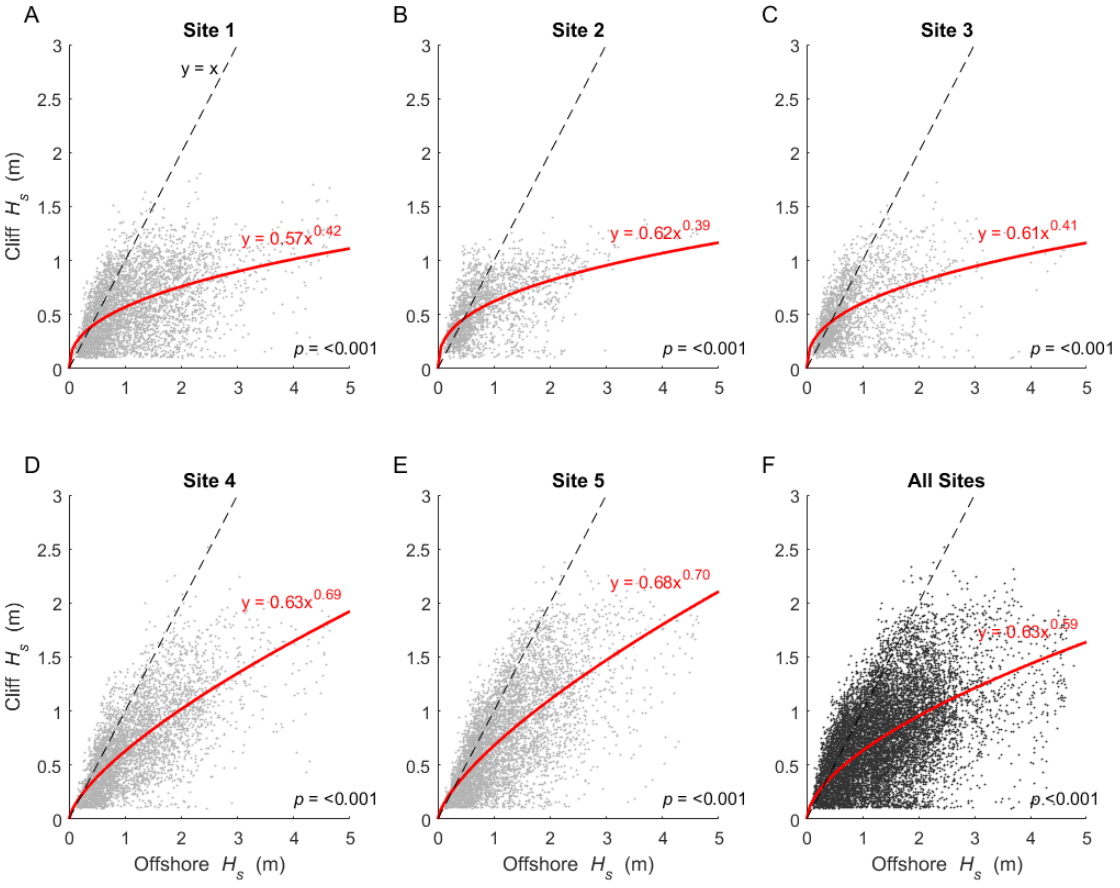

Figure 5.8: Relationship between offshore and cliff toe significant wave height (H_s) with fitted power laws for A-E) each site and F) all sites combined. Data points which lie above the black dotted line of equality ($y=x$) represent amplified waves where cliff toe H_s > offshore H_s.

Table 5.2: Cliff toe elevation (E_{toe}) and platform width (w) for each site, alongside power law constant (x) and exponent (κ) for the relationship between wave buoy H_s and cliff toe H_s in Figure 5.8.

	E_{toe} (mODN)	w (m)	x	κ
Site 1	0.86	120	0.57	0.42
Site 2	1.45	135	0.62	0.39
Site 3	1.41	166	0.61	0.41
Site 4	0.15	40	0.63	0.69
Site 5	-0.3	36	0.68	0.70
All	N/A	N/A	0.63	0.59

Whilst the power law model describes an overall decay in H_s during wave transformation across the platform, a proportion of waves at the cliff toe are greater than those offshore, displayed as those above the line of equality ($y=x$) in Figure 5.8. In the combined dataset (Figure 5.8F), 18% of all cliff toe H_s values were amplified relative to offshore H_s. Smaller waves were more likely to be amplified: 26% of all offshore H_s < 1 m were amplified at the cliff toe, compared with only 2% of H_s > 1 m. This trend is evident in the model results, which for sites 1-3 indicates that the majority (70%) of offshore H_s < 0.4 m are amplified at the cliff toe (data points above line of equality in Figure 5.8A-C).

5.4.1.2. Wave transformation and platform morphology

There is some variation in the power model coefficients x and κ between sites, which are shown in Table 5.2. In this section I attempt to explain this using the variation in platform morphology between sites.

Some of the difference in predictive capacity of the power law is due to the varying water depths produced by tidal fluctuations; higher r^2 values can be achieved using just high tide values (high tide r^2 = 0.60 compared with r^2 = 0.47 for all data points). Comparing the coefficients between sites reveals a discernible difference in both the extent of scatter and the shape of the trend,

likely resulting from their relative positions across the platform. Both κ and x are therefore indicative of wave transformation as they are a measure of the deviation from the line of equality, where no change in wave height occurred. Wave height at the cliff toe is ultimately the key variable in dictating energy transfer to the cliff (Vann Jones *et al.*, 2015). As wave shoaling, wave breaking and surf zone migration of incident waves are continuously altered by water depth (Trenhaile and Layzell, 1981), this model explores whether the resultant cliff toe wave conditions can be explained using a simplified relationship.

To investigate this further, I quantified platform morphology using the four key variables outlined by Poate *et al.* (2016) and Trenhaile and Layzell (1981): platform width (*w)*, toe elevation (E_{toe}), slope (S_p) and roughness (R). Data collection and processing of these data is described in Section 3.7; a summary of the site geometry is displayed in Table 3.2. Site geometries were then compared with the wave data in Figure 5.8 by considering the coefficient of determination (r^2) and the exponent κ, which describe the ability of the model to account for the data variance, and the curvature of the fit respectively (Figure 5.9). Of these, no significant correlation was obtained between S_p and R (in agreement with Poate *et al.*, (2018)); this may reflect the very small range in these variables and may be better observed between different platforms. Both E_{toe} (Figure 5.9A) and w (Figure 5.9B) exhibited significant ($p < 0.05$) negative linear correlation between both model variables. Despite the small sample size ($n = 5$), this gives an indication of the role of local platform morphology in cliff toe wave heights.

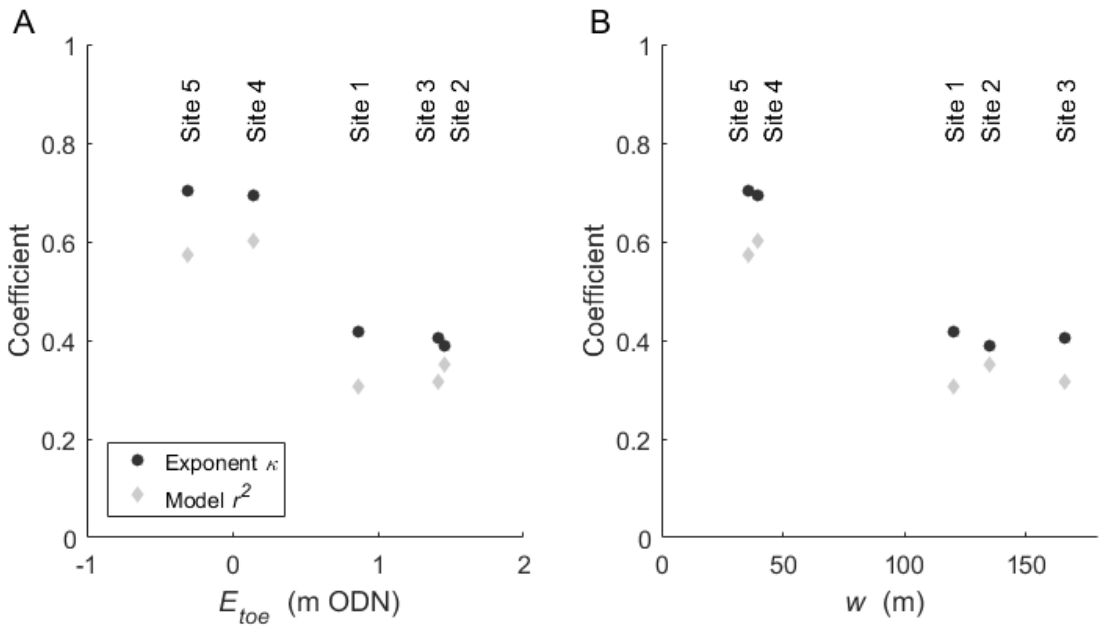

Figure 5.9: Power model exponent (κ) (black) and coefficient (r^2) (grey) from Figure 5.8 compared with A) cliff toe elevation (E_{toe}) and B) platform width (w).

A negative trend in r^2 suggests that the model variance increases with higher E_{toe} and w, reflecting an increase in the influence of platform morphology over cliff toe H_s, and a decrease in dependence on offshore H_s. Decreasing κ indicates that the rate of wave height decay increases with wider and higher platforms. Lower, shorter platforms are also less likely to exhibit amplified H_s values, although the amplification that does take place can be on larger waves. This can be seen on Figure 5.8 at sites 4 and 5, where fewer waves are amplified those that are tend to be larger, as shown by the power fit. Figure 5.10 shows a schematic of the changes in the power law due to E_{toe}. Here, wave amplification affects larger waves with increasing E_{toe} but magnitude of increase is smaller.

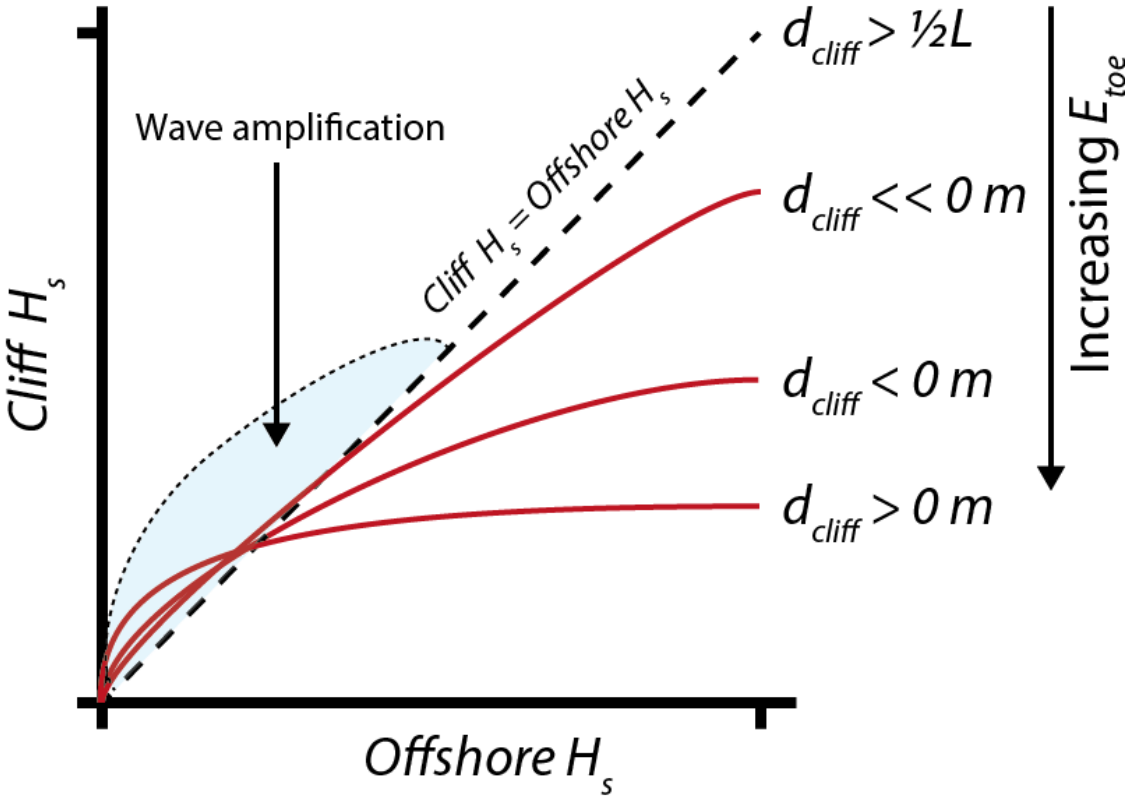

Figure 5.10: Hypothesised changes in power law model from Figure 5.8 with cliff toe elevation (E_{toe}). Relationship becomes increasingly linear with decreasing water depth (d_{cliff}), which is controlled by E_{toe}.

Using a linear trend for the pattern seen in Figure 5.9 is too simplistic to explain the behaviour observed beyond a negative correlation, and does not make physical sense. A curve which explains the trend in κ and r^2 must consider that the model will break down (r^2 = 0) when E = 3.15 m, approximately the upper limit of the HAT. The relationship will reach parity (r^2 = 1, x = 1, κ = 1) when d > ½L such that $H_{cliff} = H_0$, where bottom friction becomes negligible (Holthuijsen, 2009). As such, decreasing E_{toe} and w lead to lower model variance and higher linearity as waves become less depth-limited and more controlled directly by offshore wave heights, with less influence from tidal fluctuations.

Wave transformation across the platform can be described by the parabolic curvature of the theoretical model in Figure 5.11. Additional data points from other regions of the platform would be required to fully populate the model beyond the values for E_{toe} and w seen in this study. The section of the curves

observed by the Staithes data is shown. Scatter of the data points in Figure 5.11 would most likely be a result of other morphological variations in the platform such as S_p and w. Further complexity may be introduced via wave reflection off the cliff face, generating constructive and destructive interference (Walkden and Hall, 2011), but this is yet to be quantified (Beetham and Kench, 2011).

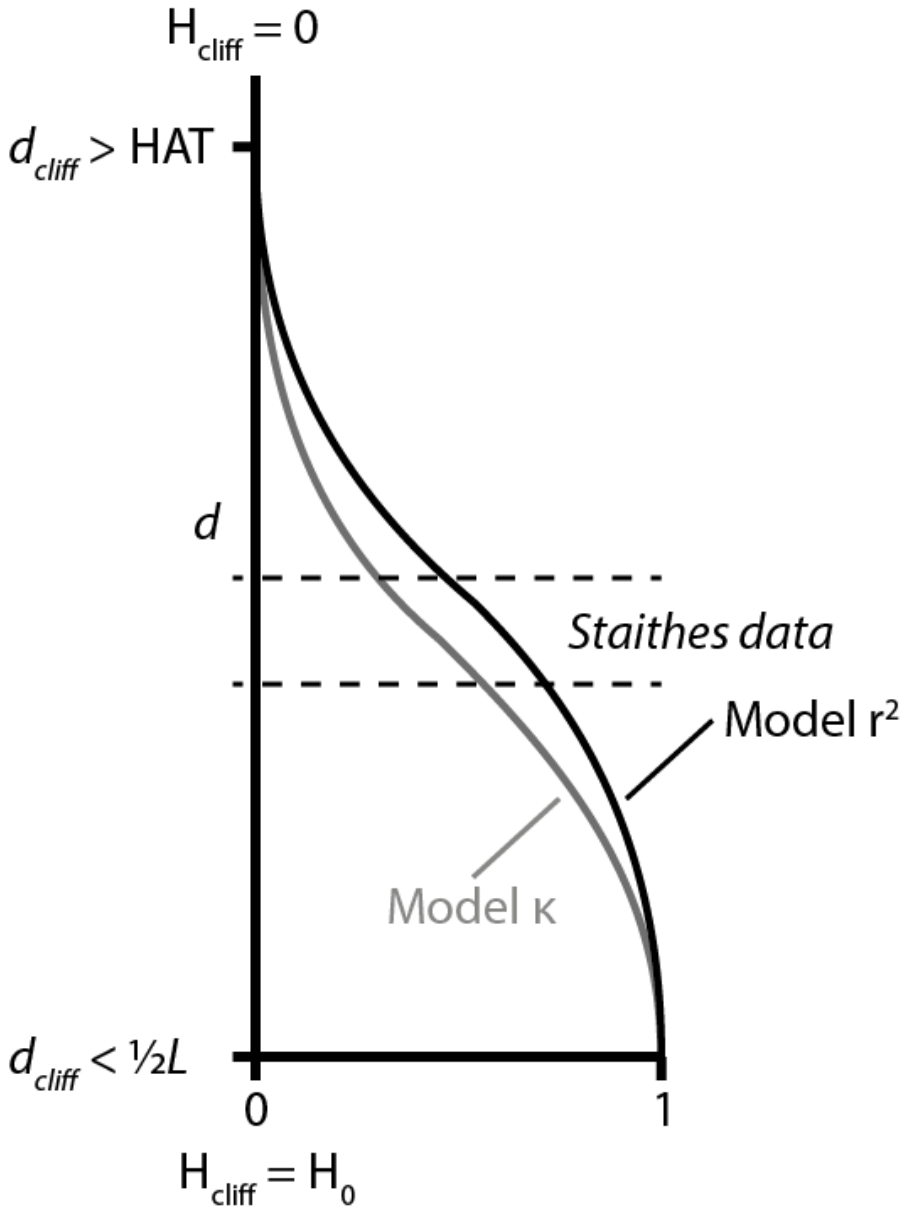

Figure 5.11: Theoretical fit and extrapolation of Figure 5.9. Increase in water depth (d_{cliff}), controlled by elevation (E_{toe}), leads to increasingly depth-limited waves. Deeper water causes cliff waves to become more similar to offshore waves, akin to plunging cliffs.

This power law behaviour is revealed only as a result of observing a wide range of H_s conditions: the increased curvature of the apparent linear relationship can be seen only under higher H_s conditions (Figure 5.8). The control of limited water depths also explains the lower standard deviation for cliff toe H_s than offshore H_s values (Table 5.1). For the less energetic conditions, my findings are in agreement with Stephenson *et al.* (2018), who found that waves on the outer platform, where elevation was lower, were less affected by depth due to shoaling than near the cliff toe. Similar observations from Poate *et al.* (2016) show a reduction in the variance of H_s closer to the cliff, as waves become depth-limited.

5.4.2. Wave energy

In this section I outline the patterns in wave energy density (ξ) conditions during the study period and describe and explain the differences in ξ between sites from the offshore to the cliff toe.

5.4.2.1. Patterns in wave energy

A selected 12-day time series of the variation in ξ between offshore ($\xi_{offshore}$) and cliff toe (ξ_{cliff}) energies is displayed in Figure 5.12. This date range was chosen due to the occurrence of a wide range of wave conditions within a short period. As wave energy is proportional to H^2 (Holthuijsen, 2009), the variation in ξ is considerably higher than the variation in H_s. Values for ξ during storms (offshore H_s = 5.0 m, $\xi_{offshore}$ = 250 kJ m^{-2}) are two orders of magnitude higher than when wave heights are lower (offshore H_s = 0.5 m, $\xi_{offshore}$ = 2.5 kJ m^{-2}). There is a clear reduction in ξ between the offshore measurements and cliff toe sites for the majority of the time series shown. Exceptions to this occurred on 29/04/17 and 07/05/17 (arrows on Figure 5.12), whereby ξ_{cliff} exceeded $\xi_{offshore}$ at site 5. Site elevation is inversely proportional to inundation duration, hence ξ = 0 for sites 2 and 3 when the tide levels are low.

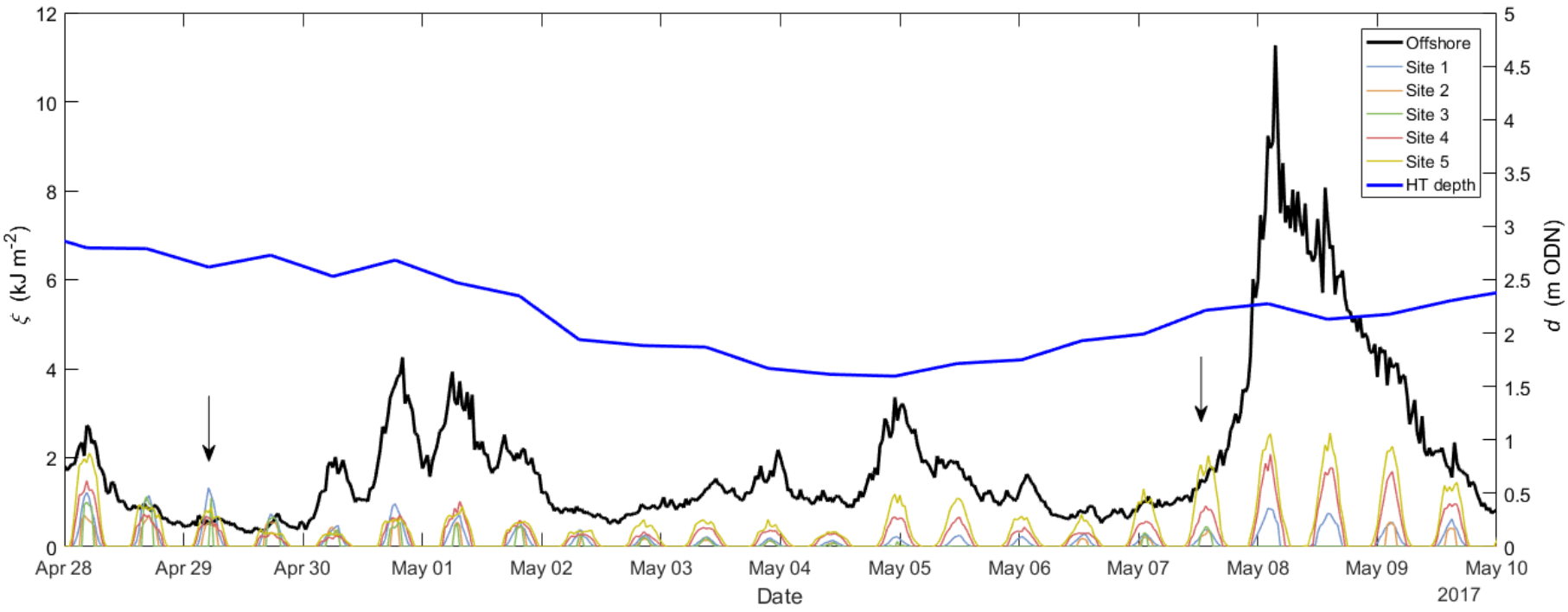

Figure 5.12: Selected wave energy density (ξ) time series between 28/04/2017 and 10/05/17 illustrating typical variation in site energy (ξ_{cliff}) compared with offshore energy ($\xi_{offshore}$) (black line). Blue line shows water depth (d_{cliff}) maxima at each high tide relative to ODN: neap tide occurred on 05/05/17. The maximum value of $\xi_{offshore}$ on 08/05/17 corresponded to H_s = 4.2 m; minimum on 29/04/17 was H_s = 0.7 m. Arrows show when $\xi_{cliff} > \xi_{offshore}$.

5.4.2.2. Wave energy transfer to the cliff toe

Over the full study period, values of $\xi_{difference}$ (Equation 5-1) fit an exponential distribution, described by:

$$P(\xi_{difference}) = \lambda\, e^{-\lambda\, \xi_{difference}} \quad (5\text{-}9)$$

The rate parameter (λ) describes the curvature of the distribution. A higher value of λ shows a smaller number of values where $\xi_{difference}$ > 100. These data range from $\xi_{difference}$ < 1%, indicating negligible energy density is observed at the cliff toe relative to offshore conditions, to $\xi_{difference}$ > 500%, indicating considerably greater energy density is observed at the cliff toe than is observed offshore. Different values of λ occur between sites (Figure 5.13A-E). Sites 1, 4 and 5 exhibit larger values of λ that can be seen in the increased gradient of the semi-log exponential PDF (Figure 5.13F), denoting an increased contribution of smaller $\xi_{difference}$ values.

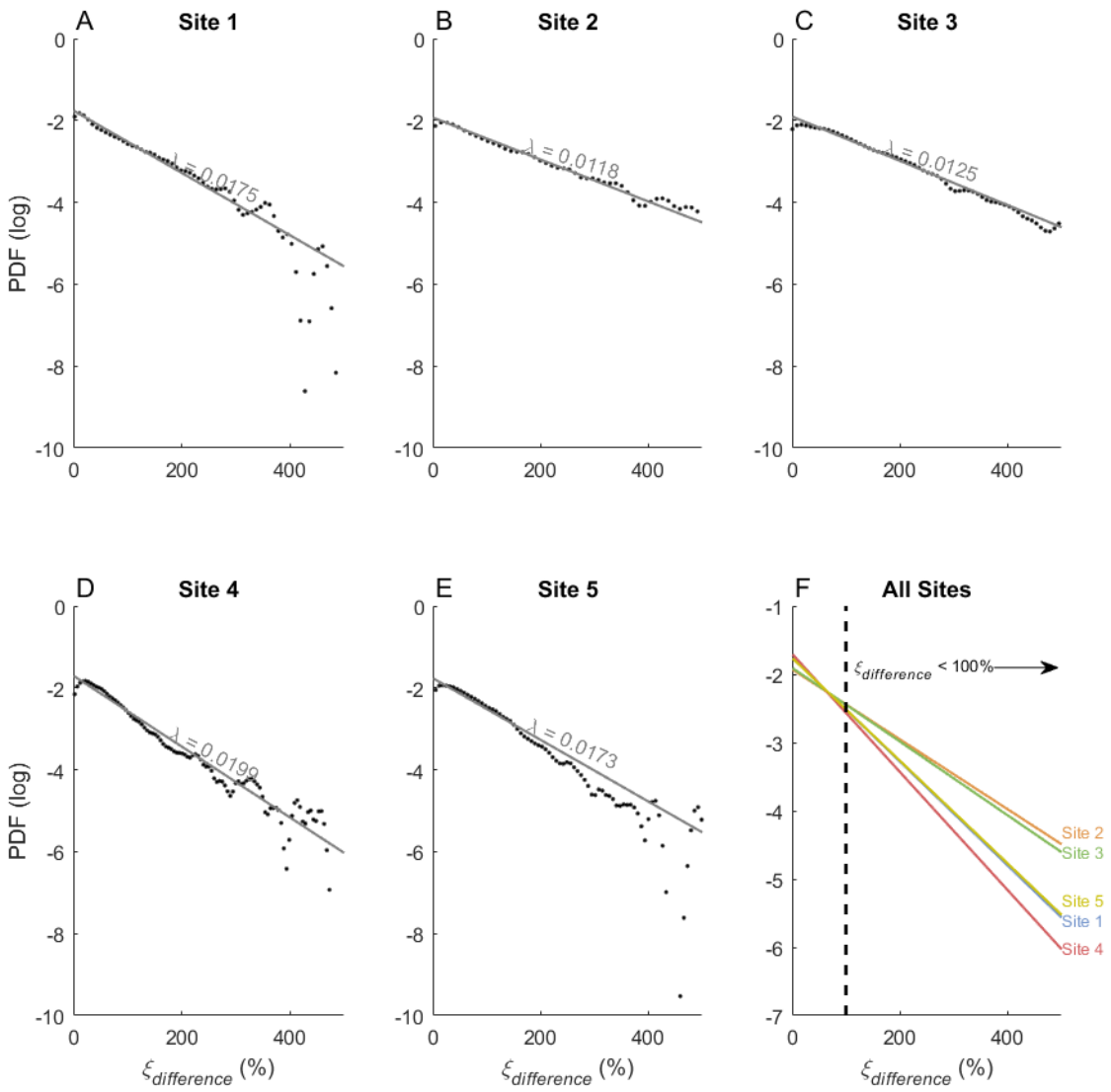

Figure 5.13: A-E) Fitted probability density functions ($p > 0.001$) for $\xi_{difference}$ for all sites plotted on semi-log axes, alongside the fitted exponential distribution and the associated rate parameter (λ); F) Each site plotted together to highlight the variation in the λ value. Values above $\xi_{difference}$ = 100% are those where $\xi_{cliff} > \xi_{offshore}$.

5.4.2.3. Wave energy amplification

In the following analysis I consider what determines the occurrence and degree of both wave energy reduction and amplification of waves at the cliff toe relative to the offshore conditions.

The data in Figure 5.8 and Figure 5.13 indicate that some values of cliff toe H_s and ξ_{cliff} are larger than those offshore. This is a result of waves reaching the

cliff during the shoaling process but prior to breaking (Beetham and Kench, 2011). Waves that are smaller at the cliff toe than offshore are indicative of waves that have broken prior to reaching this cliff toe. In this situation, the break point is seaward of the cliff toe and wave height attenuation has occurred. In this scenario, the foreshore bathymetry acts dissipatively, leading to wave height reduction and energy density loss (Kline *et al.*, 2014). Stephenson *et al.* (2018) observed a large amplification of cliff toe wave energy density over a 96-hour study at a macrotidal site in South Wales under moderate wave conditions (H_s = 1.00 - 1.43 m). This was due to the large tidal range (11 m), low cliff toe elevation relative to the tidal range and the resulting high tide water depths across the foreshore and at the cliff toe (1.4 m). The difference between deep water and cliff toe wave energy density $\xi_{difference}$ was in excess of 300 %. This is contrary to the cliff toe wave conditions observed on microtidal, horizontal shore platforms (Stephenson and Thornton, 2005; Ogawa *et al.*, 2012), where waves break at the platform edge and continually dissipate energy as they propagate shorewards up to the cliff toe. Waves may also reform multiple times during propagation (Collins and Sitar, 2008) but this was not considered in my investigation, which is a simplification previously used in other studies of these phenomena (Beetham and Kench, 2011; Ogawa *et al.*, 2011; Stephenson *et al.*, 2018).

The data presented in this chapter demonstrate that the shore platform at Staithes can act both to amplify and dissipate wave energy density depending on incident wave height, water depth, and platform morphology, as summarised in Figure 5.10. The total $\xi_{difference}$ (ξ_{total}) describes the total offshore energy transferred to the cliff toe as a percentage of offshore energy over the full study period during conditions where the cliff toe is inundated. The variation in ξ_{total} with platform morphology can be seen in Figure 5.14. Values for ξ_{total} are seen to increase with lower cliff toe elevations (Figure 5.14A) and shorter platforms (Figure 5.14B). The widest platform (w = 166 m) dissipates the most energy overall (ξ_{total} = 3%), compared with the shortest platform (w = 36 m, ξ_{total} = 23%). The importance of tidal water depth fluctuation is also demonstrated: ξ_{total} is consistently higher at high tide (64% at high tide, 23% overall for the shortest platform). Waves propagating across platforms are more likely to dissipate

energy when shallow depths and wide platforms force breaking, leading to wider surf zones prior to reaching the cliff toe (Marshall and Stephenson, 2011; Poate *et al.*, 2016).

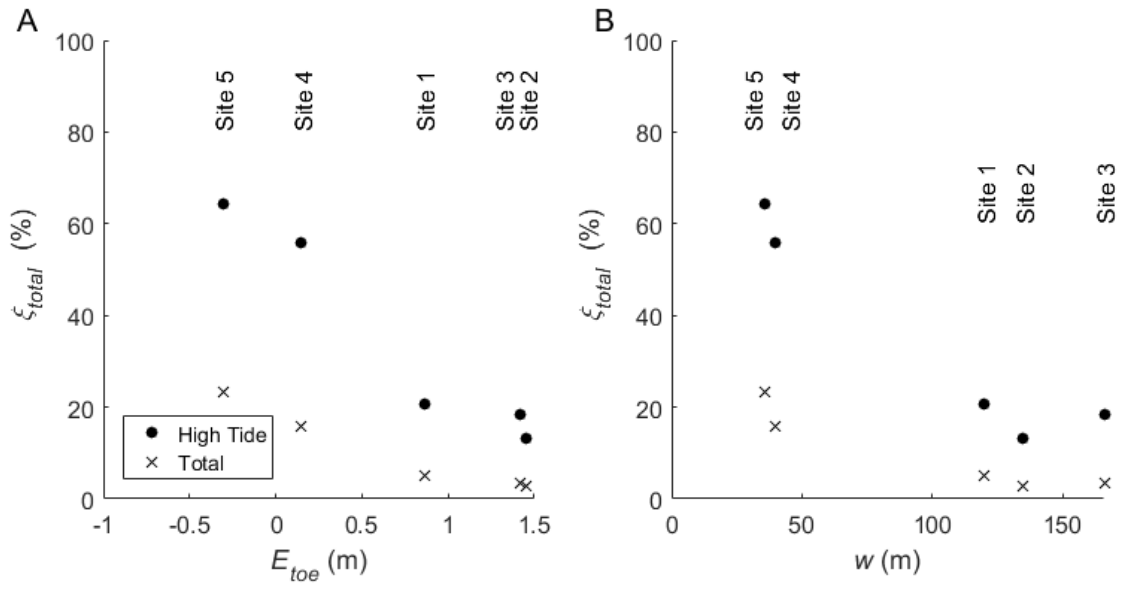

Figure 5.14: Variation in total offshore energy transferred to the cliff toe (ξ_{total}) by A) elevation (E_{toe}) and B) platform width (w).

The exponential distribution of $\xi_{difference}$ demonstrated in Figure 5.13 shows that although cliff toe $\xi_{density}$ can exceed that of offshore $\xi_{density}$, the majority of the time wave transformation produces smaller energy densities at the cliff toe. During the study period, conditions where $\xi_{difference} > 100\%$ and where $d_{cliff} > 0$ occurred during 18% of measurements. Furthermore, these amplified wave energy conditions are considerably more likely to occur during relatively quiet wave energy conditions. This is illustrated in Figure 5.15; the probability of $\xi_{difference} > 100\%$ occurring is higher with smaller offshore wave heights and zero where $H_s > 2.6$ m. As such, the wave transformation process at the field site is substantially more likely to amplify wave energy density during low energy conditions and attenuate energy density during high energy storm conditions. This does not, however, indicate that considerable wave energy cannot reach the cliff toe in storm conditions, as has been shown at other macrotidal shore platforms (Earlie *et al.*, 2015).

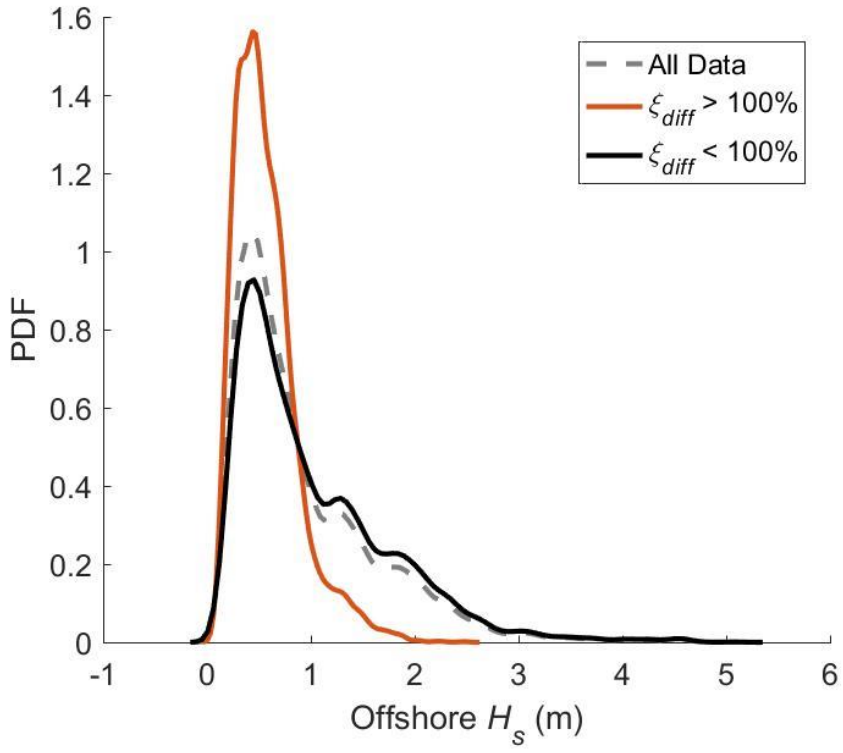

Figure 5.15: Probability density function of overall offshore H_s (dashed line); where cliff toe energy density exceeds offshore energy density (orange); where cliff toe energy density is lower than offshore energy density (black).

Stephenson *et al.* (2018) measured values of $\xi_{difference}$ during incident wave conditions of H_s = 1.00 - 1.43 m on a macrotidal platform. My results tentatively imply that the wave conditions under which this would occur would be exceedingly rare. However, it is more likely that differences in platform morphology and water depths will alter the distributions of $\xi_{difference}$. In Stephenson *et al.*'s (2018) study, cliff toe water depths exceeded 8 m, allowing larger waves to shoal up to the cliff toe without breaking. This is associated with an increase in the elevation of the HAT in the power law parameter model (Figure 5.11), allowing larger waves to propagate further across the shore platform. Therefore, the contribution of conditions where $\xi_{difference}$ > 100% will increase; the λ value for the exponential distribution of $\xi_{difference}$ in that site (Figure 5.13) will be correspondingly smaller. This is supported by the variation in offshore and cliff toe H_s due to cliff toe elevation seen in Figure 5.8 and Figure 5.10. Sites with lower cliff toe elevations, and therefore larger water depths (such as those of Stephenson *et al.* (2018) and Sites 4 and 5), exhibit a

greater number of larger amplified waves than sites with higher elevations. This supports the notion that shorter, lower platforms experience more intense wave conditions on average for any given offshore sea state.

With regard to wave transformation, this study demonstrates that wave dissipation on macrotidal shore platforms is considerably less than that observed in micro- and meso-tidal platforms. In macrotidal environments, smaller waves are more likely to propagate and reach the cliff prior to breaking, sometimes larger than their offshore height. Whilst larger waves undergo depth-controlled breaking and surf zone dissipation, greater water depths mean that cliff toe waves will be larger than experienced in microtidal environments.

5.4.3. Wave height and water depth

In this section I describe the wave height depth-limiting condition at the cliff toe, the variation in γ between each site, and discuss the estimated occurrence and type of breaking waves at the site.

5.4.3.1. Wave height depth limit

Cliff toe elevation and tidal elevation determine the water depth at the cliff toe (Trenhaile and Layzell, 1981). I assessed the degree to which wave heights become depth-limited at the cliff toe using measured still water depth (d_{cliff}) and cliff toe wave height (H) (Figure 5.16). For comparative purposes with other studies, H_{RMS} was used. There is a positive relationship between d_{cliff} and H_{RMS} with considerable scatter, whereby smaller waves occur across the full range of water depths observed. Maximum values for cliff H_{RMS} are depth-limited. Following Farrell *et al.* (2009), the envelope representing the dependence of H_{RMS} values on d_{cliff} is shown in Figure 5.16 from a modified version of Equation 5-2 in the form:

$$H_{RMS} = \gamma d_{cliff} + c \qquad (5\text{-}10)$$

in which a graphical intercept value (c) has been added. Empirically-derived values for γ from microtidal (γ = 0.28 (Ogawa *et al.*, 2011)), and mesotidal (γ = 0.42 + c (Farrell *et al.*, 2009)) platforms, as well as plunging breakers and bores on beaches (γ = 0.84 (Masselink, 1993)). For my data, γ = 0.60 and c = 0.15

provided an adequate estimate of the depth-limiting condition. This was fitted by eye in order to provide a more realistic estimate.

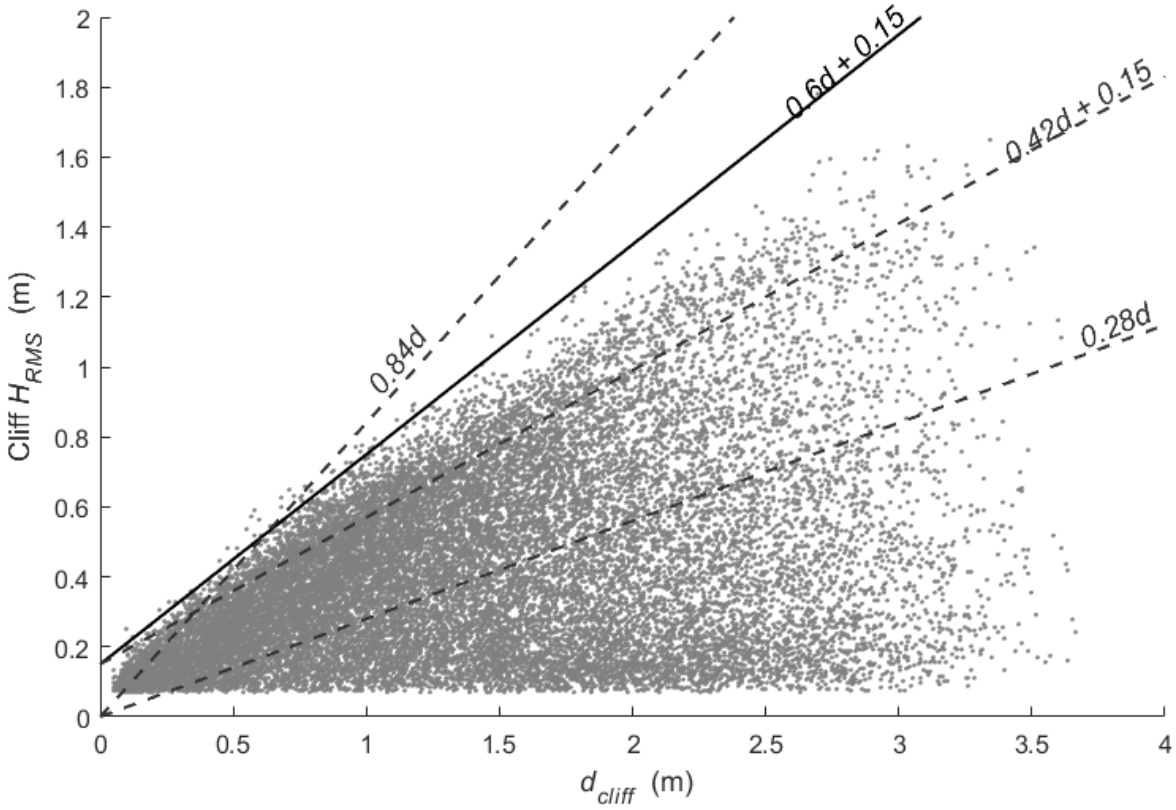

Figure 5.16: Relationship between cliff toe root-mean-square wave height (H_{RMS}) and cliff toe water depth (d_{cliff}) index for all sites considered in this study. Depth-limit envelope for these data where γ = 0.6, c = 0.15 (solid line) and previous studies (dotted line) are shown (see text for references).

Site-specific behaviour in the H_{RMS} and d_{cliff} relationship can be seen in Figure 5.17. Maximum values for d_{cliff} are controlled by cliff toe elevation between sites, whereby higher elevations reduce maximum water depth. For the depth-limiting condition, c appears to remain constant for all sites, but the data at sites 4 and 5 appear to deviate from the gradient γ, such that increase in cliff H_{RMS} with depth reduces (Figure 5.17D-E). The values for offshore H_{RMS} in Figure 5.17 illustrate that, as evident in Figure 5.8, larger cliff H_{RMS} values are associated with higher offshore H_{RMS}, but that this also depends on the value of d_{cliff}.

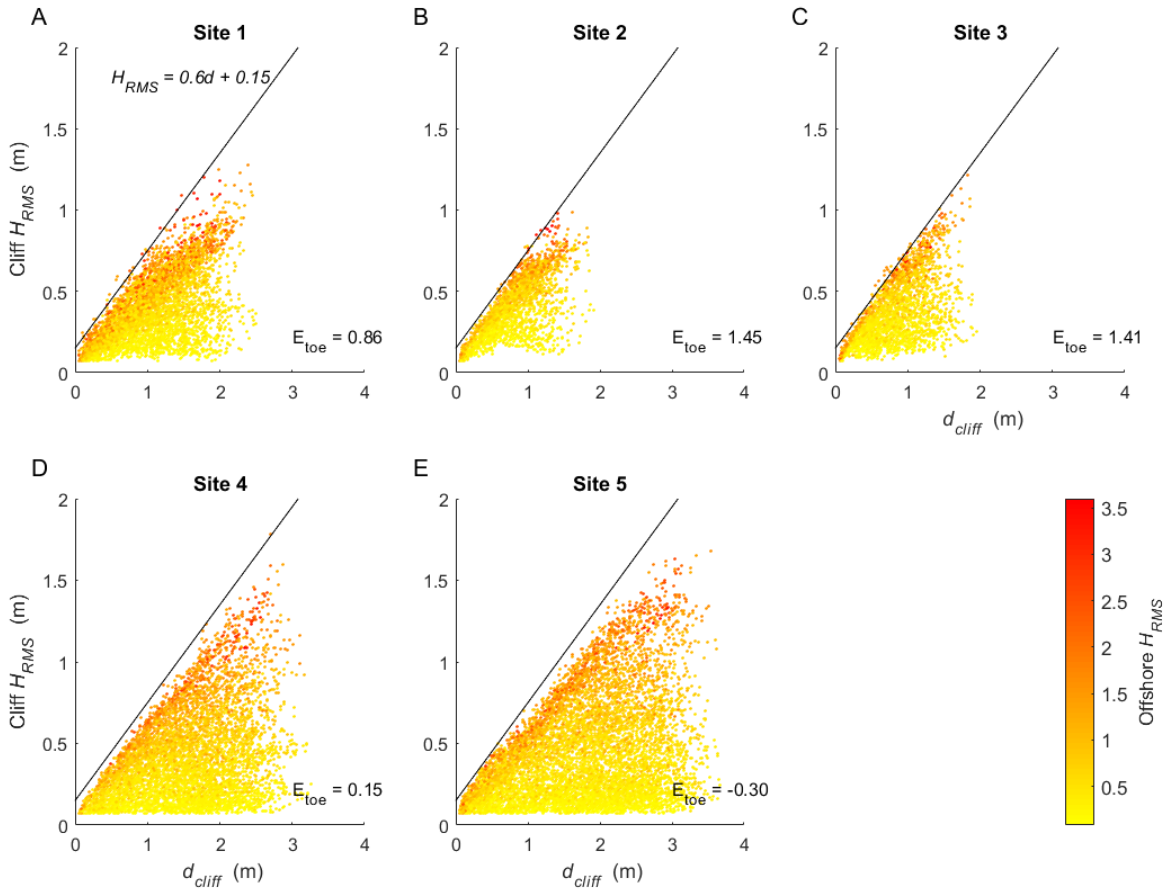

Figure 5.17: A-E) Relationship between cliff toe RMS wave height (H_{RMS}) and water depth (d_{cliff}) for each site, with cliff toe elevation (E_{toe}) also given. Solid line represents the depth-limit envelope for all sites. Colour scale represents offshore wave H_{RMS}.

5.4.3.2. Platform morphology and breaker type

In this section I explore the relationship between the wave height depth-limit constant (γ) and breaker type, and compare my data with other shore platform studies (Farrell *et al.*, 2009; Poate *et al.*, 2016).

The value of γ = 0.6 (Figure 5.16) is in line with previous studies on shore platform wave transformation. It matches that found by Poate *et al.* (2016) on a macrotidal platform and is within the range of Sallenger and Holman (1985) for beaches (0.24 < γ < 0.8). Like Farrell *et al.* (2009), these data required an intercept (c) to be applied as wave behaviour when H_{RMS} < 0.5 m appear above the line $H_{RMS} = \gamma d$. This may result from the influence of wave reflection from the cliff face (Poate *et al.*, 2016) generating wave heights in excess of the given depth limit via constructive interference of waves. The value of c for my data lies within the range observed by Farrell *et al.* (2009).

There are few studies which make observations of waves across a shore platform in conditions where H_s > 1.5 m. With a depth-limit value of γ = 0.6, larger waves are more likely to break before reaching the cliff toe. To explore how larger offshore waves behave at the cliff toe, Figure 5.18 shows the relationship between wave height and water depth at the cliff toe for increasing values of offshore wave height. The upper bounds of the data follow the depth limit (γ), and the spread of the data reduces such that the data converge on the depth limit as offshore H_s increases. This reflects the higher likelihood that waves will have broken for a given water depth and therefore be limited in height. Crucially, there is an upper limit to the cliff toe H_s at the highest tides (d_{cliff} = 3 m) based on γ whereby waves cannot exceed 2.7 m. This further explains the flattening with offshore H_s of the power model seen in Figure 5.8, where cliff toe waves cannot continually enlarge alongside offshore conditions. Figure 5.19 shows the distribution of cliff toe H_s values for the variable offshore H_s seen in Figure 5.18. The median cliff H_s does increase with larger offshore waves but the value maxima and range decrease; the highest H_s recorded at the cliff toe is 2.5 m, which is within the depth-limiting height.

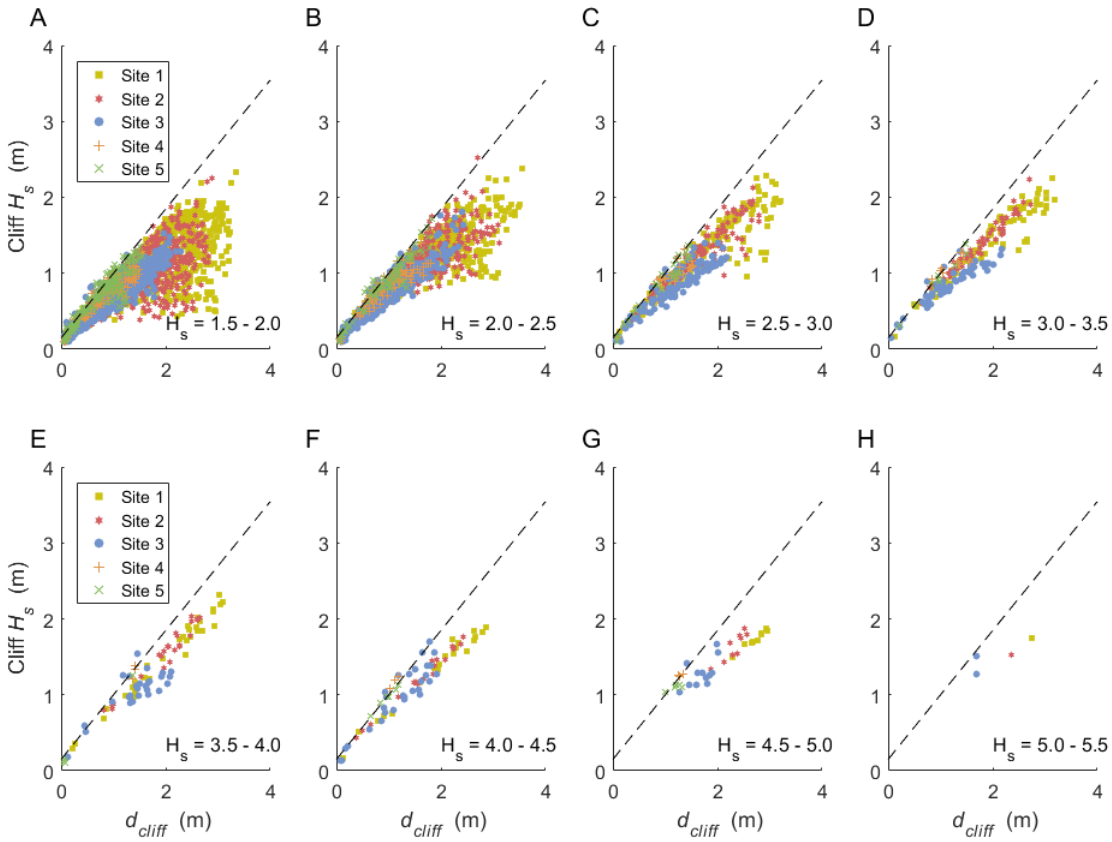

Figure 5.18: A-H) Relationship between cliff toe water depth (d_{cliff}) and cliff toe significant wave height (H_s) for different values of offshore H_s for each site. Dotted line represents the depth-limit envelope $\gamma = 0.6d+0.15$.

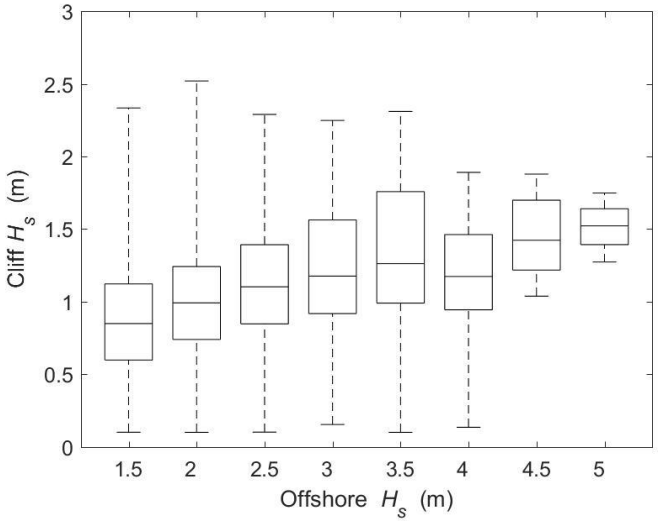

Figure 5.19: Distribution of cliff toe significant wave height (H_s) for the grouped offshore H_s data in Figure 5.18.

The highest cliff toe H_s values do not occur during the highest offshore conditions, in agreement with Trenhaile and Kanyaya, (2007). This demonstrates that very large waves (H_s > 4 m) must break offshore and attenuate energy before impacting the cliff face. Furthermore, the break point is more likely to be nearer the cliff toe during moderate wave conditions (H_s = 1.5 – 3.5 m), producing wave heights closer to their maximum value before and during breaking. This suggests that moderate offshore wave conditions are not only more common than very large waves, but also produce similar cliff toe wave heights.

5.4.3.3. Estimated cliff toe breaking conditions

Thus far in this study, I have shown that platform morphology and specifically cliff toe elevation, alongside incident wave conditions and tidally-controlled water depth govern cliff toe wave height after transformation across the platform. To estimate the breaking characteristics of the wave arriving at the cliff face throughout the study period, I calculated the location of the break point relative to the cliff line. By rearranging Equation 5-10 and employing the empirically-derived value of γ (Section 5.4.3.1), the breaking depth (d_b) relative to breaking wave height (H_b) (using H_{RMS}) is:

$$d_b = \frac{H_b}{0.6} - 0.15 \quad (5\text{-}11)$$

The following criteria from Tsujimoto (1987) were used to determine the breaking condition for any given value of cliff toe H_s:

- If $d_b > d_{cliff}$, the break point is seaward of the cliff, hence waves are broken
- If $d_b \approx d_{cliff}$, the wave is breaking at the cliff toe
- If $d_b < d_{cliff}$, the break point is landward of the cliff, hence waves are unbroken

Additionally, the Iribarren number (I) was used to constrain the breaker type. Using the equation for periodic waves propagating across a planar beach, I (Battjes, 1974) calculated from deep water wave parameters is defined using ramp slope angle (S_r) (defined in Section 3.7), H_b for random waves and wavelength (L):

$$I = \frac{\tan S_r}{\sqrt{H_b/L}} \quad (5\text{-}12)$$

Spilling breakers occur where Iribarren number $I < 0.5$, and plunging breakers where $I > 0.5$.

Figure 5.20 displays the results from this analysis for Site 1. Both plunging and spilling breakers were found, with spilling breakers much more frequent when the waves break seaward of the cliff. Larger cliff toe waves were also more likely to be broken on impact, and exhibit spilling breakers. Plunging breakers were much less likely to break before the cliff toe. As the elevation of the platform decreases away from the cliff, we can infer that surf zone width increases with $d_b - d_{cliff}$. This is due to the larger cliff H_s values here, as these represent large offshore waves breaking far from the cliff face and attenuating as they propagate shoreward. Conditions where the break point is approximately located at the cliff toe occur when $d_b \approx d_{cliff}$. As such, waves are likely to break directly on to the cliff face, although this was not confirmed with direct observations.

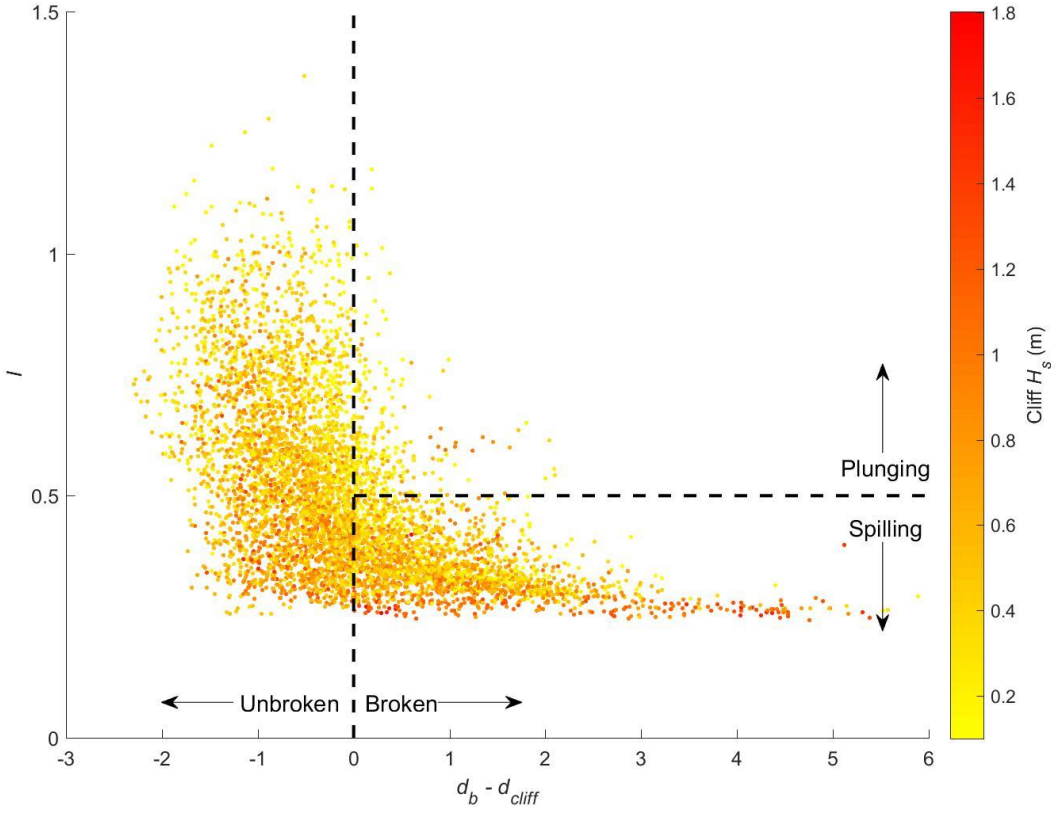

Figure 5.20: Wave breaking condition at Site 1 for all instances where $d_{cliff} > 0$. A positive value on the x-axis denotes a smaller cliff toe depth than breaking depth; hence waves will have broken seaward of this point. The colour scale displays cliff toe significant wave height (H_s). Both the Iribarren number (I) and d_b-d_{cliff} are unitless.

An estimate of cliff toe breaking could be taken as [$-0.1 > d_b \approx d_{cliff} > 0.1$], which would describe conditions under which breaking depth is approximately equal to the depth at the cliff toe, given the data precision of 0.1 m. Under this estimate, the proportion of waves which break directly at the cliff toe at Site 1 is approximately 1 in 10. In addition, I estimated the total number of waves reaching the cliff toe using T over each burst. A summary of wave conditions at all sites over the study period is shown in Figure 5.21. The total number of waves arriving at the cliff face varied considerably between sites, reflecting their respective cliff toe elevations and therefore the inundation duration. The proportion of broken waves at each site also varied. For example, Site 1 exhibited fewer waves overall than Sites 4 and 5, but the absolute number of

breaking waves was larger (385,000 for Site 1, 282,000 for Site 4). Sites 4 and 5 also exhibited proportionally more unbroken waves, likely as a result of their lower elevations, allowing a higher proportion of waves to reach the cliff prior to achieving breaking depth. The proportion of plunging and spilling breakers also varied substantially between sites. Sites 2 and 5 exhibited very few plunging breakers, probably as a result of their shallower ramp gradients. Consequently, Sites 3 and 4 had mostly plunging breakers.

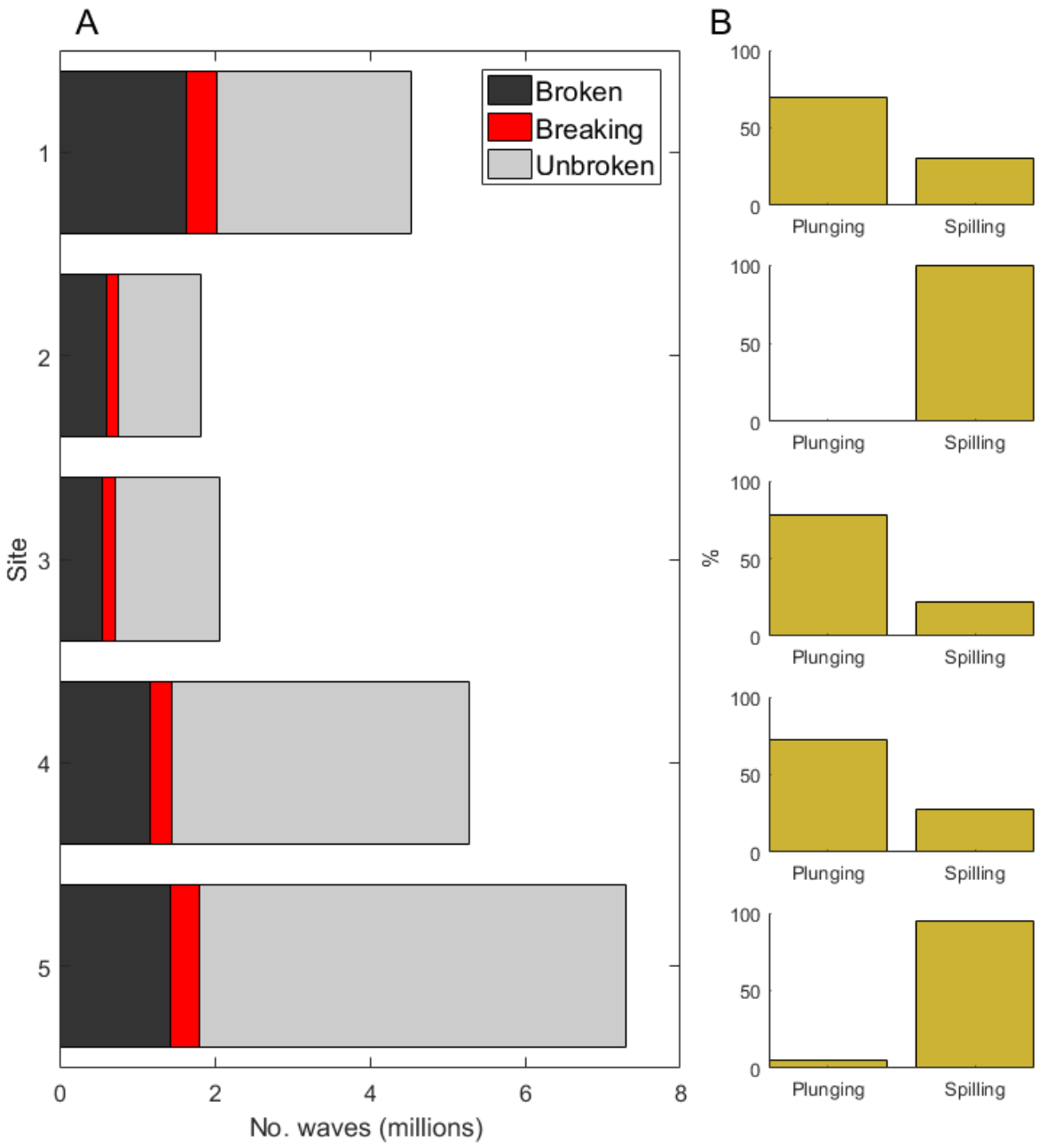

Figure 5.21: A) Number of waves impacting the cliff per site; B) their respective estimated breaking conditions over the 369-day study period.

5.5. Implications for wave forcing

In the following discussion I highlight the importance of platform morphology in dictating wave conditions and discuss the implications for the erosive potential of waves on macrotidal shore platforms and cliffs.

Wave energies on horizontal, microtidal platforms have been shown to attenuate considerably during transformation (Taylor, 2003; Ogawa *et al.*, 2012; Pappalardo *et al.*, 2017). On a shallow gradient (1°) platform investigated by Stephenson and Kirk (2000), only 0.015% of wave energy reached the cliff. In contrast, macrotidal platforms are considerably less dissipative, and therefore allow a greater proportion of wave energy to reach the cliff toe. My study has shown that 3 – 23% of offshore wave energy reached the cliff; at high tide, this range increased to 13 - 64%. This suggests that in a macrotidal environment, greater wave energy is available to drive cliff erosion. As such, my data support the findings of other direct measurements (Trenhaile and Kanyaya, 2007; Poate *et al.*, 2016) and modelling (Sunamura, 1992; Matsumoto *et al.*, 2016) of waves in macrotidal environments.

In line with the morphodynamic framework described by Stephenson and Thornton (2005), I observed elements of both reflective (plunging cliffs) and dissipative (horizontal platforms) cliff foreshores, though this was found to be in part a function of tidal water level. My data demonstrate that dissipative conditions occur where wave heights are large relative to the water depth and platforms wide and high relative to the tidal range, hence waves break far offshore and arrive as attenuated bores. In contrast, reflective conditions arise when smaller waves and deeper water allow waves to propagate across the entire platform width and arrive at the cliff toe equal in height or higher than the incident offshore waves.

Crucially, the macrotidal shore platform at Staithes frequently exhibit wave and depth conditions whereby waves break directly on to the cliff face. Commonly cited as the conditions under which most wave assailing force is applied to the cliff (Sunamura, 1977; Carter and Guy, 1988; Brossard and Duperret, 2004), breaking – and to some extent broken – waves have been shown to produce higher levels of wave energy transfer to cliffs (Young *et al.*, 2011). The higher propensity for breaking waves in my study than in both plunging cliffs – where waves are mostly unbroken – and horizontal platforms – where turbulent bores are most common – suggest a potentially larger role for wave-driven cliff erosion in macrotidal environments.

By monitoring across a relatively short (700 m) section of cliff toe, I have highlighted the extensive alongshore spatial variation in cliff toe wave conditions that exist between cliff sections. I have shown that cliff toe elevation, width and slope are key morphological factors in controlling wave energy delivery to the cliff toe. An increase in cliff toe elevation of 0.88 m between Sites 1 and 4 modified the wave transformation such that there were 14% fewer waves at the cliff toe overall during the study period at Site 1, yet a greater proportion of these waves broke directly at the toe. The apparent sensitivity of wave forcing to platform morphology is summarised in Figure 5.22, where different sections of the cliff toe receive differing breaker types and wave impact durations.

Furthermore, during storm conditions (offshore H_s > 3.25 m) cliff toe wave heights are 0.4 m lower on average at the lowest toe elevation (Site 5). In chapter 4, cliff toe elevation was found to vary by up to 2.5 m along a 700 m stretch of cliff toe. The slope of the cliff toe ramp, a key control of the Iribarren number and hence wave breaker type, also varied between 0.5-5°. As such, the wave forcing conditions are likely to vary substantially across this relatively short cliff section. A detailed knowledge of shore platform morphology is therefore required to obtain a greater understanding of cliff toe wave conditions. This underlines the importance of high-resolution profile morphological inputs in models such as those of Trenhaile (2000) and Matsumoto *et al.* (2016).

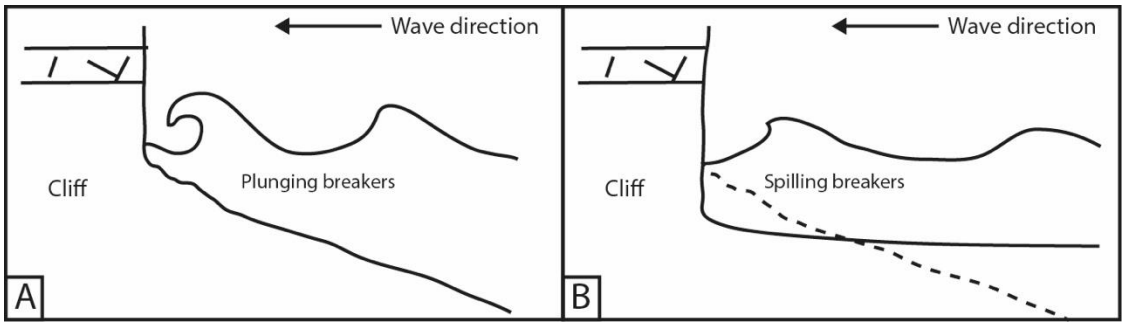

Figure 5.22: Schematic showing the variation in wave breaker type with platform morphology. A) Where cliff toe ramp angle is higher and cliff toe elevation is higher, waves are more likely to be plunging on impact with the cliff, but fewer waves will reach the toe due to inundation duration. B) In contrast, spilling breakers occur when the ramp angle is shallow, but more waves will reach the toe.

5.6. Conclusions: Cliff toe wave conditions

In this study I monitored offshore and cliff toe wave conditions at five sites across a ~700 m section of shore platform. A dataset was collected over 369 days, representing a wide range of marine conditions, although storms were approximately twice as common as the long-term average. The following conclusions were made:

- The long-term (~ 1 year) magnitude and frequency of waves at the cliff toe were observed, providing insight into a wider distribution of wave conditions than previous studies.
- The relationship between offshore and cliff toe wave heights was significant and positively correlated according to a power law. The variance and shape of the model was dependent on cliff toe elevation and width. These relationships became increasingly well-correlated when cliff toe elevation was lower and platform width was shorter. This reflects the increased mean water depth at the cliff toe, allowing waves to propagate shoreward with less influence from bed friction.
- Under low to moderate wave heights and water depths, some waves may have been amplified at the cliff toe due to shoaling pre-breaking. As such, wave energy density can be higher at the cliff toe than offshore. However, these conditions only occurred for 18% of the time the cliff toe was inundated, and exclusively to offshore waves below H_s = 2 m.
- Wave height was found to be limited to $H_{RMS} = 0.6d_{cliff} + 0.15$, which is inside the range of values found in similar environments elsewhere. Accordingly, the maximum significant wave height at the cliff toe is 2.7 m. This means that larger storm waves are attenuated and arrive at the cliff toe as turbulent bores, whereas in moderate conditions waves may be higher and breaking at the cliff. This implies that since storm waves have been shown to cause higher erosion rates, it may not simply be the increased wave heights that drive this.
- Cliff toe water depth, controlled by a combination of cliff toe elevation, tidal level and setup magnitude, is likely a key control on wave forcing. It strongly influences the number of waves reaching the cliff, the wave

height and wave breaking condition. As such, a highly variable cliff toe elevation creates a complex array of wave conditions across a relatively short alongshore section of cliff.

- Unlike horizontal platforms and plunging cliffs, the dynamic regime of macro-tidal sloping platforms may be either reflective or dissipative depending on the platform morphology and incident hydrodynamic conditions. Waves breaking at the cliff toe are much more common and may constitute up to 9% of all wave impacts, or 165,000 waves per year at this site. This may have profound implications for wave forcing of cliff erosion in this environment, and warrants further study.

6. Measuring wave impact pressures at the cliff toe

6.1. Introduction

In Chapter 5 I demonstrated that waves which break directly at the cliff toe are common in macrotidal environments. Breaking waves have been shown to produce high-magnitude impulsive, also known as shock or dynamic component, pressures on coastal structures (Rouville *et al.*, 1938; Blackmore and Hewson, 1984; Crawford, 1999; H Bredmose *et al.*, 2003). Such structures may be analogous to natural rock coast cliffs. A wide range of models have been derived from numerical, experimental and field-based measurements (Ross, 1954; Blackmore and Hewson, 1984; CERC, 1984; Oumeraci *et al.*, 2001; Larson *et al.*, 2004) and are used to predict wave forcing magnitude on coastal cliffs (Tsujimoto, 1987; Trenhaile, 2000; Walkden and Hall, 2005; Matsumoto *et al.*, 2016). However, the extent to which these models replicate conditions at natural cliff faces is unknown, as direct measurements are scarce (Section 2.3.1).

A number of studies at rock coasts have been undertaken using single-measurement dynamometers on the shore platform (Jones and Demetropoulos, 1968; Palumbi, 1984; Fuji, 1988; Helmuth and Denny, 2003), with higher pressures observed where waves broke directly on the instruments. However, these studies are spatially and temporally limited, comprising of little more than a single maximum pressure measurement at a point on the platform surface (Section 2.2.3.2). A deeper understanding of the timing, magnitude and spatial distribution of impact pressure requires comparable high temporal (<1 kHz) and spatial (cm-scale) resolution instrumentation to that used to assess impacts on coastal engineering structures.

In this chapter I describe the design of a novel method by which precise, high-resolution impact pressure data could be collected at the cliff toe in a macrotidal rock coast environment where unbroken, breaking and broken waves are known to occur. This method provides data regarding the occurrence, magnitude and spatial and temporal distribution of impact pressures.

6.2. Field measurements of wave impacts

6.2.1. Wave impact measuring equipment design

In Chapter 2 I showed that in order to measure wave impacts on a coastal structure, a vertical array of pressure sensors positioned at the base of the cliff would be the most appropriate method. However, the deployment of pressure sensors at coastal cliffs is scarce in the literature. As such, I investigated a number of array designs and sensors in order to determine the most robust method of measuring wave impact pressures on a shore platform. Pressure sensor arrays have previously been successfully deployed in flumes (Bullock *et al.*, 2007), beach surf zones (Miller *et al.*, 1974) and at engineered coastal structures (Blackmore and Hewson, 1984). In order to assess the wave breaking condition on impact, I experimented with measuring the wave shape on impact using camera imaging and laser scan profiles (Blenkinsopp *et al.*, 2010, 2012). However, these techniques proved difficult to deploy and process successfully.

A review of previous flume and field experiments measuring wave impact pressures indicated that the most suitable system for measuring static and dynamic fluid pressures were electrical resistance strain gauges (Blackmore and Hewson, 1984; Walkden *et al.*, 1995; Marzeddu *et al.*, 2013) due to their ability to record rapidly fluctuating pressure variations. Impulsive pressure rise times (t_{rise}) have previously been recorded at less than 1 ms (1000 Hz); sample rates in field experiments are typically chosen in the range of 500 – 20,000 Hz (Mogridge and Jamieson, 1980) to capture these. As such, I deemed a sample rate (φ) of 5000 Hz to be suitable: using the predictive rise time formula (further treatment of this is described in Section 6.4.1) of Cuomo *et al.* (2010), the smallest sample duration (1/5000 Hz = 0.2 ms) would give a pressure of 1160 kPa, which is larger than the maximum ever recorded field pressure (746 kPa). This sample rate was also used in field experiments by Bird *et al.* (1998).

For my study, I selected 16 IP67 Keller 25Y flush-diaphragm strain gauge absolute pressure sensors (Figure 6.1A). This would allow a 1.7 m vertical array with 0.1 m spacing to be deployed. This is double the sensor spacing used by Cuomo *et al.* (2010) for full-scale waves. These sensors have the advantage of

a very small temperature error, necessary for the rapid temperature fluctuations associated with wave impacts. They are also designed specifically for use in hazardous environments. A USB-AD16f data logger and 64-bit 1.2 GHz quad-core Fitlet PC were used to record the incoming voltages to an on-board 130 GB hard drive. A combined power consumption of 10.5 W meant a theoretical measurement time on a 21 Ah, 12V battery of 24 hours, or two complete tidal cycles. Data recording could be set up and finalised in the field via an external USB touchscreen.

I chose a pressure range of 0 – 500 ± 0.5 kPa to encompass the expected range of pressures (

Table 2.1). The signal output from the sensors was 4-20 mA, which minimised error due to external electrical interference. Process current was converted to a 1-5 V range using a 250 Ω resistor in line with the data logger (Figure 6.1B), which in turn translated to a value in a 0-500 kPa pressure range via a calibration chart supplied by the manufacturer.

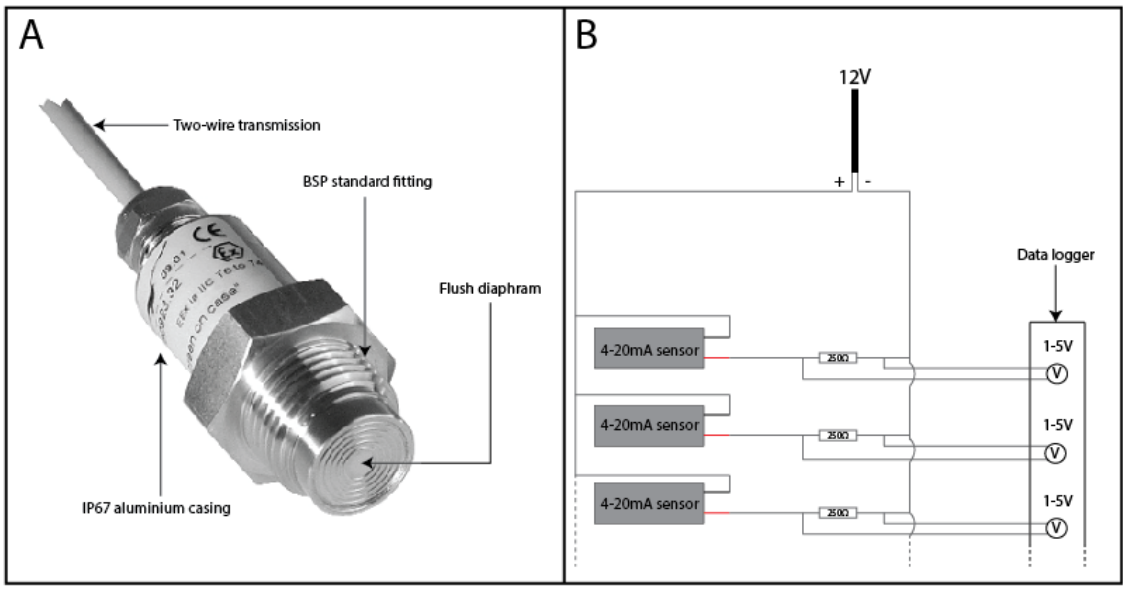

Figure 6.1: A) Keller 25Y pressure sensor; B) pressure sensor power supply and voltage measurement circuit diagram.

To quantify instrumental error, I tested the sensors in the lab prior to the field campaign. The sensor was set up using a constant 12 V, 100 mA supply and 250 Ω resistor. The resulting voltage-time signal was recorded by the data

logger at 5000 kHz. The resultant time series converted into pressure using the calibration chart from the manufacturer. Minor electrical noise was found on the signal; RMSE was calculated as 1.3 kPa, compared with a stated precision of 0.5 kPa.

6.2.2. Field set-up and sampling regime

The 16 pressure sensors and acquisition system were installed on a length of 2.0 x 0.3 x 0.3 m vertically-orientated aluminium truss anchored into the foreshore, with the pressure sensors mounted in 0.1 m vertical increments (Figure 6.2). The pressure sensors were placed within aluminium enclosures to protect from direct impacts and bolted on to the side of the frame facing seawards. The frame was anchored vertically to the foreshore and stabilised by 3-tonne-rated A4 steel chains. An aluminium pipe was fixed to the side of the frame and abutted against the cliff to improve stability. In this set-up the equipment could be deployed for two tidal cycles at a time due to battery capacity.

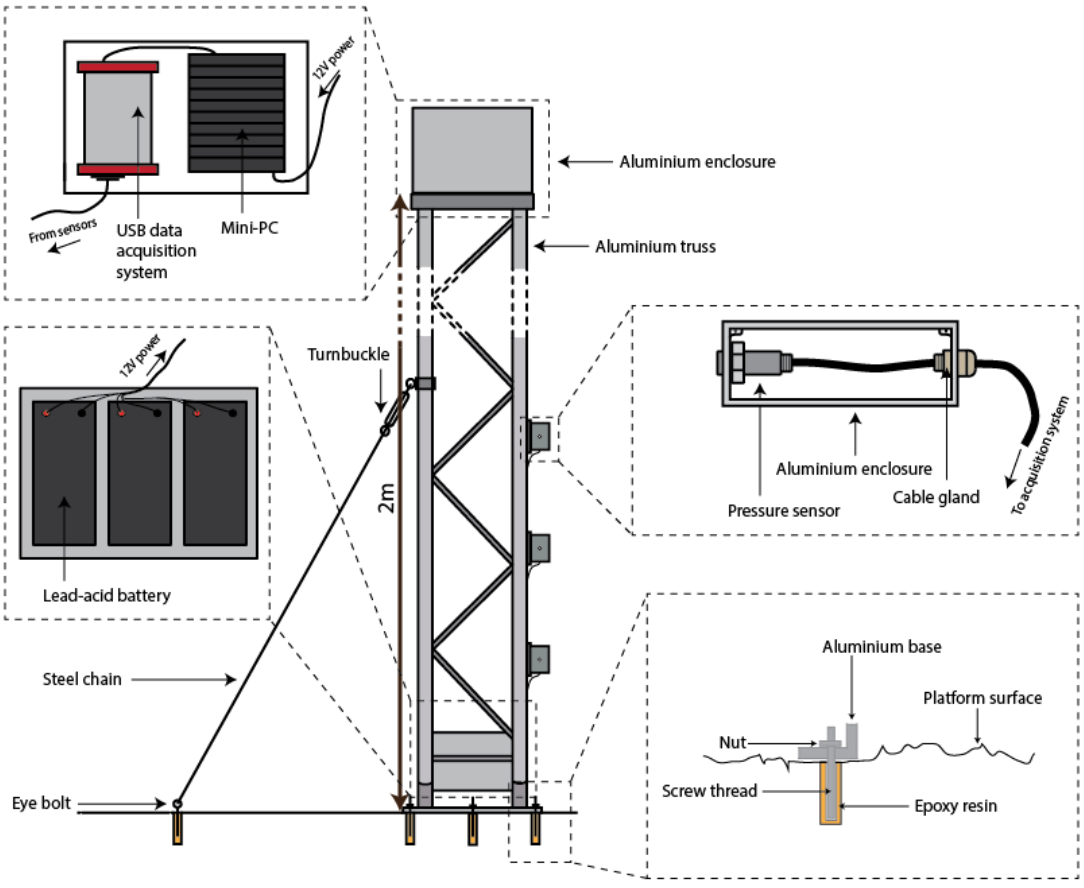

Figure 6.2: Field set-up schematic, with detail of upper and lower enclosures, pressure sensor housings and platform fixings.

The data acquisition system for the sensors, including the data logger and PC, was housed in an IP68 aluminium enclosure mounted on top of the frame. The sensors were connected to this enclosure by rugged waterproof cables running through IP68 plastic cable glands. These cables contain two internal wires, which were connected to a series of 250Ω resistors, 1A fuses, a 1.3 Ah battery and the data logger inputs via a printed circuit board. At the base of the frame was a sealed aluminium enclosure which housed three 7 Ah lead-acid batteries used to power the acquisition system. The truss and chains were anchored to the platform using 10 mm threaded rods and eye-bolts fixed with an epoxy resin (Figure 6.2 and Figure 6.3). The system was designed so that the frame, sensors, cabling and acquisition system could be transported separately. Each element was carried by fieldworkers to the study site at low tide and assembled in situ.

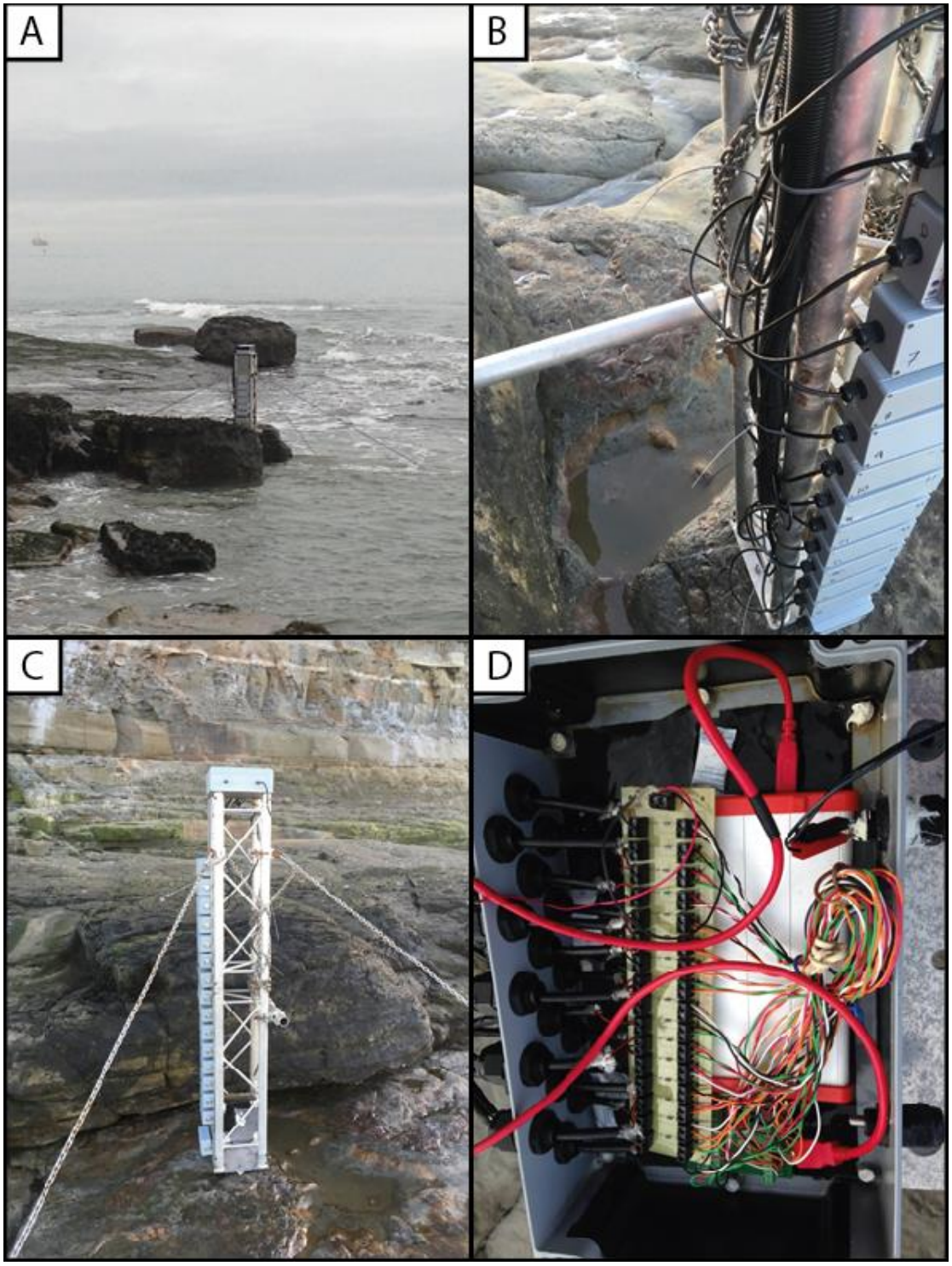

Figure 6.3: Pressure array deployed in the field A) during inundation, B) close-up of abutment tube, C) on platform in front of scarp and D) the datalogger within its housing.

6.2.3. Field data collection of direct wave impact pressures

The deployment regime over the study period was primarily dictated by the conditions at the field site, rather than a regular deployment programme. To enable a successful deployment during the period where the cliff toe was inundated, a number of prerequisite conditions had to be met. During neap tides, sites were rarely inundated sufficiently for any data to be collected from the sensors, the lowest of which was 0.1 m from the platform surface. Conversely, spring tides generally led to inundation and damage of the enclosure housing the acquisition PC. The equipment could only be deployed during daylight and batteries lasted a maximum of 24 hours. Additionally, dry and calm weather was required as well as low to moderate wave heights (wave heights above approximately 2 m tended to force water into the PC enclosure). These restrictions meant deployment could only be planned one or two days in advance after observing weather and wave forecasts, and observing tide conditions. However, sampling of a variety of wave and tide conditions was achieved.

The pressure acquisition set-up was deployed a total of 17 times. The first five deployments acted as trial runs for the acquisition system using only a small number of sensors and were used to test the equipment in the field: these were conducted between 09/02/2016 and 26/05/2016. The subsequent 9 deployments were conducted between 22/08/2016 and 13/12/2017.

More deployments were planned in order to capture a wider selection of wave conditions over the year alongside the erosion and wave monitoring, but problems with the equipment meant these had to be curtailed. These issues were mainly related to the difficulties of deploying off-the-shelf electronics in a physically and chemically destructive environment. Waterproofing the electronics proved to be most problematic. Additional issues were encountered regarding maintaining power supply, structural integrity of the sensor frame and equipment theft. These problems ultimately limited the number of deployments that were made.

6.3. Wave impact data processing

6.3.1. Preliminary pressure time series data preparation

During each deployment, the raw voltage output from the sensors was recorded on the signal recording software BMCM Nextview 4 on a single *.nvp file. This was subsequently exported to an ASCII file containing 16 data streams (one per sensor) at the original sample rate, retaining a voltage precision of 6 significant figures. This file was imported directly into Matlab using the datastore functionality for large files. Each data stream was saved as a compressed MAT file with no loss of precision (approximately ±0.01 kPa). This enabled more rapid access to the data, as ASCII reading would take up to 72 hours to achieve.

The raw voltages were first converted to pressure measurements. Air pressure for each sensor was not calibrated to 0 kPa and changes in atmospheric pressure caused sensor pressures to vary by up to 1 kPa during any given 24-hour deployment. To combat this, long term air pressure change during the deployment was detrended with a linear approximation of pressure change between the start and end of each deployment. The linear approximation was deemed adequate as atmospheric pressure is unlikely to vary above the 1 kPa uncertainty value over this period (Tanguy, 2013). Further handling of this problem is described in Section 6.3.3.

The full sample rate (5000 Hz) dataset (henceforth known as D_{5000}) was large (~1 TB) and as such demanded substantial computing time. For the initial wave analysis, a smaller dataset was created (D_{100}) which was the D_{5000} dataset smoothed using a 50-point moving average and then downsampled to 100 Hz (Figure 6.4). The D_{100} dataset was used to identify waves and periods of interest which could then be examined in higher resolution in the D_{5000} dataset.

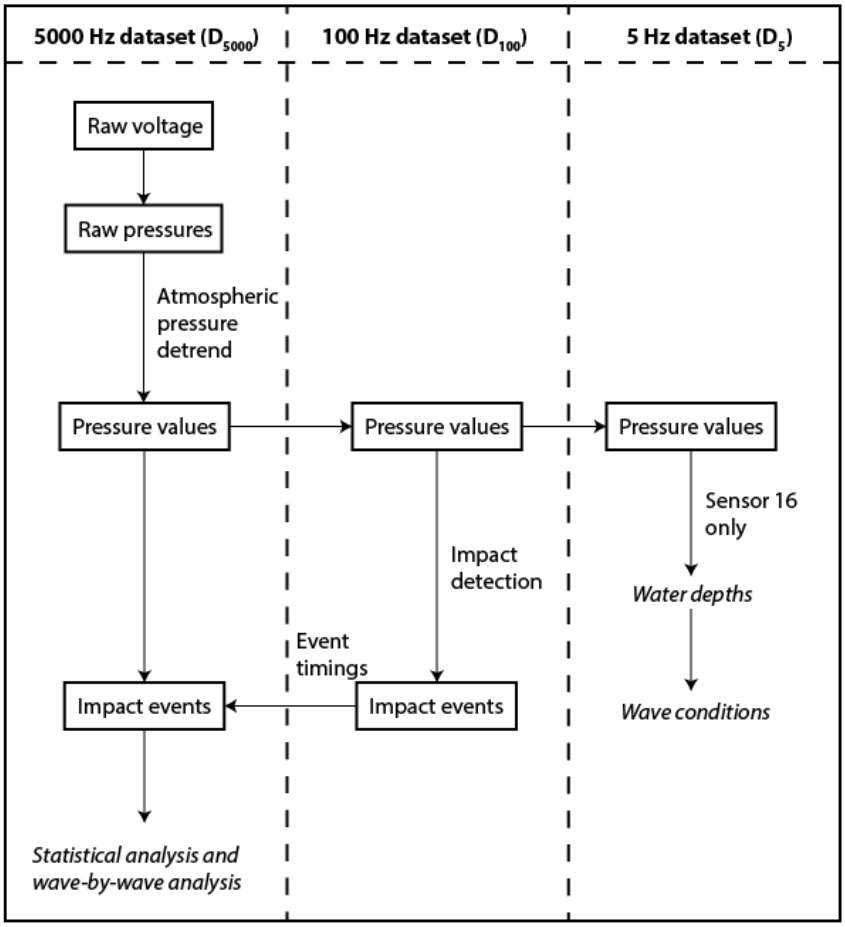

Figure 6.4: Workflow describing the use of three sample rates for processing pressure data.

6.3.2. Extracting waves and tides from pressure time series

A number of variables were extracted from the pressure time series (Figure 6.5). In order to establish the wave and water depth conditions, the lowest elevation sensor was used as a wave gauge: once the sensor was completely submerged by the rising tide, it was subject to hydrostatic pressure variation and as such, could be used to calculate the water depth plus the height of the sensor above the platform (0.1 m).

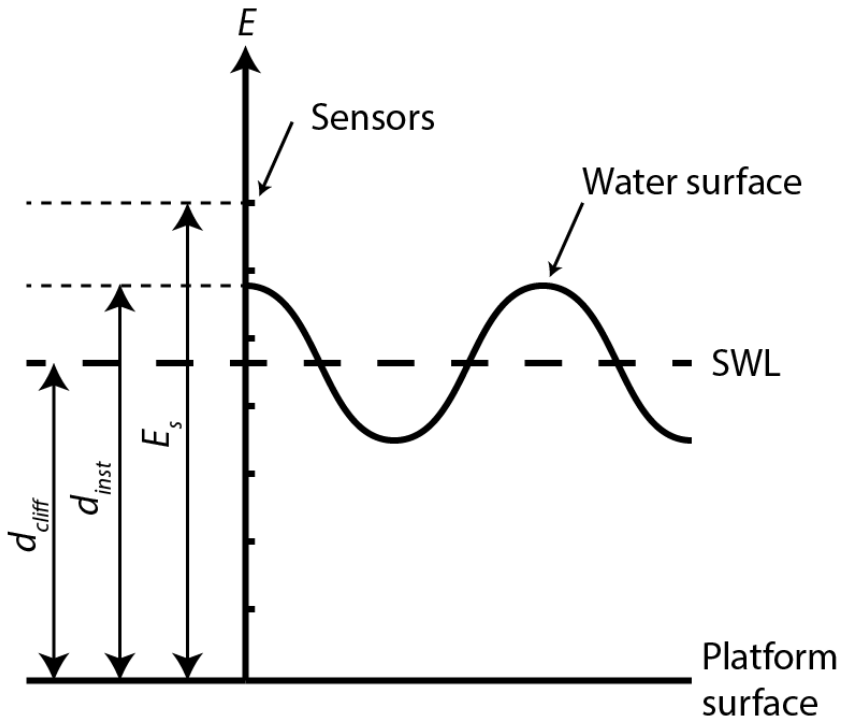

Figure 6.5: Schematic of distinction between still water depth at the cliff toe (d_{cliff}), instantaneous water depth at the cliff toe (d_{inst}) and sensor elevation (E_s) relative to the elevation (E) above the platform surface. Note that within each defined impact event, $d_{wave} = d_{inst}$.

6.3.2.1. Calculating water depth from pressure time series

The change in water elevation due to tidal fluctuations is essentially a wave with a long wavelength and a period of approximately 12 h 25.2 minutes. Therefore, to extract the pressure due to the average weight of water at any given sample time, the D_{100} dataset was further smoothed using a 100,000-point (100s) moving average. This value was chosen as it is in excess of the largest ordinary gravity waves (< 30s) (CERC, 1984). This removed the influence of the surface gravity waves such that the still water pressure was obtained (Figure 6.6A). The pressure applied to the sensor is equal to the force per unit area exerted by the mass of water above it. As such, the hydrostatic equation (Equation 2-9) was used to convert pressure (P) to still water depth at the cliff toe (d_{cliff}):

$$d_{cliff} = \frac{P}{\rho\, g} \tag{6-1}$$

Where g = acceleration due to gravity (9.81 ms^{-2}) and ρ = density of seawater (1027 kg m^{-3}) (Saunders and Fofonoff, 1976). Depth data were corrected for signal depth attenuation using a high-frequency cut-off of 1 Hz, as high frequency signals are preferentially lost with increasing depth (Inch, 2014). This produced a stable value for instantaneous water depth (d_{inst}) at each given sample time (at 100 Hz) (Figure 6.6).

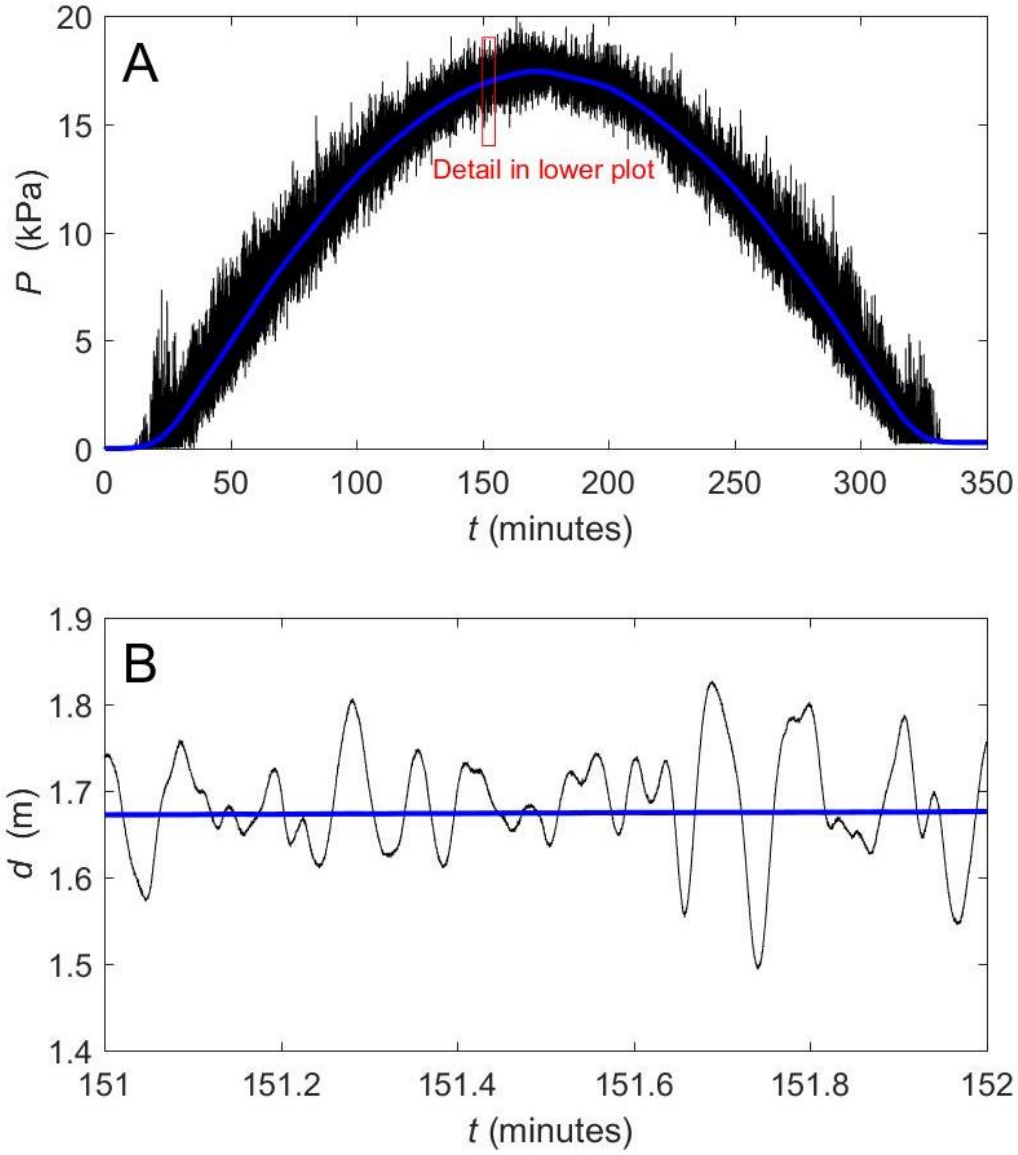

Figure 6.6: A) Raw pressure output from the D_{100} dataset (black) with still water pressure superimposed (blue); B) Detail from (A) after conversion to depth, with instantaneous water depth (d_{inst}) (black) still water depth (d_{cliff}) (blue) shown.

6.3.2.2. Calculating wave conditions from pressure time series

Once the pressure signals had been converted to d_{inst}, the time series was detrended by subtracting d_{cliff} from d_{inst}. The height of each individual wave could then be extracted. Wave statistics were extracted using the zero down-crossing method (Inch, 2014). This defines a single wave by two consecutive downward crossings of the still water depth by the d_{inst} (Figure 6.7). This was undertaken on water depth data downsampled to 5 Hz (the D_5 dataset). Wave height (H) was calculated for each wave and from this the following statistics were derived: significant (T_s) and maximum (T_m) wave period; significant (H_s), maximum (H_m) and root mean square (H_{RMS}) wave height, and wave celerity (v_s) using linear wave theory for shallow water (Holthuijsen, 2009):

$$v_s = \sqrt{gd} \tag{6-2}$$

Uncertainty values were derived from the sum of the known sources of error from the pressure signal. These were: sensor precision (± 0.5 kPa), electrical noise (± 1.3 kPa), atmospheric pressure variation (± 1 kPa). Hence, a conservative uncertainty estimate of impact pressure values is ± 2.8 kPa. When converting this to depth, electrical noise is ignored as smoothing the signal removes any deviation from the mean value; this is only important when considering the absolute magnitude of impact pressures. The sensor accuracy and atmospheric effects combine to give a water depth uncertainty of ± 0.15 m. As the sensor timings all recorded from one clock, the data point timestamps were considered accurate.

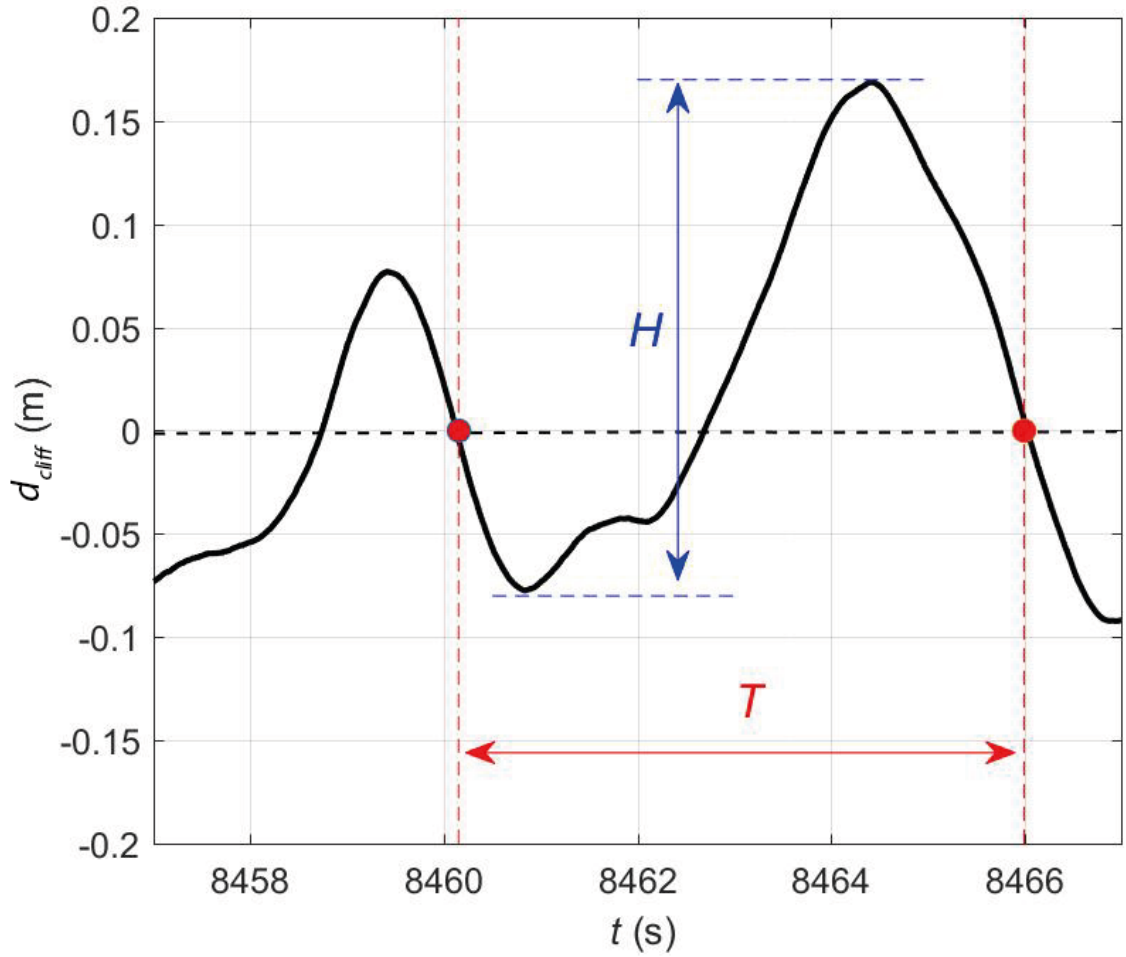

Figure 6.7: 10s section of the D_5 dataset of instantaneous water depth (d_{inst}) relative to the still water depth (d_{cliff}) (dashed black line) from the 22/08/2016 dataset (solid black line). The zero downcrossing method derives wave period (T) from two successive downward crossings of the still water line (red points). The wave height (H) is the elevation difference between the trough (minima) and peak (maxima) within the downcrossing period.

6.3.3. Wave impact event detection

This section describes the extraction of discrete wave impacts, referred to as "impact events" for this analysis, from the pressure time series. Impact event identification was undertaken on the D_{100} dataset, which were then extracted from the D_{5000} dataset for analysis. Some minor manual editing of each dataset was undertaken initially, to remove pressure measurement errors. These were almost exclusively single data points where the minimum or maximum pressure

value was recorded (-500/500 kPa), probably due to a very brief electrical surge.

Wave impacts only occur when a sensor is alternately exposed to air and water during wave propagation (Trenhaile, 1983), namely when the sensor is located between the maximum wave height (H_m) trough and crest. Sensors above this level, specifically when sensor elevation (E_s) satisfies the equation:

$$E_s > \frac{H_m}{2} + d_{cliff} \quad (6\text{-}3)$$

are above the influence of the waves. When:

$$E_s < d_{cliff} - \frac{H_m}{2} \quad (6\text{-}4)$$

the sensor is continually inundated. Since the still water depth changes progressively throughout the tide, each sensor moves in and out of the impact zone during any given deployment. Consequently, data from each sensor in the D_{100} dataset was extracted such that only periods containing impacts was retained (Figure 6.8). Data below the elevation threshold (Equation 6-4) behaved quasi-hydrostatically and were handled separately (Section 6.3.5). The point during the rising tide at which air pressure (P = 0) no longer featured in the time series was used to indicate a sensor was continually inundated.

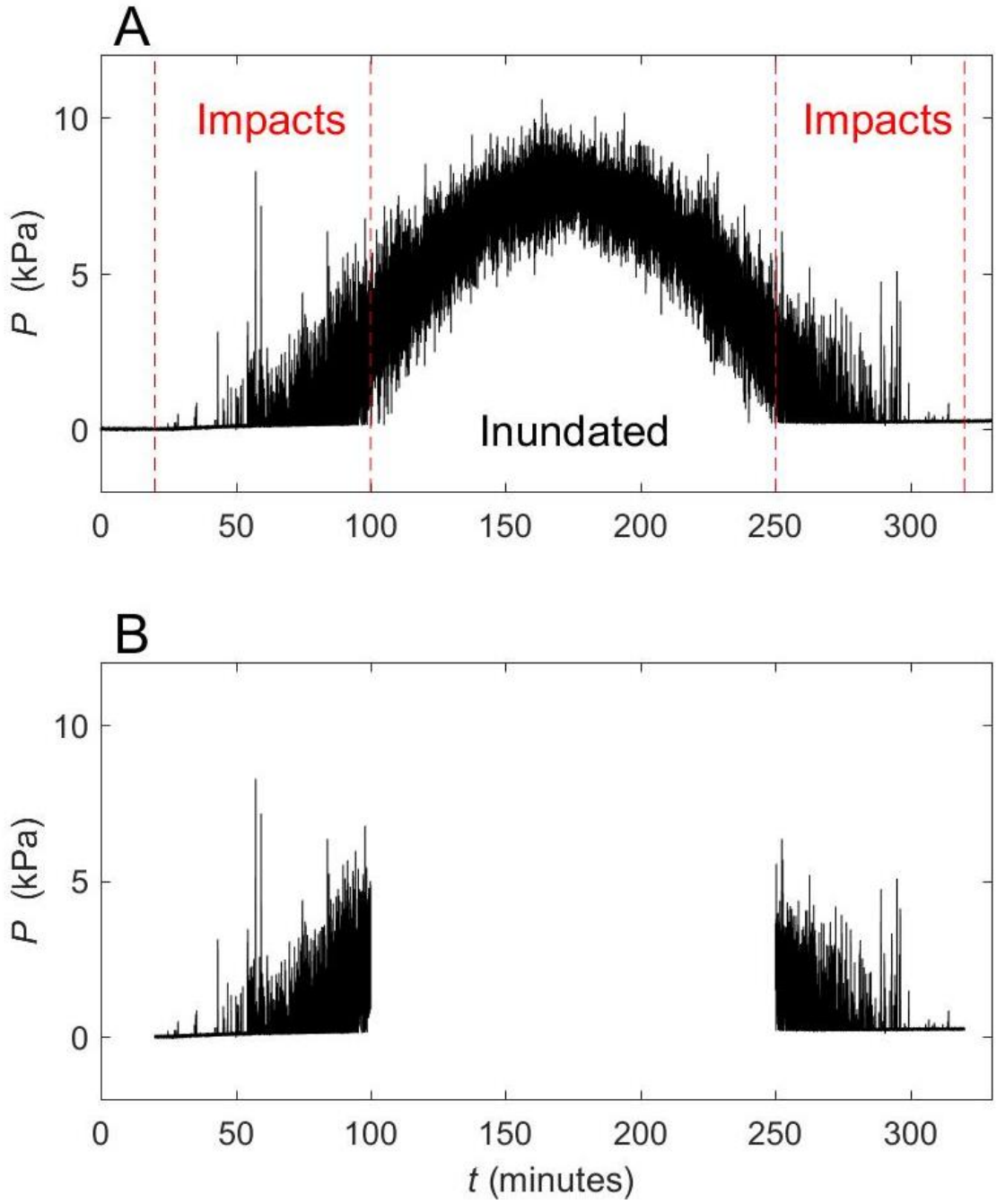

Figure 6.8: A) Zones where impacts occur on sensor 8 for the 22/08/2016 D_{100} dataset (E_s = 0.9 m); B) Edited version of D_{100} used in impact event detection analysis.

The impact event detection algorithm required the resultant dataset (Figure 6.8B) to have an air pressure baseline of exactly P = 0. Due to electrical and atmospheric error this baseline could deviate by up to 2.3 kPa. A Hampel filter (Pearson *et al.*, 2016) was applied to the D_{100} dataset. This class of filter

comprises of one tuning parameter – the window width – which was set at 5000 data points (or 1 s) based on a trial-and-error approach. When applied, the filter removes the spiked pressure response of the sensor produced by wave impacts, so is useful for generating a baseline value. Other window width values tended either to not remove the spikes or removed too much data. This baseline was then subtracted from the D_{100} dataset to produce a detrended time series where air pressure is exactly zero (Figure 6.9). This modification then allows the following analyses to take place without editing the final pressure values.

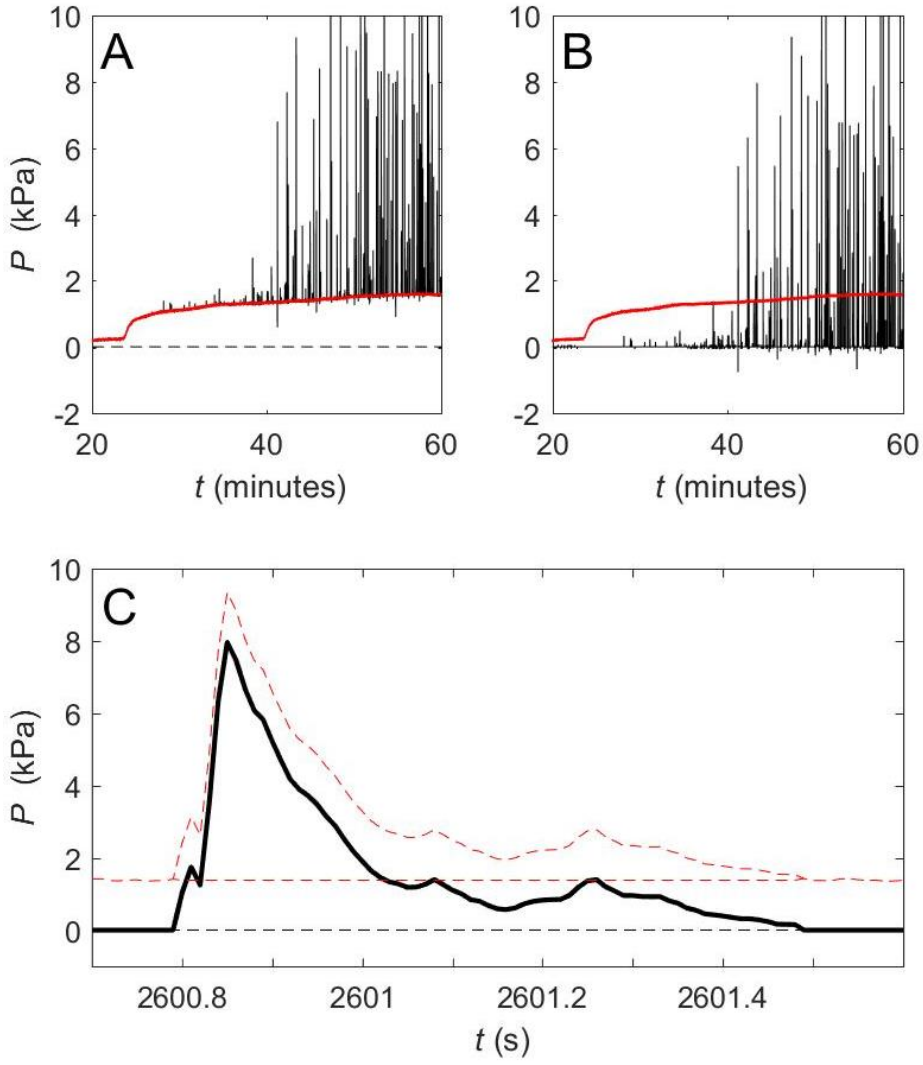

Figure 6.9: Hampel filter application on sensor 8, 13/12/2016 dataset (E_s = 0.9 m). A) Black line shows original data, red line shows data after filter of window width 5000 applied; B) this baseline was used to detrend the data from the original (panel A) to the edited (Panel B); C) close up of single impact before (dashed red) and after (solid black) filter application.

To analyse individual wave impact events, I extracted each one from the dataset using a short-term average/long-term average (STA/LTA) trigger algorithm (Joswig, 1990). This process extracts data points from a continuous time series based on the amplitude of the short period signal relative to long period background noise. In short, it calculates the average value of the amplitude across two consecutive time windows. The short-term window (STA) is responsive to the magnitude whilst the long-term window (LTA) gives information on the temporal amplitude of the noise. An impact event is delimited when the ratio between the two windows exceeds a threshold (Table 6.1). The Seismic Event Matlab Suite (Trnkoczy, 2002) was used to achieve this. This method has not been used previously for impact pressures so no precedent could be drawn upon. As such, I obtained the parameters used for the algorithm through iterative experimentation (Table 6.1).

Table 6.1: Impact event detection parameters for the STA/LTA trigger algorithm.

Parameter	**Value**
STA window length	10 ms (50 samples)
LTA window length	800 ms (4000 samples)
STA/LTA trigger on threshold	1.6 kPa
STA/LTA trigger off threshold	1.2 kPa
Post-event buffer	0
Minimum event duration	0
LTA mode	Frozen

The STA/LTA filter was applied to the D_{100} dataset and each impact event was extracted as a discrete time series. The STA/LTA picking algorithm was not completely successful in picking all impact events that were observed manually. Approximately 1% of wave impacts observed in the time series were not picked up by the algorithm. These are almost exclusively small (< 2 kPa), more complex signals occurring in fewer than 1/100 impacts, which are unlikely to be influential to the results. As such, this was deemed an acceptable level of picking error at this stage in the analysis.

Impact events where the peak pressure (P_{max}) was below 2 kPa (noise threshold) were removed. Impact events where the difference between the

minimum and maximum pressure values was less than 0.5 kPa were also removed as the signal was not clear enough to distinguish a discrete wave impact. These values were calculated through manual examination of event picking and were deemed necessary to remove spurious picks. Approximately half of impact events fell within these criteria and were distributed randomly throughout the dataset.

The impact events were picked between the initial pressure spike (t_{start}) and when pressure returns to the baseline (t_{end}) (Figure 6.10). Whilst others have previously defined these parameters with respect to just the dynamic portion of the wave (Bullock *et al.*, 2007; Tomiczek *et al.*, 2017), these values were chosen in order to encompass the full duration of the impact. Impact event characteristics varied between a simple increase and decrease in pressure (Figure 6.10A) and a complex, oscillating pressure signal (Figure 6.10B).

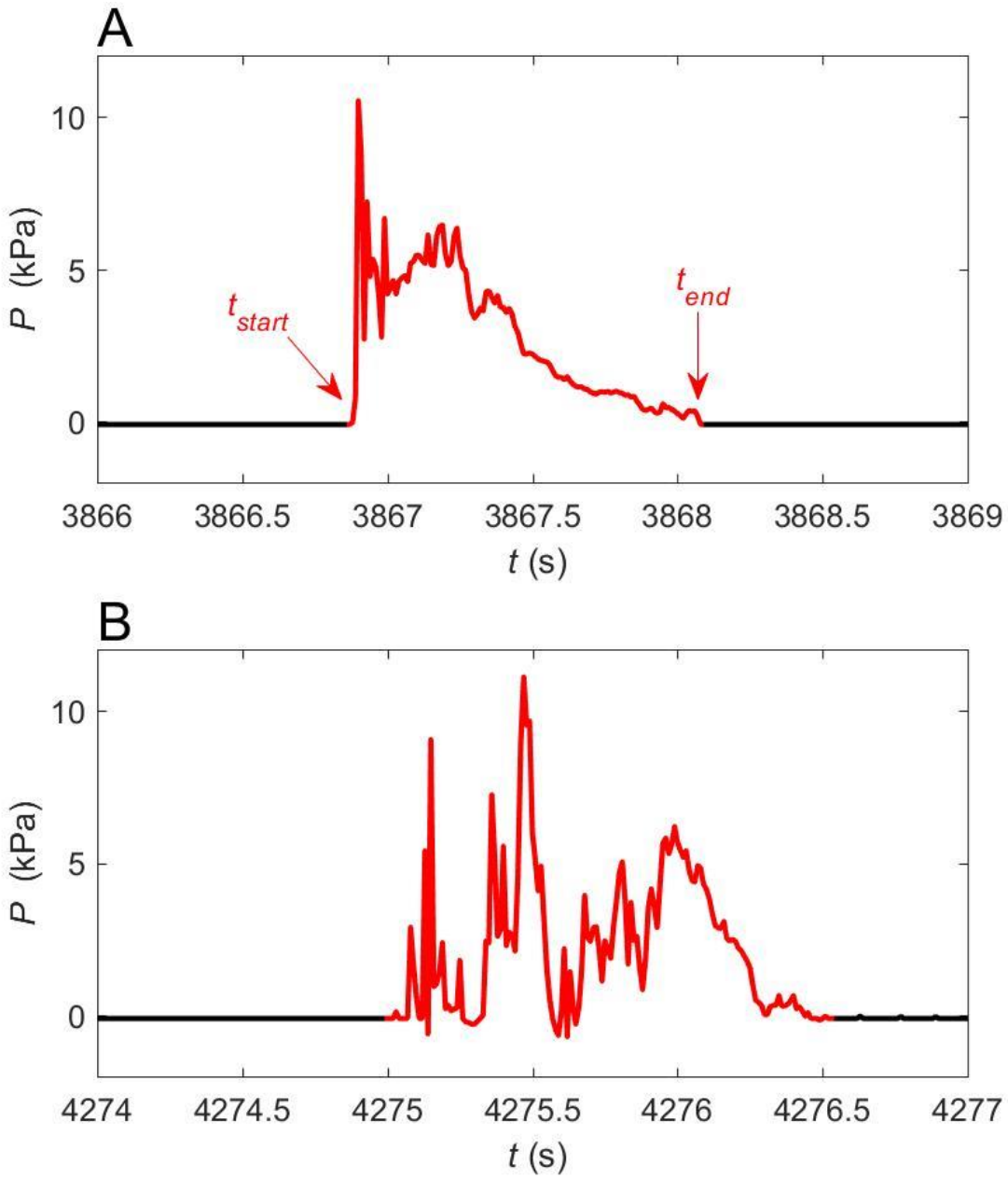

Figure 6.10: Example impact events picked by the STA/LTA algorithm for 13/12/2016 dataset sensor 5 (E_s = 0.6 m). Red line denotes stored impact event denoted between t_{start} and t_{end}. A) Simple impact signal, where pressure rises and falls to zero; B) Complex impact signal, where the pressure returns to zero during the impact event multiple times.

The final picking stage involved applying the t_{start} and t_{end} values for each impact event identified from the D_{100} dataset to the D_{5000} datasets. This produced a full sample rate impact event database of approximately c. 65,000 wave impacts,

each containing impact event start and end times (in Julian date), and pressure values.

6.3.4. Statistical properties from individual wave impact events

Statistical properties for each impact event were calculated (Figure 6.11). Impact event duration (t_P) was defined as the time between the initial pressure increase due to the wave impact and the return back to barometric pressure:

$$t_P = t_{end} - t_{start} \tag{6-5}$$

The maximum pressure (P_{max}) is the peak pressure recorded within t_P. The time of maximum pressure (t_{max}) is the time at which P_{max} occurred, in Julian date. The rise time (t_{rise}) (Blackmore and Hewson, 1984) therefore is the time between t_{start} and t_{max}:

$$t_{rise} = t_{max} - t_{start} \tag{6-6}$$

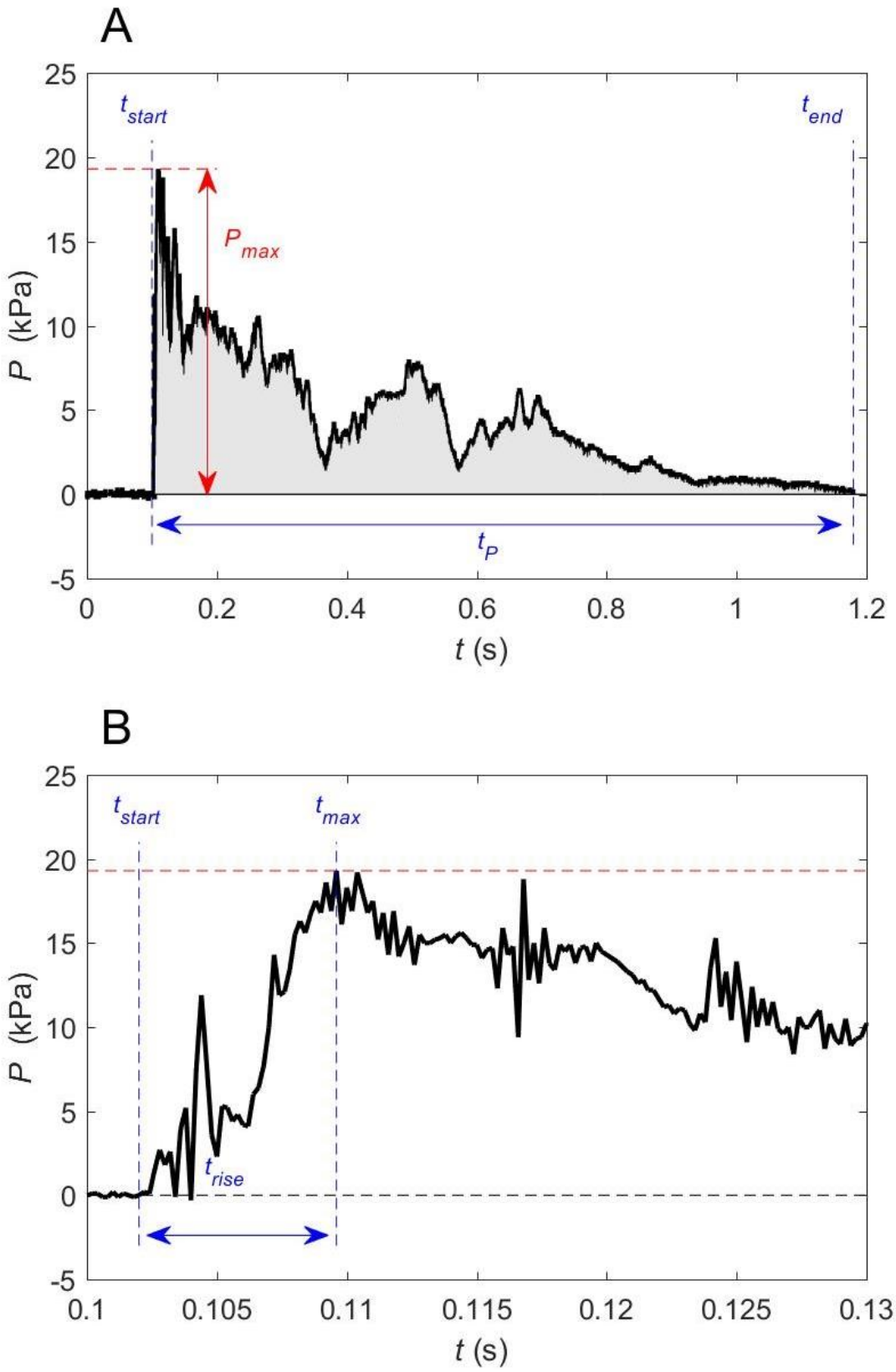

Figure 6.11: Parameterisation of impact pressure signal using example from 13/12/2016, sensor 8 (E_s = 0.9 m), n_w = 106. A) Full impact; B) detail of initial pressure spike.

6.3.5. Wave-by-wave analysis

At this stage, the wave database contained each impact event and its associated statistical properties. As the height of each wave, as measured by the lowest sensor in the array (Section 6.3.2.2), was commonly higher than the vertical resolution of the array (0.1 m) of the sensor array, each wave impact often produced multiple impact events on different sensors.

6.3.5.1. Linking individual wave impact events between sensors

In order to investigate the vertical distribution of pressure associated with a single wave impact, each impact event had to be linked with its associated wave recorded at the other sensors. To achieve this, I extracted the arrival times in Julian days for each wave peak (t_a) from the lowest sensor wave dataset (Section 6.3.2.2) using the *findpeaks* function in Matlab. This function returns the local maxima of an input signal function, which is defined as a data point which is larger than its two neighbouring samples. Then for each sensor, impact event t_{max} values that were within 1s (derived through direct experimentation) of the t_a value at the lowest sensor were assigned a wave index number (n_w) (blue dots, Figure 6.12A).

Impact events were not registered by all sensors for each wave, as some would be inundated and therefore not be included in the event picking, or else were above the wave crest. In these cases, the pressure value at each of these sensors at t_a was used (red dots, Figure 6.12A). This resulted in 16 peak pressure values between 0.1 m and 1.7 m above the platform for each wave index (Figure 6.12B). This approach was necessary, rather than just taking the pressure values from all sensors at t_a, as when wave impacts were impulsive, pressure peaks did not occur at the same time, seen in the time offset of blue and red dots in Figure 6.12A. A deviation of a few samples either side would result in a considerably underestimated value of P_{max}.

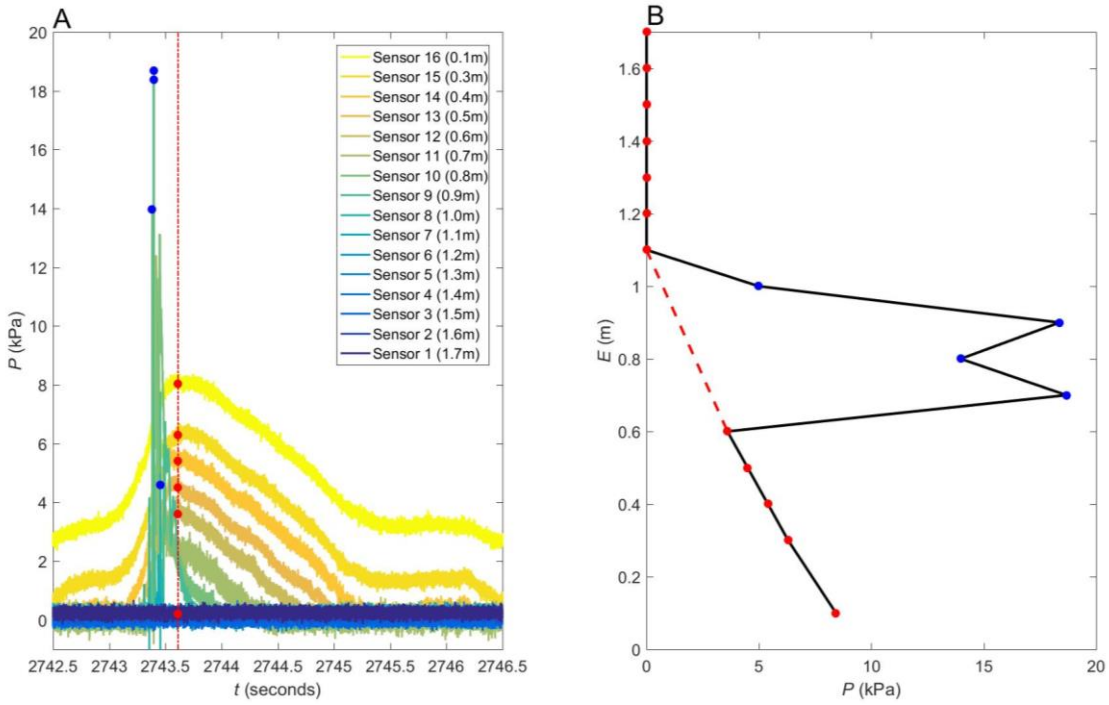

Figure 6.12: A) Pressure time series for all sensors from the D_{5000} dataset from 22/08/2016. Blue points represent peak values taken from the nearest impact event within 1s (sensors 8-11); red points represent pressure values associated with the wave arrival time (t_a) at the lowest sensor (at sensors 1 – 7 and 12 – 16); these values were combined to form wave n_w = 4352. B) Vertical distribution of measured pressure values for the wave in the left-hand plot; red dashed line represents the predicted hydrostatic pressure values for the wave height (H = 0.7 m) at each elevation.

6.3.5.2. Impulsive and pulsating impacts

To distinguish between impulsive and pulsating impact events (Cuomo *et al.*, 2010), the predicted hydrostatic pressure (P_{hyd}) was calculated. To obtain this distinction, the water depth (d_{cliff}) (Section 6.3.2.1) measurements for each wave were input into the hydrostatic equation (Equation 2-9) for each sensor elevation:

$$P_{hyd}(E) = \rho\, g\, (d_{cliff} - E) \tag{6-7}$$

From this, the measured pressure at each elevation was compared with P_{hyd}. If $P \approx P_{hyd}$ at all elevations, the wave was classed as pulsating (Figure 6.12A). Here, the measured pressure profile is approximately equal to the predicted

hydrostatic pressure. The elevated pressure extends above d_{cliff} up to the height of the wave crest (d_{wave}), which within each impact event is equal to d_{inst} as recorded by the lowest sensor (Figure 6.5). When $P > P_{hyd}$ between d_{cliff} and d_{wave} (where the wave front impacts the sensors), the impact event is classed as impulsive (Figure 6.12B). Through experimentation, a maximum threshold of $P - P_{hyd} > 1$ was found to be necessary to eliminate the influence of sensor error.

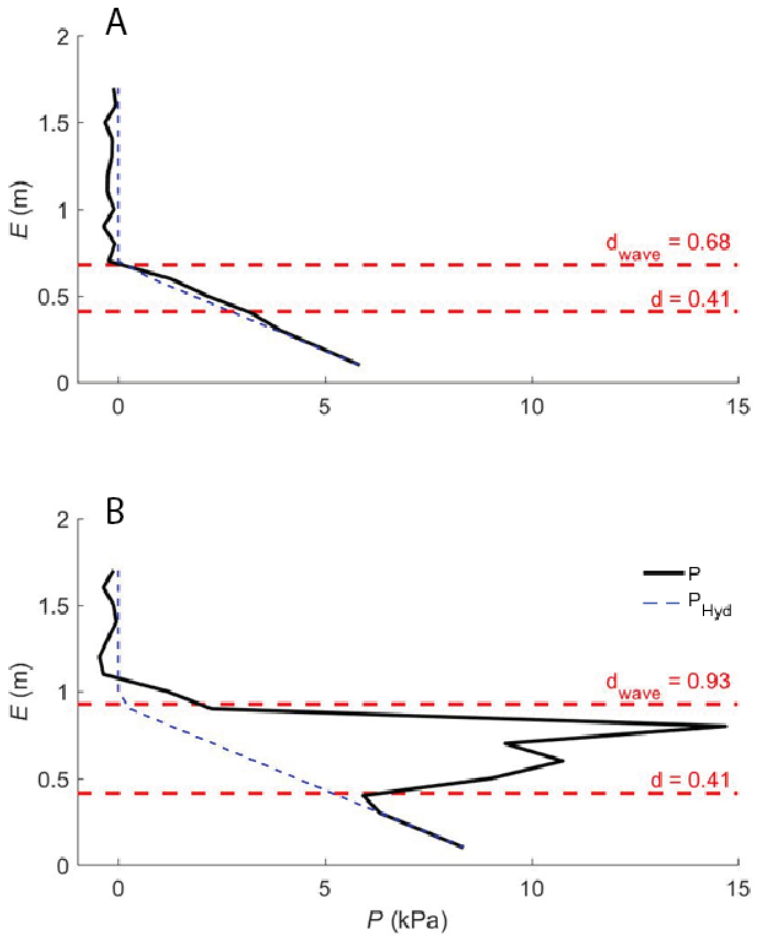

Figure 6.13: P_{max} profiles for two consecutive waves from the D_{5000} dataset from 04/11/2016, n_w = 356 - 357. A) Typical pulsating wave impact is shown where the measured pressures (P) (black line) and predicted hydrostatic pressures P_{hyd} (dotted line) are comparable; B) A typical impulsive wave impact, where $P > P_{hyd}$. The water depth (d_{cliff}) and crest depth (d_{wave}) are shown as red dotted lines.

Two issues with the impact datasets were apparent when establishing d_{cliff} and wave height (H) for each individual wave impact. Firstly, prior to the lowest sensor becoming inundated, values of d_{cliff} were not available. To combat this, I assumed that d_{cliff} was zero at t = 0: the time of the first impact pressure on the

lowest sensor, where the base of the array would be within the swash zone. Water levels rise approximately linearly during mid-tide (Underwood, 1972). As such, I linearly extrapolated d_{cliff} between t = 0 and the first depth value from the inundated lowest sensor (usually approximately d = 0.4 to 0.6 m). The inverse process was undertaken during falling tide.

Secondly, the lack of inundated sensor data during the early stages of the rising tide and latter stages of the falling tide meant no wave height data was available. Waves at this stage were most likely to be broken and consist of turbulent bores propagating shoreward in the swash zone (Miller *et al.*, 1974). Raubenheimer *et al.* (1996) found that that wave propagation across the inner surf zone is effectively depth-limited and independent of the incident wave height. As such, I estimated bore height (H_b) using the breaker criterion (Farrell *et al.*, 2009) derived for this site in Chapter 5, where:

$$H_b = 0.6d + 0.15 \tag{6-8}$$

This estimate is somewhat restricted as the breaker criterion represents an upper limit to wave heights for the given depth, rather than an estimated value. As such, values of H derived using this method are likely to be overestimated. Nevertheless, these estimates gave a reasonable result for classifying impulsive impacts.

6.3.5.3. Calculating wave impact forces

According to Goda (1985), force can be calculated from the pressure profile by integration of the pressure over area, assuming that the horizontal variation in pressure over a width of 1 m is negligible and that pressure can be interpolated linearly between vertical pressure sensors. Shoreward force (J) on the area enclosed by the sensor array between 0.1 m and 1.7 m from the platform surface assuming a width of 1 m was given by:

$$J = \int_{E=0.1}^{E=1.7} P \; dE \tag{6-9}$$

Units are given as kN per m (Crawford, 1999). The value of J represents the maximum force per wave over the measured profile. The use of one set of peak

pressures per wave circumvented the problem of managing negative pressures for the integration calculation and simplified the calculation of impact statistics for further modelling.

6.4. Discussion of preliminary results

The following section is comprised of tests regarding the rise time (t_{rise}) and sample rate (φ) that I applied to the full wave dataset in order to evaluate its reliability and conformity to previous research.

6.4.1. Relationship between pressure and rise time

It has been documented that, for any given impact event, P_{max} is negatively correlated with t_{rise} (Blackmore and Hewson, 1984; Hattori *et al.*, 1994; Walkden, 1999; Cuomo *et al.*, 2010). Conversely, some studies have found considerable scatter (Rajasekaran *et al.*, 2010) and some have been unable to identify any correlation (Zhang *et al.*, 1996). Therefore, there is some uncertainty regarding the precise nature of the relationship.

6.4.1.1. Pressure-rise time relationship characteristics

The relationship between P_{max} and t_{rise} is generally given as an upper limit function, and not a best fit, in the form of a power law (Rajasekaran *et al.*, 2010):

$$P_{max} = a\, t_{rise}{}^{-b} \tag{6-10}$$

Empirically-derived values for the power law constant (a) in the literature vary by an order of magnitude, and the exponent (b) varies between 0.6 and 1 (Table 6.2). This demonstrates the variability in the relationship, which is highly dependent on the specific geometry of the impacted structure and the wave breaking conditions.

Table 6.2: Values for *a* and *b* for the power law relationship between P_{max} and t_{rise} (Equation 6-10).

Study	***a***	***b***	**Notes**
Weggel and Maxwell (1970)	232	1	Lab tests, regular waves
Kirkgoz (1991)	250	0.9	Lab tests, regular waves, plunging breakers
Hattori *et al.* (1994)	400	0.75	Lab tests, Regular waves,
Blackmore and Hewson (1984)	3100	1	Sea wall, broken waves
Cuomo *et al.* (2010)	7000	0.6	Large flume tests, irregular waves

There is a clear negative relationship between P_{max} and t_{rise} in my data, whereby the majority of very large impact pressures (> 40 kPa) are associated with very rapid (< 0.01s) rise times (Figure 6.14). However, there is considerable scatter in the data and the majority of impacts which span any given rise time can feature low impulsive pressures (< 10 kPa). This closely mirrors the scatter found by Cuomo *et al.* (2010) for irregular breaking waves in a full-scale flume, where the upper-limit power law derived in that study best fits the observations.

The constant *a* and coefficient *b* derived by the other researchers in Table 6.2 do not fit the data well. The curve of Blackmore and Hewson (1984) appears to overestimate t_{rise} for very large pressures and underestimate for lower pressures. This may be because the sea wall in that investigation mainly experienced broken waves, rather than a wide variety of wave types and breaking conditions. Flume tests using regular waves appear to have much smaller *a*-values than those using irregular or real-world wave conditions (Table 6.2). These are not plotted in Figure 6.14 as they are located far outside the plot area. As such, it is the relationships which use waves comparable to field conditions which fit the data in my study best.

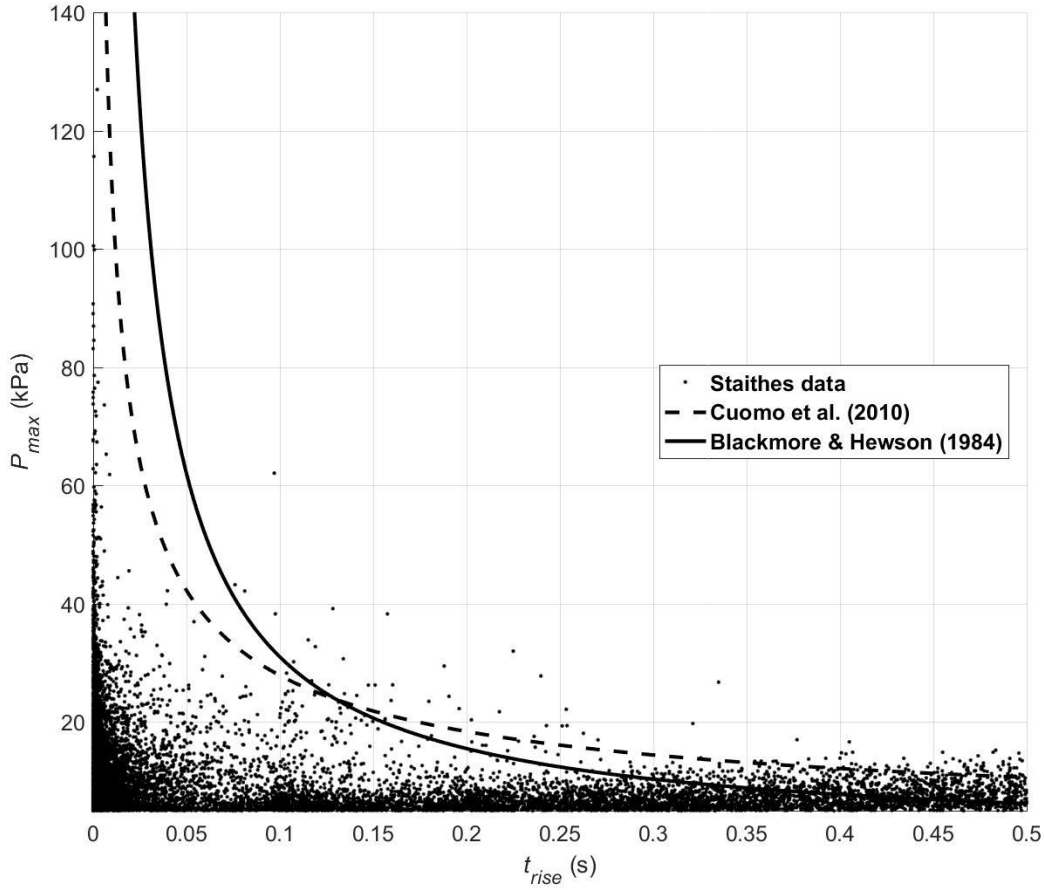

Figure 6.14: Relationship between maximum impact pressure (P_{max}) and rise time (t_{rise}) for all alternating air/water wave impact events during the study period. Upper-limit curves for two empirically-derived relationships are shown. Note the y-axis starts at 2.8 kPa, the smallest P_{max} value detectable within error.

6.4.1.2. Scatter under the pressure-rise time curve

The degree of scatter observed in Figure 6.14 demonstrates the difficulties in predicting P_{max} in this environment. Rapid rise times can occur for any pressure maxima value, and as such is a poor predictor. High pressures only occur with short rise times but a small number of anomalies do occur above the best fit curve of Cuomo *et al.* (2010). These represent < 2 % of the total number of data points, and most are located at the high end of t_{rise} values, where the relationship appears to break down. This is probably a result of small, transient spikes in chaotic impacts (such as those seen in Figure 6.10B), where P_{max} is small but rapid pressure oscillations occur. Blackmore and Hewson (1984) also

noted approximately 4% of data points occurred above the curve, but these were accepted as within tolerance.

The considerable scatter found here, including the anomalies discussed above, may be explained by the role of entrained air in the water column (Rajasekaran *et al.*, 2010). It is well-established that there is a theoretical limit to the magnitude of impulsive pressures (Bullock *et al.*, 2003) based on the acoustic velocity in the fluid equivalent to the water hammer limit (Field, 1999), which in turn is dictated by the percentage void fraction (Tijsseling and Anderson, 2004). Entrained air has also been shown experimentally to reduce impact pressure magnitudes (Oumeraci *et al.*, 2001). This implies that heavily aerated water, such as that produced by turbulent broken waves, will likely induce lower impact pressures. Entrained air may also produce substantial variability within the form of the pressure signal (Walkden, 1999). The degree of turbulence measured by flowmeters on five different shore platforms in New Zealand by Taylor (2003) was found to be considerable, greatly increasing aeration of the water column. As such, aeration may be an important influence on impact pressures on coastal cliffs.

6.4.2. The effect of sample rate on maximum wave pressure

In the previous section I showed that peak pressure values are often highly transient, and as such are dependent on the sample rate (φ) of the measurement equipment (Kirkgoz, 1991). Values of peak pressure (P_{max}) can only be sampled if the following criterion is met:

$$t_{rise} < \frac{1}{S} \tag{6-11}$$

If t_{rise} is larger than S, the peak may occur between samples; P_{max} may therefore be underestimated (Park *et al.*, 2017). When comparing P_{max} values with previous research, it is important to understand how the conditions under which these data were collected vary with my study. Measurements which were taken at a low φ may not be sampling adequately to capture such transient pressures.

In order to establish whether the peak pressures observed are representative of their true value, I systematically downsampled a series of impact events and observed the change in P_{max}. Downsampling a peaked impulsive impact by halving between φ = 5000 Hz and 39 Hz substantially decreases the magnitude of the peak (Figure 6.15). Whilst the characteristic peaked shape is retained at φ = 5000 – 1250 Hz, the magnitude of the peak is reduced by over 50 %. At φ = 625 – 156 Hz no peak is seen but the impact is still apparent, albeit with a broad signal similar to a pulsating impact. Below this φ value no impact is measured.

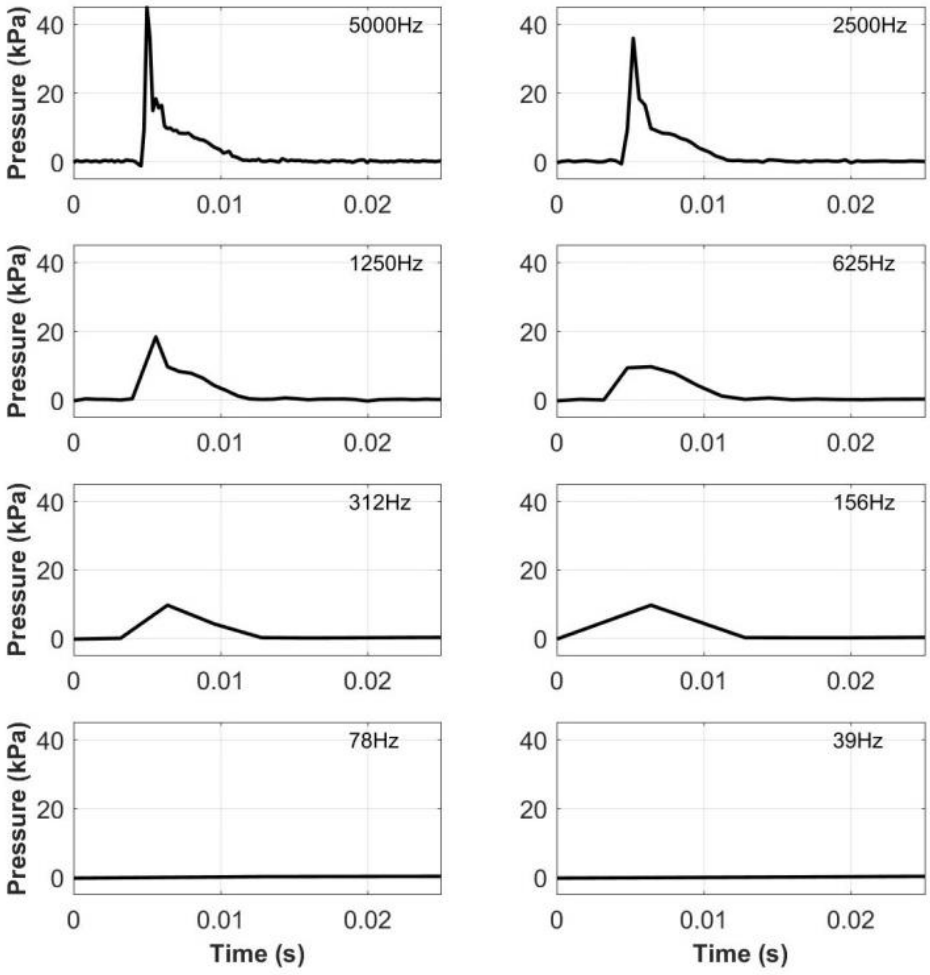

Figure 6.15: Downsampling of a single peaked impulsive impact from the D_{5000} dataset from 04/11/2016 at E = 1.0 m. Note both the changing value of the peak pressure (P_{max}) and the character of the post-peak pressure reduction.

The reduction in P_{max} can be seen when downsampling a series of impact events across an entire dataset. Using the D_{5000} dataset from 22/08/2016, each

peak was systematically downsampled in the manner of the impact event in Figure 6.15. The results show that the larger the original (φ = 5000 Hz) P_{max} value, the larger the value is underestimated when downsampled (Figure 6.16). For example, a peak pressure of 50 kPa at 5000 Hz is reduced by 20 kPa at 625 Hz, whereas a peak pressure at 100 Hz is reduced by 40 kPa for the same reduction in sample rate. This demonstrates the importance of sampling frequency when considering very rapid impulsive pressures. Furthermore, the effect on lower magnitude pulsating pressures is negligible, whereas, as seen in Figure 6.15, impulsive impact event magnitudes are severely diminished. Since $t_{rise} \propto P_{max}$, this indicates the largest pressures are more likely to be poorly sampled.

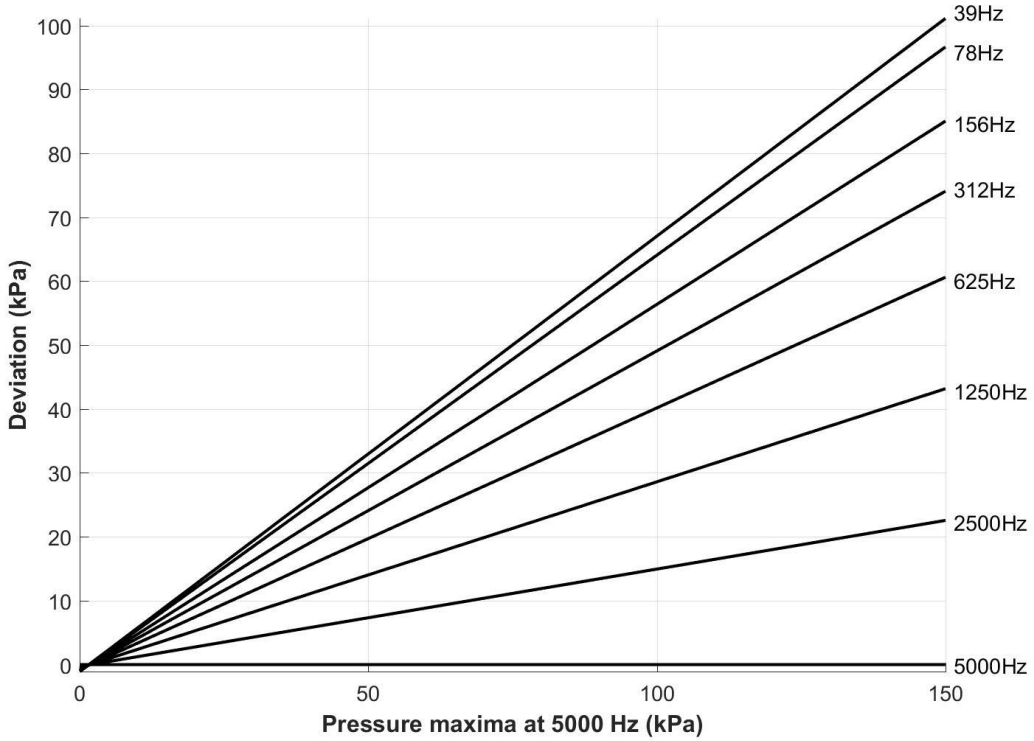

Figure 6.16: Reduction in peak pressure (P_{max}) when compared with the full sample rate (φ = 5000 Hz) for differing downsampling values. The y-axis represents the downsampled peak value subtracted from the peak value at full sample rate.

This assessment of the influence of downsampling suggests that any investigations with φ < 2500 Hz may underestimate P_{max} values for impulsive impacts but could estimate pulsating impact event values accurately down to 78

Hz. Therefore, where φ < 2500 Hz, such as Van Heteren *et al.* (1989), Howarth *et al.* (1996) and Martin *et al.* (1996), data is likely to have P_{max} values not comparable with my study. Studies where φ > 2500 Hz are likely more suitable for comparison (Blackmore, 1982; Müller *et al.*, 2003).

It is also likely that sampling at 5000 Hz may underestimate P_{max}. Marzeddu *et al.* (2013) found that a 400-fold increase in φ leads to a 1.5-fold increase in the measured impact pressure. This could suggest that if my study used a sample rate of 2 MHz, the resultant maximum P_{max} during deployment would be 190 kPa, rather than 127 kPa. This would assume that this law can be applied to any sample rate up to a theoretical maximum. The increase found by Marzeddu *et al.* (2013) in peak pressure between 4800 Hz and 19,200 Hz was only 9%, hence the peak pressure increase appears to tail off at very high sample rates. Additionally, Bullock *et al.* (2007) measured a P_{max} of 3500 kPa with a t_{rise} of 1.2 ms, which is well within the measurement capabilities of my study and an order of magnitude above the largest P_{max} value (127 kPa). This implies that the rate of 5000 Hz used in my study is adequate in capturing values for P accurate enough for relative comparisons between waves in this environment.

6.5. Conclusion: Impact wave pressure measurements

In this section, I established a novel methodology which allowed the first direct measurements of wave impact pressures at the cliff toe in a rock coast environment. This involved both a custom vertical pressure sensor array to be deployed at the cliff toe as well as a set of conventional and new processing stages, including quality control, event picking and linking wave impacts between sensors. The relationship between incident wave-by-wave conditions and a wide variety of variables associated with the vertical distribution of impact pressures was established from this dataset. The preliminary results were found to compare favourably with similar studies in other environments. As such, this methodology was used in Chapter 7 to investigate the nature of wave impacts at the cliff toe.

7. Observations of cliff toe wave impact pressures

7.1. Introduction

In Chapter 6 I demonstrated that by deploying a pressure sensor array at the cliff toe during a tidal cycle, wave impact pressures generated on the Lower Cliff could, for the first time, be measured. In turn, these could be used to inform models of cliff recession and evaluate the mechanisms by which rock coasts damage and remove cliff material.

The following chapter describes the first direct measurements of wave pressures on rock coast cliffs. Firstly, the general observations (Section 7.2.1) and overall conditions (Section 7.2.2) for a given deployment are described, followed by a breakdown of the types of pressures (Section 7.3.1), the characteristics of a wave impact profile (Section 7.3.2) and the associated conditions (Section 7.3.3). General statistical models for the prediction of the occurrence, magnitude and vertical distribution (Section 7.3.4), are generated. A summary of each section is also presented for clarity. Finally, additional controls of these are discussed (Section 7.4.1) as well as the implications for our understanding of hydraulic forcing at rock coasts (Section 7.4.2) (Figure 7.1).

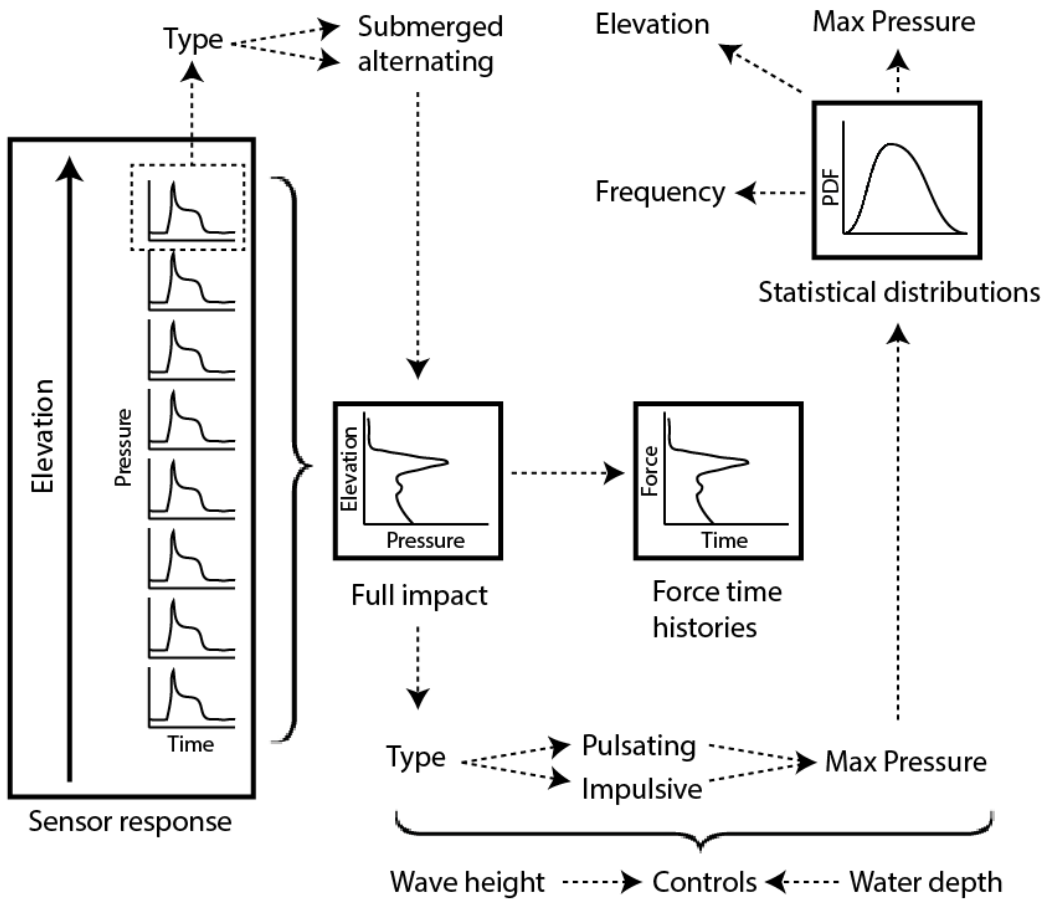

Figure 7.1: Chapter outline, illustrating how the sensor pressure time histories for each elevation are combined to produce a profile of the overall impact pressure per impact and how this translates to force on the cliff. Each impact can be categorised into pulsating (quasi-hydrostatic) and impulsive (dynamic) pressures, which in turn can be investigated in terms of their statistical distribution and controls thereof.

7.2. Cliff toe impact pressure measurements

7.2.1. Overview and general observations

The following cliff-normal pressures were collected over a 7-month study period. Table 7.1 summarises the range of conditions that were sampled during each deployment. There was no evidence that the sensor limit of 500 kPa clipped pressure measurements over the survey period, so the values for P_{max} were considered valid.

Table 7.1: Summary of marine conditions during each deployment, showing maximum wave height (H_m), significant wave height (H_s), significant wave period

(T_s), maximum water depth (d_{max}) and maximum value of the highest wave pressure (P_{max}). Bold lines denote larger gaps between deployments.

No.	Date	H_m (m)	H_s (m)	T_s (s)	d_{max} (m)	Max P_{max} (kPa)
1	22/08/2016	0.78	0.46	10.84	1.8	55
2	23/08/2016	0.69	0.41	8.21	2.08	31
3	18/10/2016	1.43	0.60	5.66	2.2	115
4	03/11/2016	1.77	0.93	7.63	1.55	127
5	04/11/2016	1.26	0.69	8.35	1.66	87
6	07/12/2016	0.68	0.39	12.23	1.14	42
7	08/12/2016 am	0.61	0.35	16.42	1.43	33
8	08/12/2016 pm	0.76	0.43	10.16	1.29	57
9	13/12/2016	1.21	0.78	8.63	1.29	100

Each dataset represented a sensor deployment during a full cycle over which the tide level rose and receded over the array, usually a 4 - 6 hour period. The range of P_{max} values were in line with previous research on vertical coastal structures. Bird *et al.* (1998) measured P_{max} = 85 kPa for an H = 3.1 m wave at Alderney breakwater. At the same site, Crawford (1999) measured P_{max} = 396 kPa for H = 2 m. Blackmore (1982) measured P_{max} = 49 kPa for H = 0.9 m and P_{max} = 27 kPa for H = 1.3m. Both H and P_{max} from my study were all within the same order of magnitude as these studies (Table 7.1).

The pressure data from each sensor was broadly categorised into three types:

1. *Subaerial:* the sensor was above the influence of the waves.
2. *Alternating air-water:* The sensor was below the highest wave crest elevations but above the lowest wave trough elevations relative to the still water depth (two-phase).
3. *Submerged:* The sensor was continuously below the level of the lowest wave troughs (single-phase).

The conditions to which each sensor was subjected varied over a tidal cycle as the water level rose and fell over the sensor array.

7.2.2. Pressure conditions over a tidal cycle

On all sensors, pressure rose and fell correspondingly with rising and falling water levels. The lower sensors were first to respond to an increase in water levels and were subject to non-zero pressure for the longest duration. During subaerial conditions, the sensor response varied with air pressure, which was generally lower than the precision of the pressure sensor so was effectively static. In submerged conditions, the pressure was proportional to the water depth above the sensor, which oscillated as waves propagated across the water surface. The most dynamic pressures were experienced in alternating air-water conditions, where rapidly oscillating, high-magnitude impact pressures occurred (Figure 7.2B). Pressures induced during submerged conditions were generally low: the maximum pressure measured during my study in submerged conditions was 22 kPa. In contrast, the maximum pressure during alternating air/water conditions was 127 kPa.

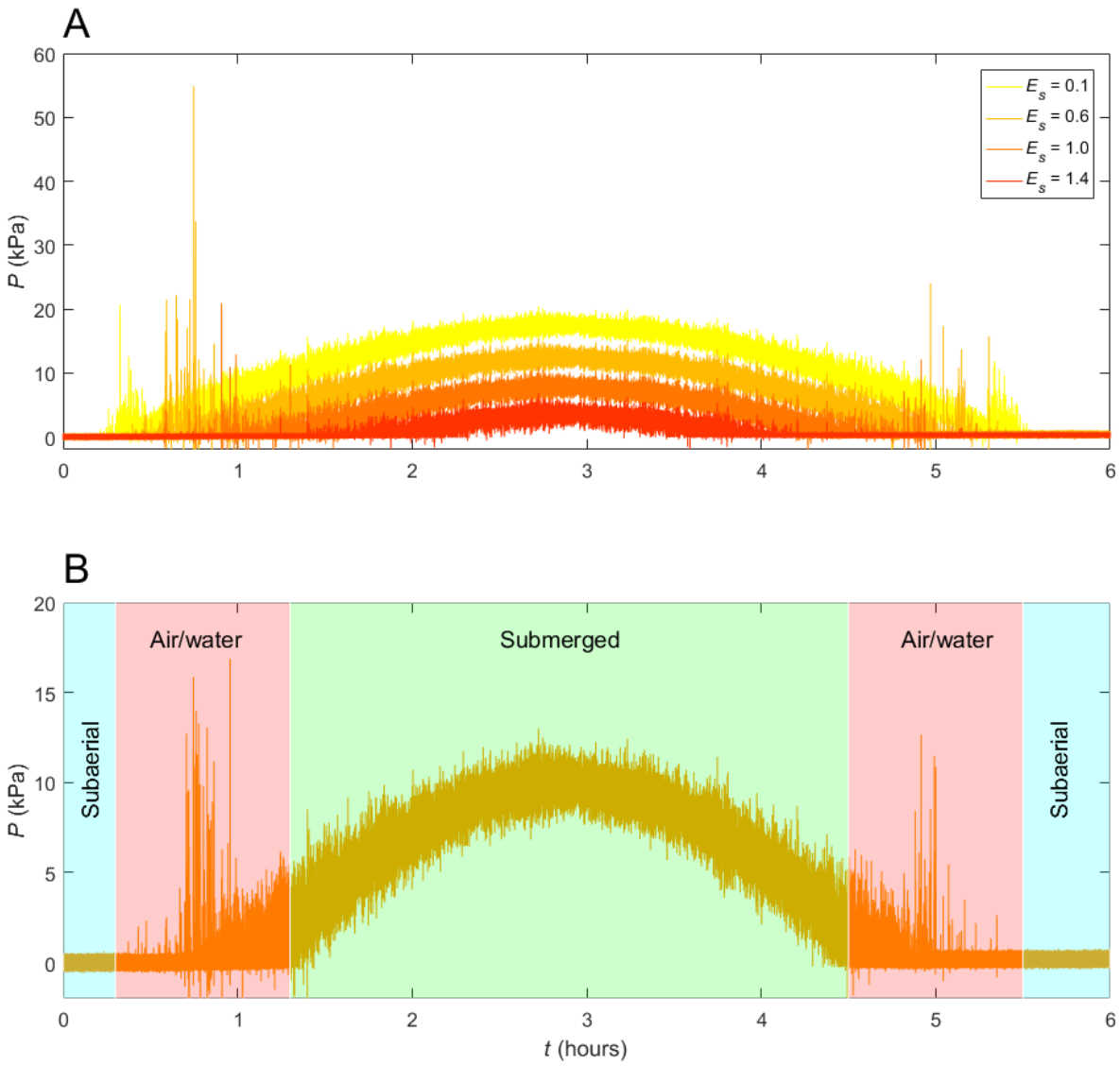

Figure 7.2: A) Raw output from four sensors at different elevations (E_s) from the D_{5000} dataset (22/8/2016) during a six-hour deployment. Rising tide occurred during the first three hours, and falling tide during the final three. Maximum water depth (d_{cliff}) was 1.8 m and significant wave height (H_s) was 0.46 m. B) Pressure time series from sensor at E_s = 0.8 m, illustrating zones of subaerial, alternating air/water and submerged conditions. Note the large spiking pressures during the alternating air/water conditions.

7.3. Impact pressures at the cliff toe

7.3.1. Introduction to wave impact pressures

Alternating air-water conditions gave rise to impact pressures on the sensors. These often differed from the broad, oscillating pressure experienced at submerged sensors by higher magnitudes and shorter periods. As each wave struck the sensor surface, the subsequent pressure rise and fall from background air pressure created a discrete pressure signal referred to here as an impact event. In the following section I will consider the different types of impact pressures, the character of their pressure-time histories and how these compare with those in the literature. This will provide a foundation upon which I will assess their occurrence and magnitude in later sections.

7.3.1.1. Categorising impact pressures

The observed impact events were categorised into two impact types: pulsating and impulsive (Oumeraci *et al.*, 1999). Examples from the 03/11/2016 dataset of each are displayed in Figure 7.3; the wave index number (n_w) for each example is displayed.

Pulsating impacts:

Pulsating impacts were characterised by a slow rise and fall of pressure from $P \approx 0$ ($t_{rise} = 10^2 – 10^4$ ms), approximately equivalent to the hydrostatic pressure of the water impinging on the sensor. Associated P_{max} values were equivalent to the maximum expected hydrostatic pressure. These fell into two categories:

Quasi-sinusoidal

These impact events were approximately sinusoidal in form and followed the rise and fall of the water level during wave propagation and impact (Figure 7.3A).

Skewed sinusoidal

Similar to quasi-sinusoidal impact events, these also rose and fell with the water level but exhibited a more rapid rise time (t_{rise}) and were asymmetrical about the peak (Figure 7.3B).

Impulsive impacts:

Impulsive impacts were characterised by rapid (t_{rise} = 10^0 – 10^1 ms) initial pressure increases unrelated to the water depth.

Single-peak

These were characterised by a very rapid (short t_{rise}) initial pressure increase of short duration (< 10 ms), producing values of P_{max} considerably higher than the equivalent hydrostatic pressure of the wave (Figure 7.3C). Pressure subsequently gradually subsided back to subaerial values, approximately following the hydrostatic pressure. These are well-described in the literature (Kirkgoz, 1982; Cooker and Peregrine, 1990a).

Chaotic

Impacts of this nature were characterised by rapid oscillations in pressure, several peaks and multiple instances of very small t_{rise} values occurring over a short duration (Figure 7.3D). Negative pressure values were often produced, which may be due to suction generated as the crest jet rises up the sensor (Hattori *et al.*, 1994), or else highly aerated water creating high-magnitude oscillations (Bullock *et al.*, 2007). These impact types also lead to very high P_{max} values.

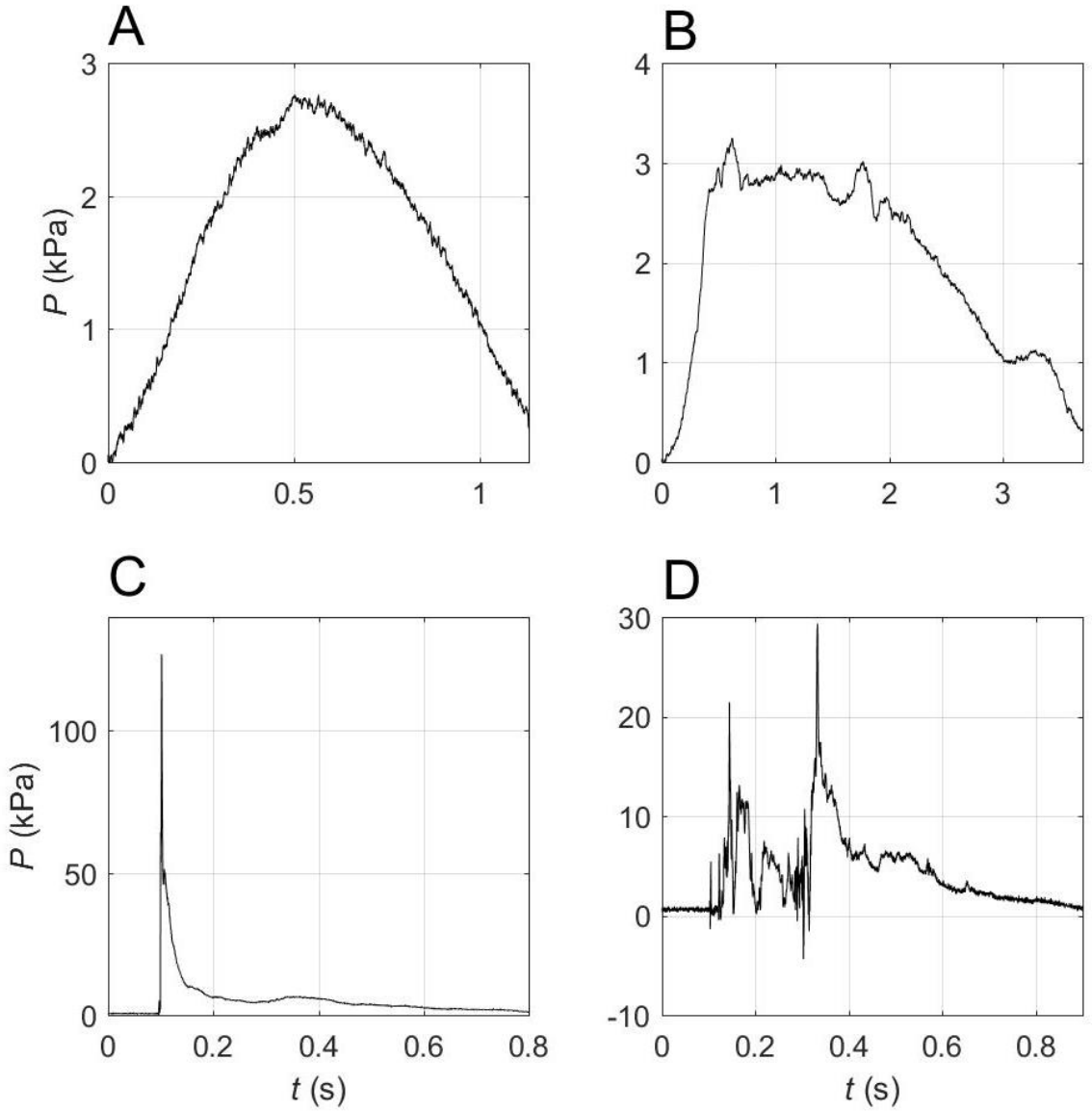

Figure 7.3: Examples from the 03/11/2016 dataset of the types of impact pressure seen during alternating air/water conditions. A) Quasi-sinusoidal pulsating impact (n_w = 1019); B) skewed sinusoidal pulsating impact (n_w = 251); C) single peak impulsive impact (n_w = 350); D) chaotic impulsive impact (n_w = 229). Note the varying vertical scale.

7.3.1.2. Types of impact pressures in the literature

All four impact types found in alternating air/water conditions in my study were consistent with those observed by other researchers. Crawford (1999) measured wave impacts on Alderney breakwater, Channel Islands, and found similar pressure-time histories on a record by record analysis, although the

frequency of each was not discussed. Walkden (1999) recorded large, solitary wave impacts in a full-scale wave flume, concluding that the progression from sinusoidal, quasi sinusoidal and peaked impacts corresponded with a steepening wave front. Peaked pressures occurred during steep, flip-through and small air pocket impacts, whilst chaotic impacts were produced by large air pocket, toe breaker and broken waves. The presence of a double peak (Figure 7.3D) may therefore be explained by the arrival of two separate water surfaces divided by an air pocket from an overturning wave front.

In previous experimental flume and coastal structure research, single-peak impulsive impact types are the most likely to produce very high pressures (Bullock *et al.*, 2007; Hofland *et al.*, 2010). The pressure-time histories of these impacts follow the characteristics of 'impact loads' on vertical breakwaters (Müller *et al.*, 2008), namely an initial, transient pressure peak followed by a quasi-hydrostatic response.

7.3.1.3. Wave impact pressure time histories

A variety of impact pressure types was generated by any given individual wave depending on the location of the sensor (E_s) relative to still water depth (d_{cliff}) (Figure 7.4A). In Figure 7.4, where E_s = 0.1 – 0.3 m, the sensors were inundated, so the pressure signal acted in response to the water depth above hydrostatically. Where E_s = 0.4 – 0.6 m, alternating air/water conditions prevailed, and the pressure signal became skewed sinusoidal. Between E_s = 0.7 – 1.2 m, a combination of peaked and chaotic impulsive impacts occurred, where the wave front impinged directly on the sensor. The P_{max} values here varied between 5 – 30 kPa but were all higher than the equivalent hydrostatic pressures, and hence were a response to dynamic pressure. Above this level, the wave crest did not impact so no response was seen, apart from some probable splash impacts at E_s = 1.7 m. The combined figure (Figure 7.4B) shows these pressure histories in profile; the location of the impact front can clearly be seen where the impulsive pressures occurred.

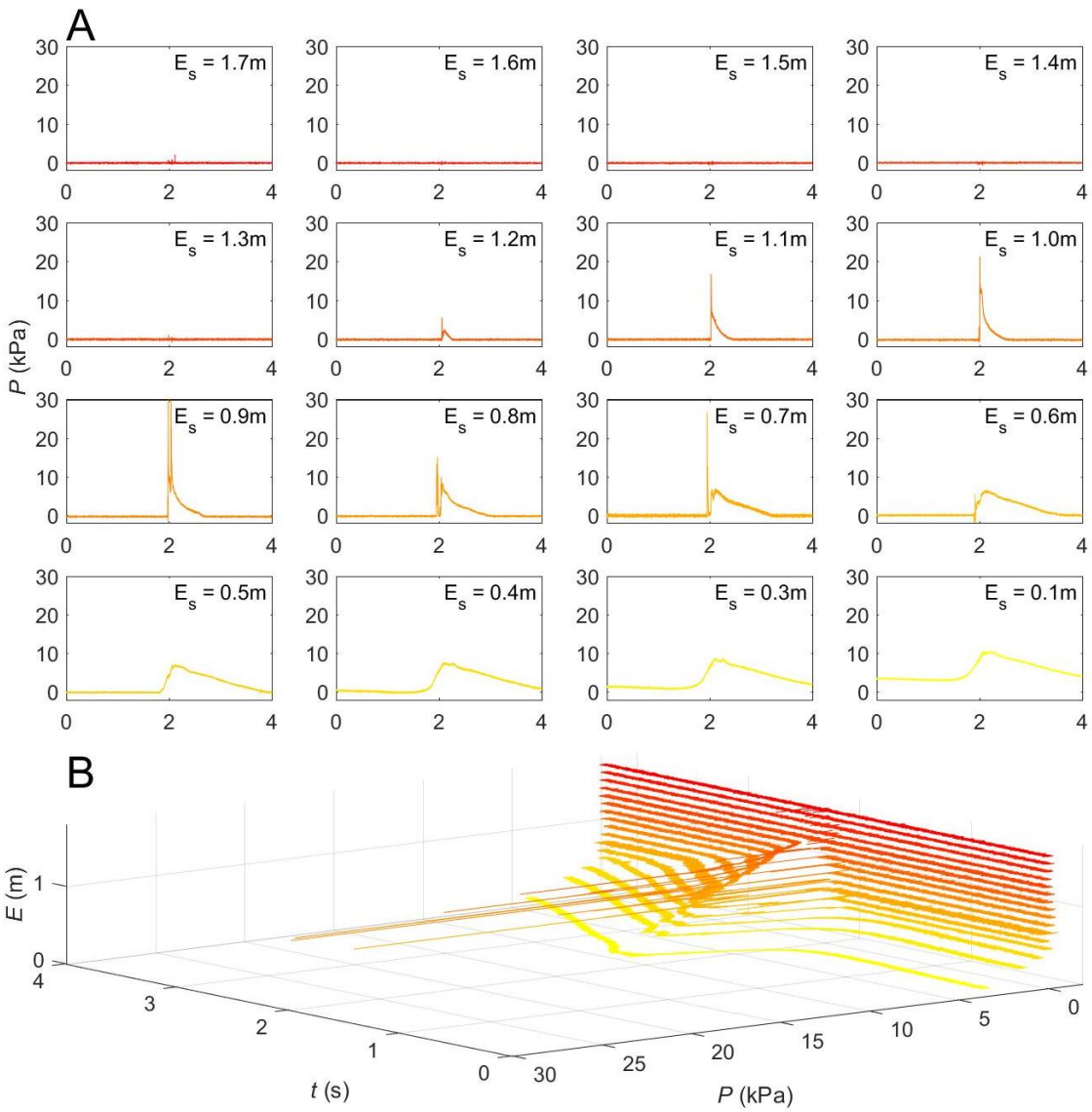

Figure 7.4: Pressure time series of an individual impulsive impact across the full pressure profile from the D_{5000} dataset (04/11/2016), n_w = 588, A) at each sensor elevation (E_s) and B) all sensors combined.

7.3.1.4. Summary

Pressure variations due to waves were detected with the cliff toe sensor array throughout the tidal cycle. Four characteristic wave impact pressures were observed during alternating air/water pressure conditions: quasi-sinusoidal and skewed pulsating pressures, and single-peaked and chaotic impulsive pressures. These were comparable in both form and magnitude with those from other wave impact studies. The type of impact pressure experienced by the cliff toe was dependent on the sensor elevation relative to the still water depth.

7.3.2. Vertical impact pressure profiles

The vertical pressure distribution and the maximum pressure (P_{max}) are both critical input elements in coastal behaviour and erosion models (e.g. Castedo *et al.*, 2012; Matsumoto *et al.*, 2016) as they dictate the change in pressure with elevation up the cliff. To identify these variables in my data, I coupled each of the discrete impact events with an individual wave impact to create a full pressure profile comprising of the combined pressure response from each of the sensors (Section 6.3.5). In this section I calculate wave pressure profiles and the elevation of maximum pressure (E_{max}) for each wave in order to assess whether current approaches to estimating impact pressure profiles are supported by my data. In addition, I evaluate how wave impact force (J) over the full measured profile – a common alternative input into coastal erosion models – differs from impact pressure (P).

Minikin (1963) developed a model for predicting the magnitude and vertical distribution of impact pressures against a vertical breakwater (Section 2.2.4). The pressure peak was predicted to occur at the still water depth (d_{cliff}) and decay parabolically to zero between the wave trough and crest, effectively the zone of wave front impact. The precise attributes of the parabolic curve were not given. The model infers that the total impact pressure profile is the sum of the hydrostatic and dynamic components. These are the water weight defined by the depth to the wave crest, and the additional pressure created the instantaneous change in velocity of water on impact respectively (Whillock, 1987) (Figure 7.5).

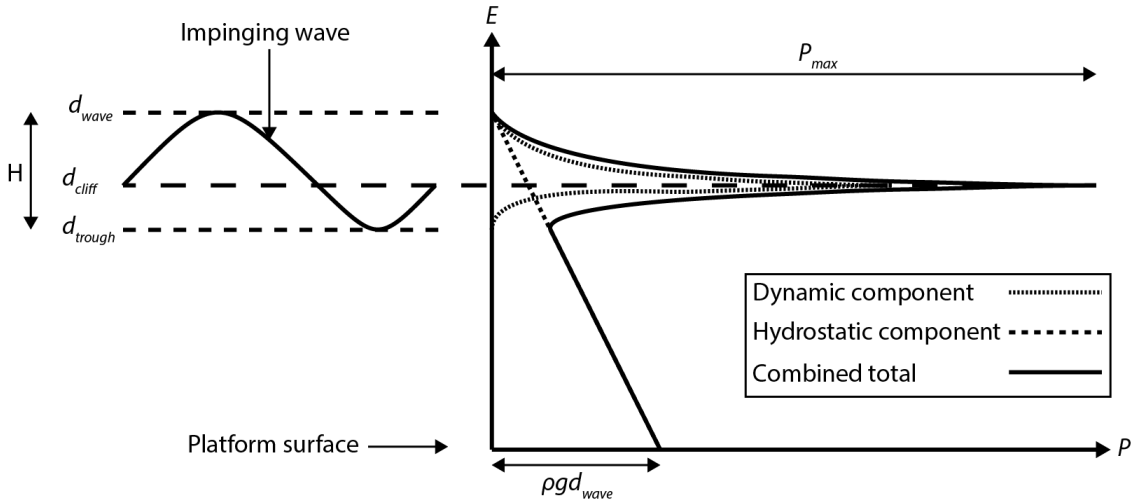

Figure 7.5: Schematic of wave impact pressure on a vertical wall outlined by Minikin (1963). Pressure (*P*) increasing to the right is induced up the wall according to elevation *E* by an impinging wave of height *H*. The maximum pressure (P_{max}) occurs at still water depth (d_{cliff}), and comprises of the sum of the hydrostatic and dynamic components of the impact. The hydrostatic component is the product of the water weight (ρg) and the depth to the wave crest (d_{wave}) and hence increases linearly with *d*. The dynamic component occurs at the impacting wave front, peaking at d_{cliff} and diminishing parabolically between d_{wave} and the trough depth (d_{trough}). Adapted from CERC (1984).

7.3.2.1. Hydrostatic and dynamic pressure components

My study suggests that the Minikin (1963) model is somewhat simplistic. Figure 7.6 shows a selection of wave impact profiles across a range of wave heights and water depths. Where measured pressure (*P*) deviates from the estimated hydrostatic pressure component (P_{hyd}), the resultant pressure is the sum of both combined hydrostatic and dynamic pressures, and the impact is considered impulsive. Pulsating impacts (Figure 7.6E and I) only exhibit hydrostatic pressures. The elevations at which the dynamic pressure deviates from P_{hyd} are generally, but not exclusively, located between the wave crest and trough, following the model in Figure 7.5 (Minikin, 1963), yet they are rarely at the still water depth (d_{cliff}). Figure 7.6D is the exception to this.

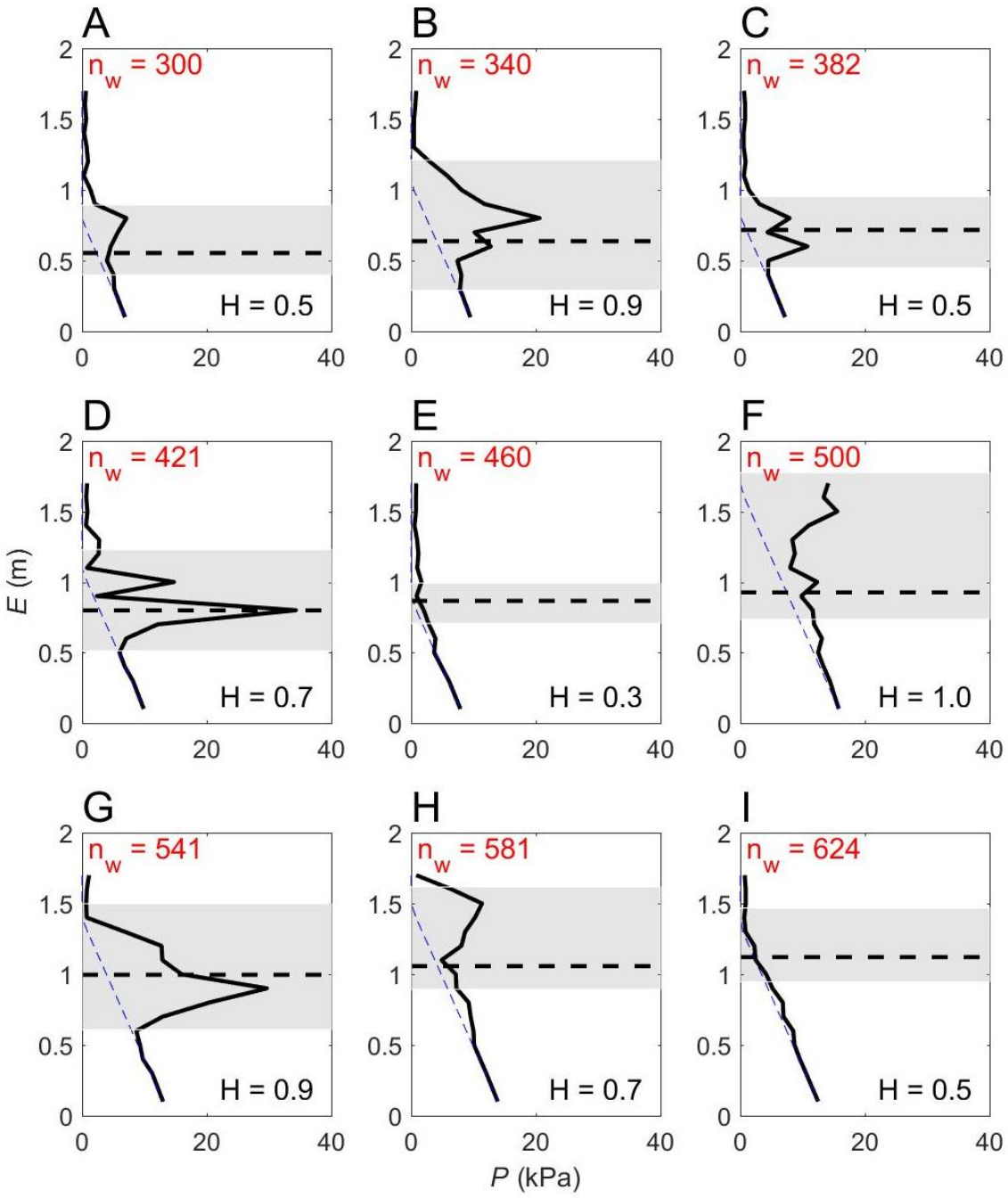

Figure 7.6: A-I) Impact profiles for a selection of incident waves from D_{5000} dataset (13/12/2016). Measured pressure (P) (solid black line) is shown alongside predicted hydrostatic pressure (P_{hyd}) (dotted blue line) up the sensor array. The shaded area denotes the location of the impacting wave front, or the zone between the wave crest and trough, with the still water depth (d_{cliff}) denoted by the dotted black line. Associated wave heights (H) and wave index number (n_w) are shown.

It is likely therefore, that dynamic pressures resulted from wave front impingement on the sensor array; non-dynamic pressures were found below the

wave trough as these sensors were fully inundated. This mechanism is generally agreed to be the primary source of high-magnitude impact pressures on coastal structures (Kirkgoz, 1982; CERC, 1984; Cuomo *et al.*, 2010). Some waves did exhibit enhanced pressure below the trough depth (Figure 7.6F and H); these were rarely high-magnitude and could have been associated with instability in the water column below the collapsing wave.

The dynamic pressure component (P_{dyn}) was found by subtracting P_{hyd} from P (Minikin, 1963). Of all the measured waves, 14% exhibited impulsive pressures, with a mean P_{dyn} of 11 $\pm$ 13 kPa and a maximum value of 122 $\pm$ 3 kPa. The distribution of P_{dyn} for all the impulsive waves was found to follow a finite-tailed generalised distribution (Figure 7.7). This indicates that very large dynamic pressures are relatively rare under the wave conditions studied in this setting, limited by the difficulties of monitoring more energetic conditions. For example, 7% of impulsive impacts exceeded the largest P_{hyd} value, 26 $\pm$ 3 kPa, corresponding to a wave crest depth (d_{wave}) of 2.6 m. This constituted only 1% of all wave impacts measured. In turn, the largest d_{wave} measured in the study area was 5.1 m (d = 3.5 m, H_{RMS} = 1.6 m, Figure 5.16), which would impart a hydrodynamic pressure on the cliff toe at the platform surface of approximately 52 kPa (Equation 2-9). As such, only 1% of impulsive impacts – 0.15% of all impacts – exceeded this.

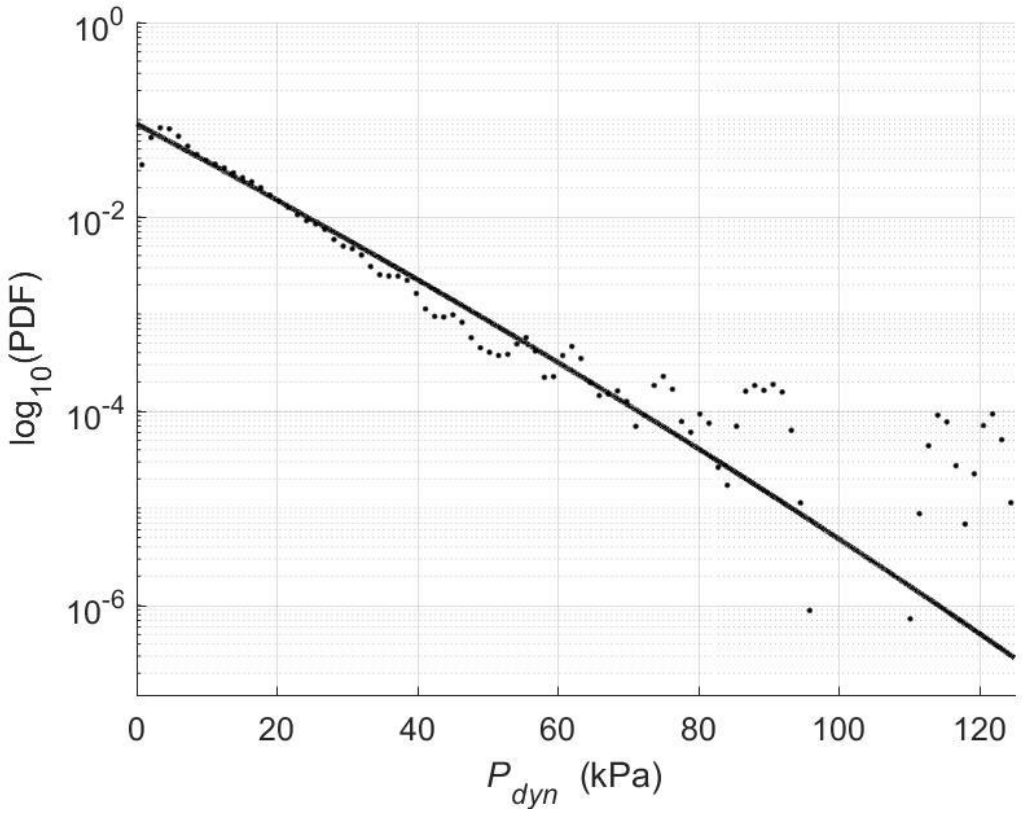

Figure 7.7: Probability density function of pressure increase associated with dynamic impacts (P_{dyn}). These data fit a generalised Pareto distribution (*shape* = -0.02, *scale* = 11.02) described by the solid black line, with a finite tail. The breakdown in the distribution where P_{dyn} > 80 kPa is probably due to very low data point frequency within this range.

7.3.2.2. Pressure distribution relative to the still water depth

The majority of research suggests that the elevation of maximum pressure (E_{max}) is located at or slightly above the still water depth (d_{cliff}) (Minikin, 1963; Oumeraci *et al.*, 1999; Bullock *et al.*, 2003), as is assumed by most rock coast erosion models (Section 2.3.1). In my study, E_{max} commonly occurred at d_{cliff}: the median value of $E_{max} - d_{cliff}$ was 0.0 ± 0.2 m (Figure 7.8). However, there was considerable variation in E_{max}, with some larger waves peaking at d_{cliff}+0.9 m. This was also observed by Crawford (1999), who found that although the Minikin (1963) model matched the profiles more closely than the Goda (1974) or Blackmore and Hewson (1984) models, considerable profile variation was apparent. Pressure often peaked above and below d_{cliff} and no clear pattern in

the distribution between d_{crest} and d_{trough} was apparent. There was also no discernible relationship between the location of E_{max} and other variables, including H, d and P_{max}.

Rock coast studies which assume wave impact pressures always occur according to the Minikin (1963) model described in Figure 7.5 (Sunamura, 1992; Stephenson, 1997; Noormets *et al.*, 2004) risk over-simplifying real-world distributions: considerable wave forcing may occur above and below d_{cliff}. However, the distribution in Figure 7.8 suggests that it is relatively safe to assume that E_{max} = 0 and pressure decreases parabolically from d to the wave crest and trough depths (Figure 7.5) for broad modelling purposes. It is also questionable as to whether small variations in E_{max} will have any major consequences.

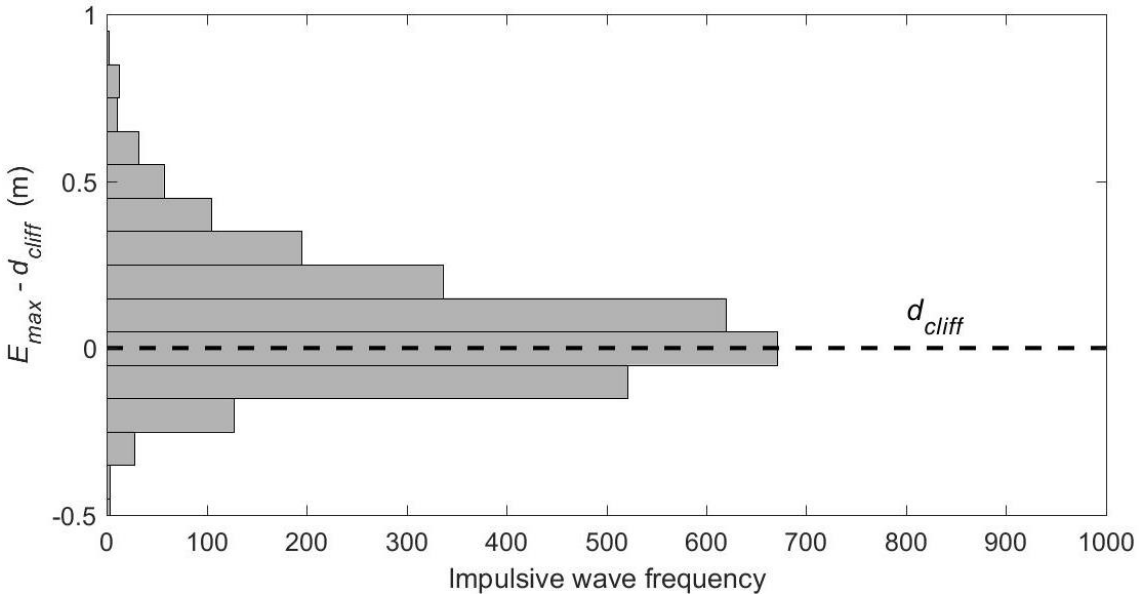

Figure 7.8: Frequency distribution of the elevation of impact pressure maxima (E_{max}) relative to the still water depth (d_{cliff}) shown by the dotted black line. Bins widths are equal to the sensor spacing (0.1 m). Median E_{max} = 0.0 ± 0.2 m. Pulsating impacts have been omitted as by definition for these waves E_{max} = 0 m.

7.3.2.3. Wave impact forces compared with pressure

An alternative measure of wave impact magnitude is wave shoreward force per m run (J), which considers the combined forcing across the wave profile. This

may provide a more stable measure of assessing wave impact profile distribution and be more representative of the total forcing where impact pressures are spatially distributed; for example, the double peak in Figure 7.6, n_w = 421. A wave which exhibits multiple large pressure peaks will exert more force over the full array than a wave with just one peak, even if the latter is larger, ergo a larger P_{max}. Impact force is commonly used in wave impact experiments (Allsop and Calabrese, 1998; Cuomo *et al.*, 2010) and force maxima for a given impact (J_{max}) have been shown to occur approximately at the time of P_{max} (t_{max}) (Kirkgöz, 1992).

Using the wave impact example from Figure 7.4, Figure 7.9 illustrates the change in J alongside P during wave impingement. J exhibited a relatively rapid increase peaking at 2.1s (J_{max}) associated with dynamic force (J_{dyn}), followed by a gradual reduction. Each of the transient pressure peaks associated with impulsive pressures was associated with a concurrent, albeit smaller, force peak. Relative to the general trend of the full impact time-history, the J peaks were considerably smaller than P. The ratio P_{max}/P_{dyn} for this wave is ~0.6, whereas J_{max}/J_{dyn} is ~0.3, suggesting that J is less sensitive than P to the impulsive mechanism.

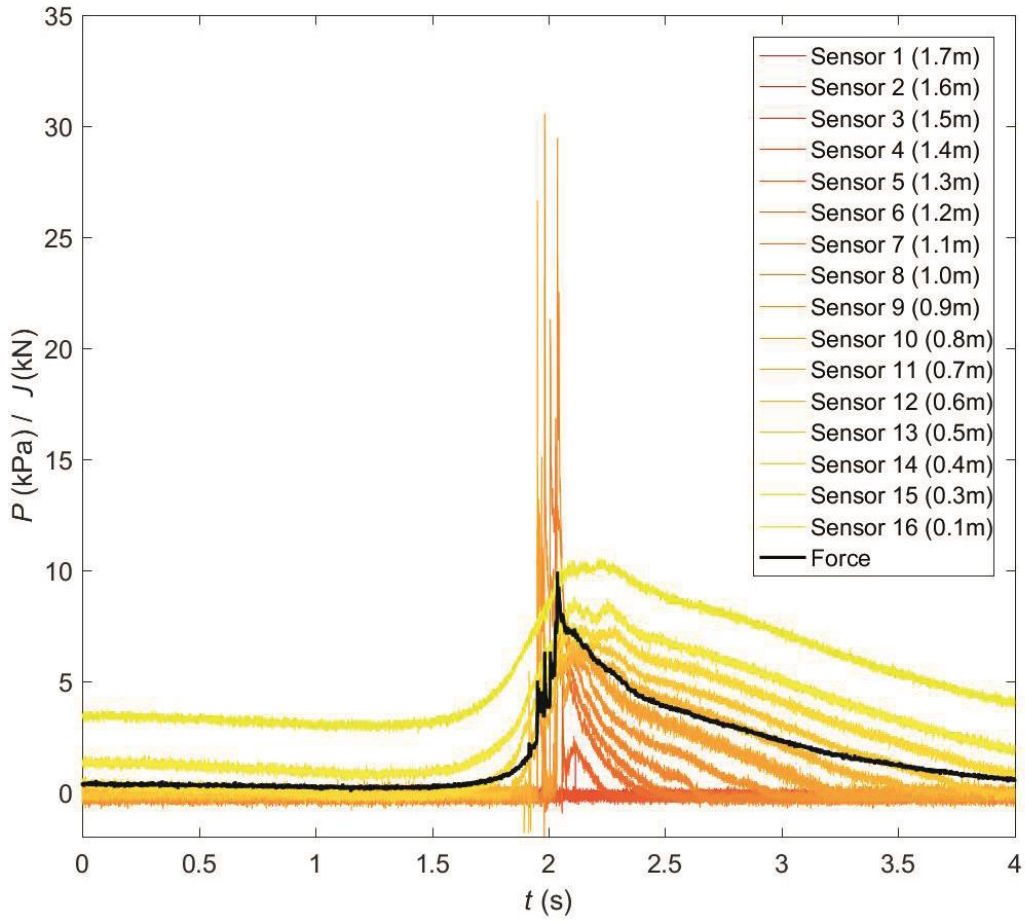

Figure 7.9: Wave impact pressure-time histories from Figure 7.4 (coloured lines, with redder lines representing sensors higher up the array) alongside the induced force (J) (kN per m) on the sensor array (black line) at 5000 Hz. Note the minor force peaks associated with each dynamic pressure spike on the sensors.

The multiple pressure peaks in Figure 7.9 suggest that t_{max} was temporally variable across the different sensors, with impulsive pressure peaks occurring up to 0.2 s apart. This implies that additional sensors placed between the existing ones would smooth out the gaps here. Instantaneous force was influenced by the pressure magnitude of the full water column; since only one sensor is exhibiting dynamic pressure at any given value of t, J at time t was only influenced by one dynamic pressure peak. This spatial and temporal variation in pressure produced a relatively small variation in J. If the impulsive peaks all occurred simultaneously (t_{max} = constant) then J_{max} would be correspondingly higher. This may explain why impacts generated by vertical

wave fronts impinging on vertical faces – so-called perfect breaking – are thought to be the most effective (Kirkgoz and Akoz, 2005). In this case, pressures are more likely to occur simultaneously and hence produce larger forces. Consequently, my results suggest instantaneous force on the array is generally lower magnitude and more stable than instantaneous pressure, and is less sensitive to the dynamic pressures associated with impulsive wave impacts.

7.3.2.4. Summary

Wave impact pressures are comprised of hydrostatic and dynamic pressure components. Impact profiles for my data show that dynamic pressures associated with wave impacts followed a finite-tailed generalised distribution. This indicates that large (>100 kPa) dynamic pressures are very rare under the conditions studied. In general, dynamic pressures occurred between the wave crest and trough and exhibited impulsive impact characteristics. The modal elevation of maximum pressure was at the still water depth, but variations of up to 1 m either side of this value also occurred. In addition, wave force was shown to be considerably less sensitive to high-magnitude peaks than wave impact pressure.

7.3.3. Controls on wave impact characteristics

The raw pressure output from the sensors over a single high tide (Figure 7.2) suggests that water depth is a key control on pressure magnitude. Furthermore, wave height is commonly used as a proxy for wave impact intensity (Barkwith *et al.*, 2014) and it is often assumed that larger waves exhibit higher erosive potential. As such, unpicking the relationship between wave height, water depth and wave impact magnitudes is key to understanding their potential as forcing mechanisms. In this section I assess the extent to which wave height and water depth can predict impact pressure magnitudes. This will enable me to compare this with the wave breaking condition in order to establish the extent of the influence of wave breaking on impact pressure. This will later feed into an empirical probabilistic approach to predicting wave pressures.

7.3.3.1. Impact pressure and depth

When considering changes in pressure maxima (P_{max}) with still water depth (d_{cliff}), a clear pattern in the distribution of pulsating and impulsive impact pressures emerges (Figure 7.10). Each dataset exhibited a different maximum measured depth (d_{max}), which was related to the maximum tide height during the deployment. Impulsive waves were clustered where d_{cliff} is low, and became less common as d_{cliff} increased. P_{max} for these were commonly – but not exclusively – considerably higher than pulsating pressures at the same depths. There was a general pattern of relatively low P_{max} where $d_{cliff} < 0.2$. These values ranged between $P_{max} \approx 1 – 10P_{hyd}$; values became less frequent with magnitude, following the distribution in Figure 7.7. The proportion of waves that were impulsive was also highly variable between datasets (5.3 – 26.5%), with more occurring with, in general, higher significant wave height (H_s) and P_{max} values. The depth range over which impulsive impacts occurred also increased with H_s, which will be explored in more detail in section 7.3.4.

Conversely, pulsating waves became more frequent with d, with the associated P_{max} increasing linearly. This pattern was also observed by Crawford (1999) and occurs due to the linear hydrostatic relationship between P and d_{cliff} (Equation 2-9). For my data, the highest instantaneous P values occurred at the base of the array. The scatter around the linear trend is due to a combination of sensor noise and the variation in d_{crest} between waves. Datasets with larger H_s therefore exhibit a wider range of pulsating P_{max} values (for example, Figure 7.10, dataset 4).

My results show that water depth in part dictates the magnitude, distribution and characteristics of wave impacts, yet the wide range of P_{max} values also appears to be influenced by H_s.

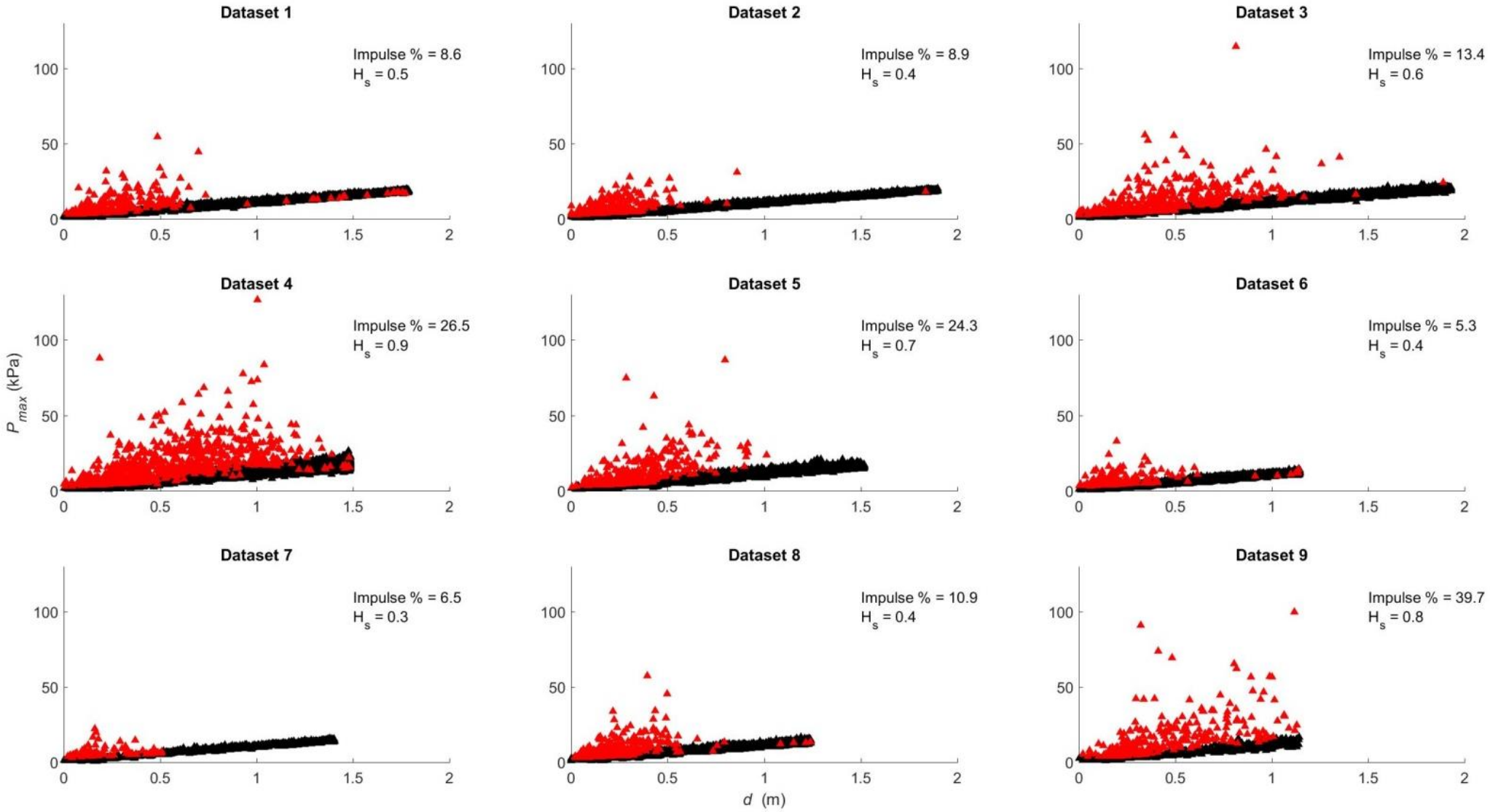
Dataset 1
Impulse % = 8.6
H_s = 0.5
Dataset 2
Impulse % = 8.9
H_s = 0.4
Dataset 3
Impulse % = 13.4
H_s = 0.6
Dataset 4
Impulse % = 26.5
H_s = 0.9
Dataset 5
Impulse % = 24.3
H_s = 0.7
Dataset 6
Impulse % = 5.3
H_s = 0.4
Dataset 7
Impulse % = 6.5
H_s = 0.3
Dataset 8
Impulse % = 10.9
H_s = 0.4
Dataset 9
Impulse % = 39.7
H_s = 0.8
P_{max} (kPa)
d (m)
0
50
100
0.5
1
1.5
2

Figure 7.10 (previous page): Wave impact pressure maxima (P_{max}) against still water depth (d_{cliff}) for all datasets (1-9, refer to Table 7.1 for dates and wave conditions). Both pulsating (black) and impulsive (red) impact categories are shown. For each dataset, the significant wave height (H_s) and the percentage of all wave impacts which are impulsive are also included.

7.3.3.2. Impact pressure and wave height

A less distinct pattern emerges when comparing wave impact pressures with wave height (H) (Figure 7.11). Whilst the largest dynamic pressure component (P_{dyn}) value (116 kPa) occurred due to the largest H (1.9 m), and a significant positive correlation was found ($p > 0.02$), the data exhibit a low coefficient of determination ($r^2 = 0.14$) (Figure 7.11A). For example, the second-highest pressure was produced by a wave almost half the size of the largest one (P_{dyn} = 106 kPa, H = 1.0 m). These pressures appear highly stochastic in nature, suggesting that impulsive wave pressures associated with relatively small waves (<1 m) are comparable in magnitude with those of larger waves.

Pulsating wave pressures exhibited a considerably more predictable variation with H (Figure 7.11B). A statistically significant positive linear correlation was found with a relatively high coefficient of determination ($r^2 = 0.67$). The gradient of the line ($y = 0.43x$) approximately equals the predicted hydrostatic response from half the wave height ($\rho gH/2 = 5.0$), as the incident wave elevated the water surface equal to the wave amplitude. The discrepancy between the two may express the shoaling wave skewness (Herbers *et al.*, 2003), whereby the crest height is higher relative to d_{cliff} than the trough depth (Miles, 2013). Scatter around the trend line, albeit with a very small number of outliers constituting <0.1% of waves, fits within the ± 3 kPa sensor uncertainty. It is likely that with a much smaller error margin, the r^2 value for the fit would be substantially higher.

These results suggest wave height within the range studied (0.1 – 2.1 m) is a robust predictor of pulsating impact pressure magnitudes, as would be expected using Sainflou (1928)'s method, but a relatively poor predictor of impulsive pressures. As such, my results support the notion that impulsive wave pressures are stochastic, and pulsating wave pressures are deterministic in nature.

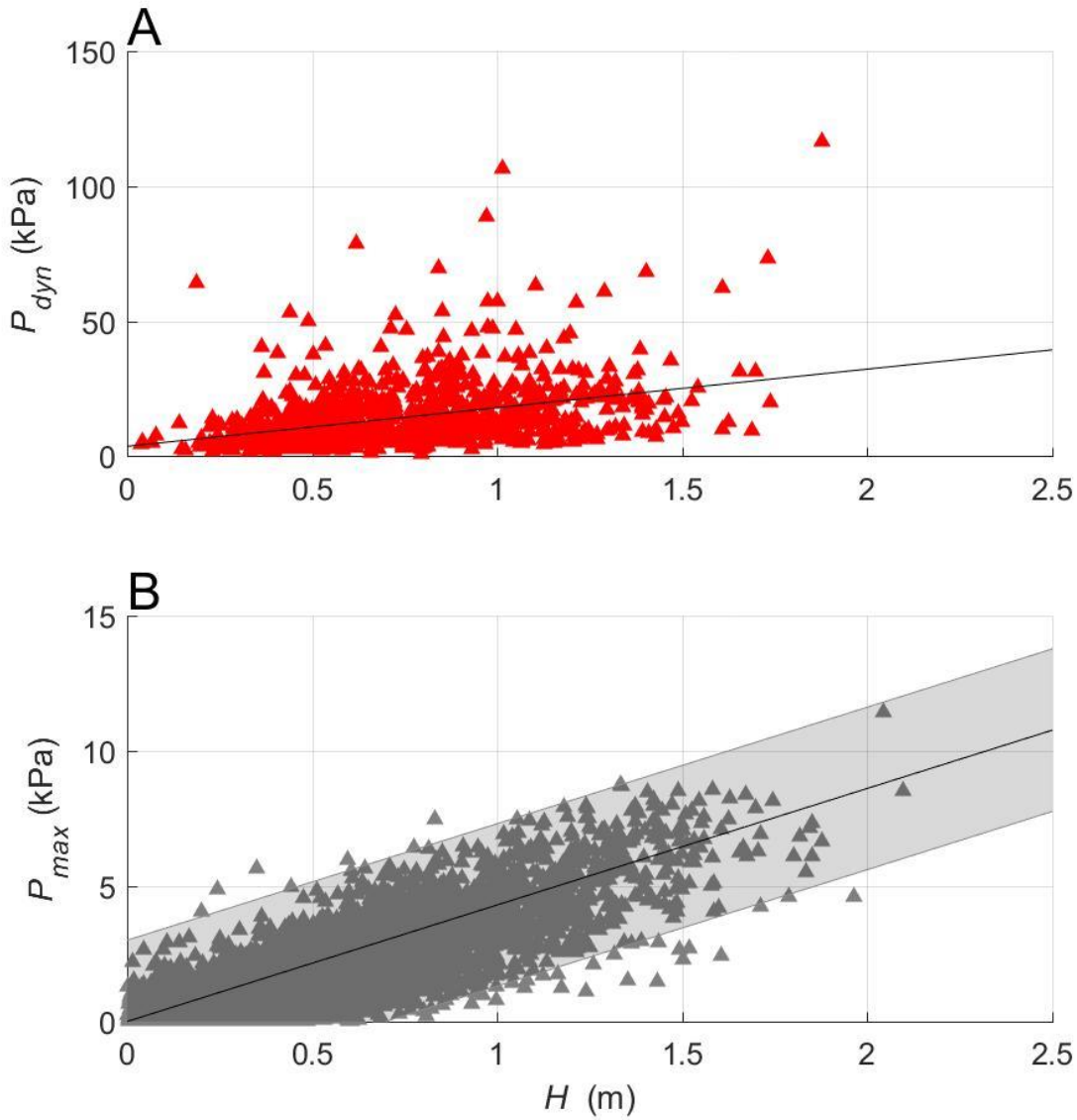

Figure 7.11: A) Impulsive wave dynamic component (P_{dyn}) variation with wave height (H) across all datasets, with linear fit (y = 14x + 3, r^2 = 0.14, p < 0.02); B) pulsating wave pressure with depth component removed, representing the maximum pressure (P_{max}) induced due to the wave impingement, with linear fit (y = 4.3x, r^2 = 0.67, p < 0.02) ± 3 kPa, with error bound shown in grey. Note the change of y-axis scale.

7.3.3.3. Wave height, water depth and the breaking criterion

Two key principles are known from the literature: waves at the cliff toe change from broken, breaking and unbroken conditions as water levels rise (Trenhaile

(2002) and Chapter 5 above); and breaking and broken waves are most likely to produce impulsive wave impacts (Miller *et al.*, 1974; Bullock *et al.*, 2005).

Whilst the lack of wave breaker shape information, such as in-situ video footage of wave impacts (Crawford, 1999), prevents wave breaking conditions from being established, it is possible to infer breaking conditions from the time-dependent water depth conditions and wave heights at the site. The breaking criterion (γ) was calculated in Chapter 5 as 0.6. As such, if H/d exceeds the breaking criterion for any given wave, it is likely that this wave is broken or breaking on impact with the sensor array. These calculations become difficult when applied to very shallow water depths, as propagating bores, particularly those in the swash zone, are difficult to measure and can be many times larger than d. As such, this breaker condition calculation is most reliable in deeper water ($H/d < 2.5$).

In my study, impulsive pressure magnitudes were highly sensitive to H/d (Figure 7.12). Waves below the breaking criterion were almost exclusively pulsating, as d was large enough in relation to H to not force breaking. Waves above this envelope did exhibit large impulsive pressures, yet most waves were still below the P_{hyd} values that would be expected. These results indicate that whilst impulsive pressures almost always occur when waves are breaking or broken, these conditions mainly produce pulsating impacts. Where H/d is very large (>2.5), waves are likely to be bores within the swash zone impacting the sensor, and are impulsive or pulsating but generally low magnitude.

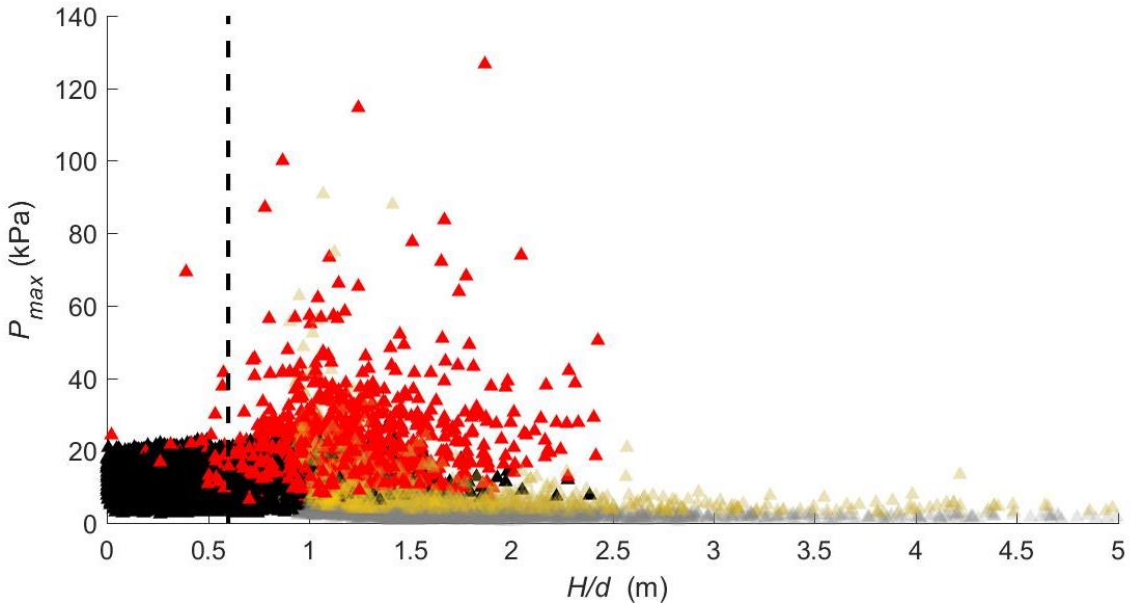

Figure 7.12: Combined wave height / water depth ratio (*H/d*) for each wave in all datasets and their corresponding maximum pressure values (P_{max}). Impulsive (red) and pulsating (black) loads are shown. *H/d* estimates, based on extrapolating *d* to zero and using the breaker criterion to find the maximum *H*, are shown in faded yellow and grey data points for impulsive and pulsating loads respectively. The breaker criterion (γ = 0.6) is shown (black dashed line).

7.3.3.4. Impact characteristics and wave shape

Waves with a high *H/d* were generally quasi-sinusoidal pulsating impacts (Figure 7.3A). These tended to evolve into skewed sinusoidal impacts (Figure 7.3B) as *H/d* decreased. This is most likely a reflection of the increasing wave asymmetry, which occurs as waves become more influenced by bottom friction (Miles, 2013). Asymmetric waves exhibit steeper wave fronts, which would induce a more rapid rise time for an impacting wave on a sensor, and increase the time the pressure takes to return to air pressure. As d_{cliff} decreases, wave front steepening eventually drives the waves to break, although the precise limiting wave shape for breaking is still not known (Toffoli *et al.*, 2010).

Single-peaked impulsive impacts (Figure 7.3C) were more common when waves were closer in *H/d* to the breaking criterion. Therefore, they appear to be associated with very steep, asymmetrical waves where the wave front is closer to vertical. This pattern was also observed by the majority of experimental

studies (Kirkgoz, 1982; Blackmore and Hewson, 1984; Oumeraci *et al.*, 1993; Bullock *et al.*, 2005). When the wave front is vertical, the water surface impacting the vertical surface is parallel. As such, all the shoreward momentum of the wave is transferred rapidly (Kirkgoz, 1995), rather than being imparted slowly and largely reflected as with pulsating impacts (Denny, 1951). The closer the wave front is to being parallel with vertical surface, the more likely this momentum transfer will be efficient and hence a higher overall pressure. This may explain why steeper waves seemed to impart the largest impact pressures in my study.

Chaotic impulsive impacts (Figure 7.3D) appeared to be more common during the initial stages of the rising tide and the corresponding final stage of the falling tide, where broken waves propagate landwards as waves of translation. Broken waves are generally highly aerated, which appears to have introduced a highly chaotic nature to the pressure signals. Chaotic impacts were also found by Mai (2017) for broken waves impacting a rigid wall in a wave tank. They were also found to occur due to enclosed air pockets in zones of high turbulence by Grüne (1988) on a sloping sea dyke. Whilst broken waves and chaotic impacts commonly exhibited dynamic pressures in my study, they tended to be lower magnitude than those associated with single-peaked pressures on breaking waves (Figure 7.12). This may be due to the higher aeration associated with turbulent bores cushioning the water hammer effect, as explained in Section 2.4.1.3.

The general pattern of impact pressure characteristics that emerged from these data is summarised in Figure 7.13. The four types of alternating air/water impacted shown in Figure 7.3 can be categorised into four zones of occurrence controlled by H/d. As the tide reached the cliff toe (d = 0), broken waves in the form of turbulent bores impacted the base of the cliff in the swash zone. These imparted chaotic impulsive pressures. As d increased, larger bores arrived associated with higher magnitude pressures. Once $H \approx d$, steep, breaking waves impact the cliff with high-magnitude peaked impulsive pressures. When $H \approx d$, waves became progressively more sinusoidal, less steep and therefore became more likely to impart skewed to quasi-sinusoidal impacts on the cliff. An increase in incident H increased the duration the cliff toe underwent turbulent

bore impacts, shifting the breaking criterion later in the rising limb. If $H/d_{max} \approx H/d$, breaking waves will impact the cliff at the maximum tide height and therefore will exist for longer at the cliff base; this did not occur in my study however.

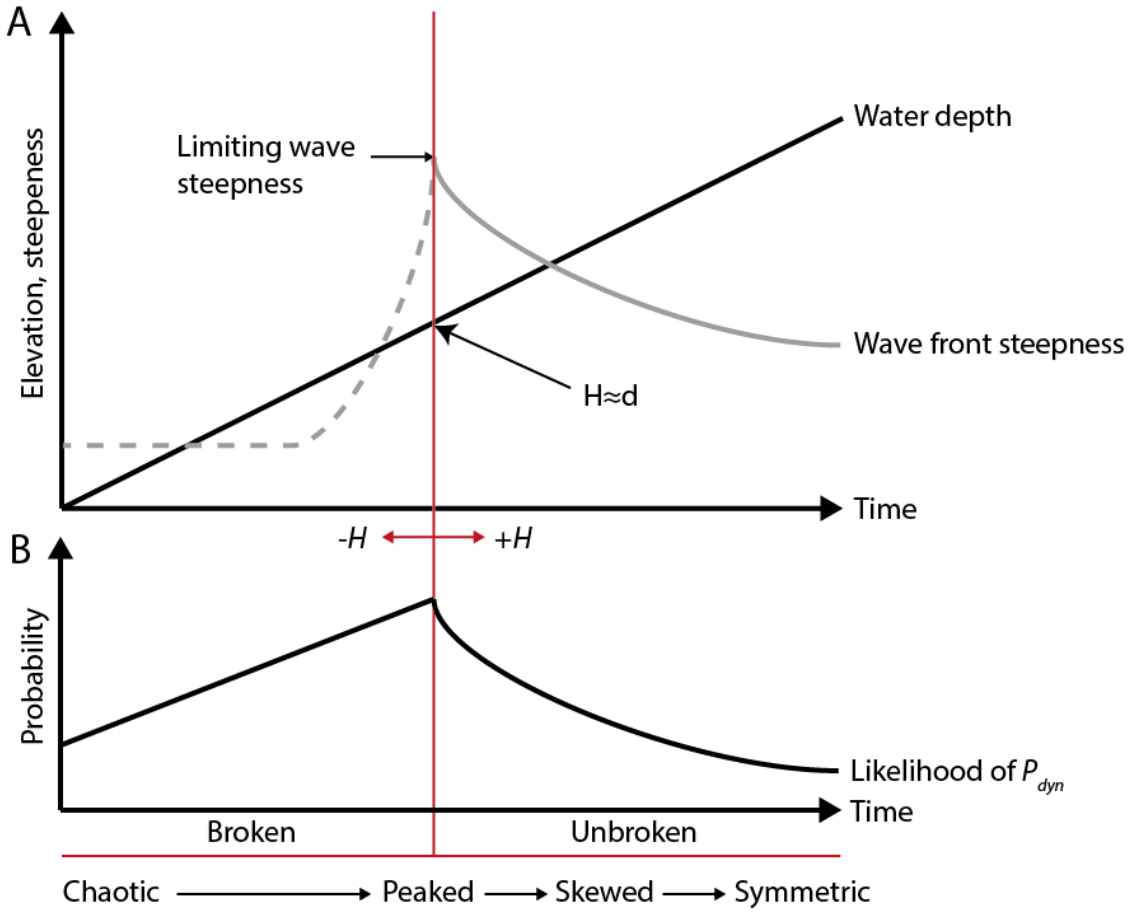

Figure 7.13: Conceptual model of A) wave steepness and B) characteristic pressure responses during a rising tide. As water depth increases, wave front steepness increases non-linearly as waves change from turbulent bores to breaking (at the critical H/d). The likelihood of dynamic pressures (P_{dyn}) occurring increases and pressure responses progress from chaotic to peaked up to the critical H/d. With deepening water depth, wave front steepness declines such that waves no longer break, dynamic pressures become less likely and pressure responses become skewed, then symmetric. Increasing wave height (H) leads to a longer duration of broken waves and vice versa.

A weak positive relationship was found between H and P_{max} (Section 7.3.3.2). Newton's second law dictates that a larger wave should have larger mass and

therefore a larger momentum, so should produce a higher overall force due to the momentum exchange with the surface. This assumes that all the wave momentum is transferred to the surface and none is lost through reflection and turbulence (Blackmore, 1982). The fact that these measurements were taken in a real wave environment suggests that they were subject to considerable aeration, oblique incidence and influence from reflected waves, and therefore would exhibit much variation around the maximum momentum transfer (Blackmore and Hewson, 1984).

7.3.3.5. Summary

The occurrence of impulsive impact pressures was shown to be highly sensitive to the ratio between wave height and water depth. Pulsating pressures could be reliably predicted using the hydrostatic equation (Equation 2-9), but impulsive pressures were poorly correlated with wave height. A conceptual model was derived which suggests that as water depth increases during rising tide, wave front steepness increases up to the break point, increasing the likelihood of dynamic pressures. After the break point, waves become unbroken and pulsating pressures dominate. Whilst wave height does not seem to be a dominant control on impact pressure magnitudes, it does dictate the location of the break point relative to water depth here.

7.3.4. Predicting wave impact pressures

In the previous section I showed that the characteristics of wave impacts are dependent on a combination of deterministic mechanisms: pulsating impacts; and stochastic processes: impulsive impacts. Predicting the occurrence, magnitude and vertical distribution of the dynamic pressure component (P_{dyn}) with the known variables is therefore challenging. The difficulty in predicting these deterministically has been observed previously (Denny, 1951; Rossi, 1984; Ramachandran *et al.*, 2013). Nevertheless, there is a wide variety of predictive formulae for both pulsating and impulsive pressures, outlined in Chapter 2. In this section I consider the distribution of impact pressures within discrete *H/d* bins, which in turn will enable a full probabilistic assessment of impact pressures within the measured range of conditions.

7.3.4.1. Deterministic and probabilistic predictive models

In many cases, applying previously established formulae to the present study is problematic, as the breaking condition of each individual wave is not explicitly known. Moreover, it is clear that very different magnitudes and spatial distributions exist for waves that are nominally identical, both for my data and in other studies (Grüne, 1988; Peregrine, 2003; Bullock *et al.*, 2007). These predictive formulae are almost exclusively derived from studies pertaining to vertical coastal structures and are therefore based on the use of a "design" wave height: an attempt to predict the maximum possible loading on the structure over its lifetime. As such, they are of little value in predicting pressure characteristics for an individual wave, or even the average pressure expected of wave impacting a cliff over a specified duration.

For example, the formula used by Tsujimoto (1987) and Matsumoto *et al.* (2016) for the prediction of pressure magnitudes for breaking waves at coastal cliffs is deterministic and derived from Ross (1955) (Equation 2-8). Applying this formula as a predictive tool for all breaking wave pressures would rely on the assumption that all breaking waves induce dynamic pressures, and that all dynamic pressures induced by the same nominal breaking wave height are of the same magnitude. The data from my study and those of others (Kirkgoz, 1991; 1995; Oumeraci *et al.*, 1999; Muller *et al.*, 2008) suggest that neither of these assumptions is valid, as both the occurrence and magnitude of dynamic pressures are largely stochastic.

Whilst it may be possible to more accurately predict impact pressures using very detailed knowledge of wave free surface shape, aeration, incidence angle and other metrics, these are difficult to measure in the field.

7.3.4.2. Statistical distribution of pressure maxima

In order to determine the distributions of pressure maxima (P_{max}) under different hydrodynamic conditions, I sorted the complete P_{max} dataset for all deployments into *H/d* bins with width 0.1 between *H/d* = 0.1 - 2.5. This allowed a minimum of 50 data points per bin, allowing a large enough dataset within each bin whilst maintaining a reasonable sensitivity between conditions within error measurements for the wave gauges (Chapter 5). *H/d* values up to 2.5 were

used because the area of interest where large values of P_{max} occurred lies within this range (Figure 7.12). Additionally, values above this were predicted, rather than measured, and did not exhibit values of P_{max} larger than ~10 kPa.

These data fit a generalised Pareto distribution (Figure 7.14), which is characterised by a heavy-tail and is skewed. The parameters vary between different bins. A chi-square goodness-of-fit test showed that *H/d* ratios up to 1.8 agreed with the generalised Pareto distribution to the 0.05% significant level. Above this value, the smaller number of data points (< 250) meant that there were not enough degrees of freedom to calculate the significance level. However, it is clear from Figure 7.14 that above this *H/d* value these data continue to broadly adhere to the distribution.

The fit parameters for scale (σ), shape (k) and location (θ) for the distribution varied with *H/d* (Figure 7.15). These values represent the horizontal width, the distribution shape and horizontal location respectively. In generalised Pareto distributions the median is always the lowest value: in this case ~2 kPa. The θ parameter for all fitted distributions is 0, indicating the median value is constant. This suggests that low magnitude wave impacts were consistently the most common, irrespective of *H/d*. The σ value decreased as *H/d* increases to 2.5, which represents the increasing magnitude of P_{max} throughout the distributions and the broader range of values once impulsive pressures started occurring. The k value increased throughout this range, suggesting a change in the steepness of the distribution, with steepness increasing with *H/d*. It follows that larger values were more common with increasing *H/d*. The change in k from negative to positive at *H/d* = 1.5 is noteworthy, as it shows a transfer from finite to polynomial tails, representing a higher likelihood of impulsive pressures.

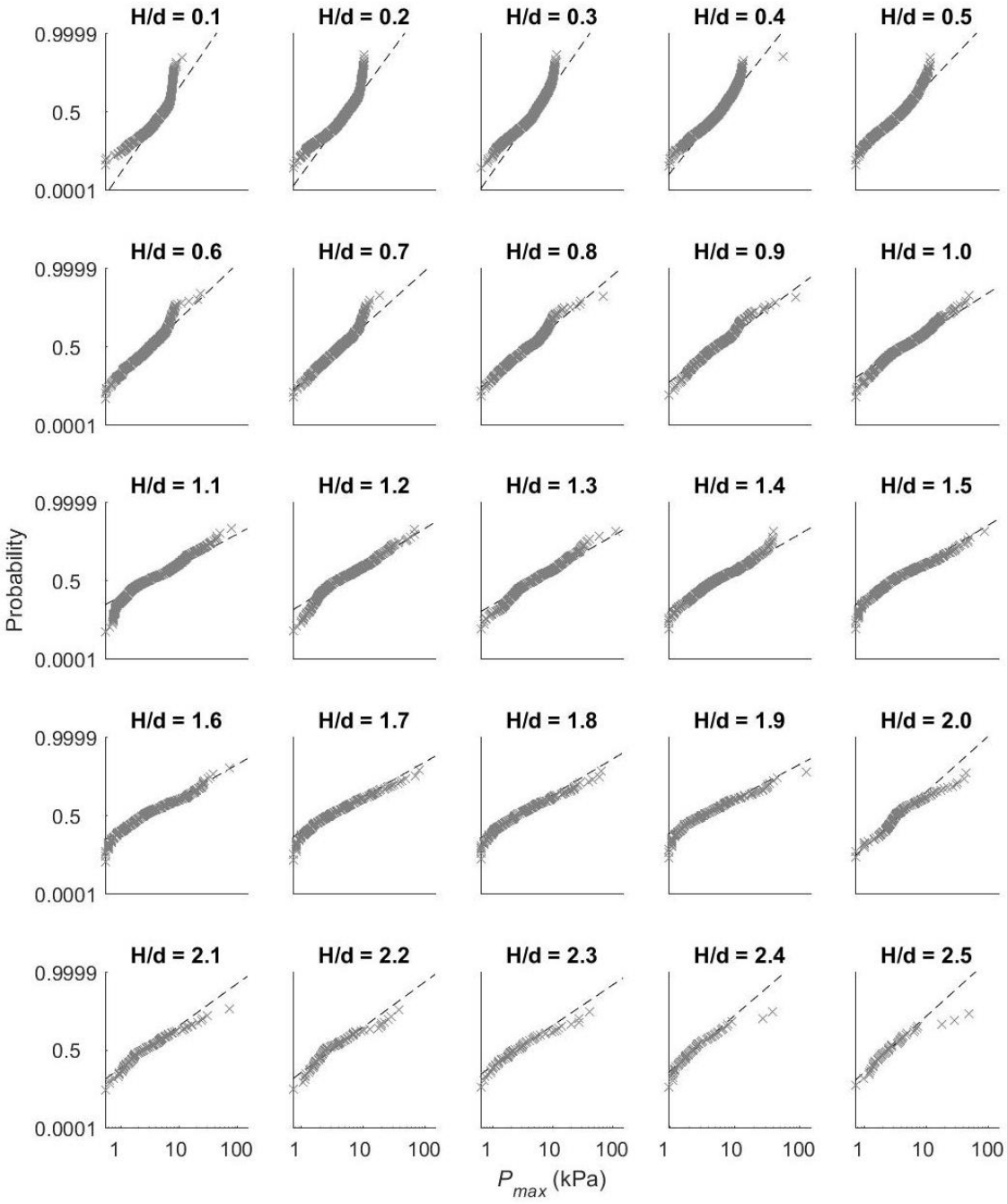

Figure 7.14: Probability plots comparing empirical P_{max} (data points) within each *H/d* bin between 0.1 and 2.5 with a generalised Pareto distribution (dashed line).

These *H/d*-dependent parameters show that the stochastic nature of wave pressures varies under changing dynamic conditions, and that the statistical properties of the resultant distributions of pressures may be estimated.

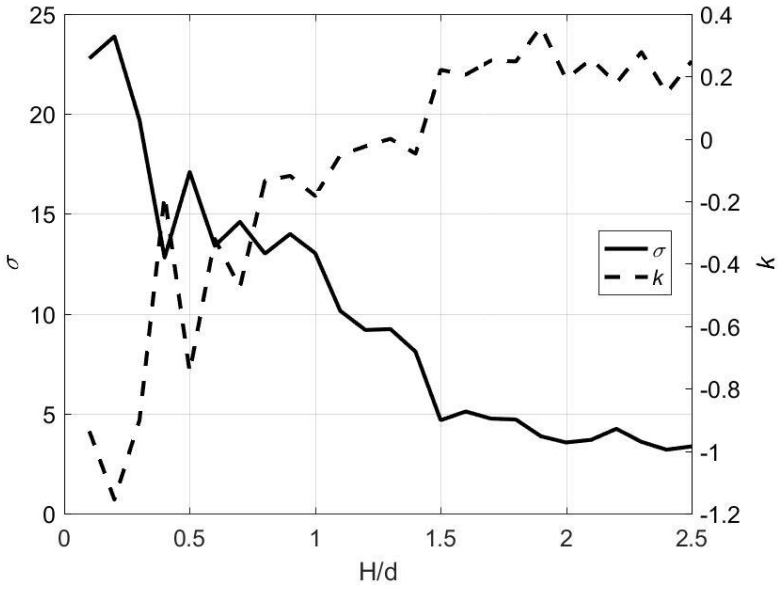

Figure 7.15: Parameter values for the generalised Pareto distribution for each *H/d* bin. The decreasing scale (σ) parameter suggests a broadening distribution; the increasing shape (k) parameter indicates a steepening distribution, as more values occupy the lengthening upper tail.

These distributions are different from those of other experiments. Grüne (1988) measured wave impact pressures on sloping sea dykes on the German Bight coast and found a lognormal distribution of P_{max} values from 520 waves over an 80-minute duration of approximately stable d and H_s conditions. Lognormal and generalised Pareto distributions are statistically similar, as both have linear or near-linear log densities, and nearly linear log cumulative density functions (Malevergne *et al.*, 2011). However, the lognormal distribution of Grüne (1988) shows that the upper tail is much longer, suggesting a much lower occurrence of small values of P_{max}. This may be explained by the dyke's sloping surface, which is known to produce different responses to wave impact as compared to vertical surfaces (Kirkgoz, 1991), as well as variations in distribution fit errors with geometry (Wilde, 2017).

Weibull distributions are commonly found in flume experiments, for example for unbroken, overtopping waves on a storm wall (Van Doorslaer *et al.*, 2017). Allsop *et al.* (1996) demonstrated that P_{max} values on vertical faces followed a Weibull distribution only when pulsating pressures were considered. Impulsive

loads caused the lower tail to deviate from the Weibull line. This can be observed in my data: in Figure 7.14, *H/d* bins where pulsating loads are dominant show a deviated lower tail (0.1 < *H/d* < 0.8). They also follow a Weibull tail more closely, underestimating the higher P_{max} values whilst maintaining a generalised Pareto distribution. When *H/d* increased, impulsive waves were common and the upper tail follows the fit distribution more closely.

7.3.4.3. Maximum pressure exceedance level

Wave pressure and force maxima are often represented by the 1/250 (99.6%) exceedance level (Goda, 1974; Van Doorslaer *et al.*, 2017). This provides a more meaningful value for measuring forcing over a given duration of wave impact, rather than using a mean or median value for each bin given the non-normal distribution.

For the following analysis, I calculated the mean of the largest 250th percentile maximum pressure (P_{max250}) for a given value of *H/d* (following Allsop *et al.* (1996)) (Figure 7.16). P_{max250} reached a maximum value when 1 < *H/d* < 2 as shown by the smoothing curve. Below this range pressures were approximately half that of the peak range, as they represent the largest pulsating wave impacts, where *H/d* was too small to drive breaking and consequent impulsive loads (Figure 7.12). Where H/d > 2.5, waves were often impulsive but are considerably reduced in impact pressure, as P_{max250} can be seen to be consistently less than 10 kPa. These represent conditions where H >> d, usually as turbulent bores propagate landward. My results compare with the impulsive zone range of 0.93 < *H/d* < 1.43 found by Bullock *et al.* (2007), which corresponds approximately with the peak in Figure 7.16.

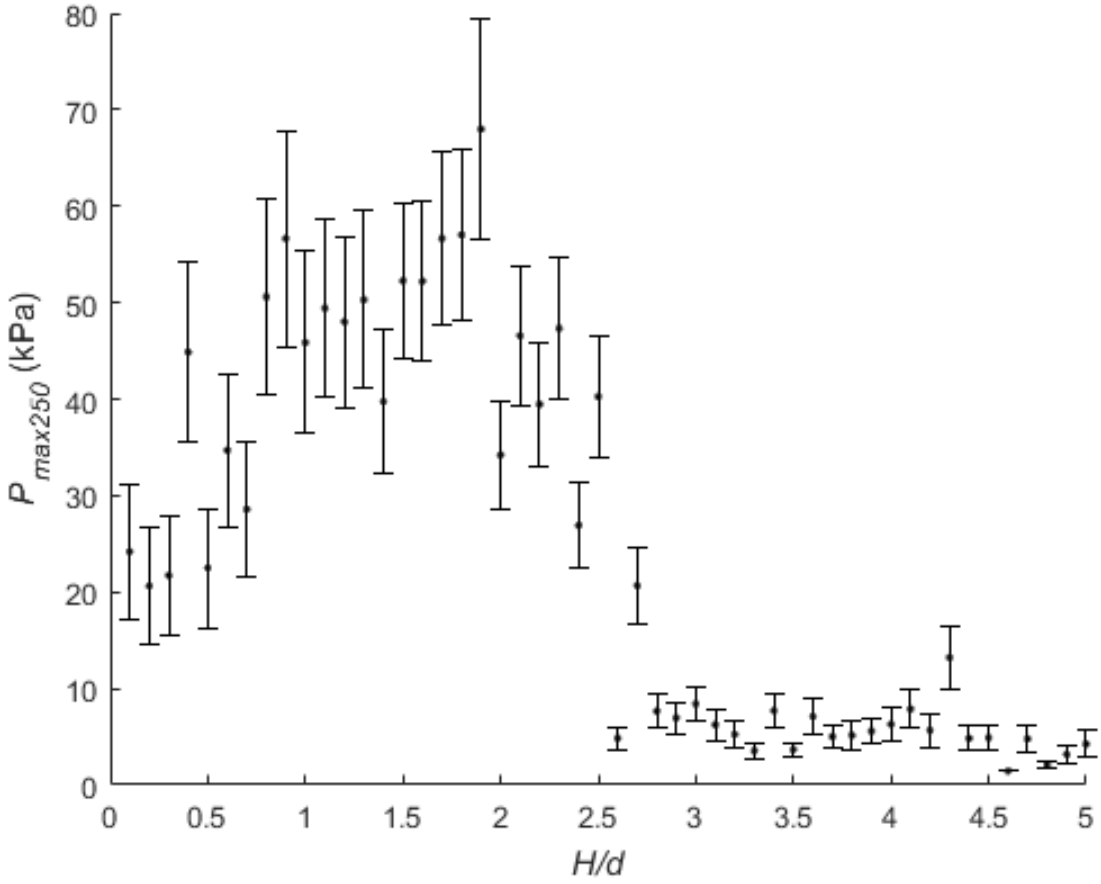

Figure 7.16: Values for the highest 1/250 P_{max} (exceedance level 99.6%) (P_{max250}) within each wave height / water depth ratio (H/d) bin. Standard deviations for each bin are shown with error bars.

My data suggest that there is an optimum range of H/d, corresponding to values of approximately 1 – 2.5, whereby there is a higher probability of larger values of P_{max}. When considered alongside the generalised Pareto distribution in Section 7.3.4.2, this data supports the notion that the longer duration of wave impact within any given wave and depth condition increases the likelihood of very large impulsive pressures occurring at the cliff toe (Müller *et al.*, 2008). Conditions which fall outside of the optimum H/d range may not follow this principle, as unbroken, pulsating impacts and broken, turbulent impacts in the swash zone appear to be governed deterministically. This is seen at either side of the peak in Figure 7.16.

7.3.4.4. Summary

Hydrodynamic wave forcing at the cliff toe appears to be governed by a combination of deterministic impulsive and stochastic dynamic mechanisms. I have shown that wave height and water depth may play a key role in determining the occurrence of stochastic impact pressures as well as their magnitude with a distribution over a given duration. My data suggest that impulsive impact pressures cannot be predicted deterministically without a much greater understanding of the precise hydrodynamic conditions during wave impact. As such, a probabilistic treatment of the dataset showed that impacts followed a generalised Pareto distribution, the parameters of which varied with the *H/d* ratio. Very large (99.6% exceedance level) pressures were also shown to be larger when *H/d* was between 1 and 2.5. This suggests that since P_{max} values followed a known distribution, it may be possible to predict overall hydrodynamic forcing over a long duration (000's of waves) despite the unpredictability of individual impact magnitudes.

7.4. Discussion and implications: impact pressures and wave forcing

My investigation has directly measured the pressure response of sensors at the cliff toe to hydraulic wave action. A broad range of impingement pressures, each with highly variable magnitude, vertical distribution and frequency, were observed. The results have provided empirical evidence that impulsive pressures exist on rock coast cliffs, and that their occurrence for a given point on the cliff toe is at least partly dependent on conventional hydrodynamic variables. Whilst in Chapter 5 I showed that waves breaking directly on the cliff toe are a frequent occurrence on macro-tidal rock coasts, these results provide further evidence for the common assertion that breaking waves induce wave pressures which can be considerably higher than unbroken or broken waves (Trenhaile, 2000; Sunamura, 2015).

In the following discussion I attempt to reconcile the measurements from my study with investigations from other researchers, with a focus on further controls on the occurrence and magnitude of impulsive conditions.

7.4.1. Second-order controls of impulsive wave characteristics

I have identified the wave height/water depth (*H/d*) ratio as a first-order control in determining the probability distribution of pressure maxima (Section 7.3.3.3). However, it is well established from previous work that a large number of additional variables have some degree of control over impact pressures, and improving understanding of these may reduce the uncertainty associated with the models developed in my study. This section is a summary these second-order variables and a consideration of the extent to which they may be attributed to the variation in pressure observed (Figure 7.17).

7.4.1.1. Controls on wave impact pressure: Aeration

As discussed in Section 2.4.1.3, water hammer pressure is dependent on the degree of aeration in the water during impact. Generally, higher levels of aeration and water turbulence have been found to reduce peak impact pressures, although some evidence suggests that it may also introduce strong sound velocity gradients that may focus pressure waves (Bredmose *et al.*, 2004). In addition to the lack of aeration measurements, comparing the effect of aeration in flume experiments with the present study is problematic because of scale effects, the difference in bubble residency times and bubble size differences (Bredmose *et al.*, 2003).

Blackmore and Hewson (1984) proposed that the degree of aeration on rock coasts would be higher than on beaches as the near-horizontal, high roughness platform may have broken and reformed waves multiple times prior to arriving at the shore, entraining large volumes of air. The suggested values for their aeration factor (ς) were thus smaller for rougher and shallower rocky platforms (Walkden, 1999). Air entrainment was found to dampen, and hence reduce more rapidly, peak pressures on sea dykes by Grüne (1988), who also suggested that the chaotic-type impacts may occur due to enclosed air pockets between the wave front and the sensor, causing higher turbulence. This may explain the highly variable response between sensors discussed in Section 7.3.1.1. In full-scale wave impact flume tests, Bullock *et al.* (2007) identified two types of breaking waves, termed low- and high-aeration impacts. The high-aeration impacts were characterised by damped post-peak oscillations, with

sub-atmospheric (negative) pressures also common. This may explain why negative pressures are also found in my study (Figure 7.3D).

The effect of aeration on peak pressures have been measured experimentally and in the field on a sea wall by Griffiths (1993). Low levels of entrained air corresponded with the generation of large water hammer shock waves, and mean bubble size was also a factor. The relationship between peak pressure, rise time and air entrainment was found to be highly complex, and could not be resolved using the instrument set-up. However, my study demonstrates that even under a potentially much higher level of aeration than on beaches and sea walls, impulsive pressures still occur on rock coast cliffs and of a magnitude which is comparable with other field-based observations. This is supported by Bullock *et al.* (2007), who found that very high impact pressures (> 1 MPa), whilst less common than in low-aeration impacts, can occur with considerable quantities of entrained air. In my study, the value of *H/d* above which impulsive pressures occurred (~0.5) was higher than the 0.35 given by Allsop and Vicinanza (1996). This may reflect the increased aeration at a rock coast compared with a flume tank, which may be acting to reduce the overall pressure and require waves to be further into the breaking process to achieve pressures above the hydrostatic.

As well as entrained air, a number of investigators have asserted that the highest impact pressures occur when a thin air pocket is trapped between the breaking wave front and the impact surface, known as entrapped air (Bagnold, 1939; Denny, 1951; Hattori *et al.*, 1994; Mai, 2017) (Figure 7.17). As with the breakwater sensor array of Blackmore (1982), the cliff toe sensor array in my study was mounted ahead of the cliff face, with sensors proud of the rock surface, hence sealed air pockets cannot have been formed. The impulsive pressures therefore cannot have been produced by Bagnold's (1939) air piston model, whereby adiabatic compression of the air pocket produces shock waves and impulsive pressures. Furthermore, many experiments based on this model assume a sealed junction between the impacting surface and the wave crest. Whilst common in a narrow flume with confining walls (Miller *et al.*, 1974), air compression is unlikely to occur on the rough, angular surface of a cliff with a highly aerated wave crest not precisely normal to it, as air is likely to escape

along the exposed crest. Alternatively, compression may be concentrated only in concavities, where a seal is more probable. Compression in crack and fissures in a cliff face however, may be common, and so will be discussed in Chapter 8.

7.4.1.2. Controls on wave impact pressure: Incidence angle

Impulsive wave impact magnitudes have been shown experimentally to be highly dependent on the incidence angle between the impinging wave crest to the impact surface (Allsop and Calabrese, 1998) (Figure 7.17). Whillock (1982) experimented with incidence angles of between 0 and 25° and found that both P_{max} and F decrease considerably with incidence angle, with the highest values occurring at 0° (Whillock, 1987). A general reduction factor where P_{max} is reduced by the $\sin^2$ of the incidence angle was suggested by CERC (1984). This would represent a reduction factor of $0.75P_{max}$ for an incidence angle of 30°. Whilst waves where incidence angle is precisely 0° are unlikely to be common at the cliff toe, the reduction in P_{max} is not considerable, and only become noteworthy above ~100 kPa, where the resultant reduction is larger than the sensor error (3 kPa) for waves where incidence angle is larger than 10°.

7.4.1.3. Controls on wave impact pressure: Wave shape

Impact pressure has been shown to be highly sensitive to the shape of the wave free surface on impact (Figure 7.17), which in turn is sensitive to small variations in water depth and wave height (Hull and Müller, 2002). Much of this variation is related to the wave front impact angle. Griffiths (1993) found two categories of breaking wave impact, termed compression and shock wave, which each arose from different contact angles between the wave front and the impacting surface. Compression waves were characterised by long rise times ($t_{rise} > 10^3$ ms), low velocities and consequently low impact pressures. These were found to be mostly spilling breakers, where the wave front angle was relatively low and contained a considerable entrained air fraction. On the other hand, shock waves were produced by steep, plunging breakers, short rise times ($t_{rise} < 10^3$ ms) and a small air fraction, leading to higher impact pressures.

The consequence of small variations in wave shape on impact pressure has also been noted by others (Hedges, 1985; Cooker and Peregrine, 1990b; Peregrine *et al.*, 2004). This may explain some of the variance seen in peak pressures in my study, whereby the wave front vertical angle determined the type of impact induced. Wave shape is particularly difficult to measure in controlled conditions, so obtaining accurate estimates in a field setting is even more challenging. Therefore, the treatment of these variations probabilistically is considered a more pragmatic approach (Hedges, 1985).

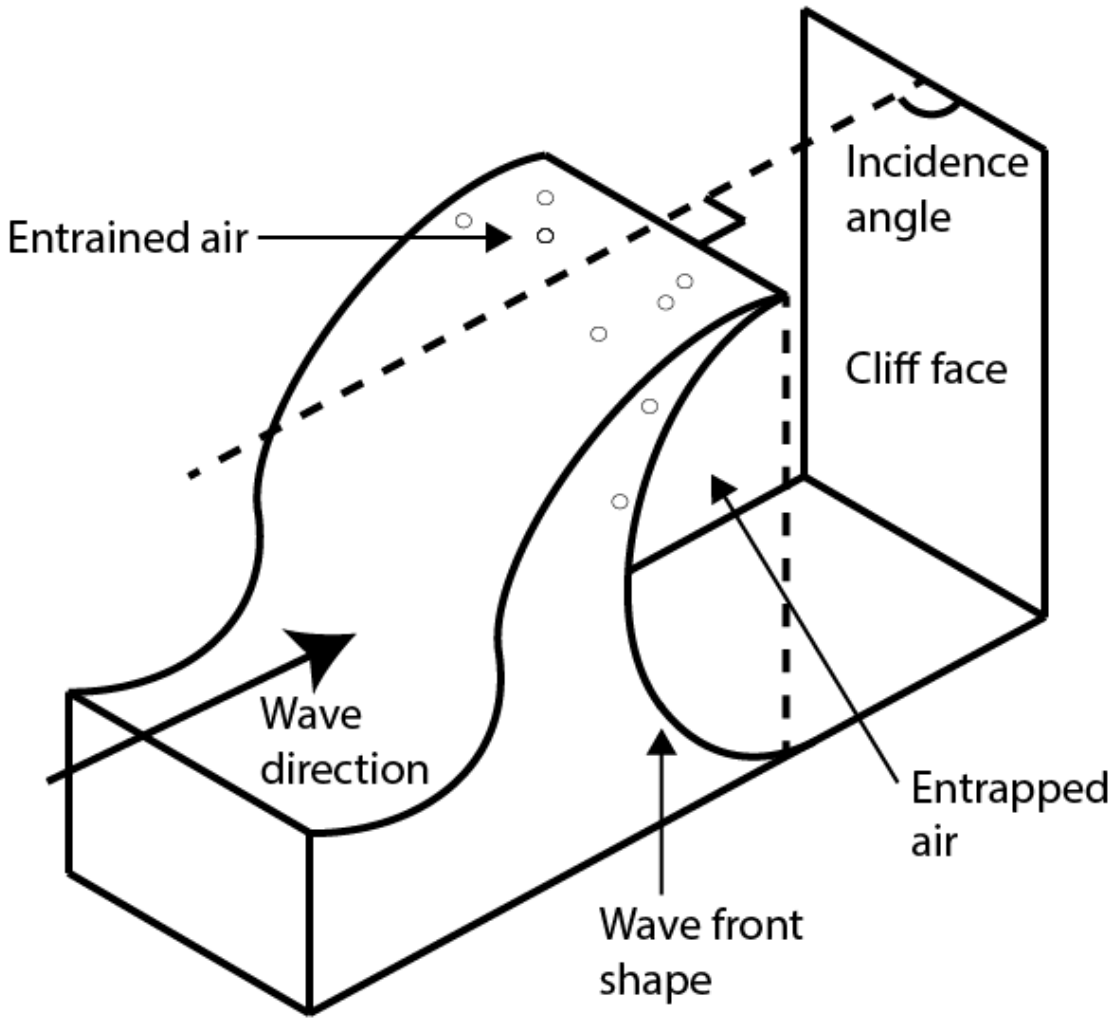

Figure 7.17: Description of the variables outlined as second-order controls of wave impact pressure.

7.4.1.4. Controls on wave impact pressure: Two-dimensional considerations

Whilst I have ensured that temporal resolution was adequate for measuring impact pressures (Section 6.4), there is some evidence to suggest that peak pressures are highly variable spatially on a centimetre-scale. Small areas of localised pressure peaks may be damaging to cracks in coastal structures. Peregrine (2003) postulated that when the wave crest is concave and waves are focused, inertia can be intensified at a point leading to higher pressures. Platform morphology can lead to wave focusing and recurring peak pressures at specific points on the cliff. Breakwaters are often found to have recurring damage in the same place, which may be the same for coastal cliffs.

Stagonas *et al.* (2011) used a two-dimensional "tactile" pressure mapping system to measure wave impacts over an area – rather than a traditional longitudinal array – with a spatial resolution of up to 0.04 mm^2. Impulsive pressures from regular breaking waves were measured over an 100 cm^2 area and found to vary by over an order of magnitude over just 1-2 cm for any instantaneous measurement (Ramachandran *et al.*, 2013). Pressure peaks were irregularly spaced across the area (Stagonas *et al.*, 2015), which suggests that for any impact measured using a vertical sensor array, a high-magnitude pressure may be produced but it may not be sampled by a sensor. Very high pressures may have occurred within a few centimetres of a sensor during impact but the actual pressure response reflects a pulsating load (Figure 7.18). Aeration may also vary across the impacting wave front, which may also influence the spatial variations in pressure characteristics across the impact. That said, the experiments of Stagonas *et al.*, 2015 are limited in spatial extent; it may also be the case that such local scale variability will be overwritten by more macro-scale variability over the length scales considered in my measurements.

This lateral variation is critical, as it suggests that high-magnitude impulsive loads during breaking may be more common than measured in my study, and some of the apparent inconsistency in their occurrence may be due to the spatial extent and hence resolution of the sensors. In other words, impulsive

loads may occur during every breaking wave impact, but are just not captured at a point (single sensor) location. The hydrodynamic relationship based on the ratio between wave height and water depth is likely still valid however, as it is supported Kirkgoz (1982) and was observed on Stagonas *et al*.'s (2015) pressure mapping system. As such, my study may represent an underestimate of the pressure loading in this environment.

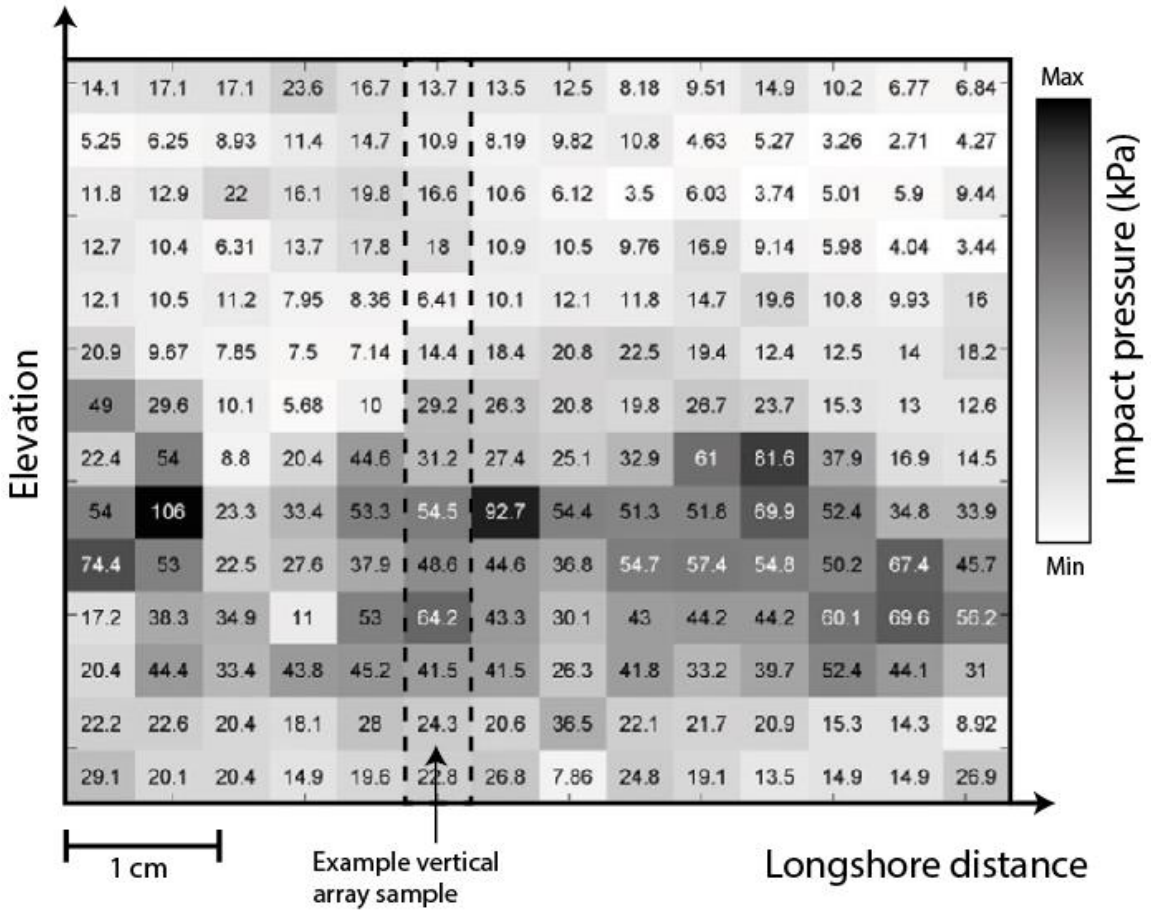

Figure 7.18: Illustration of the variation in impact pressure in both x and y directions up and along the cliff face. Grid represents impact pressure magnitude at a point on the cliff face at a given time during a wave front impact. The limitation of sampling from a longitudinal sensor array is shown, as longshore pressure variations are not sampled. Adapted from Stagonas *et al.* (2015).

7.4.2. Comparing field data with coastal erosion models

My findings demonstrate some of the limitations of the quantification of wave assailing force used by models of cliff recession outlined in Section 2.3.1. Only models which use a direct comparison between wave impact pressure and rock

strength are directly relatable to this study; some models (Hackney *et al.*, 2013; Kline *et al.*, 2014; Limber *et al.*, 2014) use wave power, rather than pressure or force, as a measure of assailing force, and as such are not comparable.

To compare model estimates with my data, I calculated wave impact pressure magnitudes for both breaking and broken waves of H = 1, d = 1 (hence H/d = 1) from each model, alongside the mean value for wave measured in my study (Table 7.2). These parameters were used as waves with these dimensions are most likely to be in a breaking or post-breaking state (Figure 7.12) and so are comparable with estimations. Other parameters were either values measured on the platform (w, T, k) or appropriate estimates (A, H_0, ρ, g). The justification for interchanging wave force with wave pressure is discussed in Section 2.3.

The results indicate that wave impact pressures for breaking waves are likely to be considerably overestimated in all the models considered, ranging between 2.1 (Walkden and Hall, 2011; Castedo *et al.*, 2012) and 13.2 (Trenhaile, 2000) times higher than the mean value for the equivalent measured wave (15 kPa). There were also both overestimates (Sunamura, 1977; Walkden and Hall, 2011; Castedo *et al.*, 2012) and underestimates (Trenhaile, 2000; Matsumoto *et al.*, 2016) of broken wave pressures.

Additionally, these predictors do not take into account the large uncertainty associated with such impacting waves: the range of measured values used was between 4 and 62 kPa. As such, no single formulae is capable of representing the range of pressures measured, without a much more comprehensive understanding and quantification of the variation in each wave (Section 7.4.1). The elevation of maximum pressure (E_{max}) has also been shown in Section 7.3.2.2 to be less predictable than these models suggest.

This analysis indicates that obtaining a general distribution of impact pressures for a given set of measured or modelled parameters (H, d, T) is likely to provide a more representative model than attempting to determine each wave value in turn (Figure 7.14). My field results are data-limited (E_s < 1.7 m, H_s < 0.9 m): a wider set of distributions, following those in Section 7.3.4.2, for different platform morphologies and incident wave conditions would be a valuable addition to such models. Furthermore, the quantification of the rock resisting force is of

equal importance as the wave assailing force in all of these models, and as such it is necessary to obtain a much greater understanding of both the modes of rock damage by waves and the relative strength of the forcing and resistance in question.

Table 7.2: Comparison between impact pressure calculations used by coastal cliff erosion models outlined in Section 2.3.1 (Equations 2-3 to 2-8) and the mean value from the present study of a wave with parameters g = 9.81, ρ = 1027, H_0 = 0.5, H_b = 1, d_{cliff} = 1, T = 10, k = 0.01 (Trenhaile, 2000), w = 120, A = 5 for breaking and broken waves. Comparison multiplier column shows difference between estimated value from the models and mean measured value where h = 1, d = 1 (15 kPa); for example, breaking wave magnitude is overestimated by 3.4 times using the Sunamura model. Note d_b is substituted for d_{cliff}.

Model	**Calculations used**		**Pressure (kPa)**		**Comparison multiplier**	
	Breaking	**Broken**	**Brea-king**	**Bro-ken**	**Brea-king**	**Bro-ken**
Sunamura	$A\rho g H_b$	$A\rho g H_b$	50	50	3.4	3.4
Trenhaile	$0.5\ \rho \frac{H_b}{0.78}\ e^{-k\,w}$	$0.5\ \rho\ g\ d_{cliff}$	198	5	13.2	0.3
SCAPE/Castedo-Paredes	$H_b{}^{\frac{13}{4}} T^{\frac{3}{2}}$	$H_b{}^{\frac{13}{4}} T^{\frac{3}{2}}$	32	32	2.1	2.1
Matsumoto	$35\ \rho\ g\ H_0$	$0.5\ \rho\ g\ d_{cliff}$	176	5	11.8	0.3

7.5. Conclusion

In this study I measured wave impact pressures using a vertical array of high sample rate pressure sensors mounted at the cliff toe on the shore platform at Staithes, North Yorkshire. I undertook nine deployments, constituting approximately 22,000 measurements of individual wave impacts. Wave and depth conditions ranged between H_s = 0.35 - 0.93 m and d_{cliff} = 0 - 2.2 m. The magnitude and vertical distribution were measured for each impact. Impact magnitudes of up to 127 kPa were measured. The following conclusions were made:

- Impulsive wave loads were common during the relatively short study period. Rise times of < 1ms were observed, and followed empirical relationships found by previous studies. Impulse loads occurred even during relatively low-energy wave conditions.
- The magnitudes of wave pressures are of the same orders of magnitude as research from coastal structures, but are often considerably less than the assumptions implicit within rock coast erosion models. The elevation of the pressure maxima, which is usually assumed to be at the still water level, here has been shown to vary by up to 1 m.
- For the measured platform morphology and range of conditions observed over the study period, impact pressure magnitude and characteristics were found to be highly dependent on the ratio between wave height and water depth. Low values (< 0.5) produced almost exclusively pulsating pressures; moderate values (0.5 – 2.5) produced pulsating and high-magnitude impulsive pressures; high values (> 2.5) produced low-magnitude impacts of both types. Maximum values were most likely associated with breaking waves, providing evidence for the common assertion that wave loading at the cliff toe is highest during breaking.
- Wave height was a strong predictor of pulsating wave magnitudes, but a poor predictor of impulsive loads. Additional variables almost certainly influence the pressure response: aeration, wave shape, incidence angle and spatial variation across the wave front. However, these were

extremely difficult to assess. As such, and in line with other research, wave impact magnitudes were considered probabilistically.

- Rather than using a deterministic model for single impacts derived for design wave heights on coastal structures, probabilistic methods were considered more suitable for predicting the overall loading at the cliff toe over a wave population. For my data, wave impact magnitudes were found to follow a generalised Pareto distribution, the parameters of which varied with wave height and water depth.

8. Discussion

8.1. Introduction

8.1.1. Overall research aim

The aim of this thesis was to evaluate the role of wave impacts in cliff toe erosion. I used a variety of techniques to achieve this. These are summarised in the following section.

8.1.2. Summary of results chapters

I collected repeat high-resolution erosion data of the lower cliff at Staithes over one year (Chapter 4). This dataset revealed considerable differences in erosion both cross-shore and with elevation. Structural and lithological controls were found to dictate the dominant detachment characteristics. Erosion rate was found to correlate with platform morphologies which control cliff toe wave and tide dynamics. Furthermore, the erosion of smaller fragments appeared to increase in a 3 m zone above the HAT, suggesting a critical role for marine erosion.

To investigate this further, I monitored offshore and cliff toe wave conditions over the study period using a wave buoy and toe-mounted wave gauges respectively (Chapter 5). A significant power law relationship was found between offshore and cliff toe wave heights, which varied with platform elevation and width. Cliff toe elevation, alongside wave height and tidal stage, also controlled the breaker type arriving at the cliff toe. Breaking waves were found to be common at the cliff toe, and as such may have a key role in erosion of the lower cliff.

I investigated the magnitude and distribution of wave forcing at the cliff toe using a vertical array of impact pressure sensors mounted in from of the cliff at Site 1 (Chapter 7). High-magnitude impulsive pressures were found to be common during the low-energy conditions (H_s < 0.9 m) monitored. These were found to be several orders of magnitude lower than the unconfined compressive strength of the cliff lithology.

8.1.3. Discussion outline

My results have provided insight into the characteristics of the wave forcing and erosion regime during the 369-day study period. However, by combining each dataset I will consider additional evidence to assess to what extent the observed lower cliff erosion can be explained by hydraulic / marine processes.

This discussion will focus on two areas of interest. Firstly, I extrapolate and combine my results in order to investigate specific erosion characteristics in relation to the broader forcing regime (Section 8.2). Secondly, I use the combined insights from all three results chapters and previous studies to inform a modified conceptual model – building on those of Sunamura (1992), Adams *et al.* (2005), Rosser *et al.* (2007), Naylor and Stephenson (2010) and Norman (2012) – of the erosion mechanisms at rock coast cliffs, focused specifically on the lower cliff (Section 8.3). A summary follows each section in order to highlight the key findings.

8.2. Comparisons between erosion and wave data

In Chapter 4, I found that the vertical profile of erosion volume was controlled by both the lithology and structure of the cliff (Figure 4.10). Shales exhibited more frequent, smaller detachments and sandstones eroded in larger blocks, shown by the detachment volume power law exponent (β). However, the rate of erosion could not be explained by either observed geological boundaries or tidal inundation duration.

When considering just smaller detachments (< 0.1 m^3), a distinct increase in erosion volume (D_v) between 4 – 6 m was apparent (Figure 4.17), located above the HAT. This matched a water level frequency (W_q) of W_q + 3.6 m. Furthermore, this elevation range also experienced a higher detachment frequency (D_q) (Figure 4.9). The apparent offset between this erosion pattern and W_q indicated that W_q alone could not explain this apparent increase in D_q and D_v at this detachment size. It may be that looking at inundation duration and water level frequency alone is too simplistic. In this section I explore the characteristics of waves within the impact zone up to the wave crest and the

potential for variation in the weathering profile in order to provide additional insight regarding the link between waves and erosion.

8.2.1. Vertical variation in measures of wave-cliff interaction

Figure 8.1 is a comparison between various measures of marine influence and the erosion profile derived from the detachment volumes (D_v) < 0.1 m^3. Following Trenhaile and Kanyaya (2007), water level frequency (W_q) calculated from the tide gauge (Figure 8.1A) is approximately equal to W_q measured by the wave gauges at Sites 2-5 (Figure 8.1B). The differences in the magnitude of the lowest elevations between sites seen in the latter figure are due to the differences in cliff toe elevation (E_{toe}) between each site. The W_q offset of 3.6 m between these peaks and the erosion peak (Figure 8.1E) is shown. The cumulative energy density (ξ) at each site (Figure 8.1C) maps approximately on to the measured W_q. This indicates that if it is assumed that the energy transfer to the cliff occurs at the water level, the differences in energy transfer between sites can be estimated using W_q.

However, wave impacts do not exclusively apply load at the still water level. In Chapter 5 I showed that loading due to wave impacts on the cliff face is applied across elevations between the wave trough and crest. It makes more physical sense therefore to apply the load distributed across the full wave front when calculating cumulative loading over time. Figure 8.1D demonstrates this by using the sum of the water depth (d) and the highest 1/10th wave heights ($H_{1/10}$), and applying the loading in Figure 8.1C uniformly over the range d-$H_{1/10}$/2 to d+$H_{1/10}$/2. Wave heights from $H_{1/10}$ rather than H_s or H_{RMS} were used as the most geomorphologically important waves were required, which are likely to be the largest (Earlie *et al.*, 2015). Wave loading distribution here is markedly different from just considering W_q alone, with the peak loading occurring at E = ~2.7 m ODN (compared with ~ 1.7 - 2.0 m for W_q). Additionally, the influence of wave loading extends further up the profile, with the highest waves affecting up to E = 5.7 m, compared with 3.3 m for W_q. This influence thus extends into within the range where the erosion volume increases (Figure 8.1E), but still does not correlate with the peak in erosion volume, which is offset by 2.3 m above the peak in Figure 8.1D.

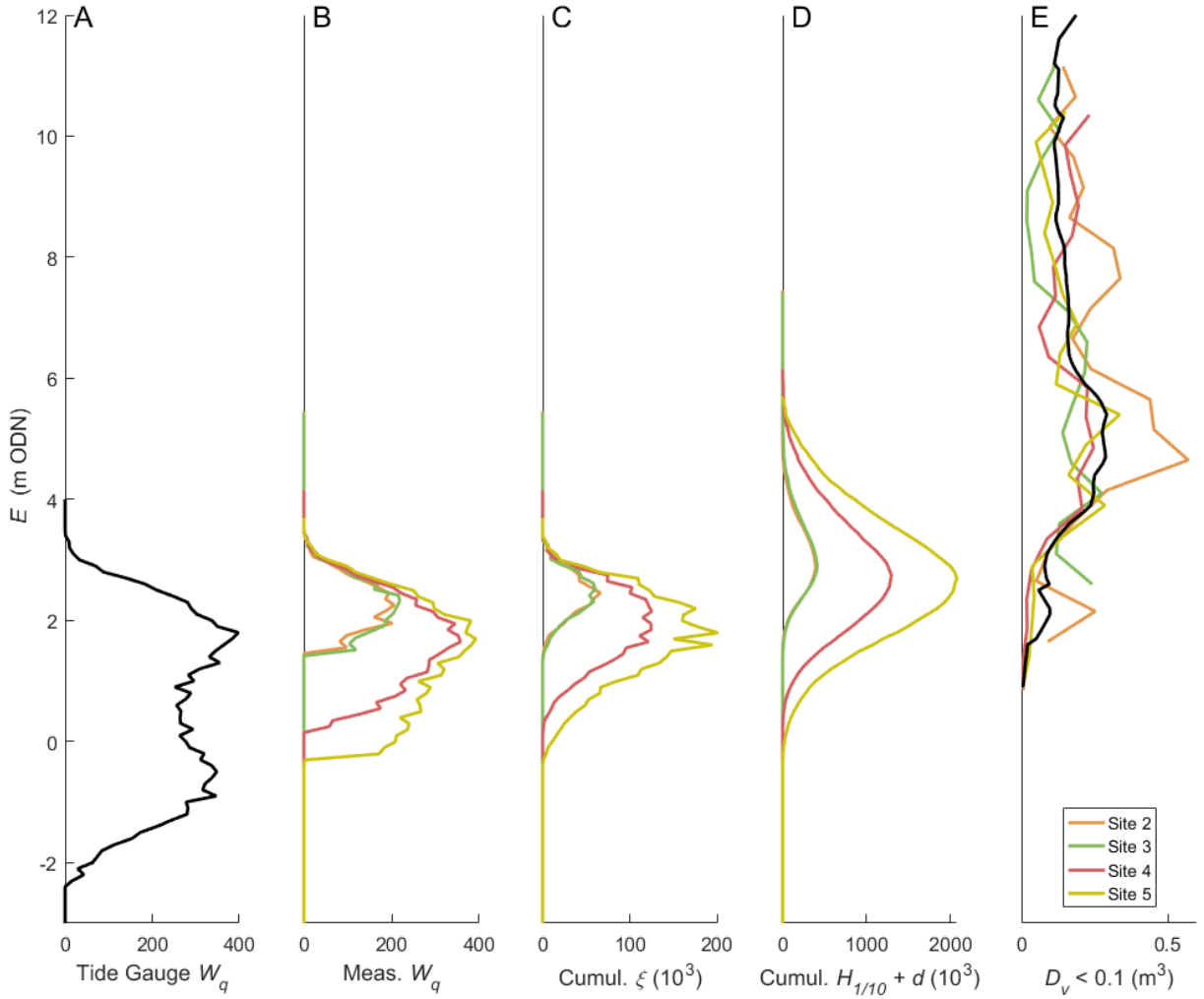
A
B
C
D
E
12
10
8
6
4
2
0
-2
E (m ODN)
0
200
400
Tide Gauge W_q
0
200
400
Meas. W_q
0
100
200
Cumul. ξ (10^3)
0
1000
2000
Cumul. $H_{1/10}$ + d (10^3)
0
0.5
D_v < 0.1 (m^3)
Site 2
Site 3
Site 4
Site 5

Figure 8.1 (previous page): Elevation profiles comparing different measures of marine forcing with observed erosion from Sites 2-5. A) Tide gauge water level frequency (W_q); B) wave gauge water level frequency (W_q); C) Cumulative wave energy density (ξ) at tidal elevation; D) Combined highest 1/10th wave amplitude ($H_{1/10}/2$) and water depth (d) into cumulative wave front impact; E) Total annual volume loss (D_v) for detachments < 0.1 m^3.

I proposed two scenarios that may explain this apparent lack of correlation between the measured marine processes and the erosion profile patterns.

8.2.1.1. Erosion scenario: differences in wave erosivity

The erosion offset (Figure 8.1D and E) may be partially explained if the waves which impact the cliff at a higher elevation provide higher forcing potential.

Figure 8.2A shows that at site 2, where the increase in erosion at the 4 - 6 m zone is most pronounced, there is a positive correlation of 1/10th wave height ($H_{1/10}$) with water depth (d). This shows that the largest waves were most likely to reach the cliff toe during high tide due to less attenuation (Figure 5.16). This suggests that whilst the lower section of the lower cliff may undergo wave attack more frequently, the upper section, and hence the zone of increased erosion of smaller detachments, is subject to impacts from much larger waves.

In addition, the frequency distribution of all waves at the cliff toe is relatively symmetrical about the wave height and water depth ratio of ~0.3 (Figure 8.2B). However, when considering only this ratio for waves where $H_{1/10}/2 + d > 4$ m, the distribution shifts upwards to a peak of around 0.5. This indicates that waves whose fronts directly impact the zone of increased volume loss of smaller detachments are not only larger, but also more likely to be breaking or near-breaking on impact.

The combination of greater water depths resulting from the setup regime during storms (Longuet-Higgins and Stewart, 1964) and the propensity for waves impacting the 4 - 6 m zone to be larger and breaking may result in considerably higher impact pressures culminating in potentially greater erosive potential in this zone.

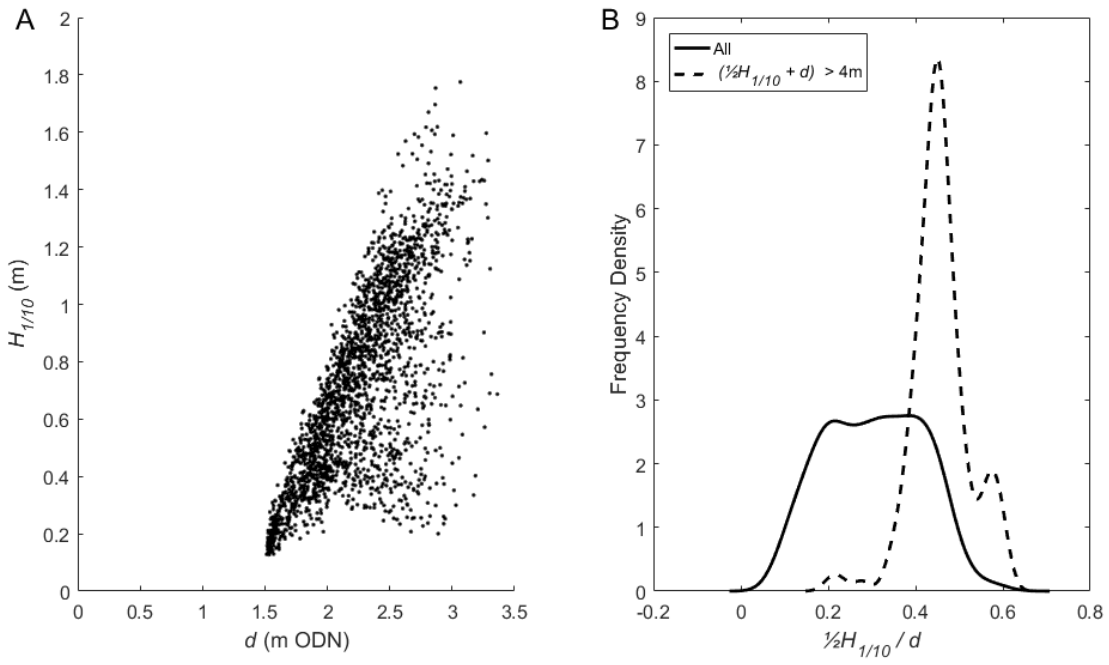

Figure 8.2: A) Positive correlation (r^2 = 0.50, p < 0.05) between one-tenth wave height ($H_{1/10}$) and water depth (d) for Site 2. B) Kernel density of the wave height and water depth ratio for all waves (solid line) and waves where $H_{1/10}/2 + d$ is larger than 4 m (dashed line) for Site 2.

8.2.1.2. Erosion scenario: combination of waves and weathering

Subaerial weathering processes driving weakening and rock frittering form a critical input into the drivers of coastal cliff recession (Moon and Healy, 1994). The magnitude and vertical distribution of salt weathering are primarily driven fluctuations in tidal level, but also exposure to wave attack. Trenhaile *et al.* (2015) found that tidal notches along the La Paz Peninsula, Mexico, were deeper and higher in areas where the cliff toe was more exposed to wave action, rather than in a protected bay where only tidal fluctuations occur. They suggested that 1) the material loosened by salt weathering was prematurely dislodged by wave action, driving more rapid erosion and 2) salt weathering affected a higher elevation in these areas due to higher splash and spray. This combination of a wider zone of influence and enhanced removal of weathered material indicates that the influence of salt weathering may be proportional to tidal elevation and wave height.

The efficacy of wetting and drying cycles is also highly dependent on tidal range and frequency. Kanyaya and Trenhaile (2006) showed that shales are considered most vulnerable to this process due to their higher clay content, as they absorb more water leading to enhanced expansion and contraction, weakening the bonds between constituent materials and reducing their strength (Hall and Hall, 1996).

Kanyaya and Trenhaile (2006) suggested that rock degradation due to wetting and drying (slaking) increases in efficiency with elevation, and that it is most effective higher up the profile (Stephenson and Kirk, 2000a). This may be due to the more rapid rates of water absorption than desorption.. Wetting processes are not only driven by the elevation of the still water level, but also the elevation of the highest wave crest and above, taking into account the impacting wave fronts, spray and splash. At Staithes, this is likely to extend to over 6 m (the maximum elevation of $H_{max} + d$) above the cliff toe. This suggests that the rapid absorption of water during high tide wave attack, followed by a longer period each tide to allow for near complete desorption, would make wetting and drying weathering more effective at and above the HAT. Coupled with enhanced salt weathering, this may lead to a considerable weakening of the higher intertidal and supratidal lower cliff, particularly in the shales and mudstones.

The combination of both weathering processes and larger, breaking waves may therefore explain the propensity of small detachments to occur at the elevation above the HAT.

8.2.2. Evaluating the influence of waves on small detachments

Whilst the processes outlined in Sections 8.2.1 may offer a mechanism for part of the erosion pattern seen on the lower cliff, the $D_V < 0.1$ m^3 detachments only constitute 11.5% of the total volume loss (but 99.9% of the detachment frequency) measured throughout the survey period. Further inferences regarding how the wave processes observed in this study contribute to the wider erosional context are limited. The relatively long scan interval (~ 1 month) in the erosion dataset does not allow for individual wave impact events, or even certain periods of high environmental activity, such as storm waves or heavy rain, to be attributed to specific detachments or sets of detachments.

Additionally, there may be a lag time between the rock damage and the detachment, particularly with large (D_v > 0.1 m) detachments. My study follows that of Lim *et al.* (2010), who found that although the overall relationship between these continual events and environmental conditions, such as sea level and wind velocity, was poor, correlation was found to increase when only smaller rockfall volumes were considered. This suggests that piecemeal erosion is more attributable to direct environmental forcing, but larger blocks may require repeat, cumulative loading. Experimentation by Wolters and Muller (2004) showed that pressure pulses caused by waves can easily exceed the tensile strength of rocks, which in turn cause failure at the crack tip and leads to progressive deterioration of the rock integrity. This however, may happen continuously over multiple cycles of crack growth without volume loss, yet this fatigue could still contribute a large proportion of the work done required for erosion to occur. Therefore, deriving the morphological signature of low-energy wave quarrying is highly problematic.

Monthly detachment volume at three out of four sites increased during the winter months within the study period, which corresponds with higher storm frequency (Figure 4.13). Notably, the daily detachment frequency did not exhibit a noticeable seasonal change (unlike volume), and the increase in winter erosion is mainly attributable to an increase in the mean detachment size (Figure 4.14), rather than an increase in detachments. This may suggest that low-energy conditions are comparative to high-energy conditions with regards to the removal of small, weathered detachments, as the loading threshold to remove these is very low. On the other hand, large detachments were more commonly removed in high-energy conditions, where larger forces are required to ultimately remove a pre-fatigued block from the cliff. Larger winter erosion rates were also observed in other studies (Earlie *et al.*, 2015, 2018; El Khattabi *et al.*, 2018).

My erosion and wave comparison therefore appears useful as an indicator of the possible role of waves in that they provide a logical set of mechanisms by which rock damage and material removal may occur, yet insufficient to provide more robust links between wave action and erosion.

8.2.3. Summary

Profiles of wave and erosion data from the study period were compared in order to investigate the extent to which vertical patterns on erosion could be explained by cliff toe wave characteristics. Whilst erosion did not correlate with forcing over the full wave front, it was shown that waves impacting at the elevation of increased smaller detachments were more likely to be larger and breaking on impact. This may provide greater forcing at this elevation which, coupled with a hypothesised increase in weathering rates at this elevation, may partially explain the erosion patterns observed.

8.3. Modified conceptual model of wave-driven erosion

My study has provided evidence for the commonly-held assertion that breaking and broken waves exert larger pressures than unbroken waves (Sanders, 1968b; Trenhaile, 1987; Brossard and Duperret, 2004; Davies *et al.*, 2006; Young *et al.*, 2013) on coastal cliffs. However, the relative magnitude of these under low energy conditions (H_s > 1 m) was shown to be much smaller than is often assumed.

In this section I outline a modified conceptual model of lower cliff erosion, given that the findings of the present study suggest that it is unlikely that wave impacts can have a direct, appreciable influence on fresh rock. Evidence from Chapters 4, 5 and 7 is utilised, with particular emphasis on the erosion patterns I found on the lower cliff at Staithes.

8.3.1. Proposed primary mechanisms of cliff erosion

Marine processes, perhaps unsurprisingly, play a major role in cliff retreat, but the magnitudes of wave impact pressures measured in this study are 3-5 orders of magnitude smaller than fresh rock compressive strength. This suggests that wave action must work in tandem with other processes that serve to reduce the effective rock resistance to facilitate erosion. I propose three main erosion mechanisms which are capable of fatiguing and removing material from the lower cliff under the known forcing regime (Figure 8.3). Each operates over

different timescales and requires a breadth of prerequisite conditions in order to function. The following section outlines the basis for these proposed mechanisms.

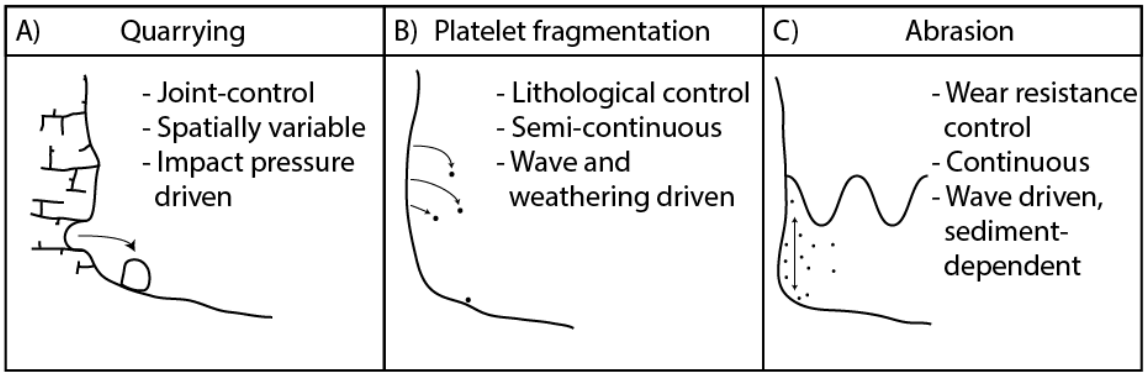

Figure 8.3: Illustrations of the three main mechanisms postulated as dominant on rock coasts. A) Wave quarrying requires direct wave impacts and pre-existing fracture networks, occurring infrequently; B) platelet fragmentation requires fissile material and is driven mainly by weathering, occurring fairly continuously; C) abrasion is controlled by the availability of suitable material and the ability of the wave and current conditions to provide suspension, working against wear resistance, operating continuously.

8.3.1.1. Erosion mechanisms: wave quarrying

Herterich *et al.* (2018) described how wave impacts can create and propagate micro-fractures within rocks and induce bending stresses. Repeated hydraulic loads can lead to complete detachment of large boulders which can then be transported from the cliff. As described in Section 2.4.1, this suggests that over time, cyclic loading from low-magnitude wave impacts can induce such fracturing. Fluid stresses need only be a small proportion of the tensile strength in order to generate microcracking, which in turn is often much lower than the overall compressive rock strength. For example, Gong *et al.* (2017) used intact rock tensile strength of 300 kPa and compressive strength of 4600 kPa to model limestone cliff collapse. Quarrying can occur ostensibly without damage to the central block, and probably requires the pre-existence of mode I fractures such as release joints (Herterich *et al.*, 2018). Eventual boulder release is likely facilitated by stress redistribution as fractures grow and coalesce.

Therefore, wave quarrying is a function of wave-induced pressure magnitude and frequency, fracture (and bedding) density and orientation (Naylor and Stephenson, 2010), the rock tensile strength, the proportion of the eroding block which is exposed to wave action, and the morphology of the lower cliff which controls the in-situ stresses on the block (Figure 8.3A). Gong *et al.* (2017) suggests a tensile strength of 46 kPa is required to damage pre-existing joints. The results from my study suggest that broken and breaking waves occur frequently at the cliff toe (Section 5.4.3.3) and exceed this magnitude for the predicted tensile strength of the rocks (Chapter 7). Whilst waves alone are still capable of quarrying fresh rock, it is likely that weathering along joints can play a role in assisting wave quarrying (Sanders, 1968a). Salt crystal growth, freeze/thaw within fractures or clast wedging (Robinson, 1977b; Whipple *et al.*, 2000; Lamb *et al.*, 2015) may force widening; wetting and drying cycles may weaken the internal structure (Moon and Healy, 1994).

The erosion data from Chapter 4 supports the notion that quarrying is an active erosional mechanism at Staithes. Section 4.3.1 describes the siltstone lithology as competent, homogenous and with a very high compressive strength, with well-defined joints with a spacing of 1.1 – 2.9 m. The detachments in this lithology consist of larger blocks which approximately conform to the joint spacing and are bounded by the bedding planes (Figure 8.4). Temporally, detachments in the siltstone were also highly intermittent, with almost no erosion at Site 3 over the study period, and much fewer overall detachments at Site 2 than the shale but with a comparable erosion rate (Figure 4.12). The angular face topography of the siltstone, visible in both the topographic drape in Figure 4.7 and the photograph in Figure 8.4, suggests that most erosion here is of bedding- and fracture-bound blocks, rather than the smooth wear, scratches and percussion marks expected from abrasion surfaces (Blanco-Chao *et al.*, 2006; Cullen and Bourke, 2018). It is also clear from Figure 3.7 and the profile in Figure 4.9A that the siltstone at Site 2 is not overhanging, suggesting that erosion in this stratum is actively driven, rather than a function of undercutting.

Large detachments are also prevalent, but are less dominant, in the shale. Fractures and joints also extend through these layers, albeit with narrower joint spacing (0.7 – 1.2 m), which may explain the slightly smaller block

detachments. This indicates that wave quarrying is also effective in this lithology; the prevalence of both siltstone and sandstone boulders on the platform supports this. The presence of large boulders on the platform also supports this, as boulders sourced from above the lower cliff have a tendency to disintegrate on impact (Rosser *et al.*, 2013).

Figure 8.4: Cliff section showing the smooth, quarried joint boundaries in the upper siltstone contrasting with the fabric-controlled, rough shale surface. Fieldworker for scale.

It is likely then, that quarrying occurs continually at the cliff toe, exploiting pre-existing fracture networks, and that the rate is controlled by *H/d*. Alongside the known existence of much larger impact magnitudes of those occurring in this study (Rouville *et al.*, 1938; Bullock *et al.*, 2007), this suggests impacts magnitude scales exponentially with wave height, which would explain the increased quarrying rate, along with increased water mass, rapid velocities leading to cavitation and larger impact area that occur with larger wave fronts. The quarrying mechanism is summarised in Figure 8.6A.

8.3.1.2. Erosion mechanisms: platelet fragmentation

Operating over a much smaller spatial scale than wave quarrying (centimetre rather than metre scale), platelet fragmentation has been shown to be a viable mechanism by which material is removed from the cliff at Staithes. Robinson (1977) referred to this as micro-quarrying. This mechanism (Figure 8.3B) relies on the gradual weakening of the rock fabric by weathering (Section 8.2.1.2). In Section 2.3.2.3 I showed that weathering can fatigue rock with high critical strengths leading to a low critical threshold for environmental forcing to dislodge. During fieldwork on days with high wind speeds, I observed centimetre-scale fragments are released almost continually from the cliff face, the rate of which decreased considerably on still days.

Wave impact pressure is unlikely to exceed the compressive strength of fresh rock (Chapter 7). As such, it is likely that platelet fragmentation would require pre-requisite weakening of the rock via weathering. Higher-energy forcing may however increase the threshold over which the weathering must decrease the rock strength. This process was identified using micro-erosion meters as the most common erosive mechanism on rock coasts in Eastern Canada by Porter *et al.* (2010), as granular disintegration and spalling from in shales, siltstones and mudstones.

The erosion data from Chapter 4 suggests that this mechanism is apparent in the shales, where the highest frequency of erosion is cm-scale detachments which are comparatively continuous through time. This can be seen in Figure 4.12, particularly in the lower half of Sites 2, 3 and the whole face of Site 4. The mean detachment volume is approximately 10^{-6} m^3 in the shales, which

approximately matches the size of single fragments defined by the rock fabric. The shale lithology is also finely laminated, which assists in the detachment of weathered platelets. Shale topography is highly textured and exhibits considerable roughness (Figure 8.5), the same surface micro-relief identified by Robinson (1977), compared with the smooth siltstone (Figure 8.4). A combination of platelets and joint-bound detachment scars are visible in the topography in Figure 4.7. This mechanism is summarised in Figure 8.6B.

Figure 8.5: Detail of shale fabric at Site 4, illustrating considerable roughness and micro-relief as an indicator of platelet fragmentation.

8.3.1.3. Erosion mechanisms: abrasion

Whilst it is unlikely that abrasion is a principle erosion mechanism at Staithes due to a lack of suitable sediment (Section 3.6.1), it is worth discussing as a point of comparison that may operate in other settings. Abrasion is described in Section 2.4.1.7 and is dependent on water velocity (for entrainment through shear stresses), but is independent of impact pressure (Sanders, 1968a).

Dynamic pressures will likely have no influence on abrasion efficacy: they are a hydraulic phenomenon only and cannot provide additional force to a suspended clast (Cooker and Peregrine, 1990a). It is however, highly likely that the large waves which impart large dynamic pressures are also capable of the high velocities required for effective abrasion (Mai, 2017). Even large unbroken waves can have oscillating water particles at the cliff toe which may wear down rock if sediment is entrained.

At Staithes, there is very little morphological evidence that erosion via saltating particles occurs, as there are few smooth rock surfaces (e.g. Blanco-Chao *et al.* (2006), Cruslock *et al.* (2010)) apart from those (pre-)defined by fracturing. Abrasion is a relatively spatially and temporally continuous process, described by Emery and Kuhn (1980) as a “grain-by-grain” process. Some degree of uniform erosion would therefore be expected from the difference plots in Figure 4.7. There are sections of the platform where loose, rounded, pebble-sized material derived from rockfalls is present. This type of material was observed to have moved some distances between tides during surveys. Some abrasion at the toe could occur when these are entrained and propelled at the toe with large waves (Robinson, 1977b; Williams and Roberts, 1995). This mechanism is summarised in Figure 8.6C).

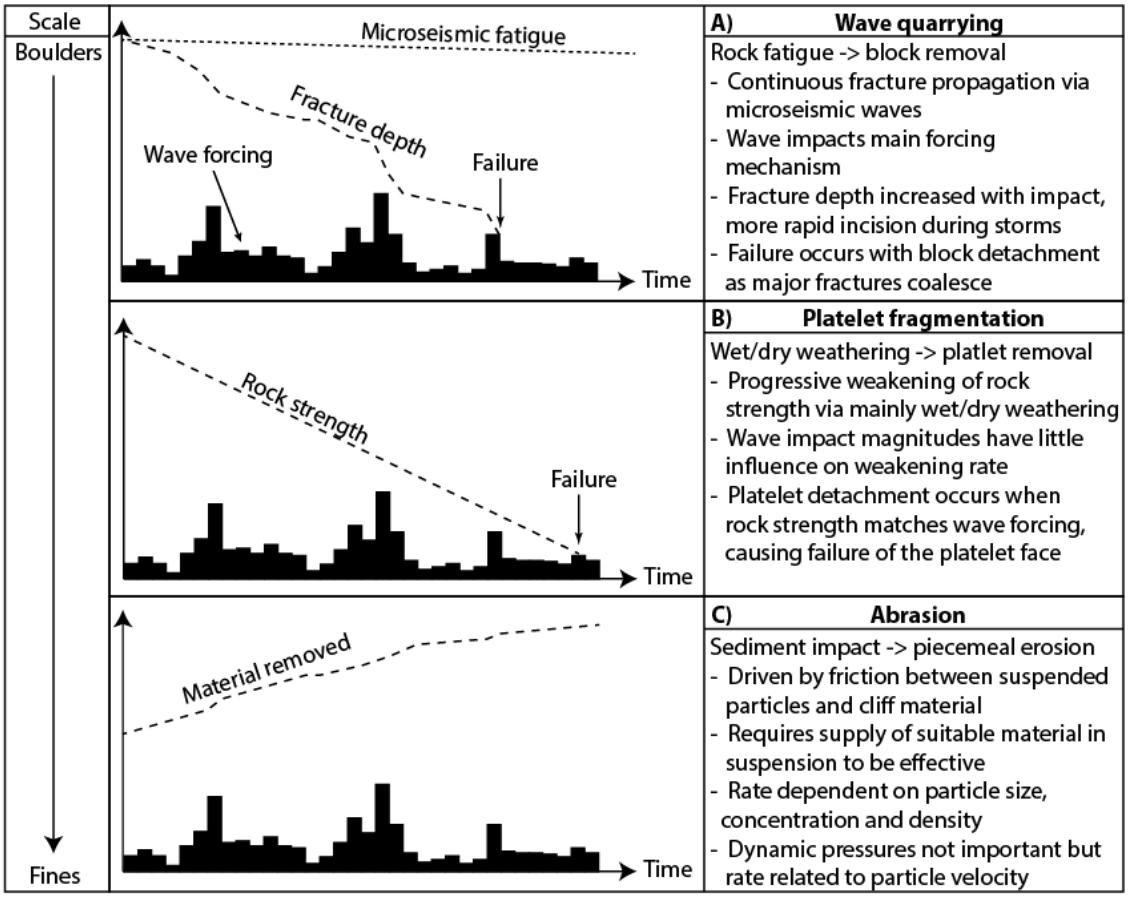

Figure 8.6: Graphical representation of the conceptual model of erosion mechanisms I have discussed in this section. A) Wave quarrying operates by increasing the fracture depth (dashed line) via wave forcing magnitude through time (shown by vertical black bars) until a critical coalescence of fractures occurs at failure. B) Platelet fragmentation occurs relatively independently of forcing via weathering, reducing the rock strength until forcing is of sufficient magnitude to remove the platelet at failure. C) Abrasion occurs when suspended clasts are saltated or propelled at the rock surface and is related to forcing only as higher waves suspend larger sediment at higher impact velocities. Abrasion rate is effectively the integral of wave forcing. The spatial scale of the detachments associated with each mechanism is shown on the left-hand side, ranging typically from boulders (quarrying) to fine sediment (abrasion).

8.3.2. Integrated hard rock cliff response to wave forcing

In light of the findings of this investigation regarding a) the mechanisms of erosion identified at the study site; b) the relative importance and efficacy of inundation duration, wave heights and impact pressures; c) the seemingly poor correlation between forcing, material controls and erosion (Vann Jones *et al.*, 2015), I propose a modified conceptual model of wave forcing at the cliff toe. This builds on that put forward by Norman (2012) at Staithes and focuses on erosion at the lower cliff, which in turn drives some of the progressive failure above. Measurements of the tidal, wave and impact conditions at the cliff toe and subsequent erosion patterns in my study suggests the likely dominant hydraulic erosion mechanisms at Staithes. Figure 8.7 describes the proposed model for how incident wave and tide conditions generate effective cliff recession. This model is a further development of Naylor and Stephenson (2010), Sunamura (1992) and Figure 2.1, taking into account the interplay between cliff morphology, toe hydrodynamics and rock properties investigated in my study.

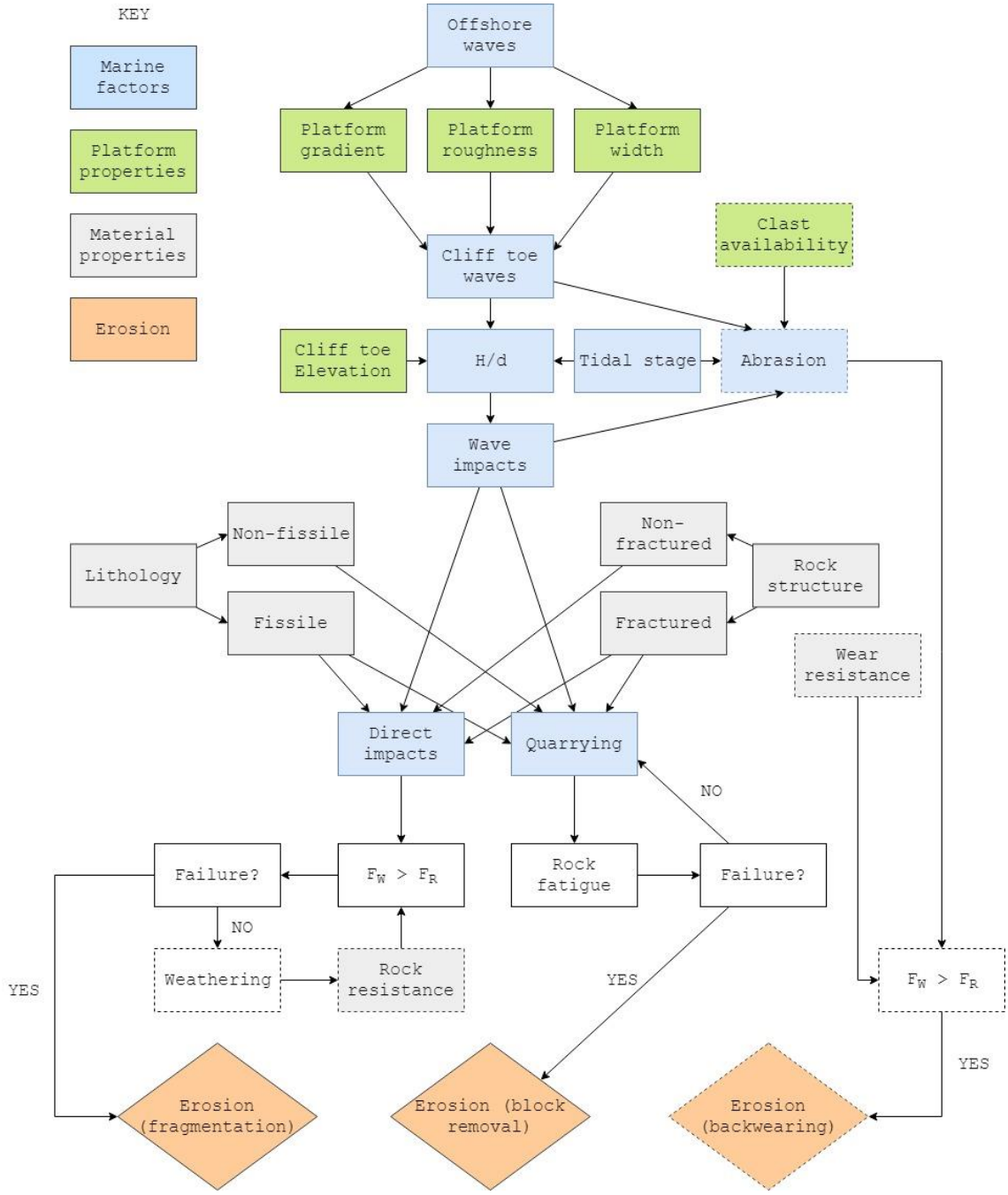

Figure 8.7: Flow model for hydraulic-driven erosion of the lower cliff. Dashed boxes represent processes not directly investigated in this thesis.

The initial cliff toe wave conditions are controlled primarily by offshore incident conditions and modified by platform morphology in the manner described in Section 5.4.1. Platform width and roughness, the latter being only be relevant in highly specific cases (Poate *et al.*, 2018), increase wave height dissipation. Platform gradient, particularly at or near the cliff toe, modifies the breaker type. The combination of cliff toe elevation, tidal stage and cliff toe wave height then

determines the wave height / water depth ratio at the toe. This in turn dictates the probability distribution of impact pressures in the manner described in Section 7.3.4.

Three processes arise at the cliff-water junction: abrasion, quarrying and direct wave impacts (Section 8.3.1); the type of erosion is governed by lithology and structure (Cruslock *et al.*, 2010). Direct wave impacts may act to dislodge and entrain weakened material from the cliff. They may also generate material fatigue though cyclic loading (Budetta *et al.*, 2000). This process can only occur when material strength is lower than the impact pressure. Results from Chapter 7 have shown that this can only occur on hard rock cliffs with prerequisite weathering. The rate of weathering therefore largely determines the rate of platelet fragmentation (Payo *et al.*, 2014).

Quarrying requires jointed, fractured material within which impact pressures can propagate. As such, the rate of quarrying is controlled by impact pressures and cumulative loading. Additional wave-driven hydraulic loading, such as cavitation and high-velocity flow, are likely to play key roles (Young *et al.*, 1996; Cheng and Ji, 2017) but are outside the scope of this study.

All the processes are subject to morphodynamic feedbacks. Long-term (decadal) feedbacks may occur as cliff recession produces wider platforms, increasing wave dissipation and wave height at the toe (Ogawa *et al.*, 2015). Downwearing may increase local mean water depth by lowering the cliff toe elevation (Moses and Robinson, 2011), affecting cliff toe wave characteristics (Section 5.4.1.2). Future climate change may also affect hydraulic forcing, via sea level rise and increased storminess (Trenhaile, 2011).

8.3.3. Summary

Wave quarrying and platelet fragmentation were identified as the most likely mechanisms driving erosion at the lower cliff. Evidence from the wave impact and erosion datasets was used to infer the occurrence and perquisite conditions for each. An conceptual model of marine-driven erosion was outlined. Major controls on erosion were identified as 1) lower cliff geology as a control of

erosion mechanism and efficiency, and weathering susceptibility; and 2) wave impact magnitude on quarrying only, governed by wave height / water depth ratio which, in turn, is controlled primarily by offshore conditions, platform morphology and tidal stage.

9. Conclusion

9.1. Evaluation of the aim

The aim of my research has been to examine the magnitude and distribution of wave impacts in a rock coast environment and investigate their role in driving erosion at the cliff toe. I have achieved this within the framework of five research objectives outlined in the following section. My study has resulted in a series of datasets which quantify both the assailing force of waves at the cliff toe and the nature of the erosion at multiple sites across the lower cliff. By combining these datasets, I have demonstrated that breaking waves occur frequently at the cliff toe in this environment, yet their impact magnitude under the conditions studied is insufficient to damage pristine rock. However, the patterns of erosion observed indicate that wave impacts drive cliff recession through discontinuous quarrying of fractured rock and piecemeal platelet fragmentation of weathered material. Furthermore, I have shown that the critical role of cliff toe elevation and wave height on dictating wave breaking conditions and therefore impact magnitudes, coupled with the importance of lithology and weathering processes on erosion mechanisms, indicates that assailing and resistive forces at the cliff toe may exhibit considerable temporal alongshore variation. This has provided further understanding of the factors governing the spatial and temporal variability of cliff erosion observed elsewhere.

9.2. Research conclusions

I have drawn the following conclusions from my research. In this section they are presented with regards to the five objectives set out in Chapter 1:

1. *To characterise erosion of the lower section of the cliff using TLS.*

I presented a 369-day, high-resolution erosion monitoring dataset focused on the lower 10 m of the cliff face in Chapter 4. The analysis of this dataset revealed a number of distinct patterns of erosion, showing both spatial and

temporal variation. Recession rates at the lower cliff varied by an order of magnitude between sites and increased substantially during winter months: 74 - 97% of erosion occurred between December and March. Lithology and structure also appeared to play a key role in dictating erosion: detachment rates were much higher and volumes smaller in the shale, indicative of frequent spalling of platelets. In contrast, siltstones exhibited infrequent, joint-controlled block removal. Erosion also displayed vertical variation: volume power law exponent values appeared to vary with lithology; detachment volume exhibited an increase about the HAT in detachments below 0.1 m^3. My results indicated that marine drivers were important in producing the characteristics observed: 1) erosion rates increased during winter, when larger waves occur; 2) erosion rates are positively correlated with cliff toe elevation, platform width and ramp slope, which dictate wave dynamics at the toe; 3) inundation duration alone cannot explain the vertical variation in erosion observed.

Whilst the results outlined here are site-specific, the methodology developed and mechanisms revealed have implications for the erosion of any macrotidal cliff. In addition, the findings here emphasised the requirement for further investigations with regard to cliff toe wave conditions, which may explain some of the observed variations in erosion.

2. *To investigate wave conditions at the cliff toe.*

This was achieved by deploying cliff toe wave gauges at five sites over the year-long study period (Chapter 5). A wide distribution of wave conditions was observed: up to a significant wave height of 7.3 m offshore and 2.5 m at the cliff toe. I found a positive correlation between offshore and cliff toe wave heights obeying a power law. This simple representation of wave transformation occurring between offshore and the cliff toe facilitated an evaluation of the influences thereof. Using site-by-site comparisons, the variance and coefficients of the power function were found to be determined in part by platform morphology. Platform width and, in particular, cliff toe elevation, controlled both a) inundation duration and b) wave heights at the toe.

For 82% of the time that the cliff toe wave inundated, cliff toe wave heights were lower than those offshore due to wave dissipation. The depth-limiting criterion was found to be $0.6d_{cliff} + 0.15$, within the range found by others in similar environments. As such, larger waves were dissipated prior to reaching the cliff toe. Some wave heights were found to be amplified at the cliff toe as a result of wave shoaling pre-breaking, but this was mainly confined to smaller offshore waves (< 2 m).

These findings show that, as found on microtidal platforms, very large wave heights (> 2.5 m) are scarce on macrotidal cliffs due to dissipation and the rarity of amplified waves of this height. However, waves were also found to be commonly breaking on impact: up to 9% of all wave impacts, or 165,000 waves per year. As such, wave height may be less important to erosive effectiveness than the propensity of waves to break on the cliff. Therefore, the higher erosion rates seem during storm periods elsewhere are likely not simply due to the commonly-asserted view that increased wave heights drive erosion directly. In addition, cliff toe water depth, controlled by toe elevation, tides and setup, is a primary control of wave heights, wave breaking conditions and therefore wave assailing force.

Whilst the transformation model in Chapter 5 is valuable in general wave height estimation at the cliff toe, it is limited by its inability to consider wave reflection and reforming between the break point and the cliff toe, as well as cross-shore processes such as refraction. Furthermore, the power laws derived for the model include considerable amounts of scatter. Higher fidelity monitoring was required to measure and understand the form of the wave on impact, which is critical in understanding dynamic pressure on the cliff. This led to a requirement for the quantification of such wave impacts in this environment.

3. *To devise a novel method of quantifying wave impact pressures at the cliff toe.*

Informed by previous investigations of wave impacts on coastal structures, I designed, built and tested an array of sensors designed to measure wave

impact pressures, as described in Chapter 6. This array was deployed at the cliff toe over a series of full tidal cycles. The system measured the shoreward pressures induced immediately in front of the lower cliff due to the presence of water and wave impacts. I developed a novel approach to processing these data. STA/LTA filtering was used to extract individual impact events from the continuous time series. I combined coincident impact events from each sensor to extract the induced pressure up the cliff face due to a single wave impingement. This allowed the statistical properties of the wave datasets to be extracted. In addition, pulsating and impulsive wave impacts were identified. The pressure - rise time relationship from the preliminary results was compared with other studies and found to agree with that of Cuomo *et al.* (2010). The sample rate used was also analysed and found to be sufficient for capturing the required pressures. This brief evaluation of the method indicated that it was adequate to achieve the objective four.

4. *To obtain measurements of wave impact pressures at the cliff toe and quantify their magnitude, frequency and vertical distribution*

Wave impacts pressures were successfully measured at the cliff toe at one of the sites over nine separate tidal cycles (Chapter 7). The resultant shoreward pressures on the lower cliff were comprised of continuous hydrostatic pressure due to the water mass, oscillating hydrostatic pressure due to the presence of waves (pulsating) and dynamic pressure induced via impacting waves (impulsive). The vertical profile of impact pressures showed that impulsive pressures occurred between the wave crest and trough; the pressure maxima were most likely to be centred on the still water depth. This supports the majority of coastal models. In addition, the induced dynamic force over the full profile was found to be substantially lower as a proportion of total force due to the asynchrony of the impulsive pressures at each elevation.

The ratio between wave height and water depth was found to be the primary control on the occurrence and magnitude of impulsive pressures. As such, breaking waves and broken waves, or those occurring above the depth-limiting criterion, were found to produce the highest pressures, in agreement with much

of the literature. The values for the highest 1/250 pressures were found to increase considerably when *H/d* was between 1 and 2.5. However, high pressures were relatively rare: the pressure maximum for each wave followed a finite-tailed generalised distribution, with only 1% of impulsive impacts exceeding the maximum pulsating pressure of 26 kPa.

Impulsive pressures were found to occur probabilistically. Whilst waves within the critical *H/d* zone were more likely to produce impulsive pressures, lower-magnitude impulsive and pulsating pressures still occurred. This lends weight to the argument that forcing should be considered stochastically, rather than deterministically. The distributions of the occurrence, magnitude and vertical distribution assembled in my study are a more appropriate method of evaluating and predicting wave forcing at coastal cliffs than deterministic formulae.

5. *To develop a modified conceptual model of the mechanisms that control marine-driven cliff erosion.*

The combination of erosion, cliff toe wave conditions and impact pressure datasets I have collected give a deeper insight into the mechanisms by which waves erode the lower cliff (Chapter 8). The combination of a) joint-controlled, intermittent block erosion in the siltstone, b) poor correlation between environmental forcing and recession rate and c) the observation of frequent breaking waves and impact forces suggests that wave quarrying is a dominant erosive process. Whilst the impact pressure magnitudes measured (<127 kPa) are incapable of damaging fresh rock, they are easily capable of initiating and propagating cracks when enhanced via discontinuities and acting against tensile strength.

The combination of a) high detachment frequency and centimetre-scale detachment volumes in the shale and b) the alignment of forcing and weathering profiles suggests that platelet fragmentation is another critical mechanism, albeit constituting only 11.5% of total volume loss. Again, prerequisite weathering is required as the impact pressures measured were too low to initiate fragmentation of fresh rock.

My research has shown that low-energy conditions may be effective erosion mechanisms through both removal of very weathered material and enhanced impact pressures within discontinuities. I have demonstrated the importance of cliff toe elevation in the control of wave forcing, through inundation duration, wave height limitation and depth-controlled breaking. My work informs an improved conceptual model of wave-driven lower cliff recession that removes material from the base of the cliff, which subsequently propagates upwards and drives overall cliff recession.

9.3. Original contribution to knowledge

My thesis has investigated a number of research questions which were still poorly understood and as such, has made a novel contribution to the understanding of coastal cliff recession in the following ways:

- I have produced the highest spatial resolution (0.5 x 0.5 cm) erosion map of the lower cliff to date. This has improved our understanding of the very small detachments which constitute platelet fragmentation from certain rock fabrics.
- Until now, waves at the cliff toe were previously only understood in the context of a narrow range of conditions. My study has captured wave conditions at five sites over a year, capturing a broad range of wave conditions. In turn, a deeper understanding of the wave heights and breaking conditions which occur at the cliff toe has been achieved, and demonstrated the importance of cliff toe elevation in governing this.
- I have designed and built the first sensor array to directly measure wave impacts at the cliff toe. My results establish, for the first time, that impulsive wave impacts occur in rock coast environments, and allow for a quantitative evaluation of wave pressures to inform future coastal erosion models. Furthermore, the field and processing techniques I have developed can inform future researchers who wish to build on this understanding.

9.4. Limitations of the study and recommendations for future research

My research has focused on monitoring the wave conditions, impact pressures and erosion characteristics at the cliff toe. Further research questions arose during the study which would benefit from further examination. In addition, a number of limitations of the approach should be considered which in turn highlight avenues for future research.

9.4.1. Observing impacts pressures over a wider range of conditions

The most novel and informative approach in my research has been the use of an impact pressure sensor at the cliff toe. Whilst the vertical resolution (0.1 m) and sample rate (5000 Hz) were sufficient to capture wave impact characteristics, the apparatus was subject to considerable limitations.

The height of the array was up to 1.7 m above the platform surface. This was adequate to capture crest heights only of up to that elevation. Waves occurring during higher tidal stages were not measured. As such, larger waves, which are more likely to occur at higher cliff toe depths due to the decreased influence of depth-controlled dissipation, were unable to be captured. This limited the study to capturing the full wave front of waves higher than approximately 1 m; larger waves of up to 1.5 m were measured but not up to the crest height.

Storm waves have been shown to generate a considerable increase in erosion rate during single events (Earlie *et al.*, 2015), yet the mechanisms by which the material is removed is poorly understood. My results outlined in Section 7.3.3.2 suggest that there is a positive correlation between wave height and impact pressure, but that this relationship is poorly defined, suggesting further mechanisms are involved. Therefore, a larger array able to measure up to 6 m up the lower cliff would capture these waves. This would shed light on the processes acting during these energetic events and further define the relationships between wave height, water depth and impact pressures.

Due to difficulties during fieldwork, I was only able to monitor wave impacts pressures at one cliff toe site. In Chapter 5 I showed that platform morphology,

particularly cliff toe elevation and platform width, were major influences on cliff toe wave conditions. Platform toe slope angle also affects breaker types (Section 5.4.3.2). These factors imply that my results may not be applicable to all platform morphologies. As such, our understanding of cliff toe wave impacts would benefit from further deployments of similar impact measurement equipment at different sites. This may include micro- and mesotidal environments, A-type horizontal platforms, beach fronted cliffs and a range of toe elevations and platform widths. This will further unpick the major controls on wave forcing in this manner.

9.4.2. Second-order controls on wave impact magnitudes

In Chapter 7 I outlined the likely second-order controls that may explain the variability and stochasticity seen in wave impact occurrence and magnitude: aeration, incident angle, wave shape and two-dimensional considerations. Further investigation of these could improve modelled predictions of wave assailing force on rock coasts.

The shape of the breaking wave on impact, in turn controlled by bathymetry, wave height and wind conditions, has been shown to be an influence on its impact magnitude. In my study, I attempted to categorise this using cameras mounted above the sensors and timing differentials between the sensors, but neither method proved reliable. However, cameras have been used successfully observe breaker shapes (Bird *et al.*, 1998) on coastal structures and as such, should be a viable approach for cliffs. Just a simple visual assessment of each wave into the groups in Figure 2.3 would permit more robust categorisation of the waves associated with each impact type, building on my suggestions in Section 7.3.3.4. In addition, wave incidence angle could also be observed. I suggest coupling impact pressure measurements with camera observations would be the most advantageous technique to improve understating in this field.

10. References

Aarnes, O. J., Reistad, M., Breivik, Ø., Bitner-gregersen, E., Eide, L. I., Gramstad, O., Magnusson, A. K., Natvig, B. and Vanem, E., **2017**. Projected changes in significant wave height towards the end of the 21st century - Northeast Atlantic, *Journal of Geophysical Research: Oceans*, **122**(4), pp. 3394–3403.

Abellán, A., Jaboyedoff, M., Oppikofer, T. and Vilaplana, J. M., **2009**. Detection of millimetric deformation using a terrestrial laser scanner: experiment and application to a rockfall event, *Natural Hazards and Earth System Science*, **9**(2), pp. 365–372.

Abellán, A., Oppikofer, T., Jaboyedoff, M., Rosser, N. J., Lim, M. and Lato, M. J., **2014**. Terrestrial laser scanning of rock slope instabilities, *Earth Surface Processes and Landforms*, **39**(1), pp. 80–97.

Adams, P. N., Anderson, R. S. and Revenaugh, J., **2002**. Microseismic measurement of wave-energy delivery to a rocky coast, *Geology*, **30**(10), pp. 895–898.

Adams, P. N., Storlazzi, C. D. and Anderson, R. S., **2005**. Nearshore wave-induced cyclical flexing of sea cliffs, *Journal of Geophysical Research: Earth Surface*, **110**(2).

Agar, R., **1960**. Postglacial erosion of the North Yorkshire coast from the Tees estuary to Ravenscar, *Proceedings of the Yorkshire Geological Society*, **32**(19), pp. 409–428.

Allan, J. C., Komar, P. D., Allant, J. C. and Komart, P. D., **2006**. Climate Controls on US West Coast Erosion Processes, *Journal of Coastal Research*, **22**(3), pp. 511–529.

Allirot, D., Boehler, J. P. and Sawczuk, A., **1977**. Irreversible deformations of an anisotropic rock under hydrostatic pressure, *International Journal of Rock Mechanics, Mining Sciences and Geomechanics Abstracts*, **14**(2), pp. 77–83.

Allsop, N. W. H. and Calabrese, M., **1998**. Impact Loadings on Vertical Walls

in Directional Seas, *Coastal Engineering Proceedings*, pp. 2056–2068.

Allsop, N. W. H., Mckenna, J. E., Vicinanza, D. and Whittaker, T. T. J., **1996**. New design methods for wave impact loadings on vertical breakwaters and seawalls, *Coastal Engineering,* **25**, pp. 2508–2521.

Allsop, N. W. H., Vann, A. M., Howarth, M. W., Jones, R. J. and Davis, J. P., **1996**. Measurements of wave impacts at full scale: results of fieldwork on concrete armour units, *Advances in coastal structures and breakwaters*, pp. 287–302.

Allsop, N. W. H. and Vicinanza, D., **1996**. Wave impact loadings on vertical breakwaters: development of new prediction formulae, *Proceedings of the International Harbour Congress*, **11**, pp. 275–284.

Allsop, N. W. H., Vicinanza, D., Calabrese, M. and Centurioni, L., **1996**. Breaking Wave Impact Loads on Vertical Faces, *Proceedings of the 6th International Offshore and Polar Engineering Conference*, **3**, pp. 185–191.

Almeida, L. P., Masselink, G., Russell, P. E., Davidson, M., Poate, T., Mccall, R., Blenkinsopp, C. and Turner, I., **2013**. Observations of the swash zone on a gravel beach during a storm using a laser-scanner (Lidar), *Journal of Coastal Research*, **65**, pp. 636–641.

Antoine, A. L. C., **2009**. *Dynamics of wave breaking at a coastal sea wall*. Master's Thesis, Texas A&M University.

Antonioli, F., Lo Presti, V., Rovere, A., Ferranti, L., Anzidei, M., Furlani, S., Mastronuzzi, G., Orru, P. E., Scicchitano, G., Sannino, G., Spampinato, C. R., Pagliarulo, R., Deiana, G., de Sabata, E., Sansò, P., Vacchi, M. and Vecchio, A., **2015**. Tidal notches in Mediterranean Sea: a comprehensive analysis, *Quaternary Science Reviews*, **119**(5), pp. 66–84.

Ashton, A. D., Walkden, M. J. A. and Dickson, M. E., **2011**. Equilibrium responses of cliffed coasts to changes in the rate of sea level rise, *Marine Geology*, **284**(1–4), pp. 217–229.

Bagnold, R. A., **1939**. Wave-Pressure Research, *Journal of the Institution of*

Civil Engineers, **12**, pp. 200–226.

Barkwith, A., Thomas, C. W., Limber, P. W., Ellis, M. A. and Murray, A. B., **2014**. Coastal vulnerability of a pinned, soft-cliff coastline - Part I: Assessing the natural sensitivity to wave climate, *Earth Surface Dynamics*, **2**(1), pp. 295–308.

Barlow, J., Lim, M., Rosser, N., Petley, D., Brain, M., Norman, E. and Geer, M., **2012**. Modeling cliff erosion using negative power law scaling of rockfalls, *Geomorphology*, **139–140**, pp. 416–424.

Barnes, H. L., **1956**. Cavitation as a geological agent, *American Journal of Science*, **254**(8), pp. 493–505.

Barnes, M. P., O'Donoghue, T., Alsina, J. M. and Baldock, T. E., **2009**. Direct bed shear stress measurements in bore-driven swash, *Coastal Engineering*, **56**(8), pp. 853–867.

Battjes, J. A., **1974**. Surf similarity, *Coastal Engineering*, **14**, pp. 466–480.

Beetham, E. P. and Kench, P. S., **2011**. Field observations of infragravity waves and their behaviour on rock shore platforms, *Earth Surface Processes and Landforms*, **36**(14), pp. 1872–1888.

Benjamin, J., **2018**. *Regional-scale controls on rockfall occurrence*. PhD Thesis: University of Durham.

Benumof, B. T. and Griggs, G. B., **1999**. The Dependence of Seacliff Erosion Rates on Cliff Material Properties and Physical Processes: San Diego County, California, *Shore and Beach*, **67**(4), pp. 29–41.

Bezerra, M. M., Moura, D., Ferreira, Ó. and Taborda, R., **2011**. Influence of Wave Action and Lithology on Sea Cliff Mass Movements in Central Algarve Coast, Portugal, *Journal of Coastal Research*, **275**, pp. 162–171.

Bird, P. A. ., Crawford, A. ., Hewson, P. . and Bullock, G. ., **1998**. An instrument for field measurement of wave impact pressures and seawater aeration, *Coastal Engineering*, **35**(1–2), pp. 103–122.

Blackmore, P., **1982**. *Evaluation of wave forces on seawalls*. PhD Thesis:

University of Plymouth.

Blackmore, P. A. and Hewson, P. J., **1984**. Experiments on full-scale wave impact pressures, *Coastal Engineering*, **8**, pp. 331–346.

Blanco-Chao, R., Pérez-Alberti, A., Costas-Casais, M. and Valcárcel-Díaz, M., **2006**. Abrasion processes in coarse-clastic beaches linked to rocky shore platforms, *Journal of Coastal Research*, **48**, pp. 21–28.

Blanco Chao, R., Casais, M. C., Cortizas, A. M., Alberti, A. P. and Trenhaile, A. S., **2003**. Evolution and inheritance of a rock coast: Western Galicia, Northwestern Spain, *Earth Surface Processes and Landforms*, **28**(7), pp. 757–775.

Blenkinsopp, C. E., Mole, M. A., Turner, I. L. and Peirson, W. L., **2010**. Measurements of the time-varying free-surface profile across the swash zone obtained using an industrial LIDAR, *Coastal Engineering*, **57**(11–12), pp. 1059–1065.

Blenkinsopp, C. E., Turner, I. L., Allis, M. J., Peirson, W. L. and Garden, L. E., **2012**. Application of LiDAR technology for measurement of time-varying free-surface profiles in a laboratory wave flume, *Coastal Engineering*, **68**, pp. 1–5.

Blenkinsopp, C. E., Turner, I. L., Mole, M. A., Garden, L. and Peirson, W. L., **2011**. Light detection and ranging (LiDAR) for measurement of coastal processes., in *20th Australasian Coastal and Ocean Engineering Conference 2011 and the 13th Australasian Port and Harbour Conference 2011, COASTS and PORTS 2011*. Curran Associates, NY, pp. 757–762.

BODC, **2017**. *UK Tide Gauge Network: Processed data for Whitby*. Available at: https://www.bodc.ac.uk/data/hosted_data_systems/sea_level/uk_tide_gauge_network/processed/ (Accessed: 3 November 2017).

Boukhanovsky, A. V., Lopatoukhin, L. J. and Guedes Soares, C., **2007**. Spectral wave climate of the North Sea, *Applied Ocean Research*, **29**(3), pp. 146–154.

Bowen, A. J. and Lindley, D., **1977**. A wind-tunnel investigation of the wind speed and turbulence characteristics close to the ground over various escarpment shapes, *Boundary-Layer Meteorology*, **12**, pp. 259–271.

Bradley, W. C. and Griggs, G. B., **1976**. Form, genesis, and deformation of central California wave-cut platforms, *Bulletin of the Geological Society of America*, **87**(3), pp. 433–449.

Brain, M. J., Rosser, N. J., Norman, E. C. and Petley, D. N., **2014**. Are microseismic ground displacements a significant geomorphic agent?, *Geomorphology*, **207**, pp. 161–173.

Brain, M. J., Rosser, N. J. and Tunstall, N., **2017**. The control of earthquake sequences on hillslope stability, *Geophysical Research Letters*, **44**(2), pp. 865–872.

Bray, M. J. and Hooke, J. M., **1997**. Prediction of Soft-cliff Retreat with Accelerating Sea-level Rise, *Journal of Coastal Research*, **13**(2), pp. 453–467.

Brayne, R. P., **2015**. *The Relationship between Nearshore Wave Conditions and Coarse Clastic Beach Dynamics*. PhD Thesis: University of Exeter.

Bredmose, H., Brocchini, M., Peregrine, D. H. and Thais, L., **2003**. Experimental investigation and numerical modelling of steep forced water waves, *Journal of Fluid Mechanics*, **490**, pp. 217–249.

Bredmose, H., Bullock, G., Obhrai, C., Gerald, M. and Wolters, G., **2004**. Extreme wave impact pressures and the effect of aeration, in *Proceedings of the 19th International Workshop on Water waves and Floating Bodies*. Cortona, Italy.

Bredmose, H., Hunt-Raby, A., Jayaratne, R. and Bullock, G. N., **2010**. The ideal flip-through impact: experimental and numerical investigation, *Journal of Engineering Mathematics*, **67**, pp. 115–136.

Bredmose, H., Peregrine, D. H. and Porter, A., **2003**. Wave impact and aerated water, in *18th International Workshop on Water Waves and Floating Bodies*. Le Croisic, France, pp. 2–6.

Brodie, K. L., Slocum, R. K. and McNinch, J. E., **2012**. New Insights into the Physical Drivers of Wave Runup from a Continuously Operating Terrestrial Laser Scanner, in *2012 Oceans*. Virginia, U.S.A.: IEEE, pp. 1–8.

Brossard, J. and Duperret, A., **2004**. Coastal chalk cliff erosion: experimental investigation on the role of marine factors, *Geological Society, London, Engineering Geology Special Publications*, **20**(1), pp. 109–120.

Budetta, P., Galietta, G. and Santo, A., **2000**. A methodology for the study of the relation between coastal cliff erosion and the mechanical strength of soils and rock masses, *Engineering Geology*, **56**, pp. 243–256.

Bullock, G. N., Crawford, A. R., Hewson, P. J., Walkden, M. J. A. and Bird, P. A. D., **2001**. The influence of air and scale on wave impact pressures, *Coastal Engineering*, **42**(4), pp. 291–312.

Bullock, G. N., Obhrai, C., Müller, G., Peregrine, D. H. and Bredmose, H., **2005**. Advances in the understanding of wave-impact forces, in *International Conference on Coastlines, Structures and Breakwaters*. London, pp. 111–120.

Bullock, G. N., Obhrai, C., Müller, G., Wolters, G., Peregrine, D. H. and Bredmose, H., **2003**. Field and Laboratory Measurement of Wave Impacts, in *Proceedings of the 3rd Coastal Structures Conference,* ASCE, pp. 343–355.

Bullock, G. N., Obhrai, C., Peregrine, D. H. and Bredmose, H., **2007**. Violent breaking wave impacts. Part 1: Results from large-scale regular wave tests on vertical and sloping walls, *Coastal Engineering*, **54**, pp. 602–617.

Burdine, N. T., **1963**. Rock Failure Under Dynamic Loading Conditions, *Society of Petroleum Engineers Journal*, **3**, pp. 1–8.

Caputo, T., Marino, E., Matano, F., Somma, R., Troise, C. and De Natale, G., **2018**. Terrestrial Laser Scanning (TLS) data for the analysis of coastal tuff cliff retreat: application to Coroglio cliff, Naples, Italy., *Annals of Geophysics*, **61**(1), pp. 1-18.

Cardozo, N. and Allmendinger, R. W., **2013**. Spherical projections with OSXStereonet, *Computers & Geosciences*, **51**, pp. 193–205.

Carpenter, N. E., Dickson, M. E., Walkden, M. J. A., Nicholls, R. J. and Powrie, W., **2014**. Effects of varied lithology on soft-cliff recession rates, *Marine Geology*, **354**, pp. 40–52.

Carr, J. H., **1954**. Breaking wave forces on plane barriers, *Pasadena: Hydraulic Laboratory, California Institute of Technology,* **Report No. E11.3**.

Carter, C. H. and Guy, D. E., **1988**. Coastal erosion: Processes, timing and magnitudes at the bluff toe, *Marine Geology*, **84**, pp. 1–17.

Carter, R. W. G., **1991**. *Coastal Environments: An Introduction to the Physical, Ecological and Cultural Systems of Coastlines*. London: Academic Publishing.

Castedo, R., Fernández, M., Trenhaile, A. S. and Paredes, C., **2013**. Modeling cyclic recession of cohesive clay coasts: Effects of wave erosion and bluff stability, *Marine Geology*, **335**, pp. 162–176.

Castedo, R., de la Vega-Panizo, R., Fernández-Hernández, M. and Paredes, C., **2015**. Measurement of historical cliff-top changes and estimation of future trends using GIS data between Bridlington and Hornsea - Holderness Coast (UK), *Geomorphology*, **230**, pp. 146–160.

Castedo, R., Murphy, W., Lawrence, J. and Paredes, C., **2012**. A new process-response coastal recession model of soft rock cliffs, *Geomorphology*, **177–178**, pp. 128–143.

Castedo, R., Paredes, C., Vega-Panizo, R. de la and Santos, A. P., **2017**. The Modelling of Coastal Cliffs and Future Trends, in Shukla, D. (ed.) *Hydro-Geomorphology - Models and Trends*. London: IntechOpen.

CERC, **1984**. *Shore Protection Manual*, *Coastal Engineering Research Center*. Washington D.C.

Channel Coastal Observatory, **2017**. *Whitby wave buoy realtime data*. Available at: http://www.channelcoast.org/data_management/real_time_data/charts/?chart=109 (Accessed: 18 November 2017).

Cheng, F. and Ji, W., **2017**. Cavitation erosion of a single bubble in water as a

kind of dynamic damage, *Proceedings of the Institution of Mechanical Engineers, Part J: Journal of Engineering Tribology*, **231**(11), pp. 1383–1389.

Cheng, R. T., Ling, C. H., Gartner, J. W. and Wang, P. F., **1999**. Estimates of bottom roughness length and bottom shear stress in South San Francisco Bay, California, *Journal of Geophysical Research*, **104**(4), pp. 7715–7728.

Clauset, A., Shalizi, C. R. and Newman, M. E., **2009**. Power-law distributions in empirical data, *SIAM review*, **51**(4), pp. 661–703.

Collins, B. D. and Sitar, N., **2008**. Processes of coastal bluff erosion in weakly lithified sands, Pacifica, California, USA, *Geomorphology*, **97**, pp. 483–501.

Collins, B. D. and Stock, G. M., **2016**. Rockfall triggering by cyclic thermal stressing of exfoliation fractures, *Nature Geoscience*, **9**, pp. 395–400.

Collins, B. D., Stock, G. M., Eppes, M.-C., Lewis, S. W., Corbett, S. C. and Smith, J. B., **2018**. Thermal influences on spontaneous rock dome exfoliation, *Nature Communications*, **9**(1), pp. 762.

Cooker, M. J. and Peregrine, D. H., **1990a**. A Model for Breaking Wave Impact Pressures, *Coastal Engineering*, pp. 1473–1486.

Cooker, M. J. and Peregrine, D. H., **1990b**. Violent Water Motion at Breaking-Wave Impact, *Coastal Engineering Proceedings*, **22**, pp. 164–176.

Cooker, M. J. and Peregrine, D. H., **1995**. Pressure-impulse theory for liquid impact problems, *Journal of Fluid Mechanics*, **297**(1), pp. 193–214.

Cot, P. D., **1954**. Le laboratoire du Harve pour la measuer des efforts dus aux lambs, in *Proceedings of the 5th Conference on Coastal Engineering*.

Cox, R., Jahn, K. L., Watkins, O. G. and Cox, P., **2018**. Extraordinary boulder transport by storm waves (west of Ireland, winter 2013–2014), and criteria for analysing coastal boulder deposits, *Earth-Science Reviews*, **177**, pp. 623–636.

Crawford, A. R., **1999**. *Measurement and Analysis of Wave Loading on a Full Scale Coastal Structure*. PhD Thesis: University of Plymouth.

Cruslock, E. M., Naylor, L. A., Foote, Y. L. and Swantesson, J. O. H., **2010**.

Geomorphologic equifinality: A comparison between shore platforms in Hoga Kusten and Faro, Sweden and the Vale of Glamorgan, South Wales, UK, *Geomorphology*, **114**, pp. 78–88.

Cullen, N. D. and Bourke, M. C., **2018**. Clast abrasion of a rock shore platform on the Atlantic coast of Ireland, *Earth Surface Processes and Landforms*, **43**, pp. 2627-2641.

Cuomo, G., Allsop, W., Bruce, T. and Pearson, J., **2010**. Breaking wave loads at vertical seawalls and breakwaters, *Coastal Engineering*, **57**(4), pp. 424–439.

Dai, F. C. and Lee, C. F., **2001**. Frequency-volume relation and prediction of rainfall-induced landslides, *Engineering Geology*, **59**(3–4), pp. 253–266.

Damgaard, J. S. and Dong, P., **2004**. Soft cliff recession under oblique waves: physical model tests, *Journal of Waterway Port Coastal and Ocean Engineering - ASCE*, **130**(5), pp. 234-242.

Davies, P., Sunamura, T., Takeda, I., Williams, H., T, S. and Park, N., **2006**. Controls of Shore Platform Width: the Role of Rock Resistance Factors at Selected Sites in Japan and Wales, UK, *Journal of Coastal Research*, **2004**(39), pp. 160–164.

Delmonte, R., **1972**. *Forces exerted by waves breaking seaward of a vertical seawall*. PhD Thesis: University Berkeley, California.

Denny, D., **1951**. Further Experiments on Wave Pressures, *Journal of the Institution of Civil Engineers*, **35**(4), pp. 330–345.

Dewez, T. J. B., Rohmer, J., Regard, V. and Cnudde, C., **2013**. Probabilistic coastal cliff collapse hazard from repeated terrestrial laser surveys: case study from Mesnil Val (Normandy, northern France), in *12th International Coastal Symposium (ICS)*. Plymouth, UK, pp. 702–707.

Dickson, M. E., **2006**. Shore platform development around Lord Howe Island, southwest Pacific, *Geomorphology*, **76**(3–4), pp. 295–315.

Dickson, M. E., Kennedy, D. M. and Woodroffe, C. D., **2004**. The influence of

rock resistance on coastal morphology around Lord Howe Island, Southwest Pacific, *Earth Surface Processes and Landforms*, **29**(5), pp. 629–643.

Dickson, M. E., Ogawa, H., Kench, P. S. and Hutchinson, A., **2013**. Sea-cliff retreat and shore platform widening: Steady-state equilibrium?, *Earth Surface Processes and Landforms*, **38**(9), pp. 1046–1048.

Dickson, M. E. and Pentney, R., **2012**. Micro-seismic measurements of cliff motion under wave impact and implications for the development of near-horizontal shore platforms, *Geomorphology*, **151–152**, pp. 27–38.

Dickson, M. E. and Woodroffe, C. D., **2005**. Rock coast morphology in relation to lithology and wave exposure, Lord Howe Island, southwest Pacific, *Zeitschrift für Geomorphologie*, **49**(2), pp. 239–251.

Dong, P. and Guzzetti, F., **2005**. Frequency-size statistics of coastal soft-cliff erosion, *Journal of Waterway Port Coastal and Ocean Engineering - ASCE*, **131**(1), pp. 37–42.

Van Doorslaer, K., Romano, A., De Rouck, J. and Kortenhaus, A., **2017**. Impacts on a storm wall caused by non-breaking waves overtopping a smooth dike slope, *Coastal Engineering*, **120**, pp. 93–111.

Dornbusch, U., Moses, C., Robinson, D. A. and Williams, R., **2008**. Soft copy photogrammetry to measure shore platform erosion on decadal timescales, *Journal of Coastal Conservation*, **11**(4), pp. 193–200.

Dornbusch, U., Robinson, D. A., Moses, C. A. and Williams, R. B. G., **2008**. Temporal and spatial variations of chalk cliff retreat in East Sussex, 1873 to 2001, *Marine Geology*, **249**(3–4), pp. 271–282.

Duperret, A., Genter, A., Martinez, A. and Mortimore, R. N., **2004**. Coastal chalk cliff instability in NW France: role of lithology, fracture pattern and rainfall, *Geological Society, London, Engineering Geology Special Publications*, **20**(1), pp. 33–55.

Earlie, C., Masselink, G. and Russell, P. E., **2018**. The role of beach morphology on coastal cliff erosion under extreme waves, *Earth Surface*

Processes and Landforms, **43**(6), pp. 1213–1228.

Earlie, C. S., Masselink, G., Russell, P. E. and Shail, R. K., **2014**. Application of airborne LiDAR to investigate rates of recession in rocky coast environments, *Journal of Coastal Conservation*, **19**(6), pp. 831–845.

Earlie, C. S., Young, A. P., Masselink, G. and Russell, P. E., **2015**. Coastal cliff ground motions and response to extreme storm waves, *Geophysical Research Letters*, **42**(3), pp. 847–854.

Emery, A., **2016**. Palaeopressure reconstruction to explain observed natural hydraulic fractures in the Cleveland Basin, *Marine and Petroleum Geology*, **77**, pp. 535–552.

Emery, K. O. and Kuhn, G. G., **1980**. Erosion of rock shores at La Jolla, California, *Marine Geology*, **37**(3–4), pp. 197–208.

Eppes, M. C. and Keanini, R., **2017**. Mechanical weathering and rock erosion by climate-dependent subcritical cracking, *Reviews of Geophysics*, **55**(2), pp. 470–508.

Farrell, E. J., Granja, H., Cappietti, L., Ellis, J. T., Li, B. and Sherman, D. J., **2009**. Wave Transformation across a Rock Platform, Belinho, Portugal, *Journal of Coastal Research*, **56**, pp. 44–48.

Field, J. E., **1999**. Liquid impact: Theory, experiment, applications, *Wear*, **233**, pp. 1–12.

Forman, S. E. and Secor, G. A., **1974**. The Mechanics of Rock Failure Due to Water Jet Impingement, *Society of Petroleum Engineers Journal*, **14**(1), pp. 10–18.

French, J. R. and Burningham, H., **2009**. Coastal geomorphology: trends and challenges, *Progress in Physical Geography*, **33**(1), pp. 117–129.

Fuji, A., **1988**. Measuring Wave Force on a Rocky Intertidal Shore, *Bulletin of the Faculty of Fisheries, Hokkaido University*, **39**(4), pp. 257–264.

Furlan, C., **2008**. Hierarchical random effect models for coastal erosion of cliffs

in the Holderness coast, *Statistical Methods and Applications*, **17**(3), pp. 335–350.

Gaillard, D. D., **1904**. *Wave Action in relation to Engineering Structures*. Washington D.C.: Government Printing Office.

Garcia, W. J., **1968**. *An experimental study of breaking wave pressures*. Research Report H-68-1, US Army Engineer Waterways Experiment Station, Vicksburg, MS.

Gibbons, D. T., Jones, G., Siegel, E., Hay, A. and Johnson, F., **2005**. Performance of a new submersible tide-wave recorder, in *Proceedings of MTS/IEEE OCEANS*. New York: IEEE, pp. 1057–1060.

Goda, Y., **1974**. New wave pressure formulae for composite breakwaters, *Coastal Engineering Proceedings*, **14**, pp. 1702–1720.

Goda, Y., **1985**. *Random seas and maritime structures*. Tokyo: University of Tokyo Press.

Gong, B., Wang, S., Sloan, S. W., Sheng, D. and Tang, C., **2017**. Modelling Coastal Cliff Recession Based on the GIM–DDD Method, *Rock Mechanics and Rock Engineering*, **51**(4), pp. 1077-095.

Google Maps, 2017. *Staithes, North Yorkshire, UK,* Available at: www.google.co.uk/maps (Accessed 31 January 2018).

Goudie, A. S., **2016**. Quantification of rock control in geomorphology, *Earth-Science Reviews*, **159**, pp. 374–387.

Green, T., **1989**. *Wave forces on vertical walls: an overview of recent work*. Washington D.C.: US Army Corps of Engineers.

Griffiths, J., **1993**. *The effects of aeration on wave impacts*. PhD Thesis: University of Plymouth.

Grohmann, C. H., Smith, M. J. and Riccomini, C., **2011**. Multiscale analysis of topographic surface roughness in the Midland Valley, Scotland, *IEEE Transactions on Geoscience and Remote Sensing*, **49**(4), pp. 1200–1213.

Grüne, J., **1988**. Wave-induced shock pressures under real sea state conditions, *Coastal Engineering Proceedings*, **1**(21), pp. 2340–2354.

Haas, F., Heckmann, T., Wichmann, V. and Becht, M., **2012**. Runout analysis of a large rockfall in the Dolomites/Italian Alps using LIDAR derived particle sizes and shapes, *Earth Surface Processes and Landforms*, **37**(13), pp. 1444–1455.

Hackney, C., Darby, S. E. and Leyland, J., **2013**. Modelling the response of soft cliffs to climate change: A statistical, process-response model using accumulated excess energy, *Geomorphology*, **187**, pp. 108–121.

Hall, A. M., Hansom, J. D. and Jarvis, J., **2008**. Patterns and rates of erosion produced by high energy wave processes on hard rock headlands: The Grind of the Navir, Shetland, Scotland, *Marine Geology*, **248**(1–2), pp. 28–46.

Hall, J. W., Meadowcroft, I. C., Lee, E. M. and Van Gelder, P. H. A. J. M., **2002**. Stochastic simulation of episodic soft coastal cliff recession, *Coastal Engineering*, **46**(3), pp. 159–174.

Hall, K. and Hall, A., **1996**. Weathering by wetting and drying: some experimental results, *Earth Surface Processes and Landforms*, **21**(4), pp. 365–376.

Hampton, M. A. and Griggs, G. B., **2004**. *Formation, evolution, and stability of coastal cliffs : status and trends*. USGS Professional Paper 1693.

Hansom, J. D., Barltrop, N. D. P. and Hall, A. M., **2008**. Modelling the processes of cliff-top erosion and deposition under extreme storm waves, *Marine Geology*, **253**(1–2), pp. 36–50.

Hapke, C. and Plant, N., **2010**. Predicting coastal cliff erosion using a Bayesian probabilistic model, *Marine Geology*, **278**, pp. 140–149.

Hattori, M., Arami, A. and Yui, T., **1994**. Wave impact pressure on vertical walls under breaking waves of various types, *Coastal Engineering*, **22**, pp. 79–114.

Hayashi, T. and Hattori, M., **1958**. Pressure of the breaker against a vertical

wall, *Coastal engineering in Japan*, **1**, pp. 25–37.

Hedges, T. S., **1985**. Experiments on full-scale wave impact pressures - discussion, *Coastal Engineering*, **9**, pp. 387–389.

Helmuth, B. and Denny, M. W., **2003**. Predicting wave exposure in the rocky intertidal zone: Do bigger waves always lead to larger forces?, *Limnology and Oceanography*, **48**(3), pp. 1338–1345.

Herbers, T. H. C., Orzech, M., Elgar, S. and Guza, R. T., **2003**. Shoaling transformation of wave frequency-directional spectra, *Journal of Geophysical Research*, **108**(C1), pp. 3013-3029.

Hergarten, S., **2003**. Landslides, sandpiles, and self-organized criticality, *Natural Hazards and Earth System Science*, **3**(6), pp. 505–514.

Herterich, J. G., Cox, R. and Dias, F., **2018**. How does wave impact generate large boulders? Modelling hydraulic fracture of cliffs and shore platforms, *Marine Geology*, **399**, pp. 34–46.

Van Heteren, J., Botma, H. C. and Roskam, A. P., **1989**. Field measurements of directional wave loads on coastal structures, *Applied Ocean Research*, **11**(2), pp. 58–74.

Hills, E. S., **1972**. Shore platforms and wave ramps, *Geological Magazine*, **109**(2), pp. 81–88.

Hiroi, I., **1920**. The force and power of waves, *The Engineer*, pp. 184–185.

Hoek, E., Marinos, P. and Benissi, M., **1998**. Applicability of the geological strength index (GSI) classification for very weak and sheared rock masses. The case of the Athens Schist Formation, *Bulletin of Engineering Geology and the Environment*, **57**(2), pp. 151–160.

Hofland, B., Kaminski, M. L. and Wolters, G., **2010**. Large-scale wave impacts on a vertical wall, *Coastal Engineering Proceedings*, **32**, pp. 1–15.

Holthuijsen, L. H., **2009**. *Waves in oceanic and coastal waters*. Cambridge University Press, pp. 404.

Horton, B. P., Rahmstorf, S., Engelhart, S. E. and Kemp, A. C., **2014**. Expert assessment of sea-level rise by AD 2100 and AD 2300, *Quaternary Science Reviews*, **84**, pp. 1–6.

Howarth, M. W., Allsop, N. W. H., Vann, A. M., Jones, R. J. and Davis, J. P., **1996**. Scale effects of wave impact pressures on cob armour units, *Coastal Engineering Proceedings*, **1**(25), pp. 2522–2533.

Hull, P. and Müller, G., **2002**. An investigation of breaker heights, shapes and pressures, *Ocean Engineering*, **29**, pp. 59–79.

Huthnance, J., **1991**. Physical oceanography of the North Sea, *Ocean and Shoreline Management*, **16**(3–4), pp. 199–231.

Inch, K. W., **2014**. Surf Zone Hydrodynamics: Measuring Waves and Currents, *Geomorphological Techniques*, **3**, pp. 1–13.

IPCC, **2014**. *Climate Change 2014: Synthesis Report. Contribution of Working Groups I, II and III to the Fifth Assessment Report of the Intergovernmental Panel on Climate Change*. Edited by R. K. Pachauri and L. A. Meyer. Geneva, Switzerland.

Jiang, H., Liu, Z. and Gao, K., **2017**. Numerical simulation on rock fragmentation by discontinuous water-jet using coupled SPH/FEA method, *Powder Technology*, **312**, pp. 248–259.

Johnstone, E., Raymond, J., Olsen, M. J. and Driscoll, N., **2016**. Morphological Expressions of Coastal Cliff Erosion Processes in San Diego County, *Journal of Coastal Research*, **76**, pp. 174–184.

Jones, W. E. and Demetropoulos, A., **1968**. Exposure to wave action: Measurements of an important ecological parameter on rocky shores on Anglesey, *Journal of Experimental Marine Biology and Ecology*, **2**(1), pp. 46–63.

Joswig, M., **1990**. Pattern recognition for earthquake detection, *Bulletin of the Seismological Society of America*, **80**(1), pp. 170–186.

Kanyaya, J. I. and Trenhaile, A., **2006**. Tidal wetting and drying on shore

platforms: An experimental study of surface expansion and contraction, *Geomorphology*, **76**(3–4), pp. 316–331.

Von Karman, T., **1929**. *The impact on seaplane floats during landing*. National Advisory Committee for Aeronautics, Washington D.C.

Katz, O. and Mushkin, A., **2013**. Characteristics of sea-cliff erosion induced by a strong winter storm in the eastern Mediterranean, *Quaternary Research*, **80**(1), pp. 20–32.

Kennedy, D. M., **2015**. Where is the seaward edge? A review and definition of shore platform morphology, *Earth-Science Reviews*, **147**, pp. 99–108.

El Khattabi, J., Carlier, E. and Louche, B., **2018**. The Effect of Rock Collapse on Coastal Cliff Retreat along the Chalk Cliffs of Northern France, *Journal of Coastal Research*, **34**(1), pp. 136–150.

King, C. A. M., **1972**. *Beaches and Coasts*. London: Edward Arnold Ltd.

Kirkgöz, M. S., **1982**. Shock Pressure of Breaking Waves on Vertical Walls, *Journal of the Waterway, Port, Coastal and Ocean Division*, **108**(1), pp. 81–95.

Kirkgöz, M. S., **1983**. Secondary Pressures of Waves Breaking on Seawall, *Journal of Waterway, Port, Coastal, and Ocean Engineering*, **109**(4), pp. 487–490.

Kirkgöz, M. S., **1991**. Impact pressure of breaking waves on vertical and sloping walls, *Ocean Engineering*, **18**(1), pp. 45–59.

Kirkgöz, M. S., **1992**. Influence of water depth on the breaking wave impact on vertical and sloping walls, *Coastal Engineering*, **18**(3–4), pp. 297–314.

Kirkgöz, M. S., **1995**. Breaking wave impact on vertical and sloping structures, *Ocean Engineering*, **22**(1), pp. 35–48.

Kirkgöz, M. S. and Akoz, M. S., **2005**. Geometrical properties of perfect breaking waves on composite breakwaters, *Ocean Engineering*, **32**, pp. 1994–2006.

Kjeldsen, S. P. and Myrhaug, D., **1979**. Breaking Waves in Deep Water and

Resulting Wave Forces, in *11th Offshore Technology Conference*. Houston, Texas, pp. 2515–2522.

Kline, S. W., Adams, P. N. and Limber, P. W., **2014**. The unsteady nature of sea cliff retreat due to mechanical abrasion, failure and comminution feedbacks, *Geomorphology*, **219**, pp. 53–67.

Kogure, T. and Matsukura, Y., **2010**. Critical notch depths for failure of coastal limestone cliffs: Case study at Kuro-shima Island, Okinawa, Japan, *Earth Surface Processes and Landforms*, **35**(9), pp. 1044–1056.

Komar, P. D. and Gaughan, M. K., **1972**. Airy Wave Theory and Breaker Height Prediction, in *13th International Conference on Coastal Engineering July 10-14*. Vancouver.

Kortenhaus, A. and Oumeraci, H., **1998**. Classification of Wave Loading on Monolithic Coastal Structures, *Coastal Engineering*, **1**(26), pp. 867–880.

Kraus, N. C., **1996**. *History and Heritage of Coastal Engineering*. Florida: ASCE Publications.

Kuribayashi, T., Muraki, Y. and Udai, G., **1959**. Field investigation of wave forces on breakwater, *Coastal Engineering in Japan*, **2**, pp. 17–27.

Lamb, M. P., Finnegan, N. J., Scheingross, J. S. and Sklar, L. S., **2015**. New insights into the mechanics of fluvial bedrock erosion through flume experiments and theory, *Geomorphology*, **244**, pp. 33–55.

Larson, M., Erikson, L. and Hanson, H., **2004**. An analytical model to predict dune erosion due to wave impact, *Coastal Engineering*, **51**(8–9), pp. 675–696.

Lee, E. M., **2008**. Coastal cliff behaviour: Observations on the relationship between beach levels and recession rates, *Geomorphology*, **101**(4), pp. 558–571.

Lee, E., Meadowcroft, I., Hall, J. and Walkden, M., **2002**. Coastal landslide activity: a probabilistic simulation model, *Bulletin of Engineering Geology and the Environment*, **61**(4), pp. 347–355.

Letortu, P., Costa, S., Cador, J. M., Coinaud, C. and Cantat, O., **2015**. Statistical and empirical analyses of the triggers of coastal chalk cliff failure, *Earth Surface Processes and Landforms*, **40**(10), pp. 1371–1386.

Letortu, P., Costa, S., Maquaire, O., Delacourt, C., Augereau, E., Davidson, R., Suanez, S. and Nabucet, J., **2015**. Retreat rates, modalities and agents responsible for erosion along the coastal chalk cliffs of Upper Normandy: The contribution of terrestrial laser scanning, *Geomorphology*, **245**, pp. 3–14.

Lim, M., **2006**. *Coastal cliff evolution with reference Staithes, North Yorkshire*. PhD Thesis: Durham University.

Lim, M., **2014**. The rock coast of the British Isles: cliffs, *Geological Society, London, Memoirs*, **40**(1), pp. 19–38.

Lim, M., Petley, D. N., Rosser, N. J., Allison, R. J. and Long, A. J., **2005**. Combined digital photogrammetry and time-of-flight laser scanning for monitoring cliff evolution, *The Photogrammetric Record*, **20**(June), pp. 109–129.

Lim, M., Rosser, N. J., Allison, R. J. and Petley, D. N., **2010**. Erosional processes in the hard rock coastal cliffs at Staithes, North Yorkshire, *Geomorphology*, **114**(1–2), pp. 12–21.

Lim, M., Rosser, N. J., Petley, D. N. and Keen, M., **2011**. Quantifying the Controls and Influence of Tide and Wave Impacts on Coastal Rock Cliff Erosion, *Journal of Coastal Research*, **27**(1), pp. 46–56.

Limber, P. W., Murray, A. B., Adams, P. N. and Goldstein, E. B., **2014**. Unraveling the dynamics that scale cross-shore headland relief on rocky coastlines: 1. Model development, *Journal of Geophysical Research*, **119**(4) pp. 854–873.

Lin, G., Chen, H., Hovius, N., Horng, M., Dadson, S., Meunier, P. and Lines, M., **2008**. Effects of earthquake and cyclone sequencing on landsliding and fluvial sediment transfer in a mountain catchment, *Earth Surface Processes and Landforms*, **33**(9), pp. 1354–1373.

Longuet-Higgins, M. S. and Stewart, R. W., **1964**. Radiation stresses in water

waves; a physical discussion, with applications, *Deep Sea Research and Oceanographic Abstracts*, **11**(4), pp. 529–562.

Lugni, C., Brocchini, M. and Faltinsen, O. M., **2006**. Wave impact loads: The role of the flip-through, *Physics of Fluids*, **18**(12), pp. 1–17.

Lundgren, H., **1969**. Wave shock forces: An analysis on deformations and forces in the wave and in the foundation, *Symposium on Research on Wave Action*, **2**, pp. 1–20.

Mai, T., **2017**. *On the role of aeration, elasticity and wave-structure interaction on hydrodynamic impact loading*. PhD Thesis: University of Plymouth.

Malamud, B. D., Turcotte, D. L., Guzzetti, F. and Reichenbach, P., **2004**. Landslide inventories and their statistical properties, *Earth Surface Processes and Landforms*, **29**(6), pp. 687–711.

Malevergne, Y., Pisarenko, V. and Sornette, D., **2011**. Testing the Pareto against the lognormal distributions with the uniformly most powerful unbiased test applied to the distribution of cities, *Physical Review E - Statistical, Nonlinear, and Soft Matter Physics*, **83**(3), pp. 1–11.

Marani, M., D'Alpaos, A., Lanzoni, S. and Santalucia, M., **2011**. Understanding and predicting wave erosion of marsh edges, *Geophysical Research Letters*, **38**(21), pp. 1-5.

Marques, F. M. S. F., **2008**. Magnitude-frequency of sea cliff instabilities, *Natural Hazards and Earth System Science*, **8**, pp. 1161–1171.

Marshall, R. J. E. and Stephenson, W. J., **2011**. The morphodynamics of shore platforms in a micro-tidal setting: Interactions between waves and morphology, *Marine Geology*, **288**(1–4), pp. 18–31.

Marth, R., Müller, G. and Wolters, G., **2005**. Damages of blockwork coastal structures due to internal wave impact induced pressures, *WIT Transactions on the Built Environment*, **79**, pp. 405–414.

Martin, F. L., Losada, M. A., Vidal, C. and Diaz Rato, J. L., **1996**. Prototype measurements of wave pressures on a wave screen comparison to physical

and analytical models, *Coastal Engineering*, **25**, pp. 1762–1775.

Martins, K., C, B. and J, Z., **2016**. Monitoring Individual Wave Characteristics in the Inner Surf with a 2-Dimensional Laser Scanner (LiDAR), *Journal of Sensors*, **461379**, pp. 1–11.

Marzeddu, A., Gironella, X. and Conejo, A. S.-A., **2013**. Impulsive wave loads on rigid structures , an experimental approach, *Journal of Coastal Research*, **65**, pp. 332–337.

Masselink, G., **1993**. Attenuation coefficients on natural beaches, in *11th Australian Conference on Coastal and Ocean Engineering*. Queensland, pp. 105–111.

Matsumoto, H., Dickson, M. E. and Kench, P. S., **2016**. An exploratory numerical model of rocky shore profile evolution, *Geomorphology*, **268**, pp. 98–109.

Matsumoto, H., Dickson, M. E. and Masselink, G., **2016**. Systematic Analysis of Rocky Shore Morphology along 700km of Coastline Using LiDAR-derived DEMs, in *AGU Fall Meeting, EP14A-07*. San Francisco, CA, USA.

Md Noar, N. A. Z. and Greenhow, M., **2015**. Wave impacts on structures with rectangular geometries: Part 1. Seawalls, *Applied Ocean Research*, **53**, pp. 132–141.

Met Office, **2017**. *UK Climate Summaries*. Available at: https://www.metoffice.gov.uk/climate/uk/summaries (Accessed: 13 November 2017).

Miles, J., **2013**. Wave shape effects on sediment transport, *Journal of Coastal Research*, (Special Issue **65**), pp. 1803–1808.

Miller, R. L., Leverette, S., O'Sullivan, J., Tochko, J. and Theriault, K., **1974**. Field measurements of impact pressures in surf, *Coastal Engineering*, **1**(14), pp. 1761–1777.

Minikin, R. C. R., **1963**. *Winds, Waves, and Maritime Structures: Studies in Harbour Making and in the Protection of Coasts*. London: Griffin, pp. 216.

Mitsuyasu, H., **1966**. Shock Pressure of Breaking Waves, *Coastal Engineering*, **10**, pp. 268–283.

Mogridge, G. R. and Jamieson, W. W., **1980**. Wave Impact Pressures on Composite Breakwaters, *Coastal Engineering Proceedings*, **1**(17), pp. 1829–1848.

Van Der Molen, J. and De Swart, H. E., **2001**. Holocene wave conditions and wave-induced sand transport in the southern North Sea, *Continental Shelf Research*, **21**(16–17), pp. 1723–1749.

Molitor, D., **1935**. Wave pressures on seawalls and breakwaters, *Transactions of the American Society of Civil Engineers*, **100**(1), pp. 984–1002.

Momber, A. W., **2003**. Cavitation damage to geomaterials in a flowing system, *Journal of Materials Science*, **38**(4), pp. 747–757.

Momber, A. W., **2004a**. Deformation and fracture of rocks due to high-speed liquid impingement, *International Journal of Fracture*, **130**(3), pp. 683–704.

Momber, A. W., **2004b**. Wear of rocks by water flow, *International Journal of Rock Mechanics and Mining Sciences*, **41**(1), pp. 51–68.

Moon, V. G. and Healy, T., **1994**. Mechanisms of Coastal Cliff Retreat and Hazard Zone Delineation in Soft Flysch Deposits, *Journal of Coastal Research*, **10**(3), pp. 663–680.

Moses, C. A., **2014**. The rock coast of the British Isles: shore platforms, *Geological Society, London, Memoirs*, **40**, pp. 39–56.

Moses, C. and Robinson, D., **2011**. Chalk coast dynamics: Implications for understanding rock coast evolution, *Earth-Science Reviews*, **109**(3–4), pp. 63–73.

Moses, C., Robinson, D. and Barlow, J., **2014**. Methods for measuring rock surface weathering and erosion: A critical review, *Earth-Science Reviews*, **135**, pp. 141–161.

Müller, G., **1997**. Wave Impact Pressure Propagation Into Cracks, *Proceedings*

of the ICE - Water Maritime and Energy, **124**(2), pp. 79–85.

Müller, G., Allsop, W., Bruce, T., Kortenhaus, A., Pearce, A. and Sutherland, J., **2008**. The occurrence and effects of wave impacts, *Proceedings of the ICE - Maritime Engineering*, **160**(4), pp. 167–173.

Müller, G., Wolters, G. and Cooker, M. J., **2003**. Characteristics of pressure pulses propagating through water-filled cracks, *Coastal Engineering*, **49**(1–2), pp. 83–98.

Muraki, Y., **1966**. Field observations of wave pressures, wave run-up and oscillation of breakwaters, *Coastal Engineering Proceedings*, **10**, pp. 302–321.

Nagai, S. and Kurata, K., **1974**. Investigations of Wave-Pressure Formulas Due to Damages of Breakwaters, *Coastal Engineering*, **14**, pp. 1721–1740.

Nagai, S. and Otsubo, T., **1968**. Pressures by breaking waves on composite-type breakwaters, *Coastal Engineering*, **1**(11) pp. 920–933.

Naylor, L. A. and Stephenson, W. J., **2010**. On the role of discontinuities in mediating shore platform erosion, *Geomorphology*, **114**(1–2), pp. 89–100.

Naylor, L. A., Stephenson, W. J., Smith, H. C. M., Way, O., Mendelssohn, J. and Cowley, A., **2016**. Geomorphological control on boulder transport and coastal erosion before, during and after an extreme extra-tropical cyclone, *Earth Surface Processes and Landforms*, **41**(5), pp. 685–700.

Naylor, L. A., Stephenson, W. J. and Trenhaile, A. S., **2010**. Rock coast geomorphology: Recent advances and future research directions, *Geomorphology*, **114**(1–2), pp. 3–11.

Naylor, L. A. and Viles, H. A., **2002**. A new technique for evaluating short-term rates of coastal bioerosion and bioprotection, *Geomorphology*, **47**(1), pp. 31–44.

NECO, **2017**. *North East Coastal Observatory wave and tide data*. Available at: http://www.northeastcoastalobservatory.org.uk/data/Wave_&_Tide_Data/ (Accessed: 10 November 2017).

Noormets, R., Crook, K. A. W. and Felton, E. A., **2004**. Sedimentology of rocky shorelines: 3. Hydrodynamics of megaclast emplacement and transport on a shore platform, Oahu, Hawaii, *Sedimentary Geology*, **172**(1–2), pp. 41–65.

Norman, E. C., **2012**. *Microseismic monitoring of the controls on coastal rock cliff erosion*. PhD Thesis: Durham University.

Norman, E. C., Rosser, N. J., Brain, M. J., Petley, D. N. and Lim, M., **2013**. Coastal cliff-top ground motions as proxies for environmental processes, *Journal of Geophysical Research: Oceans*, **118**(12), pp. 6807–6823.

Nott, J., **2003**. Waves, coastal boulder deposits and the importance of the pre-transport setting, *Earth and Planetary Science Letters*, **210**(1–2), pp. 269–276.

Obu, J., Lantuit, H., Grosse, G., Günther, F., Sachs, T., Helm, V. and Fritz, M., **2016**. Coastal erosion and mass wasting along the Canadian Beaufort Sea based on annual airborne LiDAR elevation data, *Geomorphology*, **293**, pp. 331–346.

Ogawa, H., **2013**. Observation of wave transformation on a sloping type B shore platform under wind-wave and swell conditions, *Geo-Marine Letters*, **33**, pp. 1–11.

Ogawa, H., Dickson, M. E. and Kench, P. S., **2011**. Wave transformation on a sub-horizontal shore platform, Tatapouri, North Island, New Zealand, *Continental Shelf Research*. Elsevier, **31**(14), pp. 1409–1419.

Ogawa, H., Dickson, M. E. and Kench, P. S., **2015**. Hydrodynamic constraints and storm wave characteristics on a sub-horizontal shore platform, *Earth Surface Processes and Landforms*, **40**(1), pp. 65–77.

Ogawa, H., Kench, P. and Dickson, M., **2012**. Field Measurements of Wave Characteristics on a Near-Horizontal Shore Platform, Mahia Peninsula, North Island, New Zealand, *Geographical Research*, **50**(2), pp. 179–192.

Olsen, M. J., Johnstone, E., Driscoll, N., Kuester, F. and Ashford, S. A., **2016**. Fate and Transport of Seacliff Failure Sediment in Southern California, *Journal of Coastal Research*, **76**, pp. 185–199.

Oumeraci, H., Allsop, N. W. H., Groot, M. B. de, Crouch, R. S. and Vrijling, J. K., **1999**. *MAST III PROVERBS Final Report: Volume 1*.

Oumeraci, H., Klammer, P. and Partenscky, H., **1993**. Classification of breaking wave loads on vertical structures, *Journal of Waterway, Port, Coastal, and Ocean Engineering*, **119**(4), pp. 381–397.

Oumeraci, H., Kortenhaus, A., Allsop, W., Groot, M. de, Crouch, R., Vrijling, H. and Voortman, H., **2001**. *Probabilistic Design Tools for Vertical Breakwaters*. Lisse: A.A.Balkema.

Palaseanu-Lovejoy, M., Danielson, J., Thatcher, C., Foxgrover, A., Barnard, P., Brock, J. and Young, A., **2016**. Automatic Delineation of Seacliff Limits using Lidar-derived High-resolution DEMs in Southern California, *Journal of Coastal Research*, **76**, pp. 162–173.

Palumbi, S. R., **1984**. Measuring intertidal wave forces, *Journal of Experimental Marine Biology and Ecology*, **81**(2), pp. 171–179.

Pappalardo, M., Cappietti, L., Llopis, I. A., Chelli, A. and Fabritiis, L. De, **2017**. Development of Shore Platforms along the NW Coast of Italy: The Role of Wind Waves, *Journal of Coastal Research*, **33**(5), pp. 1102–1112.

Park, H. J., Kim, D. Y., Park, S. Y., Jo, A. J. and Kang, K., **2016**. Direct measurement of bottom shear stress under high-velocity flow conditions, *Flow Measurement and Instrumentation*, **50**, pp. 121–127.

Park, H., Tomiczek, T., Cox, D. T., van de Lindt, J. W. and Lomonaco, P., **2017**. Experimental modeling of horizontal and vertical wave forces on an elevated coastal structure, *Coastal Engineering*, **128**, pp. 58–74.

Payo, A., Hall, J. W., Dickson, M. E. and Walkden, M. J. A., **2014**. Feedback structure of cliff and shore platform morphodynamics, *Journal of Coastal Conservation*, **19**(6), pp. 847–859.

Pearson, R. K., Neuvo, Y., Astola, J. and Gabbouj, M., **2016**. The class of generalized hampel filters, *EURASIP Journal on Advances in Signal Processing*, **87**, pp. 2501–2505.

Peregrine, D. H., **2003**. Water-wave Impact of Walls, *Annual Review of Fluid Mechanics*, **35**(1), pp. 23–43.

Peregrine, D. H., Bredmose, H., Bullock, G., Obhrai, C., Müller, G. and Wolters, G., **2004**. Violent water wave impact on a wall and the role of air, in *Proceedings of the 29th International Conference on Coastal Engineering*. Lisbon, Portugal, pp. 4005–4017.

Plumerault, L. R., Astruc, D., Villedieu, P. and Maron, P., **2012**. A numerical model for aerated-water wave breaking, *International Journal for Numerical Methods in Fluids*, **69**, pp. 1851–1871.

Poate, T., Masselink, G., Austin, M., Dickson, M. and Kench, P., **2016**. Observation of Wave Transformation on Macro-tidal Rocky Platforms, *Journal of Coastal Research*, **75**, pp. 602–606.

Poate, T., Masselink, G., Austin, M. J., Dickson, M. and McCall, R., **2018**. The Role of Bed Roughness in Wave Transformation Across Sloping Rock Shore Platforms, *Journal of Geophysical Research: Earth Surface*, **123**(1), pp. 97–123.

Porter, N. J., Trenhaile, A. S., Prestanski, K. and Kanyaya, J. I., **2010**. Patterns of surface downwearing on shore platforms in eastern Canada, *Earth Surface Processes and Landforms*, **35**(15), pp. 1793–1810.

Raby, A., Bullock, G. N., Banfi, D., Rafiq, Y. and Cali, F., **2016**. Wave loading on rock lighthouses, *Proceedings of the Institution of Civil Engineers - Maritime Engineering*, **169**(3), p. 140.

Rajasekaran, C., Sannasiraj, S. and Sundar, V., **2010**. Breaking Wave Impact Pressure on a Vertical Wall, *The International Journal of Ocean and Climate Systems*, **1**(3), pp. 155–166.

Ramachandran, K., Schimmels, S., Stagonas, D. and Müller, G., **2013**. Measuring Wave Impact on Coastal Structures with High Spatial and Temporal Resolution – Tactile Pressure Sensors a Novel Approach, in *Proceedings of 2013 IAHR Congress*. Beijing: Tsinghua University Press.

Rampino, M. R., **2005**. Erosion Processes, in Schwartz, M. L. (ed.) *Encyclopedia of Coastal Science*. Dordrecht: Springer Netherlands, pp. 432–433.

Raubenheimer, B., Guza, R. T. and Elgar, S., **1996**. Wave transformation across the inner surf zone, *Journal of Geophysical Research*, **101**(C10), p. 25,589-25,597.

Raubenheimer, B., Guza, R. T. and Elgar, S., **2001**. Field observations of wave-driven setdown and setup, *Journal of Geophysical Research*, **106**(C3), pp. 4629–4638.

Rawson, P. F. and Wright, J. K., **2000**. The Yorkshire Coast, *Geologists Association Guide*. London, **34**, pp. 16–24.

Robinson, D. A. and Jerwood, L. C., **1987**. Frost and salt weathering of chalk shore platforms near Brighton, Sussex, U.K., *Transactions of the Institute of British Geographers*, **12**(2), pp. 217–226.

Robinson, L. A., **1977a**. Erosive processes on the shore platform of northeast Yorkshire, England, *Marine Geology*, **23**(4), pp. 339–361.

Robinson, L. A., **1977b**. Marine erosive processes at the cliff foot, *Marine Geology*, **23**(1964), pp. 257–271.

Ross, C., **1954**. Shock pressures of breaking waves, *Coastal Engineering Proceedings*, **1**(23), pp. 268–283.

Ross, C., **1955**. *Laboratory study of shock pressures of breaking waves*, *Beach Erosion Board, Tech. Memo No. 59*.

Rosser, N. J., Brain, M. J., Petley, D. N., Lim, M. and Norman, E. C., **2013**. Coastline retreat via progressive failure of rocky coastal cliffs, *Geology*, **41**(8), pp. 939–942.

Rosser, N. J., Petley, D. N., Lim, M., Dunning, S. A. and Allison, R. J., **2005**. Terrestrial laser scanning for monitoring the process of hard rock coastal cliff erosion, *Quarterly Journal of Engineering Geology and Hydrogeology*, **38**(4), pp. 363–375.

Rosser, N., Lim, M., Petley, D., Dunning, S. and Allison, R., **2007**. Patterns of precursory rockfall prior to slope failure, *Journal of Geophysical Research*, **112**(F4), p. F04014.

Rossi, A., **1984**. *Impact pressures of sea waves*. PhD Thesis: Plymouth University.

Rouville, M., Besson, P. and Petry, P., **1938**. Etat actual des etudes internationales sur les efforts dus aux lambs, *Annales de Ponts et Chaussees*, **108**(2), pp. 5–113.

Ruessink, B. G., Ramaekers, G. and Van Rijn, L. C., **2012**. On the parameterization of the free-stream non-linear wave orbital motion in nearshore morphodynamic models, *Coastal Engineering*. Elsevier B.V., **65**, pp. 56–63.

Sainflou, M., **1928**. Essai sur les diques maritimes verticales, *Annales de Ponts et Chaussees*, **98**, pp. 5–48.

Sallenger, A. H. and Holman, R. A., **1985**. Wave Energy Saturation on a Natural Beach of Variable Slope, *Journal of Geophysical Research*, **90**(6), pp. 11,939–11,944.

Sanders, N. K., **1968a**. *The development of Tasmanian shore platforms*. PhD Thesis: University of Tasmania.

Sanders, N. K., **1968b**. Wave tank experiments on the erosion of rocky coasts, *Papers and Proceeding of the Royal Society of Tasmania*, **102**, pp. 11–17.

Saunders, P. M. and Fofonoff, N. P., **1976**. Conversion of pressure to depth in the ocean, *Deep-Sea Research and Oceanographic Abstracts*, **23**(1), pp. 109–111.

Schürch, P., Densmore, A. L., Rosser, N. J., Lim, M. and Mcardell, B. W., **2011**. Detection of surface change in complex topography using terrestrial laser scanning: Application to the Illgraben debris-flow channel, *Earth Surface Processes and Landforms*, **36**(14), pp. 1847–1859.

Shaw, J., Taylor, R. B., Solomon, S., Christian, H. A. and Forbes, D., **1998**. Potential impacts of global sea level rise on Canadian coasts, *The Canadian*

Geographer, **42**(4), pp. 365–379.

Simms, M. J., Chidlaw, N., Morton, N. and Page, K. N., **2004**. *British Lower Jurassic Stratigraphy*. Peterborough: Joint Nature Conservation Committee.

Skafel, M. G., **1995**. Laboratory measurement of nearshore velocities and erosion of cohesive sediment (Till) shorelines, *Coastal Engineering*, **24**(94), pp. 343–349.

Skafel, M. G. and Bishop, C. T., **1994**. Flume experiments on the erosion of till shores by waves, *Coastal Engineering*, **23**, pp. 329–348.

Sklar, L. S. and Dietrich, W. E., **2001**. Sediment and rock strength controls on river incision into bedrock, *Geology*, **29**(12), pp. 1087–1090.

Stagonas, D., Marzeddu, A., Gironella, X., Sánchez-Arcilla, A. and Müller, G., **2015**. Measuring wave impact induced pressures with a pressure mapping system, *Coastal Engineering*, **112**, pp. 44–56.

Stagonas, D., Müller, G., Batten, W. and Magagna, D., **2011**. Mapping the temporal and spatial distribution of experimental impact induced pressures at vertical seawalls: a novel method, in *5th International Short Conference on Applied Coastal Research*. Aachen, Germany, pp. 388–394.

Staniforth, A., **1993**. *Geology of the North York Moors*. Helmsley: North York Moors National Park.

Stephenson, W. J., **1997**. *Development of shore platforms on Kaikoura Peninsula, South Island, New Zealand*. PhD Thesis: University of Canterbury.

Stephenson, W. J. and Finlayson, B. L., **2009**. Measuring erosion with the micro-erosion meter-Contributions to understanding landform evolution, *Earth-Science Reviews*, **95**(1–2), pp. 53–62.

Stephenson, W. J. and Kirk, R. M., **1998**. Rates and patterns of erosion on inter-tidal shore platforms, Kaikoura Peninsula, South Island, New Zealand, *Earth Surface Processes and Landforms*, **23**, pp. 1071–1085.

Stephenson, W. J. and Kirk, R. M., **2000a**. Development of shore platforms on

Kaikoura Peninsula, South Island, New Zealand II: The role of subaerial weathering, *Geomorphology*, **32**(1–2), pp. 43–56.

Stephenson, W. J. and Kirk, R. M., **2000b**. Development of shore platforms on Kaikoura Peninsula, South Island, New Zealand Part one: The role of waves, *Geomorphology*, **32**, pp. 21–41.

Stephenson, W. J., Taylor, A. J., Hemmingsen, M. A., Tsujimoto, H. and Kirk, R. M., **2004**. Short-term microscale topographic changes of coastal bedrock on shore platforms, *Earth Surface Processes and Landforms*, **29**(13), pp. 1663–1673.

Stephenson, W. J. and Thornton, L. E., **2005**. Australian Rock Coasts: review and prospects, *Australian Geographer*, **36**(1), pp. 95–115.

Stephenson, W. S. J., Naylor, L. A., Smith, H., Chen, B. and Brayne, R. P., **2018**. Wave Transformation Across a Macrotidal Shore Platform Under Low to Moderate Energy Conditions, *Earth Surface Processes and Landforms*, **43**, pp. 298–311.

Stone, J., Lambeck, K., Fifield, L. K., Evans, J. M. and Cresswell, R. G., **1996**. A Lateglacial age for the Main Rock Platform, western Scotland, *Geology*, **24**(8), pp. 707–710.

Sunamura, T., **1975**. A Laboratory Study of Wave-Cut Platform Formation, *The Journal of Geology*, **83**(3), pp. 389–397.

Sunamura, T., **1977**. A Relationship between Wave-Induced Cliff Erosion and Erosive Force of Waves, *The Journal of Geology*, **85**(5), pp. 613–618.

Sunamura, T., **1982**. A wave tank experiment on the erosional mechanism at a cliff base, *Earth Surface Processes and Landforms*, **7**, pp. 333–343.

Sunamura, T., **1991**. The Elevation of Shore Platforms: A Laboratory Approach to the Unsolved Problem, *The Journal of Geology*, **99**(5), pp. 761–766.

Sunamura, T., **1992**. *Geomorphology of rocky coasts*. Chichester: Wiley.

Sunamura, T., **1994**. Rock control in coastal geomorphic processes,

Transactions, Japanese Geomorphological Processes, **15**(3), pp. 253–272.

Sunamura, T., **2015**. Rocky coast processes: with special reference to the recession of soft rock cliffs, *Proceedings of the Japanese Academy, Series B*, **91**(9), pp. 481–500.

Sunamura, T., Tsujimoto, H. and Aoki, H., **2014**. The rock coast of Japan, *Geological Society, London, Memoirs*, **40**, pp. 203–223.

Swantesson, J. O. H., Gomez-Pujol, L., Cruslock, E. M., Fornos, J. J. and Balaguer, P., **2006**. Processes and patterns of erosion and downwearing on micro-tidal rock coasts in Sweden and the western Mediterranean, *Zeitschrift für Geomorphologie Supplementbande*, **144,** pp. 137-160.

Swenson, M. J., Wu, C. H., Edil, T. B. and Mickelson, D. M., **2006**. Bluff Recession Rates and Wave Impact Along the Wisconsin Coast of Lake Superior, *Journal of Great Lakes Research*, **32**(3), pp. 512–530.

Swirad, Z. M., Rosser, N. J., Brain, M. J. and Vann, E. C., **2016**. What controls the Geometry of Rocky Coasts at the Local Scale?, *Journal of Coastal Research*, **1**(75), pp. 6–11.

Tanguy, J. M., **2013**. *Physical Processes and Measurement Devices*. Hoboken, NJ: Wiley.

Taylor, A. J., **2003**. *Change and processes of change on shore platforms*. PhD Thesis: University of Canterbury.

Telling, J., Lyda, A., Hartzell, P. and Glennie, C., **2017**. Review of Earth science research using terrestrial laser scanning, *Earth-Science Reviews*, **169**, pp. 35–68.

Thiruvengadem, A., **1965**. *The concept of erosion strength*, *Hydronautics Technical Report 233-9*.

Thompson, E. F. and Vincent, C. L., **1985**. Significant Wave Height for Shallow Water Design, *Journal of Waterway Port Coastal and Ocean Engineering*, **111**(5), pp. 828-842.

Tien, Y. M., Lee, D. H. and Juang, C. H., **1990**. Strain, pore pressure and fatigue characteristics of sandstone under various load conditions, *International Journal of Rock Mechanics, Mining Sciences and Geomechanics Abstracts*, **27**(4), pp. 283–289.

Tijsseling, A. S. and Anderson, A., **2004**. The Joukowsky equation for fluids and solids, in *Proceedings of the 9th International Conference on Pressure Surges*. Chester, UK, pp. 739–751.

Tingstad, A., **2008**. Simulation of salt weathering in a closely replicated coastal environment, *Geografiska Annaler, Series A: Physical Geography*, **90**(2), pp. 165–171.

Toffoli, A., Babanin, A., Onorato, M. and Waseda, T., **2010**. Maximum steepness of oceanic waves: Field and laboratory experiments, *Geophysical Research Letters*, **37**(L05603).

Tomiczek, T., Prasetyo, A., Mori, N., Yasuda, T. and Kennedy, A., **2017**. Effects of a macro-roughness element on tsunami wave amplification, pressures, and loads: Physical model and comparison to Japanese and US Design Equations, *Coastal Engineering*, **59**(1).

Trenhaile, A. S., **1983**. The Width of Shore Platforms; A Theoretical Approach, *Geografiska Annaler. Series A, Physical Geography*, **65**(1), pp. 147–158.

Trenhaile, A. S., **1987**. *The Geomorphology of Rock Coasts*. Oxford University Press.

Trenhaile, A. S., **1999**. The Width of Shore Platforms in Britain, Canada and Japan, *Journal of Coastal Research*, **15**(2), pp. 355–364.

Trenhaile, A. S., **2000**. Modeling the development of wave-cut shore platforms, *Marine Geology*, **166**(1–4), pp. 163–178.

Trenhaile, A. S., **2001**. Modelling the Quaternary evolution of shore platforms and erosional continental shelves, *Earth Surface Processes and Landforms*, **26**(10), pp. 1103–1128.

Trenhaile, A. S., **2002**. Rock coasts, with particular emphasis on shore

platforms, *Geomorphology*, **48**(1–3), pp. 7–22.

Trenhaile, A. S., **2005a**. Modelling the effect of waves, weathering and beach development on shore platform development, *Earth Surface Processes and Landforms*, **30**(5), pp. 613–634.

Trenhaile, A. S., **2005b**. Rock Coast Processes, in Schwartz, M. L. (ed.) *Encyclopaedia of Coastal Science*. Springer Netherlands, pp. 815–818.

Trenhaile, A. S., **2009**. Modeling the erosion of cohesive clay coasts, *Coastal Engineering*, **56**(1), pp. 59–72.

Trenhaile, A. S., **2011**. Predicting the response of hard and soft rock coasts to changes in sea level and wave height, *Climatic Change*, **109**(3–4), pp. 599–615.

Trenhaile, A. S., **2014**. Rock Coast Geomorphology: A Global Synthesis - Climate change and its impact on rock coasts, *Geological Society, London, Memoirs*, **40**, pp. 7–17.

Trenhaile, A. S., **2015**. Coastal notches: Their morphology, formation, and function, *Earth-Science Reviews*, **150**, pp. 285–304.

Trenhaile, A. S., Gagnon, J., Prestanski, K. J. and Porter, N. I., **2015**. Cliff notch formation along the sub-tropical La Paz Peninsula, Southern Baja California, Mexico, *Marine Geology*, **368**, pp. 15–24.

Trenhaile, A. S. and Kanyaya, J. I., **2007**. The Role of Wave Erosion on Sloping and Horizontal Shore Platforms in Macro- and Mesotidal Environments, *Journal of Coastal Research*, **232**, pp. 298–309.

Trenhaile, A. S. and Layzell, M. G. J., **1981**. Shore platform morphology and the tidal duration factor, *Transactions, Institute of British Geographers*, **6**(1), pp. 82–102.

Trenhaile, A. S. and Rudakas, P. A., **1981**. Freeze-thaw and shore platform development in Gaspé, Québec, *Géographie physique et Quaternaire*, **35**(2), pp. 171–181.

Trnkoczy, A., **2002**. Understanding and parameter setting of STA/LTA trigger algorithm, *IASPEI New Manual of Seismological Observatory Practice*.

Tsujimoto, H., **1987**. *Dynamic Conditions for Shore Platform Initiation*. PhD Thesis: University of Tsukuba.

Underwood, A. J., **1972**. Sinusoidal tide models: Design, construction and laboratory performance, *Journal of Experimental Marine Biology and Ecology*, **8**, pp. 101–111.

Vann Jones, E. C., Rosser, N. J., Brain, M. J. and Petley, D. N., **2015**. Quantifying the environmental controls on erosion of a hard rock cliff, *Marine Geology*, **363**, pp. 230–242.

de Vilder, S. J., Rosser, N. J. and Brain, M. J., **2017**. Forensic analysis of rockfall scars, *Geomorphology*, **295**, pp. 202–214.

Viles, H. A., **2013**. Linking weathering and rock slope instability: Non-linear perspectives, *Earth Surface Processes and Landforms*, **38**(1), pp. 62–70.

Walkden, M., **1999**. *Model wave impulse loads on caisson breakwaters: aeration, scale and structural response*. PhD Thesis: University of Plymouth.

Walkden, M. J. A., Crawford, A. ., Bullock, G. N., Hewson, P. J. and Bird, P. A., **1995**. *Wave impact loading of vertical structures*, *Advances in coastal structures and breakwaters*. London: Thomas Telford, pp. 273-286.

Walkden, M. J. A. and Hall, J. W., **2005**. A predictive Mesoscale model of the erosion and profile development of soft rock shores, *Coastal Engineering*, **52**(6), pp. 535–563.

Walkden, M. J. and Hall, J. W., **2011**. A Mesoscale Predictive Model of the Evolution and Management of a Soft-Rock Coast, *Journal of Coastal Research*, **27**(3), pp. 529–543.

Weggel, J. R. and Maxwell, W., **1970**. Experimental study of breaking wave pressures, in *Second Annual Offshore Technology Conference*. Houston, Texas, pp. 1–14.

Weisse, R., von Storch, H., Niemeyer, H. D. and Knaack, H., **2012**. Changing North Sea storm surge climate: An increasing hazard?, *Ocean & Coastal Management*, **68**, pp. 58–68.

Whadcoat, S., **2017**. *Numerical modelling of rockfall evolution in hard rock slopes*. PhD Thesis: Durham University.

Wheaton, J. M., Brasington, J., Darby, S. E. and Sear, D. A., **2010**. Accounting for uncertainty in DEMs from repeat topographic surveys: improved sediment budgets, *Earth Surface Processes and Landforms*, **35**, pp. 136–156.

Whillock, A. F., **1982**. *Forces on Sea Walls Under Oblique Wave Attack*. Report No. IT225, Hydraulics Research Station, Wallingford, UK.

Whillock, A. F., **1987**. Measurements of forces resulting from normal and oblique wave approaches to small scale sea walls, *Coastal Engineering*, **11**(4), pp. 297–308.

Whipple, K. X., Hancock, G. S. and Anderson, R. S., **2000**. River incision into bedrock: Mechanics and relative efficacy of plucking, abrasion and cavitation, *Bulletin of the Geological Society of America*, **112**(3), pp. 490–503.

Wilcock, P. R., Miller, D. S., Shea, R. H. and Kerkin, R. T., **1998**. Frequency of effective wave activity and the recession of coastal bluffs: Calvert Cliffs, Maryland, *Journal of Coastal Research*, **14**(1), pp. 256–268.

Wilde, S. De, **2017**. *Statistical analysis of overtopped wave impacts on storm walls*. Master's Thesis: Ghent University.

Williams, A. T. and Roberts, G. T., **1995**. The measurement of pebble impacts and wave action on shore platforms and beaches: the swash force transducer (swashometer), *Marine Geology*, **129**(1–2), pp. 137–143.

Williams, J., Carling, P., Leyland, J. and Esteves, L., **2017**. Formation of Shore-Normal Grooves (Gutters) in Sandstone by Wave Action, in *Coasts and Ports*. Cairns, 21-23 June 2017.

Williams, J. G., Rosser, N. J., Hardy, R. J., Brain, M. J. and Afana, A. A., **2017**. Optimising 4-D surface change detection: an approach for capturing

rockfall magnitude–frequency, *Earth Surface Dynamics*, **6**, pp. 101–119.

Wilson, G., **1952**. The influence of rock structures on coast-line and cliff development around Tintagel, North Cornwall, *Proceedings of the Geologists' Association*. The Geologists' Association, **63**(1), pp. 20–48.

Wolters, G. and Müller, G., **2004**. The propagation of wave impact induced pressures into cracks and fissures, *Engineering Geology Special Publications*, **20**, pp. 121–130.

Wolters, G. and Müller, G., **2008**. Effect of cliff shape on internal stresses and rock slope stability, *Journal of Coastal Research*, **24**(1), pp. 43–50.

Wolters, G., Müller, G., Bruce, T. and Obhrai, C., **2005**. Large-scale experiments on wave downfall pressures, *Maritime Engineering*, **158**(MA4), pp. 137–145.

Wu, N. T., Oumeraci, H. and Partenscky, H. W., **1994**. Numerical Modelling of Breaking Wave Impacts on a Vertical Wall, *Coastal Engineering Proceedings*, **24**, pp. 1672–1686.

Yang, X., **2017**. Study on slamming pressure calculation formula of plunging breaking wave on sloping sea dike, *International Journal of Naval Architecture and Ocean Engineering*, **9**(4), pp. 439–445.

Young, A. P., **2017**. Decadal-scale coastal cliff retreat in southern and central California, *Geomorphology*, **300**, pp. 164–175.

Young, A. P., Adams, P. N., O'Reilly, W. C., Flick, R. E. and Guza, R. T., **2011**. Coastal cliff ground motions from local ocean swell and infragravity waves in southern California, *Journal of Geophysical Research: Oceans*, **116**(9), pp. 1–11.

Young, A. P., Guza, R. T., Dickson, M. E., O'Reilly, W. C. and Flick, R. E., **2013**. Ground motions on rocky, cliffed, and sandy shorelines generated by ocean waves, *Journal of Geophysical Research: Oceans*, **118**(12), pp. 6590–6602.

Young, A. P., Guza, R. T., Flick, R. E., O'Reilly, W. C. and Gutierrez, R.,

2009. Rain, waves, and short-term evolution of composite seacliffs in southern California, *Marine Geology*, **267**, pp. 1–7.

Young, A. P., Guza, R. T., O'Reilly, W. C., Burvingt, O. and Flick, R. E., **2016**. Observations of coastal cliff base waves, sand levels, and cliff top shaking, *Earth Surface Processes and Landforms*, **41**(11), pp. 1564–1573.

Young, R. W., Bryant, E. A. and Price, D. M., **1996**. Catastrophic wave (tsunami?) transport of boulders in southern New South Wales, Australia, *Zeitschrift für Geomorphologie*, **40**(2), pp. 191–207.

Zhang, S., Yue, D. and Tanizawa, K., **1996**. Simulation of plunging wave impact on a vertical wall, *Journal of Fluid Mechanics*, **327**, pp. 221–254.

11. Appendix

Matlab: Extracting impact data from raw pressure

```
%% Choose dataset and load data from master table

% Inputs
depdate = '20170220';
sitenum = '2';

% Get data
data = sprintf('site%s_%s.mat',sitenum,depdate);
tabledata = sprintf('T%s',depdate);
foldername = sprintf('Field_%s',depdate);
T = loa d('D:\OneDrive\Fieldwork\Pressure
tower\Master_tables\Proc_table.mat',tabledata);
load(char(sprintf(string('Y:\\017_PhDs\\SV\\Field_data\\Pressure_tower
\\%s\\%s')...
    ,foldername,data)));

% Convert from table
datavars = struct;
datavars.start_time = char(T.(tabledata){1,1});
num_sensors = T.(tabledata){1,2};
datavars.wl_trend_cutoff = T.(tabledata){:,3};
datavars.wave_gauge_range = cell2mat(T.(tabledata){1,4});
datavars.edits = cell2mat(T.(tabledata){1,5});
datavars.hampel_baseline = T.(tabledata){:,6};
datavars.pressure_shift = T.(tabledata){1,7};
datavars.atmos = T.(tabledata){1,8};

clearvars time time_sm50 tabledata T

%% Edits
if ~isempty(datavars.edits)
    z = cell(1,1);
    zz = cell(1,1);
    edits = strsplit(datavars.edits,',');
    for k = 1:length(edits)
        z{k} = strsplit(edits{k},':');
        if length(z{k}) == 1
           zz{k} = str2double(z{k});
        elseif length(z{k}) == 2
           zz{k} = str2double(z{k}{1}):str2double(z{k}{2});
        end
    end
    for i = 1:num_sensors
        for j = 1:length(zz)
            pres{i}(zz{j}(1):zz{j}(end)) = pres{i}(zz{j}(1)-1);
        end
    end
    clearvars edits z zz i j k
end

% Remove downward spikes??

%% If wl_trend already loaded, ignore. If not, create and store
```

```
% Tidal level (long-term smoothed average) of each
if ~exist('wl_trend','var')
    wl_trend = cell(1);
    for i = 1:num_sensors
        wl_trend{i} = smooth(pres_sm50{i},100000);
        fprintf('sensor %d wl trend complete \n',i)
    end

save(char(sprintf(string('Y:\\017_PhDs\\SV\\Field_data\\Pressure_tower
\\%s\\%s'),...
    foldername,data)),'wl_trend','-append');
end

%% Tidal stats from lowest sensor
if datavars.wave_gauge_range ~= 0
    stats = struct;

    % Find high tide time and height
    [HT_pres,HT_loc] =
findpeaks(wl_trend{16},'MinPeakDistance',length(wl_trend{16})-2);
    tide_temp = datenum(datavars.start_time);
    tide_temp = addtodate(tide_temp, (floor(HT_loc/100/60)),
'minute');
    stats.HT_time = datestr(tide_temp,'mm/dd/yyyy HH:MM:SS');
    stats.HT_height = (round((HT_pres*1000)/(1029 * 9.81),2))+0.1;
    clearvars tide_temp HT_loc HT_pres

    % Downsample sensor 16, detrend and create wave gauge
    downsample16 = downsample(pres{16},1000);
    downsample16 = downsample16(datavars.wave_gauge_range(1)...
        :datavars.wave_gauge_range(end));
    depth16 = (downsample16*1000)/(1029 * 9.81);
    depth16 = depth16 + 0.1;
    downsample16_wl = downsample(wl_trend{16},20);
    depth16_wl = (downsample16_wl*1000)/(1029 * 9.81);
    depth16_wl = depth16_wl(datavars.wave_gauge_range(1)...
        :datavars.wave_gauge_range(end));
    stats.wave_gauge = depth16 - depth16_wl;

    % Calculate wave stats
    format short g
    [stats.Hmax, stats.Hsig, stats.Hrms, stats.Tsig, stats.Tmean,...
        stats.Tmax] = ZDC(stats.wave_gauge,5);
    stats.Celerity = round(sqrt(stats.Hrms*9.81),2);
    stats.atiltness =
atiltness(stats.wave_gauge,5,length(stats.wave_gauge));

    % Save data to matlab table file

    save(char(sprintf(string('D:\\OneDrive\\Fieldwork\\Pressure
tower\\Master_tables\\stats_%s.mat'),...
        depdate)),'stats');

    clearvars downsample16 depth16 downsample16_wl
end
%% Time vectors

% Create time vector for full dataset
```

```
timevec = struct;
timevec.full = datenum(datavars.start_time);
zz = datenum(datavars.start_time);
for i = 1:length(pres{16})
    timevec.full(i) = zz + (i*(1/24/60/60/5000))-(1/24/60/60/5000);
end
clearvars zz

% Create time vector for sm50 dataset
timevec.sm50 = datenum(datavars.start_time);
zz = datenum(datavars.start_time);
for i = 1:length(pres_sm50{16})
    timevec.sm50(i) = zz + (i*(1/24/60/60/100))-(1/24/60/60/100);
end
clearvars zz

% Create time vector for wave gauge
if datavars.wave_gauge_range ~= 0
    timevec.wg = datenum(datavars.start_time);
    zz = datenum(datavars.start_time);
    zz = addtodate(zz,(datavars.wave_gauge_range(1)/5),'second');
    for i = 1:length(stats.wave_gauge)
        timevec.wg(i) = zz + (i*(1/24/60/60/5))-(1/24/60/60/5);
    end
    clearvars zz
end

% Plot and save

if datavars.wave_gauge_range ~= 0
    dateFormat = 15;
    h =
figure;set(h,'Color','w');plot((timevec.wg),stats.wave_gauge,'k',...
        'LineWidth',1.5);
    datetick('x',dateFormat);set(h, 'Position', [100,100,1666,630]);
    xlabel 'Time';ylabel('Local water level (m)');set(h,'Color','w');
    saveas(h,(char(sprintf(string('D:\\OneDrive\\Fieldwork\\Pressure
tower\\Master_graphs\\wave_gauge_%s.jpg'),...
        depdate))),'jpeg');close(h)
end

%% Create edited smoothed dataset
%  Do atmospheric pressure compensation if required

pres_sm50_edit = pres_sm50;
if datavars.atmos == 1
    mean_end = 1;
    atmos_trend = cell(1,1);
    for i = 1:num_sensors
        mean_end = mean(pres_sm50{i}((length(pres_sm50{i})-
1000):(length(pres_sm50{i}))));
        atmos_trend{i} = (0:mean_end/length(pres_sm50{i}):mean_end-
(mean_end/length(pres_sm50{i})));
        atmos_trend{i} = atmos_trend{i}';
        pres_sm50_edit{i} = pres_sm50{i} - atmos_trend{i};
        wl_trend{i} = wl_trend{i} - atmos_trend{i};
        clearvars mean_end
    end
    clearvars atmos_trend
end
```

```
%% Remove indundated data from smoothed edited dataset

for i = 1:num_sensors
    rows_to_remove = any(wl_trend{i}>datavars.wl_trend_cutoff(i), 2);
    pres_sm50_edit{i}(rows_to_remove,:) = 0;
end
clearvars rows_to_remove

%% Hampel filter of edited data

if ~isnan(datavars.hampel_baseline(1))
    for i = 1:num_sensors
        baseline = pres_sm50_edit{i};
        baseline(baseline>datavars.hampel_baseline(i)) = NaN;
        baseline = hampel(baseline,5000);
        pres_sm50_edit{i} = pres_sm50_edit{i} - baseline;
        clearvars baseline
        fprintf('Sensor %d Hampel filter applied \n',i)
    end
end

%% Zero last 30 seconds of data on each pick due to filter artefacts

temp = pres_sm50_edit;
for i = 1:num_sensors
    temp{i} = flipud(temp{i});
    vec = find(temp{i},1);
    temp{i}(vec:(vec+3000)) = 0;
    temp{i} = flipud(temp{i});
end
pres_sm50_edit = temp;
clearvars vec temp

%% Add/subtract pressure to aid picking algorithm
for i = 1:num_sensors
    pres_sm50_edit{i} = pres_sm50_edit{i} + datavars.pressure_shift;
end

%% Input EDP for STA-LTA picking

l_sta = 0.01;% STA window length (s)
l_lta = 0.8;% LTA window length (s)
t_on = 1.6;% STA/LTA trigger on threshold
t_off = 1.2;% STA/LTA trigger off threshold
min_sep = 0.0;% Skip ahead after end of event (s)
min_dur = 0.0;% Minimum event duration (s)

edp = [l_sta l_lta t_on t_off min_sep min_dur];
clearvars l_sta l_lta t_on t_off min_sep min_dur

%% Event picking

%Create waveform objects
w = cell(1,1);
for i = 1:num_sensors
    w{i} = waveform('network.station.location.p1',100,...
        datavars.start_time, pres_sm50_edit{i},'kPa');
end
```

```
% Pick events

raw_sst_w = w;
for i = 1:num_sensors
    raw_sst_w{i} = sta_lta(w{i},'edp',edp,'eot','wfa',...
        'lta_mode','frozen'); % waveform out
    fprintf('sensor %d picked \n',i)
end

%% Event picks clean-up
% Remove events with max value under 0.2 kPa

filt_sst_w{i} = raw_sst_w{i};
for i = 1:num_sensors
    filt_sst_w{i} = raw_sst_w{i};
    for j = 1:length(raw_sst_w{i})
        filt_sst_w{i}(j) = set(filt_sst_w{i}(j), 'data',...
            inpaint_nans(get(filt_sst_w{i}(j),'data')));
        if le((max(get(filt_sst_w{i}(j),'data'))),0.2) == 1
            filt_sst_w{i}(j) = set(filt_sst_w{i}(j), 'freq', 1);
        end
    end
end
disp('Small events removed (w)')

filt_sst_m = cell(1,1);
for i = 1:num_sensors
    filt_sst_w{i} = filt_sst_w{i}(get(filt_sst_w{i},'freq')~=1);
    if isempty(filt_sst_w{i}) == 0
        filt_sst_m{i} = wfa2sst(filt_sst_w{i});
    else
        filt_sst_w{i} =
waveform('network.station.location.p1',100,...
            datavars.start_time,[],'kPa');
        filt_sst_m{i} =  0;
    end
end
clearvars raw_sst_w raw_sst_m
disp('Small events removed (m)')

%% Remove sensors with no picks

empty_wave = zeros(1,num_sensors);
for i = 1:num_sensors
    if isempty(filt_sst_w{i})
        empty_wave(i) = 1;
    end
end
if sum(empty_wave) ~= 0
    min_sensors = num_sensors-find(fliplr(empty_wave),1)+2;
else
    min_sensors = 1;
end
clearvars empty_wave

%%Remove events where max-min is less than 0.5 kPa

for i = min_sensors:num_sensors
```

```
    for j = 1:length(filt_sst_w{i})
        if max(get(filt_sst_w{i}(j),'data'))-
min(get(filt_sst_w{i}(j),'data')) <= 0.5
            filt_sst_w{i}(j) = set(filt_sst_w{i}(j), 'freq', 1);
        end
    end
end
for i = min_sensors:num_sensors
    filt_sst_w{i} = filt_sst_w{i}(get(filt_sst_w{i},'freq')~=1);
end
disp('Small event differences removed (w)')
for i = min_sensors:num_sensors
    filt_sst_m{i} = wfa2sst(filt_sst_w{i});
end
disp('Small event differences removed (m)')

%% Combine duplicate events and remove overlaps
% Overlaps are removed such that only highest max event is kept

samp_length = 1/(24*60*60*100);
for i = min_sensors:num_sensors
    for j = 1:(length(filt_sst_w{i})-1)
        startt = get(filt_sst_w{i}(j),'start');
        durt = get(filt_sst_w{i}(j),'duration');
        startt_next = get(filt_sst_w{i}(j+1),'start');
        if startt_next == startt + durt - samp_length
            filt_sst_m{i}(j+1,1) = filt_sst_m{i}(j,1);
            filt_sst_m{i}(j,1) = 0;
            filt_sst_m{i}(j,2) = 0;
        end
    end
    clearvars startt durt startt_next
    % Add manual pad
    for j = 1:(length(filt_sst_w{i}))
        filt_sst_m{i}(j,1) = filt_sst_m{i}(j,1) - 5*samp_length;
    end
end
for i = min_sensors:num_sensors
    filt_sst_m{i}(any(filt_sst_m{i}==0,2),:)=[];
    filt_sst_w{i} = sst2wfa(filt_sst_m{i},w{i});
    fprintf('sensor %d duplicates cleared and splits combined \n',i)
end
clearvars samp_length edp pres_sm50_edit

%% Plot picks

m = cell(1,1);
for i = min_sensors:num_sensors
    for j = 1:length(filt_sst_w{i})
        m{i}(j) = max(get(filt_sst_w{i}(j),'data'));
    end
    m{i} = max(m{i});
end
m = max(cell2mat(m));
for i = 1:num_sensors
    subplot(4,4,i)
    for j = 1:length(filt_sst_w{i})
        if i < min_sensors
            plot(1,0);ylim([-0.1 m]);xlim([0 1]);
            title(sprintf('Sensor %d, 0 events',i))
```

```
        else
            xplot = 0:0.01:(length(get(filt_sst_w{i}(j),'data'))/100)-
0.01;
            plot(xplot,get(filt_sst_w{i}(j),'data')); ylim([-0.1 m])
            if i == 5
                ylabel('Pressure (kPa)');
            end
            if i == 14
                xlabel('Seconds');
            end
            if j == length(filt_sst_w{i})
            title(sprintf('Sensor %d, %d events',i,j))
            end
            hold on
        end
    end
    fprintf('sensor %d plotted \n',i)
    set(gcf,'Color','w');
    hold off
end
set(gcf, 'Position', [1,41,1920,960]);
saveas(gcf,(char(sprintf(string('D:\\OneDrive\\Fieldwork\\Pressure
tower\\Master_graphs\\picksplot_%s.jpg'),...
    depdate))),'jpeg');close(gcf)
clearvars i j m xplot

%% Convert picks to full sample rate
filt_sst_f_w = cell(1,1);
 w_f = cell(1,1);
for i = min_sensors:num_sensors
    w_f{i} = waveform('network.station.location.p1',5000,...
        datavars.start_time, pres{i},'kPa');
    disp('Waveform created')
end
for i = min_sensors:num_sensors
    filt_sst_f_w{i} = sst2wfa(filt_sst_m{i},w_f{i});
    disp('Converted')
end

%% Save out picks

if
exist(sprintf('Y:\\017_PhDs\\SV\\Field_data\\Pressure_tower\\%s\\Analy
sis',...
        foldername),'dir') ~= 7

mkdir(sprintf('Y:\\017_PhDs\\SV\\Field_data\\Pressure_tower\\%s\\Analy
sis'...
        ,foldername))
end

save(char(sprintf(string('Y:\\017_PhDs\\SV\\Field_data\\Pressure_tower
\\%s\\Analysis\\picks_%s'),...

foldername,depdate)),'w','w_f','filt_sst_w','filt_sst_m','filt_sst_f_w
','-v7.3');


%% Wave impact stats for table
```

```
% Wave height

% Max impact pressure
Pmax = cell(1,1);
for i = min_sensors:num_sensors
    Pmax{i} = 1:length(filt_sst_f_w{i});
    for k = 1:length(filt_sst_f_w{i})
        Pmax{i}(k) = max(get(filt_sst_f_w{i}(k),'data'));
    end
    Pmax{i} = Pmax{i}';
end

% Find impact max time
Tmax = cell(1,1);
for i = min_sensors:num_sensors
    Tmax{i} = 1:length(filt_sst_w{i});
    for k = 1:length(filt_sst_w{i})
        time = get(filt_sst_w{i}(k),'start');
        [~,max_loc] = max(get(filt_sst_w{i}(k),'data'));
        Tmax{i}(k) = (max_loc/(24*60*60*100)) + time;
        clearvars max_loc time;
    end
    fprintf('sensor %d complete \n',i)
    Tmax{i} = Tmax{i}';
end


% Find wave impact times
if exist('stats','var')
    Htime = zeros(1,1);
    [indH,indLoc] =
findpeaks(stats.wave_gauge,5,'MinPeakDistance',1,'MinPeakProminence',0
.1);
    for i = min_sensors:length(indLoc)
        Htime(i) =
addtodate(timevec.wg(1),indLoc(i)*1000,'millisecond');
    end
    clearvars indLoc
    Wheight = cell(1,1);
    Wtime = cell(1,1);
    for i = min_sensors:num_sensors
        for j = 1:length(Tmax{i})
            [c,index] = min(abs(Htime-Tmax{i}(j)));
            closestValues = Htime(index);
            if abs(closestValues - Tmax{i}(j)) < ((1/24/60/60)*1)
                Wheight{i}(j) = indH(index);
                Wtime{i}(j) = closestValues;
            else
                Wheight{i}(j) = NaN;
                Wtime{i}(j) = NaN;
            end
        end
    end

    % Match impact times with wave times
    % Is basically a clustering analysis with threshold of 1s
    index_rmv = cell(1,16);
    index_rmv2 = cell(1,16);
    for i = min_sensors:num_sensors
        index_rmv2{i} = zeros(1,length(Wheight{i}));
```

```
        for j = 2:(length(Wheight{i}))
            if ~isnan(Wheight{i}(j)) && Wheight{i}(j) == Wheight{i}(j-
1)
                index_rmv{i}(j) = 1;
            else
                index_rmv{i}(j) = 0;
            end
        end
    end
    % Remove duplicates and create index to remove duplicates for
other
    % variables
    for i = min_sensors:num_sensors
        for j = 2:(length(Wheight{i})-1)
            if index_rmv{i}(j) == 1 && index_rmv{i}(j-1) == 0 &&
index_rmv{i}(j+1) == 0
                [~,loc] = max([Pmax{i}(j-1) Pmax{i}(j)]);
                if loc == 1
                    index_rmv2{i}(j) = 1;
                else
                    index_rmv2{i}(j-1) = 1;
                end
            elseif index_rmv{i}(j) == 1 && index_rmv{i}(j-1) == 0 &&
index_rmv{i}(j+1) == 1
                [~,loc] = max([Pmax{i}(j-1) Pmax{i}(j) Pmax{i}(j+1)]);
                if loc == 1
                    index_rmv2{i}(j) = 1;
                    index_rmv2{i}(j+1) = 1;
                elseif loc == 2
                    index_rmv2{i}(j+1) = 1;
                    index_rmv2{i}(j-1) = 1;
                else
                    index_rmv2{i}(j-1) = 1;
                    index_rmv2{i}(j) = 1;
                end
            elseif index_rmv{i}(j) == 0
                1;
            end
        end
    end
    index_rmv = index_rmv2';
    clearvars index_rmv2 closestValues c

    % Replace ssts?????

    % Remove duplicates from Wheight
    for i = min_sensors:num_sensors
        Wheight{i} = Wheight{i}';
        Wheight{i}(index_rmv{i} == 1) = [];
    end
    Wheight =
cat(1,Wheight{1},Wheight{2},Wheight{3},Wheight{4},Wheight{5},...

Wheight{6},Wheight{7},Wheight{8},Wheight{9},Wheight{10},Wheight{11},..
.
        Wheight{12},Wheight{13},Wheight{14},Wheight{15},Wheight{16});

    % Remove duplicates from Wtime
    for i = min_sensors:num_sensors
        Wtime{i} = Wtime{i}';
        Wtime{i}(index_rmv{i} == 1) = [];
```

```
    end
    Wtime = cat(1,Wtime{1},Wtime{2},Wtime{3},Wtime{4},Wtime{5},...
        Wtime{6},Wtime{7},Wtime{8},Wtime{9},Wtime{10},Wtime{11},...
        Wtime{12},Wtime{13},Wtime{14},Wtime{15},Wtime{16});

    % Remove duplicates from Pmax
    for i = min_sensors:num_sensors
        Pmax{i}(index_rmv{i} == 1) = [];
    end
    Pmax =
cat(1,Pmax{1},Pmax{2},Pmax{3},Pmax{4},Pmax{5},Pmax{6},Pmax{7},Pmax{8}.
..

,Pmax{9},Pmax{10},Pmax{11},Pmax{12},Pmax{13},Pmax{14},Pmax{15},Pmax{16
});

    % Remove duplicates from Tmax
    for i = min_sensors:num_sensors
        Tmax{i}(index_rmv{i} == 1) = [];
    end
    Tmax =
cat(1,Tmax{1},Tmax{2},Tmax{3},Tmax{4},Tmax{5},Tmax{6},Tmax{7},Tmax{8}.
..

,Tmax{9},Tmax{10},Tmax{11},Tmax{12},Tmax{13},Tmax{14},Tmax{15},Tmax{16
});
else
    % If sensor 16 is out and there's no wave gauge
    % Find duplicates and create index
    index_rmv = cell(1,1);
    for i = min_sensors:num_sensors
        index_rmv{i} = [0;diff(Pmax{i}) == 0];
        Pmax{i}(index_rmv{i} == 1) = [];
    end
    if num_sensors == 16
        Pmax =
cat(1,Pmax{1},Pmax{2},Pmax{3},Pmax{4},Pmax{5},Pmax{6},Pmax{7},Pmax{8}.
..

,Pmax{9},Pmax{10},Pmax{11},Pmax{12},Pmax{13},Pmax{14},Pmax{15},Pmax{16
});
    elseif num_sensors == 15
        Pmax =
cat(1,Pmax{1},Pmax{2},Pmax{3},Pmax{4},Pmax{5},Pmax{6},Pmax{7},Pmax{8}.
..

,Pmax{9},Pmax{10},Pmax{11},Pmax{12},Pmax{13},Pmax{14},Pmax{15});
    end

    % Replace unknown values
    SigH = nan(length(Pmax),1);
    waterdepth = zeros(length(Pmax),1);
    WaveH = nan(length(Pmax),1);
    hH0 = nan(length(Pmax),1);
    Wheight = nan(length(Pmax),1);
    Wtime = nan(length(Pmax),1);
    % use Pmax duplicate index to create impact times
    for i = min_sensors:num_sensors
        Tmax{i}(index_rmv{i} == 1) = [];
    end
    if num_sensors == 16
```

```
        Tmax =
cat(1,Tmax{1},Tmax{2},Tmax{3},Tmax{4},Tmax{5},Tmax{6},Tmax{7},Tmax{8}.
..

,Tmax{9},Tmax{10},Tmax{11},Tmax{12},Tmax{13},Tmax{14},Tmax{15},Tmax{16
});
    elseif num_sensors == 15
        Tmax =
cat(1,Tmax{1},Tmax{2},Tmax{3},Tmax{4},Tmax{5},Tmax{6},Tmax{7},Tmax{8}.
..

,Tmax{9},Tmax{10},Tmax{11},Tmax{12},Tmax{13},Tmax{14},Tmax{15});
    end
end

% Create wave index from number of impacts
t = cell(1,1);
wave_index = 1:length(Pmax);
for i = 1:length(wave_index)
    t(i) = cellstr(num2str(wave_index(i)));
end
wave_index = t';

% Elevation of impact above platform

elevs = [1.7 1.6 1.5 1.4 1.3 1.2 1.1 1.0 0.9 0.8 0.7 0.6 0.5 0.4 0.3
0.1];
elevation = cell(1,1);
for i = min_sensors:num_sensors
    elevation{i} = ones(length(filt_sst_f_w{i}),1)*elevs(i);
end
% Remove duplicates from elevation

for i = min_sensors:num_sensors
    elevation{i}(index_rmv{i} == 1) = [];
end
if num_sensors == 16
    elevation =
cat(1,elevation{1},elevation{2},elevation{3},elevation{4},...

elevation{5},elevation{6},elevation{7},elevation{8},elevation{9},...

elevation{10},elevation{11},elevation{12},elevation{13},elevation{14},
...
        elevation{15},elevation{16});
elseif num_sensors == 15
    elevation =
cat(1,elevation{1},elevation{2},elevation{3},elevation{4},...

elevation{5},elevation{6},elevation{7},elevation{8},elevation{9},...

elevation{10},elevation{11},elevation{12},elevation{13},elevation{14},
...
        elevation{15});
end

clearvars elevs

% Impulse
format long g
```

```
Impulse = cell(1,1);
for i = min_sensors:num_sensors
    Impulse{i} = 1:length(filt_sst_f_w{i});
    for k = 1:length(filt_sst_f_w{i})
        impulse = get(filt_sst_f_w{i}(k),'data');
        impulset =
([1:length(get(filt_sst_f_w{i}(k),'data'))]./5000)';
        Impulse{i}(k) = trapz(impulset,impulse);
    end
    Impulse{i} = Impulse{i}';
end
clearvars impulse impulset
% Remove duplicates from Impulse
for i = min_sensors:num_sensors
    Impulse{i}(index_rmv{i} == 1) = [];
end
if num_sensors == 16
    Impulse =
cat(1,Impulse{1},Impulse{2},Impulse{3},Impulse{4},Impulse{5},...

Impulse{6},Impulse{7},Impulse{8},Impulse{9},Impulse{10},Impulse{11},..
.
        Impulse{12},Impulse{13},Impulse{14},Impulse{15},Impulse{16});
elseif num_sensors == 15
    Impulse =
cat(1,Impulse{1},Impulse{2},Impulse{3},Impulse{4},Impulse{5},...

Impulse{6},Impulse{7},Impulse{8},Impulse{9},Impulse{10},Impulse{11},..
.
        Impulse{12},Impulse{13},Impulse{14},Impulse{15});
end

% Maximum rate of change of pressure

Pdiff  = cell(1,1);
for i = min_sensors:num_sensors
    Pdiff{i} = 1:length(filt_sst_f_w{i});
    for k = 1:length(filt_sst_f_w{i})
        Pdiff{i}(k) = max(diff(get(filt_sst_f_w{i}(k),'data')));
    end
    Pdiff{i} = Pdiff{i}';
end
% Remove duplicates from Pdiff
for i = min_sensors:num_sensors
    Pdiff{i}(index_rmv{i} == 1) = [];
end
if num_sensors == 16
    Pdiff =
cat(1,Pdiff{1},Pdiff{2},Pdiff{3},Pdiff{4},Pdiff{5},Pdiff{6},Pdiff{7},.
..

Pdiff{8},Pdiff{9},Pdiff{10},Pdiff{11},Pdiff{12},Pdiff{13},Pdiff{14},..
.
        Pdiff{15},Pdiff{16});
elseif num_sensors == 15
    Pdiff =
cat(1,Pdiff{1},Pdiff{2},Pdiff{3},Pdiff{4},Pdiff{5},Pdiff{6},Pdiff{7},.
..

Pdiff{8},Pdiff{9},Pdiff{10},Pdiff{11},Pdiff{12},Pdiff{13},Pdiff{14},..
.
```

```
        Pdiff{15});
end

% Average significant wave height over deployment
if exist('stats','var')
    Hs = ones(length(wave_index),1)*stats.Hsig;
else
    Hs = nan(length(wave_index),1);
end
% Water depth
if exist('stats','var')
    waterdepth  = ((wl_trend{16}*1000)/(1029 * 9.81))+0.1;
    waterdepth_wvfm = waveform('network.station.location.p1',100,...
            datavars.start_time, waterdepth,'metres');
    waterdepth = cell(1,1);
    for i = min_sensors:num_sensors
        waterdepth{i} = sst2wfa(filt_sst_m{i},waterdepth_wvfm);
    end
    waterdepth2 = cell(1,1);
    for i = min_sensors:num_sensors
        waterdepth2{i} = 1:length(waterdepth{i});
        for k = 1:length(waterdepth{i})
            waterdepth2{i}(k) = mean(get(waterdepth{i}(k),'data'));
        end
        waterdepth2{i} = waterdepth2{i}';
    end
    waterdepth = waterdepth2;
    % Remove duplicates from waterdepth
    for i = min_sensors:num_sensors
        waterdepth{i}(index_rmv{i} == 1) = [];
    end
    waterdepth =
cat(1,waterdepth{1},waterdepth{2},waterdepth{3},waterdepth{4},...

waterdepth{5},waterdepth{6},waterdepth{7},waterdepth{8},waterdepth{9},
...

waterdepth{10},waterdepth{11},waterdepth{12},waterdepth{13},...
        waterdepth{14},waterdepth{15},waterdepth{16});
    waterdepth(waterdepth < 0.2) = 0; % Remove depths when sensor 16
is not inundated

    clearvars waterdepth_wvfm waterdepth2 i j k depth16_wl

    % Wave height / Water depth ratio
    hH0 = (Wheight./waterdepth);
end
%% Create table


wavetable =
table(elevation,Pmax,Impulse,Pdiff,Hs,waterdepth,Wheight,...
    hH0,Tmax,Wtime,'RowNames',wave_index);

wavetable.Properties.VariableNames =...
    {'Elevation' 'PressureMax' 'PressureImp' 'PressureChng' 'SigH'
'WaterDpth' 'WaveH' 'hH0' 'ImpactTime' 'WaveTime'};

writetable(wavetable,(char(sprintf(string...
```

```
    ('D:\\OneDrive\\Fieldwork\\Pressure
tower\\Master_tables\\wavetable_%s.xlsx'),...
    depdate))))

save(char(sprintf(string('D:\\OneDrive\\Fieldwork\\Pressure
tower\\Master_tables\\wavetable_%s.mat'),...
    depdate)),'wavetable');


%%
```